A Thermodynamic Approach to Modelling Brittle-Ductile and Localised Failure of Rocks Using Damage Mechanics and Plasticity Theory

A Thesis Submitted for the Degree of Doctor of Philosophy

School of Civil, Environmental and Mining Engineering, the University of Adelaide

by

Arash Mir

May 2017

Abstract

A Thermodynamic Approach to Modelling Brittle-Ductile and Localised Failure of Rocks Using Damage Mechanics and Plasticity Theory

A Thesis Submitted for the Degree of Doctor of Philosophy

Arash Mir

School of Civil, Environmental and Mining Engineering, the University of Adelaide May 2017

Recent advances in computational mechanics and numerical simulation techniques enable more efficient and realistic geotechnical and mining designs and analyses. A successful numerical simulation requires a robust and rigorous constitutive model, which is capable of predicting the most fundamental features of material behaviour. In conjunction with numerical simulations, the complex behaviour observed in geomaterials also encourages the development of more capable and realistic constitutive models. The key aspects of developing constitutive models for rocks are to capture the essential features of rock deformation and failure, observed in experimental studies or in the field. These features include brittle behaviour, which refers to a sudden post-peak strain softening, ductile behaviour which is interpreted as the capacity for undergoing substantial inelastic deformation without gross fracturing and the transitional state between these two regimes of behaviour. Another important behavioural feature of rocks and also other geomaterials is the localisation of deformation within a narrow band. Upon the onset of localisation, the homogeneity of stress and strain fields is lost and any macroscopic definition of stress and strain is no longer physically meaningful. It is also essential for any constitutive model to be thermodynamically admissible.

The focus of this study is on the development of thermodynamically consistent constitutive models for rocks. The development of the constitutive models is carried out within the framework of generalised thermodynamics to ensure the thermodynamic admissibility of the models. The key feature of the generalised thermodynamic framework is that the entire constitutive relations can be derived by explicitly defining two scalar functions, namely, an energy potential and a dissipation function. In this study, it is demonstrated that how the most fundamental mechanisms of deformation and energy dissipation can be incorporated into the model formulation by enriching the two thermodynamic functions with extra kinematic constraint equations. The theories of plasticity and continuum damage mechanics are also used to describe the mechanisms of energy dissipation and

deformation. By adopting the thermodynamic approach, the coupling between damage and plasticity is specified in the formulation of the dissipation function, which is subsequently transformed (using a degenerate Legendre transformation) to a single generalised yield function. This method for coupling damage and plasticity facilitates the numerical implementation of the models as a single yield function controls the simultaneous evolution of damage and plastic strains. An important aspect of the coupled-damage plasticity models developed in this study is that, in accordance with experimental observations, the initial yield surface is transformed to a final failure envelope due to the evolution of the internal variables of the models. Owing to this feature of the models, rock mechanical behaviour under various stress states can be captured without any need for separately introducing hardening/softening rules into the model formulation.

The constitutive models developed in this study are examined against experimental data from drained triaxial tests on rock specimens available in the literature. It should be noted that the localisation of deformation and the subsequent inhomogeneity of the kinematic field and stress redistribution give rise to the deterministic size effect problem. It is, therefore, inferred that experimental data from rock specimens are not merely representative of intrinsic rock material behaviour but are also influenced by the specimen size. Finite element (FE) simulations of cylindrical rock specimens are, therefore, carried out to study the specimen size effect on its overall mechanical response. Classical constitutive models are developed for a homogeneous representative volume element (RVE) without considering the features of localised failure and deterministic size effect. After the completion of model formulation, regularisation techniques, such as non-local or gradient enhancements, are employed to eliminate the numerical instabilities and ill-posedness of the boundary value problems (BVPs) caused by the localisation of deformation. These approaches, however, may lead to computational inefficiency, particularly, in large scale modelling applications. In this study, a thermodynamic approach is developed to model the localised deformation and failure of geomaterials in a rigorous and consistent manner. To this end, the underlying mechanisms of localised failure are described at the material level for a non-homogeneous RVE (an RVE containing a localisation band). Hence, the kinematic dependency between the two material phases beyond the onset of localisation is described by means of some kinematic constraint equations. Due to the direct incorporation of the essential mechanisms of localised failure in the constitutive equations, calibration and identification of model parameters can be carried out in a more consistent and physically meaningful manner. Additionally, introducing the features of localised failure at the material level can significantly reduce the cost of computation in large scale modelling applications in geotechnical and mining engineering.

Acknowledgement

I would like to express my sincere gratitude to my major advisor Dr Giang D. Nguyen for his continuous and generous support of my Ph.D studies and for his patience, encouragement, and immense knowledge. His guidance and his insightful remarks helped me in all the time of research and writing of this thesis. I would also like to acknowledge the invaluable assistance and support from my co-advisor, Dr Abdul Hamid Sheikh.

I would also like to especially thank my major advisor Dr Giang D. Nguyen for his financial supports (grant DP140100945 (Australian Research Council)) during the last few months of my Ph.D studies.

I would also like to express my gratitude to Professor Guy T. Houlsby for generating the idea of developing a thermodynamic approach for modelling the localised failure of geomaterials, presented in Chapter 6 of this thesis.

My sincere thanks also go to Dr Navid Mozzafari and Dr Mousumi Mukherjee for technical discussions and their help with numerical simulations. I also greatly appreciate the support of Ms Jillian Hume, who helped me for winning the Adelaide Graduate Research Scholarship (AGRS).

Finally, my special thanks go to my wife, Dr Shadab Rashtak, for her love, understanding, and endurance during the years of my Ph.D studies. We both are grateful to our parents for their love and encouragement during the course of my Ph.D.

Table of Contents

List of Figures

List of Figures

List of Tables

CHAPTER 1

Introduction

1.1. Introduction

Constitutive modelling of rock and rock masses is the backbone of any numerical simulation in many mining and civil engineering projects. Proper understanding and modelling of rock behaviour would facilitate a safe and economical design in geotechnical and mining engineering field operations. Like any other geological material, such as concrete and soil, rock behaviour is also sensitive to pressure and it can change dramatically from very brittle at low pressure to ductile under substantially high pressure. Other important factors that can influence the mechanical response of rock material include temperature and rate of deformation. In mining and geotechnical operations, the effects of blasting, drilling or tunnelling and also seismic forces can dramatically change the stresses acting on the surrounding rock formations. Therefore, the prediction of failure (or an excessive inelastic deformation) would necessitate a model able to capture, as accurately as possible, the macroscopic behaviour of rocks under rather complex stress states, varying temperature and different loading rates.

Nevertheless, the complex behaviour of rocks and rock masses, owing to their non-homogeneous and anisotropic nature, cannot always be reflected correctly and straightforwardly in constitutive models. Furthermore, the inelastic deformation and failure of rock material involve localisation of deformation, which introduces an additional heterogeneity to the already non-homogeneous material. Localised failure poses serious challenges in constitutive modelling and numerical simulation of rock structures, particularly in large-scale problems. A constitutive model which accurately reflects the complex behaviour of rock material would facilitate the numerical simulation of large-scale problems, commonly encountered in mining and civil engineering projects.

1.2. Aims and Scope of the Present Study

The main objective of this study is to develop thermodynamically admissible constitutive models for rocks, with emphasis on rigour and consistency of the model formulation and identification of model parameters based on experimental observations. In the development of the constitutive models, the focus is put on capturing essential macroscopic features of rock behaviour under various stress conditions. These features include brittle behaviour with post-peak softening, the transitional state from brittle to ductile and ductile behaviour under high pressure, dilative and contractive responses corresponding to the applied pressure and the localisation of deformation. Another important feature that is usually ignored or not addressed adequately in constitutive modelling of rocks is localised failure, which includes the onset and orientation of localisation bands, together with their evolution during post-peak deformation processes. To accomplish this aim, theories of plasticity and continuum damage mechanics are used to construct the constitutive models within the well-established framework of generalised thermodynamics or thermodynamics with internal variables (TIV).

It is important for any constitutive model to be thermodynamically admissible. Constitutive models which are not thermodynamically admissible, although useful is some engineering applications, may not be always confidently relied upon, especially under conditions different from those under which the model has been developed. Examples of such models can be given as those developed based on the traditional micro-plane approach. Since it was first proposed by Bazant and Oh [1], the micro-plane approach became progressively more popular for the description of the constitutive behaviour of a number of engineering materials such as concrete, rock, ceramics and ice [2-17]. Although successfully implemented and extensively verified with experimental results, the thermodynamic consistency of traditional micro-plane models could not be guaranteed in all loading situations. It turned out later that, in the way these models were introduced, some of the stress variables used at the micro-plane level are not conjugate quantities to their strain counterparts. The lack of full thermodynamic consistency (actually common to many constitutive models used in engineering practice) seems to have had little influence on the representation of available experimental data, given the excellent fits obtained under numerous different loading conditions. Nevertheless, there must undoubtedly exist load sequences for which energy is spuriously dissipated or generated and could be large enough to distort the predicted material response [18]. In any case, it is obvious that an approach in

which conjugacy of variables and thermodynamic consistency is assured should always be preferable. In fact, thermodynamics admissibility is a necessary, but not sufficient, condition for a constitutive model.

In principle, it is possible to apply the requirements for the thermodynamic admissibility of a constitutive model retrospectively after the completion of the model formulation. This approach, however, may lead to introducing *ad hoc* assumptions in the formulation of the model. A more rigorous and consistent approach is to construct the constitutive model within a well-established thermomechanical framework. To this end, the framework of generalised thermodynamics [19-21] will be extensively used in this study as a basis for the development of constitutive models and also for enhancing them to effectively deal with localisation issues at the constitutive level. The key aspect of the generalised thermodynamics framework is that the entire constitutive relations can be obtained through explicitly defining two scalar functions, i.e. an energy potential and a dissipation function [19, 21, 22]. In this regard, it is possible both to recast the existing models [e.g. 23] and to develop new constitutive models within this frame work [e.g. 24]. Generalised thermodynamics is a thermodynamic field theory which has a strong link with (and even inseparable from) continuum mechanics [21]. Therefore, theories of continuum mechanics, such as elasticity, plasticity and continuum damage mechanics can be employed to explicitly define the two scalar thermodynamic functions.

Theories of plasticity and continuum damage mechanics (CDM) have been widely used to describe the inelastic behaviour of rocks. However, neither of these theories alone can appropriately account for both the observable strength, stiffness reduction and residual strains, which are characteristic of the inelastic behaviour of most engineering materials. Therefore, the specification of coupling and interaction between damage and plasticity in the model formulation is necessary if the model is to follow the experimental observations accurately. A coupled damage-plasticity approach is hence adopted in this study to describe the mechanical behaviour of rocks. In this sense, the strain softening, stiffness degradation and residual strains can be captured by means of coupled damage-plasticity models. From a phenomenological perspective, it is common practice in constitutive modelling to encompass all the underlying micro-mechanisms leading to strength and stiffness degradation (e.g. micro-cracking, grain crushing, etc.) within a damage indicator, which can be a scalar or a tensor of higher orders. Similarly, all the micromechanical phenomena, the manifestation of which, is observed as residual strains at the macro scale (e.g. frictional sliding, asperity

interlocking, diffusional flow etc.) are represented by plastic strain tensor. On this account, the damage indicator and plastic strain tensor can be interpreted as macroscopic variables which, characterise the material behaviour at the microscopic level. In thermodynamics terminology, the damage variable and plastic strains are termed as internal variables, within which, the history of inelastic deformations or dissipative processes is encapsulated. In principle, in order to accurately replicate the material behaviour, an infinite number of internal variables can be introduced into the model formulation. In practice, however, only a few internal variables, provided ingenuity is practised in selecting them, would suffice to give reasonable approximations to the real material behaviour [19].

In this study, coupled damage plasticity models are developed to describe the mechanical behaviour of rocks. Coupling between damage and plasticity is specified in the formulation of the dissipation rate function, which in turn, gives rise to the existence of a single yield function. This yield function then controls the simultaneous evolution of all internal variables, i.e. the scalar damage variable and plastic strains. It is also demonstrated that owing to this single generalised yield function that evolves to a failure function, under the effects of both damage and plastic deformation, the proposed model facilitates the simulation of rock behaviour under a wide range of confining pressures. In particular, both brittle and ductile responses and the brittle-ductile transition, together with the dilative and contractive behaviour, are captured due to the inherent features of the model, without any need for separately introducing softening/hardening laws. In addition, it is demonstrated, through the development of two separate constitutive models for porous and compact rocks, how different deformation mechanisms can be taken into consideration by appropriately selecting and defining the internal variables of the models. The main motivation for these developments is the observed differences between the dilational/contractive responses of porous and compact rocks. According to experimental observations, while porous rocks exhibit compaction under high confining pressures compact rocks show a marked dilative response even at pressures well beyond the pressure pertaining to the brittle-ductile transition [25-30]. After presenting the details of the model formulations, parameter identification and calibration procedures, the performance of the models are assessed (at material level) against sets of experimental data from drained triaxial tests on cylindrical rock specimens available in the literature.

One of the most important aspects that must be taken into consideration when it comes to constitutive modelling of geomaterials, including rocks, is the localisation of

deformation within a band of narrow width, compared to the characteristic size of the structure. The width of the localisation band is predominantly determined by the material microstructure and it is an inherent attribute of the material. For instance, the localisation band is relatively thick in porous sandstones, whereas the thickness of localisation band in hard rocks is infinitesimal [30]. In addition, after the onset of localisation, inelastic deformation mostly concentrates within the localisation band, while the bulk outside the band undergoes unloading. The localisation phenomenon can be viewed from physical, mathematical and numerical perspective.

From a physical perspective, the overall response of a structure (or specimen), its ultimate failure and the total amount of dissipated energy during the course of inelastic deformation are predominantly governed by the material behaviour inside the localisation band. Upon the formation of localisation band, the homogeneity of kinematic fields is lost which in turn leads to the redistribution of the stress field and its bifurcation from the homogeneous state. Therefore, the definitions and measurements of macroscopic stresses and strains are no longer physically meaningful, except as averages. The localisation of deformation and the associated non-homogeneity in stress and strain fields causes the mechanical response of the structure to be dependent on its size and/or characteristic dimensions. This is a rather well-known problem in continuum mechanics, referred to as the deterministic size effect [31]. After the onset of bifurcation the total amount of dissipated energy, due to irreversible deformations, depends only on the width of the localisation band, but not the size of the structure. However, it should be noted that the total strain energy which is stored within a structure scales up with its size. Therefore, whenever the consequence of material failure is the post-peak softening or the lack of ductility, a size effect must be expected [31]. Therefore, the effect of the size of a rock structure (or specimen) on its mechanical response can be observed as progressively steeper post-peak curves and finally the development of a snapback, as the slenderness of the specimen increases.

From a mathematical point of view, localisation of deformation poses some serious challenges to the constitutive modelling of geomaterials based on conventional continuum mechanics. At the onset of localisation, the governing partial differential equations (PDEs) lose their ellipticity and the uniqueness of the solution is lost. In turn, this gives rise to the ill-posedness of the boundary value problems (BVPs) [32]. In numerical simulations, localisation of deformation takes place in the smallest softening zone that can be captured by the numerical discretisation. As a consequence of this localisation, the numerical solution

becomes mesh-dependent and the energy dissipation in the softening zone may approach zero upon mesh refinement. Use of classical continuum mechanics, in this case, has been proven to be inadequate [33-35]. Numerical instability problems that arise due to the localisation of deformation can be eliminated if the ellipticity of the governing differential equations is preserved by means of some regularisation technique, such as nonlocal and gradient approaches or rate-dependent enhancement. However, employing nonlocal and gradient regularisation schemes are still computationally expensive. Hence, the regularisation of the constitutive models developed in this study is based on a simple and computationally cheap rate-dependent enhancement scheme.

Although the numerical instabilities of the BVPs due to the localisation phenomenon can be eliminated by means of a regularisation scheme, ranging from a simple rate-dependent enhancement to more sophisticated approaches (non-local or gradient regularisations), numerical simulations of very large scale problems, commonly encountered in geotechnical and mining engineering, may still be computationally expensive if not impossible. The reason for the computational inefficiency of these models in large scale is that they require a finer numerical resolution than the width of the localisation band in order to simulate the localised failure. It should also be noted that since the locations of the localisation zones are unknown, a very fine numerical resolution would be needed for the entire domain under consideration, resulting in very large and sometimes unmanageable models. This problem can be alleviated by means of kinematic enhancements of the numerical scheme. Examples of these approaches are extended finite element method (XFEM) or enhanced assumed strain (EAS). These approaches, however, have their own limitations, particularly in handling cases where more than one single crack or localisation zone appear within the material element (especially in three dimensional problems).

In this study, a thermodynamic approach is developed to model the localised deformation and failure of geomaterials in a rigorous and consistent manner. To this end, the underlying mechanisms of localised failure are described in the formulation of the energy potential and dissipation function. Towards this aim, the kinematic relationships between the two material phases beyond the onset of localisation are described by means of some kinematic constraint equations and are subsequently used to supplement the dissipation function. This thermodynamic approach produces similar results to those produced by a two-scale approach developed by Nguyen et al [36, 37]. In particular, due to directly incorporating the fundamental mechanisms of localised failure in the definition of the two

thermodynamic functions and subsequently in the constitutive equations, numerical implementation of the model does not require a finer resolution than the bandwidth of the localisation zone. This important feature of the model makes it desirable for large scale modelling applications in geotechnical and mining engineering.

It is beyond dispute that in the process of constitutive modelling for engineering materials numerical aspects such as integration schemes for the rate constitutive equations and also the employment of relevant numerical algorithms for the nonlinear finite element analysis, are of utmost importance. However, the aim of this research is not to carry out extensive numerical simulations of structural problems, but to propose and develop consistent and rigorous approaches for constitutive modelling of geomaterials, focusing on rocks in particular.

1.3. Outline of the Thesis

This thesis is organised into seven chapters; including the current chapter, which serves as an introduction to the aims and scope of this study while outlining the structure of the thesis. The contents of the successive chapters are as follows:

Chapter 2 presents a brief review on various aspects of the mechanical behaviour of rocks observed in experimental studies, as well as in the field. This review distinguishes between two different types of rock material, namely, porous and compact or non-porous rocks. Major issues in constitutive modelling of rock material along with the strengths, weaknesses and limitations of currently existing models and/or modelling frameworks are also briefly addressed in Chapter 2. A tight connection between the parameters of a model and the experimentally measured material properties, as well as the capacity of the model in faithfully reflecting the important behavioural features of rock material, is the basis for comparing different models. This brief review supports the advantages of coupled elastoplastic-damage models over both elastoplastic and elastic-damage models for describing the mechanical behaviour of geomaterials including rocks. In addition, the limitations and shortcomings of the existing coupled-damage plasticity models for rocks are investigated and discussed. Overcoming some of these limitations is the main motivation and objective of the development of the constitutive models in this study.

In Chapter 3, fundamental aspects of the framework of generalised thermodynamics or thermodynamics with internal variable (TIV), which is the basis for the development of constitutive models in this study, are discussed in detail. Conceptual discussions on the

applications of the laws and principles of thermodynamics in constitutive modelling of engineering materials are also presented in Chapter 3. Furthermore, the formulation and features of the framework is presented in such a manner which further facilitates the application of the framework to the constitutive modelling of engineering materials. The focus is particularly put on the incorporation of the kinematic interdependencies of a physical problem into the model formulation by adding kinematic constraint equations to either the energy potential or the dissipation function. Furthermore, additional internal variables, which are representative of an underlying mechanism of irreversible deformation and energy dissipation, can also be added to the model formulation through introducing kinematic constraint equations and supplementing the two scalar thermodynamic functions.

Chapter 4 is concerned with the development of a coupled damage-plasticity model for porous rocks within the framework of generalised thermodynamics. It is demonstrated in Chapter 4 that the proposed model facilitates the simulation of rock behaviour under a wide range of confining pressures. In particular, both brittle and ductile responses and the brittle-ductile transition, together with the dilative and contractive behaviour, are captured thanks to the inherent features of the model, without any need for separately introducing softening/hardening laws. The model behaviour is assessed (at material level) against a few sets of experimental data on porous sandstones available in the literature. Towards the end of the chapter, the localisation features of the proposed model are investigated in detail and rate-dependent regularisation is carried out. Furthermore, in order to investigate the effect of the specimen size on the mechanical response of rock specimens, finite element (FE) implementation of the proposed coupled-damage plasticity model is carried out in ABAQUS software package by developing a UMAT subroutine. In this analysis, structural behaviour of cylindrical specimens of rocks in drained triaxial tests is simulated.

In Chapter 5, a new coupled damage-plasticity model is developed for describing the behaviour of compact rocks. The motivation for this development is that the underlying mechanisms of deformation in porous and compact rocks, as well as their macroscopic responses, are significantly different. Unlike porous rocks, compact, non-porous rocks exhibit a distinct dilational behaviour even under substantially high confining pressure at room temperature. This dilational behaviour of compact rocks is captured by accounting for the effects of irreversible damage induced volumetric deformations on the mechanical response of rock. The coupling features of the proposed constitutive model in Chapter 5 is the same as that proposed for porous rocks in Chapter 4, and therefore this model also

benefits from possessing a single generalised yield function which evolves to a failure function as damage and plastic deformation develop within the material. Furthermore, the model response and its predictive capability are assessed by providing some numerical examples through comparison between the model predictions and a few sets of experimental data available in the literature. Finally, the localisation features of the proposed model are briefly discussed and rate-dependent enhancement of the model is also carried out.

In Chapter 6, a thermodynamics approach is developed in order to model the localised failure of geomaterials, including rocks. The most important premise in the development of this thermodynamic approach is to describe the kinematic relationships between two material phases within a representative volume element (RVE) of the continuum which has bifurcated from the homogeneous state at the onset of localisation. These kinematic interdependencies are introduced into the model formulation by means of kinematic constraint equations. The coupled damage-plasticity model developed for a homogeneous RVE of porous rocks, in Chapter 4, is then used to describe the mechanical response of material phases inside and outside the localisation band in sandstones, where the thickness of the localisation zone is considerable. For hard rocks, on the other hand, the mechanical behaviour of the infinitesimally thin fracture process zone (FPZ) can be described by a cohesive-frictional interface as outlined in Appendix B. The modelling framework developed in Chapter 6 is then used to study the deterministic size effect on the mechanical response of rock specimens.

Chapter 7, summarises and concludes this study and provides discussions and proposes possible research directions for the future studies.

CHAPTER 2

Constitutive Modelling of Rock Material: a brief review

2.1. Introduction

The importance and necessity of numerical simulations in modern day geotechnical engineering is beyond dispute. At the core of a successful and reliable numerical simulation, however, is a material model that describes the mechanical behaviour of the material out of which the structure is made. Material models (often termed as constitutive models) establish a relation between the applied, or naturally present (in-situ), stresses and the resultant deformations for a material of some known properties. In regards to geomaterials, a constitutive model which can realistically reflect the most fundamental aspects of the rather complex behaviour of such materials is of great necessity in engineering design projects. Although a large number of constitutive models for geomaterials, with different levels of complexity and applicability, have been developed during the past few decades, there still is a long way towards the aim of acknowledging and reflecting all fundamental features of the material behaviour in these models. Therefore, extensive research and development are always required.

Fundamental features of the mechanical behaviour of cohesive-frictional geomaterials, such as rock and concrete, and the efforts made hitherto to capture such features in constitutive models are briefly reviewed in this chapter. In this regard, the focus is put mainly on continuum theories such as plasticity theory, continuum damage mechanics and their coupling. The main features, advantages and shortcomings of constitutive models will be critically discussed in order to provide a general background and motivation for the development of constitutive models in this study. As a basis for this critical study, the mechanical behaviour of rock material is briefly reviewed subsequently.

2.2. Mechanical Behaviour of Rocks

Some most fundamental aspects of the mechanical behaviour of rocks, observed in experiments as well as in the field, are summarised in this section. This brief review serves as a benchmark for comparing and evaluating the existing models and provides a basis for the development of new constitutive models for rocks. Some aspects of micromechanisms of deformation are also addressed in this section as they will be referred to in the successive chapters for physical justification of some assumptions made in the development of constitutive models. In such regards, this study distinguishes between compact and porous rocks as their microstructure, underlying deformation mechanisms and consequently, their macroscopic responses are markedly different under similar stress conditions. Fundamental aspects of macroscopic responses of rock material which will be addressed in this brief review include; brittle and ductile behaviour, as well as the transition from brittle to ductile, dilation and compaction, localisation of deformation.

2.2.1. Brittle to Ductile Behaviour

In association with the mechanical behaviour of rocks, the term brittle refers to a post-peak strain softening. Under certain conditions, rocks may also exhibit ductility. The term ductility refers to the capacity for undergoing substantial inelastic deformation without disintegration, compared to the specimen dimensions. Brittle and ductile behaviour and brittle-ductile transition in rocks are associated with a wide variety of deformation mechanisms which in turn depend on many different factors, such as confining pressure, temperature, loading rate and the rock microstructure. The rock mechanical response in brittle regime is mainly governed by micro-cracking and cracking accompanied by frictional sliding. However, the underlying mechanisms which give rise to the observable macroscopic ductile behaviour may, in addition, include a variety of other microscopic flow mechanisms, such as crystal plasticity, diffusional flow, and granular flow [30]. In addition, there are various microstructural features initially present in rock that can significantly influence its mechanical response. These features include grain boundaries, the contrast between different minerals and other constituents and, more importantly, different forms of micro-cavities. Among the micro-cavities, it is important to distinguish between pores and micro-cracks. In this section, the underlying mechanisms of brittle and ductile behaviour, as well as the brittle-ductile transition, is briefly reviewed for porous and compact rocks. Furthermore, this study focuses merely on the effect of confining pressure on the brittle-ductile response of rocks.

2.2.1.1. Mechanisms of brittle and ductile behaviour in compact rocks

Most non-porous and unaltered rocks exhibit a brittle behaviour under tension and compression at room temperature even under substantially high confining pressure [38-42]. Microscopic studies on hard, compact rocks under compression [43-46] have revealed the development of both intergranular and intragranular micro-fracturing. Intragranular micro-cracks may be either at grain boundaries or in the cementing matrix (in cases like low-porosity calcite-cemented sandstone). In compression under low confining pressure, micro-cracks first scatter throughout the specimen or structure. As the microcrack density increases with strain, they tend to concentrate and localise in an inclined zone from which the macroscopic fracture develops by step-wise joining of the micro-cracks, beginning in the centre of the specimen (see Figure 2.6).

In compact rocks, the transition from brittle to ductile behaviour is associated with more stable micro-crack development which may continue to larger strains. A pivotal difference between the mechanisms involved in the brittle and ductile responses lies in the capacity for accommodating the uniformity of the microcrack distribution [30, 47]. Numerous experimental studies suggest that with increasing confining pressure the micro-fracturing is progressively inhibited [48, 49]. The main features observed towards the upper end of the brittle range are the broadening of the localisation zone and the occurrence of considerable deformation outside the localisation zone. In compact crystalline rocks under low confining pressure, microcracks mostly develop at grain boundaries. With further increase in pressure, the probability of occurrence of inelastic deformation within the grains increases (either in the form of crystal plasticity of micro-fracturing) [39, 50-54].

In some compact rocks, like marble, under high confining pressure the pervasive micro-cracking that precedes macroscopic fracture continues to develop up to larger strains [29, 55, 56] and the sharply defined localisation zone that forms at low pressure broadens into a thicker zone of micro-crack concentration. Figure 2.1 (a) shows the change in the mechanical response of marble from brittle to ductile with increasing confining pressure. The appearance of the marble specimens at the end of some tests is also shown in Figure 2.1 (b). This figure shows the effect of pressure on stabilising the micro-cracking or damage processes, which in turn results in broadening the localisation zone. The bulging or barrelling observed in the marble specimen at higher confining pressures can be explained by appealing to the hypothesis of micro-crack (or damage) stabilisation effect of confining pressure.

Higher confining pressures allow the micro-cracks to spread through a larger volume of the material. This large volume fraction of the material replete with microcracks governs the macroscopic observable response of the specimen. This hypothesis is the basis of model development in Chapter 5, where the formulation of a coupled damage-plasticity model for compact rocks is presented.

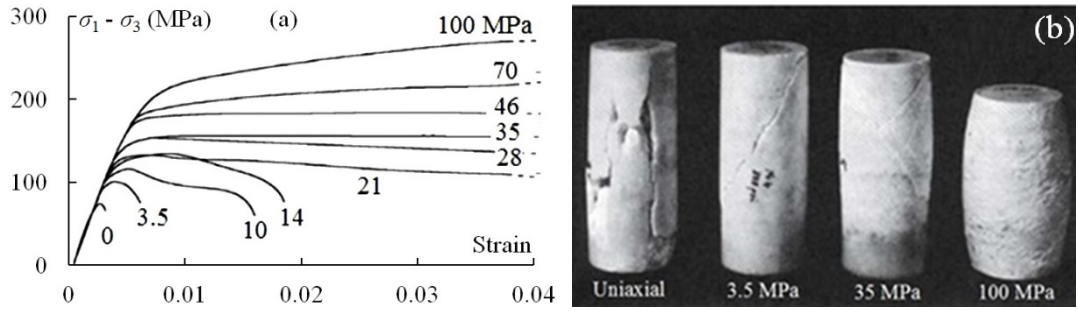

Figure 2.1: (a) Progression from brittle to ductile response and (b) appearance of Wombeyan marble under different confining pressures (after Patterson and Wong [30]).

2.2.1.2. Mechanism of brittle and ductile behaviour in porous rocks

Experimental observations suggest that micromechanical processes involved in brittle to ductile transition of porous rocks are fundamentally different from those observed in compact rocks. Nevertheless, similar to compact rocks, microcracking occurs both within the cement matrix and within grains, leading to the fragmentation of grains and formation of local microscopic localisation zones (Figure 2.2) [57-64]. In porous rocks, the larger strains in the ductile field result mainly from the relative movement of grains or grain fragmentation [65-68]. This deformation mechanism is often referred to as “cataclastic flow”, which can be inferred as a combination of micro-cracking and granular flow. In general, higher porosity favours a lower brittle-ductile transition pressure, but the transition pressure is also sensitive to grain size and other microstructural features, such as the nature of the cement, the presence of clay minerals or alteration products [59, 61-63, 69, 70].

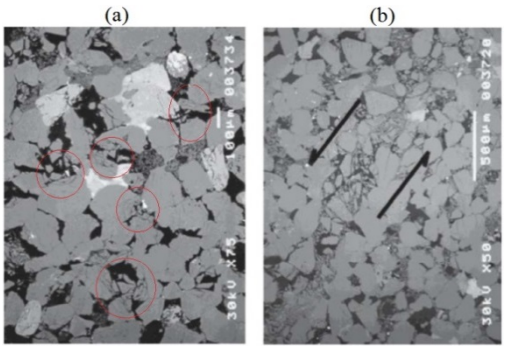

Figure 2.2: Damage and shear localisation in Berea sandstone. (a) Isolated clusters of Hertzian fractures emanating from grain contacts. (b) Coalescence of clusters of damage to form a macroscopic localisation band (after Menéndez et al. [59])

In both porous and compact rocks, under low confining pressure, microcracking (or damage) is localised along a shear band, while the material undergoes dilatancy and strain softening [59, 67, 71-73]. At higher confining pressure, on the other hand, the material compacts and hardens with damage distributed homogeneously in the samples. It should be noted however that the pressures at which brittle or ductile modes of deformation and failure are observed are significantly different for porous and compact rocks. Furthermore, while the ductile behaviour in compact rocks can be attributed, mainly, to the effects of confining pressure in stabilising the micro-crack development, the ductile behaviour of porous rocks involves some other additional and rather complex scenarios. In porous rocks, under high pressure, proliferation of micro-cracks and accumulation of damage in the cement matrix gives rise to the relative movement of grains and increases the chance for grain to grain contacts. This will, in turn, lead to the development of Hertzian stresses and consequently to grain fragmentation or grain crushing, which causes the rock to be progressively more compact [65, 68, 74, 75]. The macroscopic manifestation of these underlying cataclastic scenarios is observed in the macroscopic response of porous rocks as a ductile (or progressively hardening) response with increasing strain. In spite of the different mechanisms of deformation in compact and porous rocks, upon the formation of the macroscopic fracture and failure, the various types of behaviour tend to converge towards a “critical state” condition of constant volume and constant flow stress [30]. This will be discussed in further detail through the development of coupled-damage plasticity models for porous and compact rocks in Chapter 4 and Chapter 5.

2.2.2. Dilation and Compaction

The inelastic volumetric deformation of rocks is of considerable practical importance. Much of the early studies on inelastic volume changes in rocks were motivated by the hypothesis of its central role in the mechanism of earthquakes and its association with possible premonitory signs for earthquakes, such as changes in elastic wave speeds or in the levels of the Earth's surface [76-79]. Inelastic volume changes are often referred to as dilation or compaction depending on whether the initial volume increases or decreases, respectively. Under hydrostatic pressure, inelastic dilation is unlikely to occur, and inelastic compaction is only expected in porous rocks. Under deviatoric stress, on the other hand, dilation or compaction may be observed depending on the level of confining pressure and the microstructure of the rock.

Dilatancy often occurs in rocks prior to the occurrence of the macroscopic fracture when the rock is loaded under conditions conducive to brittle fracture. The effect of confining pressure on the magnitude of dilatancy prior to macroscopic fracture varies considerably from one type of rock to another. In this sense, while an increase in confining pressure causes a diminution in dilatancy in porous rocks [25-28], it does not give rise to a marked decrease in dilatancy in compact rocks like marble and granite. Figure 2.3, illustrates the dilative and contractive responses of two porous (Adamswiller [28] and Bentheim Sandstones [80]) and two compact (Kareliya granite and Ural Marble [29]) rocks. In compact rocks, dilatancy can be attributed to the occurrence of pervasive micro-cracking prior to the macroscopic failure. The underlying mechanisms leading to inelastic volumetric deformation are much more complex in porous rocks.

Volume changes that occur during the deformation of porous rocks derive from two opposing effects. On one hand, the formation and propagation of micro-cracks in the cement matrix give rise to dilatancy. On the other hand, the collapse of pores under the combined effect of the high pressure and the deviatoric stress field leads to decrease in volume. In deviatoric stressing of porous rocks under pressures greater than that of the brittle-ductile transition, the collapse of pores during deformation tends to counterbalance the tendency to dilatancy due to damage and micro-cracking and hence porous rocks commonly exhibit contraction under relatively high pressure. Furthermore, in porous rocks with high porosity, the mechanism of compaction has been shown by many researchers to be associated with grain crushing as a result of Hertzian contact stresses [59, 68, 81-83].

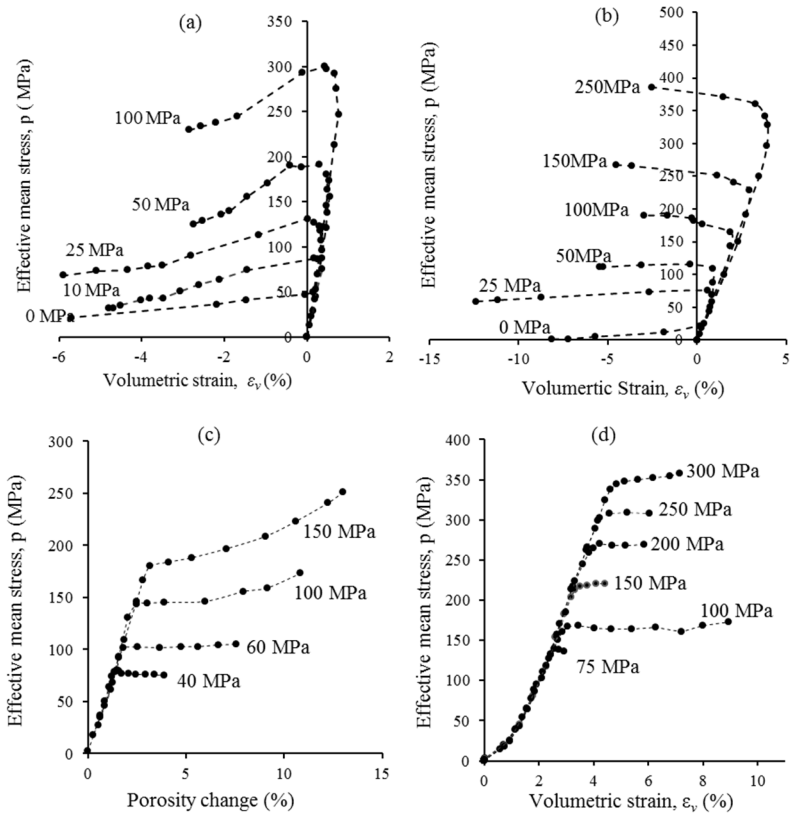

Figure 2.3: Volumetric deformation of (a) Kareliya granite [29] (b) Ural Marble [29] (c) Adamswiller sandstone [28] and (d) Bentheim sandstone [80] at different confining pressures in drained triaxial tests

In porous rocks, as the ductile field is approached with increasing pressure, the localisation zone broadens and its inclination to the compression axis increases. This broad and highly inclined shear zone is often referred to as the shear-enhanced compaction. During and after the formation of the shear-enhanced compaction zone the material exhibits compaction, as opposed to the case of shear-dilation under low confining pressures. The phenomenon of shear-enhanced compaction has been systematically investigated in sandstones [27, 28] and carbonate rocks [25, 26, 84]. Figure 2.4 illustrates the shear-enhanced compaction in Bleurswiller sandstone [85]. If the loading is continued to higher strains a completely horizontal compaction zone is formed, after which any increase in confining pressure leads to a uniform distribution of microcracks throughout the specimen [65, 85]. The phenomenon of shear-enhanced compaction has been systematically investigated in sandstones [27, 28] and carbonate rocks [25, 84].

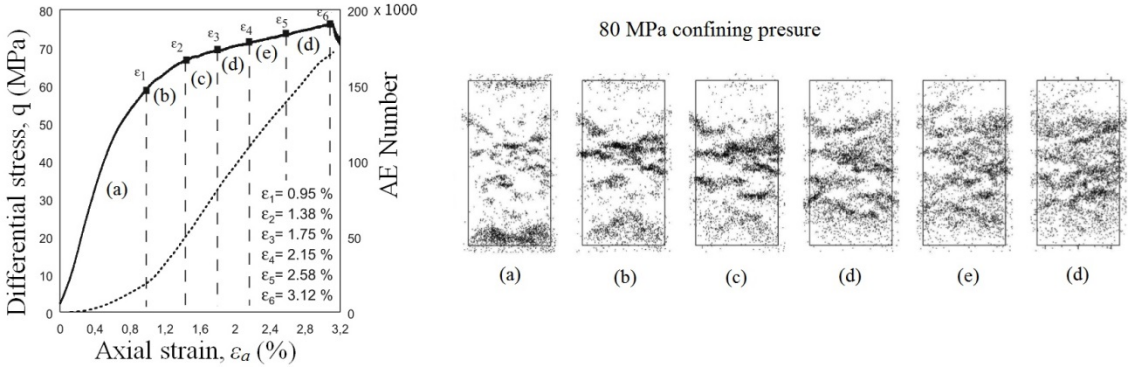

Figure 2.4: Accumulation of AE in juxtaposition with different stages of the stress-strain response showing the development of shear-enhanced compaction bands in Bleurswiller sandstone in drained triaxial test under 80 MPa confining pressure (after Fortein et al. [85])

2.2.3. Localisation of Deformation in Rocks

Deformation and failure of both compact and porous rocks involve localisation of deformation within a band of finite width. Localisation of deformation in rocks has been observed in the form of shear and compaction bands at large scale in the field, as well as at small scale in laboratory experiments. Several researchers [72, 86-90] documented naturally occurring localisation bands associated with a significant volume change. However, field studies can only be carried out on the existing localisation bands, and thus the initiation and development of localisation bands cannot be monitored from field studies. Therefore, over the past few decades, numerous experimental studies have been devoted to the macroscopic and microscopic investigation of initiation and development of the localisation band in rocks, e.g. [25-28, 60, 80, 91-93].

Macroscopic observations of localisation band along with stress-strain data provide enough information to link the brittle-ductile and dilative-contractive responses with the mode of failure. In this sense, under low pressures, the formation and development of shear localisation band are associated with a dilational response which finally leads to a brittle shear fracture (Figure 2.5). Under high pressure, on the other hand, ductile behaviour and contractive volumetric deformation and finally cataclastic mode of failure are results of the formation and development of compaction bands (Figure 2.5). However, the latter has been observed hitherto only in porous and/or soft rocks.

Theoretical modelling of rock behaviour also requires knowledge of the favourable stress state at which the localisation band first initiates. Various observations indicate that the onset of localisation occurs somewhere in the vicinity of the peak load. However, the

observations are apparently contradictory as to whether the onset of localisation occurs in the pre- or post-peak stage of loading. In general, acoustic emission (AE) measurements and microstructural observations commonly indicate that the onset of localisation does not occur until the peak stress has been attained while strain and surface deformation measurements seem to indicate the occurrence of pre-peak localisation [30]. It seems that the observations of the occurrence of the onset of localisation are to some extent influenced by the method adopted to record this event. For instance, locating the spatial origin of the micro-cracks by means of an array of acoustic sensors hinges on the assumption that the wave speed in the structure is known. However, appreciable wave speed anisotropy and attenuation may develop in a stressed rock, and the location and density of a micro-crack cluster, for instance, may be biased if these effects are not appropriately taken into account [94].

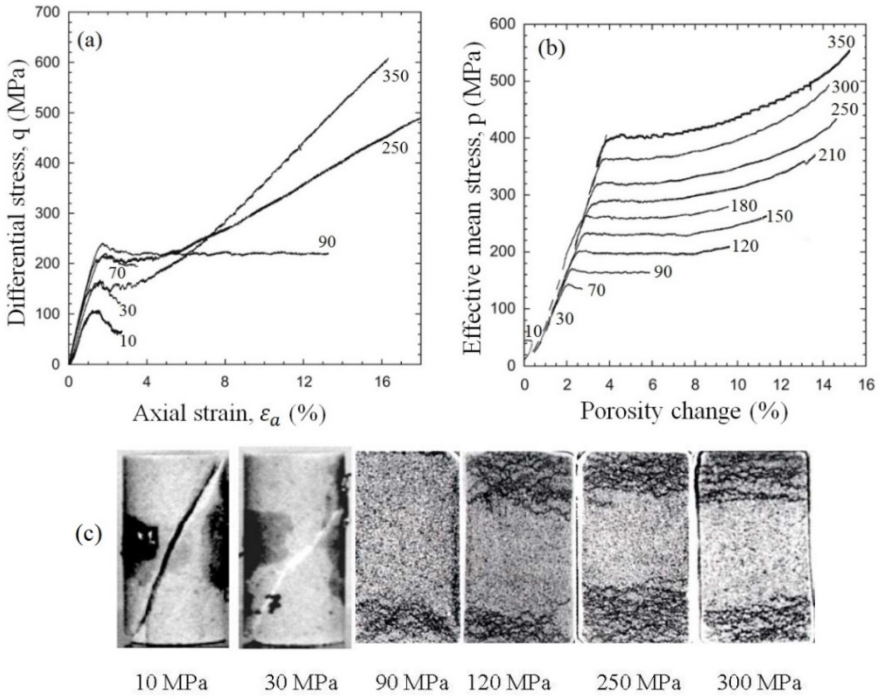

Figure 2.5: Macroscopic observations of localisation band in drained triaxial tests on Bentheim sandstone under different confining pressures: (a) and (b) stress-strain responses [95] and (c) deformed specimens with shear and compaction localisation bands [80, 96].

Observations of formation of localisation band in argillaceous quartzite were presented by Haullbauer et al. [45]. The tests were stopped at predetermined points along the stress-strain curve. The growth of micro-cracks and fracture in relation to the stress-strain curve was observed through longitudinal section cuts along the axis of the specimen (Figure 2.6). In region III of the stress-strain curve, as illustrated in Figure 2.6 the first visible structural damage appears as elongated micro-cracks having their axes oriented parallel (within $\pm 10^{\circ}$) to the direction of the

maximum compressive stress. In region IV the cracks were distributed throughout the sample but were concentrated in the centre. Towards the end of region IV, the number of micro-cracks increased drastically and the cracks began to coalesce along a plane located in the central region of the specimen. At the point of maximum axial stress, the micro-cracks begin to link up to form a macroscopic fracture. Finally, in the region V, the fracture extends through the entire specimen. As illustrated in Figure 2.6, the onset of localisation seems to occur at about 95% of the maximum load.

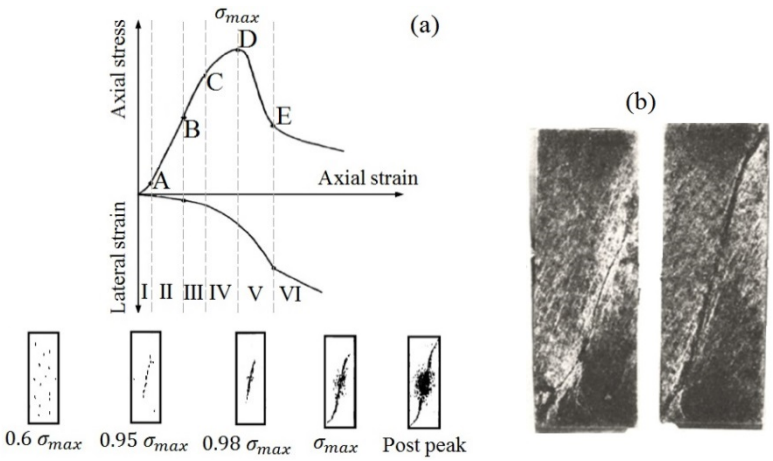

Figure 2.6: (a) Schematic representation of localisation and brittle failure based on observations by Hallbauer et al. [45] in test specimens during triaxial compression tests and (b) longitudinal section cuts

In contrast to the above observations, in triaxial compression experiments on compact rocks such as Westerly granite [94], spatial clustering of acoustic emission activity is not evident in the pre-peak stage. However, intensive acoustic emission activity in the post-peak stage is observed to accumulate along an elongated volume that propagates progressively to develop a through-going shear band across the sample (Figure 2.7). In addition, microstructural observations in other granites [97, 98] and gabbro [99] show that the localised coalescence of microcracks that extends over two or more grains is evident in the post-peak stage.

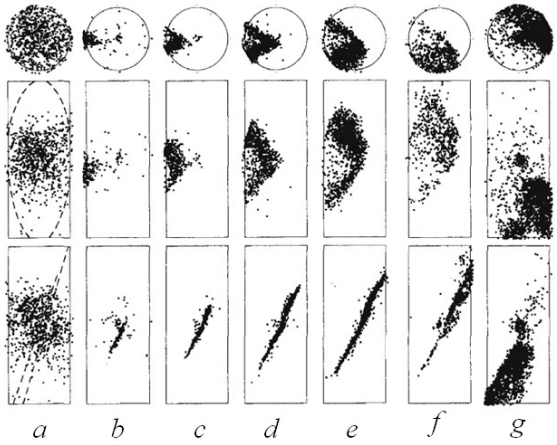

Figure 2.7: Localisation of AE activity for Westerly granite under triaxial compression with 50 MPa confining pressure. Each point represents an AE event recorded for (a) in the pre-peak stage and (b) – (g) in the post-peak stage (after Lockner et al. [94]).

Localisation of acoustic emission activity follows somewhat different patterns in porous rocks. For instance in Berea sandstone diffuse clusters of acoustic activity are observed before the peak stress is attained. So far studies on the localisation of deformation in porous rocks have been focused mostly on sandstone, and further study on other rock types would provide a more general understanding of localised deformation in porous rocks. In sandstones localisation band is either in the form of a shear-dilation band (at low confining pressures) or a shear enhanced (or pure) compaction band (at substantially high confining pressures).

Important advances have also been made in the analysis of shear localisation based on the principles of continuum mechanics. A constitutive model which is formulated to describe realistically the inelastic and dilatant behaviour of rocks should also correctly predict the onset of localisation to occur under critical conditions. At this critical condition, an incremental change in the applied stress (to a specimen or structure) results in a deformation field that is non-unique, with separate (unique) solutions corresponding to localised inelastic deformation within the localisation band and relatively homogeneous inelastic deformation outside the band. This issue will be further discussed in Sections 2.4.

2.3. Constitutive Modelling of Rock Material

Regarding the constitutive models developed for rock material, it is desirable for a constitutive model to be able to capture all essential characteristics of rock behaviour as outlined in the previous section. As discussed in detail in the previous section, these essential features of rock behaviour can be listed as; brittle and ductile behaviour depending on the

applied pressure, dilative and contractive responses to the applied pressure and localisation of deformation or localised failure. Furthermore, a good constitutive model should be able to reflect the stiffness reduction and the residual strain, observed during unloading (Figure 2.8). As was discussed earlier, this reduction in stiffness arises as a consequence of the occurrence and accumulation of microcracking (or damage) within the material during loading. Also, the sources of the residual strains are a variety of underlying phenomena ranging from frictional sliding between the surfaces of microcracks and asperity interlocking to crystal plasticity and cataclastic flow.

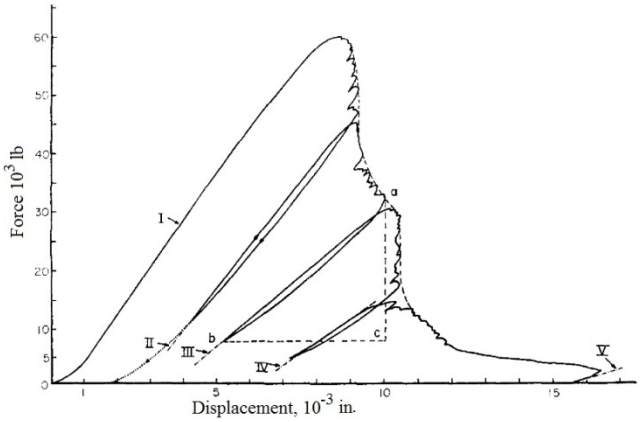

Figure 2.8: Force-displacement curve for Tennessee marble under uniaxial loading [56]

Other important aspects of the observable mechanical behaviour of rocks are their yielding behaviour and different failure modes under various stress states. In particular, rocks, like any other geomaterial, exhibit pressure dependency and their yielding behaviour and failure modes vary with respect to the level of applied pressure. Figure 2.9 illustrates initial yield stresses and the evolution of the yielding behaviour for two porous sandstones (Bentheim and Adamswiller [92]) along with the evolution of the yield surface of the Carroll's [100] critical state model for different levels of plastic volumetric strain. The focus here is on the experimentally observed initial yield stresses as well as the evolution of the yielding behaviour of rocks. Two important conclusions can be drawn from these experimental observations. Firstly, the yielding behaviour of porous rocks can be well described by means of an elliptical or a teardrop-shaped yield function in $p - q$ stress space which is closed on both ends along the p-axis. Secondly, as inelastic loading continues after the occurrence of the initial yield the subsequent yield stresses evolve towards a final failure (critical) state. Similar discussion can be stated for the yielding and failure of compact rocks. However, the initial yield stress under isotropic compression for hard, compact crystalline rocks has not hitherto been measurable in experimental studies, as it requires a substantially

high pressure (beyond the capability of any experimental equipment) for hard, compact rocks to yield, if ever, under isotropic compression.

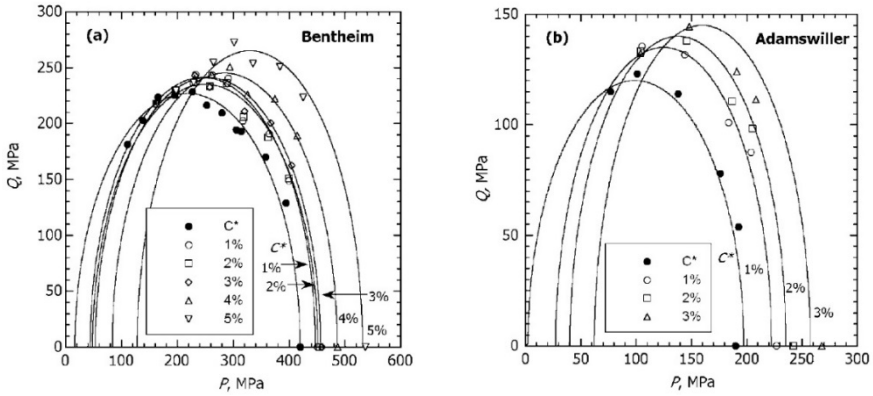

Figure 2.9: Initial yield stresses and the evolution of the yielding behaviour for (a) Bentheim and (b) Adamswiller sandstones [92]

Furthermore, the failure process of rocks involves localisation of deformation within a band of finite thickness. The mode of localisation is mainly governed by the microstructure of rocks and the applied pressure. For compact crystalline rocks, such as granite or gabbro, shear localisation bands can only be observed under pressures conducive to brittle failure and compaction bands have never been observed. This may be because at room temperature loading, hard compact crystalline rocks under pressures conducive to ductile response is not usually possible. Nevertheless, compaction bands have not been observed even in relatively soft compact rocks, such as marble, which can be loaded beyond the brittle-ductile transition pressure in laboratory experiments. In fact, in such cases, the ductile behaviour is associated with a dilational response and can be observed as bulging or barrelling of the specimens (Figure 2.10 (a)) without a distinct localisation band. In porous rocks, on the other hand, shear localisation is observed at low pressures (brittle regime) and compaction bands have been observed to form at high pressures (Figure 2.10 (b)).

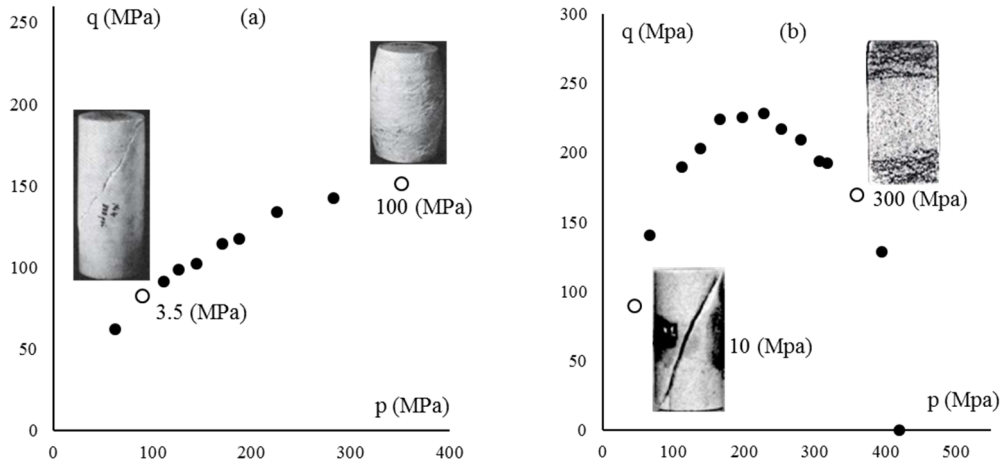

Figure 2.10: Initial yield stresses and failure modes in low and high pressures for (a) Wombeyan marble (data extracted from [30]) and (b) Bentheim sandstone (data extracted form [80, 95, 96]).

Describing the above-mentioned behavioural features by means of a constitutive model has captured the attention of many researchers over the past few decades. In the context of constitutive modelling, the domain under consideration can be treated as a continuous body and all the physical quantities pertaining to this body can be described by means of continuous mathematical functions. This is the approach of continuum mechanics. Although the same body if viewed under sufficient degree of magnification, may contain discontinuities in the form of, for example, micro-voids, micro-cracks and the like, the continuum approach can still take the effects of these discontinuities into account by means of continuous mathematical functions. However, an alternative approach is to consider the body to consist of a number of particles. In this approach, the physical quantities are defined discretely for any individual particle and the interaction between a particle and its neighbouring particles are prescribed. This approach is referred to as the discrete approach.

For materials, such as concrete, rock and especially soil, with a high level of discontinuity at the micro-scale, the discrete approaches have been widely used, as they facilitate the description of the material micro-structure, as well as the micro-mechanisms of deformation. In other words, in the context of constitutive modelling for geomaterials discrete approaches offer excellent access to the underlying physics of deformation at the micro-scale [101-110]. Nevertheless, the link between the microscopic and macroscopic physical quantities may not be always clear in models based on discrete approaches. Therefore, in discrete approaches, the micro-parameters are often determined by means of curve fitting procedures at the macro-scale. For example, in discrete modelling of cohesive

frictional geomaterials the properties of the bond between the particles, including the bond strength, can only be determined by means of fitting the macroscopic stress-strain curves generated by the model to their macroscopic experimental counterparts [see e.g. 107, 111, 112]. Furthermore, discrete approaches are considered as computationally expensive for largescale problems and hence their application is somehow limited by the available computational power.

Accordingly, the continuum approach can be viewed as a viable alternative, in view of the capabilities of current computing power. In this regard, the focus of this study is on continuum theories, such as plasticity theory, continuum damage mechanics and their coupling. Therefore, the remainder of this review is restricted only to constitutive models based on continuum approaches. To this end, analysis and evaluation of different continuum constitutive models are carried out based on the capability of these continuum models in capturing the essential characteristic features of rock behaviour, as outlined above and in more detail in the previous section. Furthermore, instead of analysing a large number of continuum models on a case by case basis, continuum models are classified into certain groups, based on the continuum approach through which they are developed, and then the capability of each group of models in capturing the mechanical behaviour of rocks is assessed.

Theories of plasticity and continuum damage mechanics (CDM) have been widely used to describe the inelastic behaviour of rocks. However, neither of these theories alone can appropriately account for both the observable strength and stiffness reduction and residual strains, which are characteristic of the inelastic behaviour of not only rocks but also other cohesive-frictional geomaterials, such as concrete. Therefore, the specification of coupling and interplay between damage and plasticity in the model formulation is of necessity if the model is to follow the experimental observations closely. In this sense, the strain softening and stiffness degradation and residual strains can be captured by means of coupled damage-plasticity models. As the fracturing progresses and the volume fraction of intact rock decreases, the elastic stiffness of the specimen, correspondingly, decreases. This effect can be made evident if the force is cycled in the post-peak region. Based on this discussion, continuum models can be classified into three groups;

- Elastoplastic models

- Elastic-damage models

- Coupled elastoplastic-damage models

It should be noted that although coupled damage-plasticity models are capable of capturing the stiffness reduction and the observed residual strains during unloading, their capability in predicting the onset of localisation and the orientation of the localisation band is still to be assessed. In what follows, the above-mentioned groups of continuum models are briefly investigated and their capability in replicating the experimentally observed behaviour of rock material is discussed.

2.3.2. Elastoplastic Models

Plasticity theory, which was originally developed to model the irreversible deformation of metallic materials, was later modified and it has been widely used to describe the inelastic behaviour of geomaterials. Drucker and Prager [113] were the first to apply the plasticity theory to soils, using normality principle together with a three-dimensional version of the Mohr-Coulomb criterion as the yield condition. In general, the development of plasticity models requires an elastic constitutive relationship, decomposition of the total strain tensor, the definition of a yield function with hardening/softening rules, and flow rules. It is also important to note that in order to avoid unrealistic plastic dissipation due to the frictional behaviour of rocks (and also other geomaterials), a non-associated flow rule, which is defined by employing a plastic potential rather than the yield function, should be used [114-118]. It can be shown that if associated flow rule is used for frictional geomaterials no energy is dissipated due to plastic deformation and all the plastic work will be stored within the material [19]. This issue will be further investigated in Chapter 4.

Furthermore, in plasticity theory, the plastic potential is selected somehow arbitrarily, usually through slightly modifying the yield function by adding one or more parameters, which often lack any physical meaning. The only basis for selecting these parameters is to mathematically enforce the normality condition, i.e. making the plastic flow vectors normal to the plastic potential. An alternative and perhaps more convenient approach is to define the entire formulation of a plasticity model using the principles of thermodynamics. In this class of plasticity theories, which are termed as hyperplastic [19], the normality condition and the condition of maximum plastic dissipation are always met owing to the existence of a convex yield potential. This yield potential is defined in dissipative stress space rather than the true stress space and it is a direct result of the rate-independent material behaviour. The latter approach is taken in this study and the

fundamental aspects of hyperplasticity, or in a more general sense, the framework of the generalised thermodynamics will be further studied in depth in Chapter 3.

Numerous forms of yield surfaces have been proposed since 1773 when Coulomb, the first and one of the most widely used yield criteria. These yield functions can be classified either based on the number of parameters in their formulation or based on the shape of their representative surface in principal stress space [114, 119]. The simplest of all are Von Mises and Tresca criteria which are two typical examples of one-parameter pressure-independent yield surfaces. These yield functions, which were initially proposed for describing the yielding behaviour of metallic materials, cannot, in general, be applied to model the pressure-dependent behaviour exhibited by geomaterials materials, such as concrete, soil and rock (see section 2.2.4). Nevertheless, these functions can be modified, by means of introducing a tensile cut-off, to make them applicable to the modelling of the pressure-dependent behaviour of geomaterials.

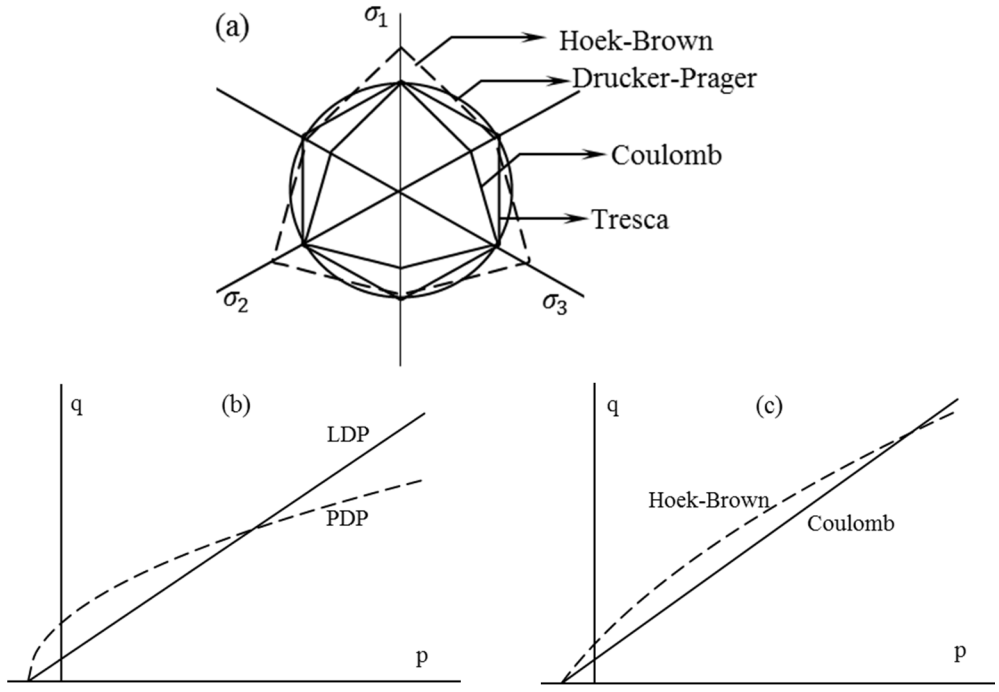

Figure 2.11: (a) The cross section of the Hoek-Brown, Drucker-Prager, Tresca and Coulomb yield surfaces on the deviatoric plane (b) Linear Drucker-Prager (LDP) and parabolic Drucker-Prager (PDP) and (c) The Hoek-Brown and Coulomb in $p - q$ spcae.

Alternatively, yield functions that have been developed specifically to describe the yielding behaviour of geomaterials can be used. Amongst numerous functions that have been proposed to characterise the yielding behaviour of geomaterials, the Coulomb and the Drucker-Prager yield functions are probably the simplest and the most widely used.

However, these yield functions may not accurately represent the experimentally observed yielding behaviour of many geomaterials, in particular, rocks. As illustrated in Figure 2.11, while both Coulomb and Drucker-Prager predict linear yield envelopes on the Meridian plane, as discussed in Section 2.2.4, almost all experimental observations on rocks (and other geomaterials) suggest that the yield envelope is nonlinear on the Meridian (and also in $p-q$ space).

Although, yield functions with nonlinear Meridian sections, for instance, parabolic Drucker-Prager and Hoek-Brown (Figure 2.11), have also been proposed and widely used for modelling the behaviour of rock material, the open shape of such yield surfaces does not adequately reflect the behaviour of many geomaterials, e.g. porous rocks (see Figure 2.9), under hydrostatic loading. A solution to this problem could be given by modifying the expression of the open shaped yield surface so that it becomes a closed shaped for the plastic deformation under hydrostatic loading can be captured [116, 120]. As illustrated in Figure 2.12, under loading the initial closed shaped yield surface eventually opens towards the compressive hydrostatic axis.

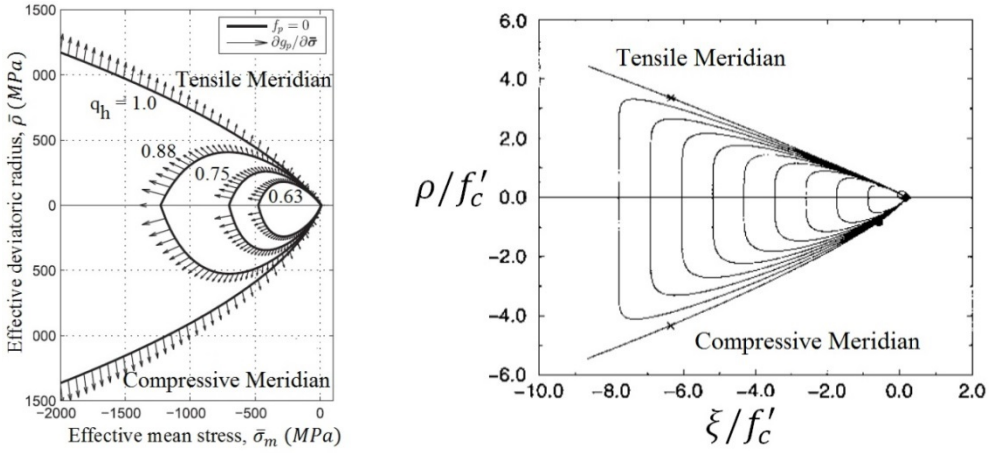

Unteregger et al. 2015 Kang and William, 1999

Figure 2.12: Evolution of the initial yield surface in stress space during hardening by explicitly postulating hardening rules

Additionally, other elastoplastic models, in particular, the critical state model [121] and cap plasticity model [122] and their several modified versions, have been widely used for describing the macroscopic behaviour of rocks. The main advantages of models based on the critical state concept are that they distinguish between the initial yielding and final failure states and they may use only a single set of parameters for both high and low-pressure regimes. However, in some cases they can only describe the macroscopic behaviour of rocks

for a limited range of stress states, e.g. only in brittle faulting regime [123] and in other cases [124], they are unable to capture the localisation of deformation. Models based on the cap plasticity model [e.g. 122, 125, 126] are advantageous in the sense that they account for the contractive behaviour of rocks due to porosity reduction. However, these models can predict the evolution of yield surface within a limited range of volumetric strain and are also valid for certain sandstones only [91]. There are also models which combine cap plasticity model and critical state soil mechanics model to describe the macroscopic behaviour of rocks [127-135]. Despite the remarkable fitting capability of some of these models, they pay no attention to the material stiffness reduction due to damage growth.

Although many plasticity-based models can successfully describe some behavioural aspects of geomaterials and rocks, such as strain hardening/softening in monotonic loading, they, in general, do not take into consideration the effect of proliferation and coalescence of microcracks on the behaviour of cohesive geomaterials like concrete and rock. However, the nonlinear behaviour of cohesive-frictional geomaterials is partially caused by the propagation and coalescence of the existing microcracks as well as the initiation of new microcracks. Due to initiation and growth of microcracks within a material during loading the mechanical properties of the material will progressively change. In particular, as discussed in Section 2.2.4, the load carrying capacity and stiffness of the material will deteriorate. Such aspects should be included in any theory designed to describe the inelastic deformation and failure of cohesive-frictional geomaterials. These aspects of the inelastic deformation of cohesive-frictional geomaterials cannot be appropriately modelled by means of conventional plasticity theory, which was originally developed for metallic materials and later modified to fit the experimental data of geomaterials, without the underlying microscopic failure mechanisms of the material being taken into proper consideration. In order to overcome these limitations, the theory of continuum damage mechanics (CDM) was first developed by Kachanov [136]. In a nutshell, CDM describes the damage of a material as progressive processes due to which the material breaks and thus loses strength and stiffness.

2.3.2. Elastic-Damage Models

The exact description of the actual evolution of the micro-crack pattern in a progressively failing rock would be nontrivial. However, this process can be reflected, in an average sense, through degradation of the material elastic stiffness due to the progressive

growth and coalescence of microcracks. The process of progressive failure and stiffness degradation may be quantified by introducing a continuous field variable, namely, the damage variable. Continuum Damage Mechanics (CDM) approach has been employed for constitutive modelling of geomaterials, such as concrete and rock, by many researchers [e.g. 137, 138-143].

A constitutive model based on damage theory is usually formulated based on a stress-strain law with the presence of a damage variable to characterise the material deterioration and a damage criterion and/or an evolution law for damage. Due to the anisotropic nature of damage, even for initially isotropic materials, a tensorial representation of damage is required. To this end, the effective (or elastic-damage) stiffness tensor $\bar{C}_{ijkl}$ is defined as:

$$\bar{C}_{ijkl} = D_{ijpq} C_{pqkl} \tag{2.1}$$

where D_{ijkl} represents the damage influence tensor and C_{ijkl} is the elastic stiffness tensor. Nevertheless, damage models which employ scalar damage variables are still preferred, because of their simplicity in the formulation, numerical implementation and parameter identification [119, 144, 145]. In the simplest case, when the stiffness degradation property of damage is represented using a single scalar damage variable, D, the damage influence tensor D_{ijkl} in equation (2.1) can be replaced simply by $(1 - D)$. The selection of a single damage variable implies that damage (or micro-cracking) is spread uniformly in all directions throughout the representative volume element (RVE) for which the constitutive relations are derived. Although this assumption is not realistic, since it considerably simplifies the process of modelling and implementation, it has been (and still is) adopted by many researchers and it will also be adopted in this study. This simple representation of damage (using a scalar damage variable) implies isotropic behaviour of the models, but helps to considerably simplify the formulation and allows for more focus on other more important aspects of constitutive modelling of rock material. They are: thermodynamics admissibility of the models, and the capability of the models to capture the mechanical behaviour (ductile-brittle and the associated compaction/dilation) under both pre- and post-localisation regimes. Of course, it is the author's own view point to put more focus on these features, as the anisotropy in pre-peak regime is minor to a much stronger one that appears once localisation of deformation occurs. That latter and stronger anisotropy due to localisation deserves attention in this work and is also considered as an important feature of rock behaviour.

As illustrated in Figure 2.13, due to damage the cross-sectional area is reduced and the effective cross-sectional area, $\bar{A}$, can be defined as $A - A_D$ in which A is the original cross sectional area and A_D is the total area of micro-cracks. The stress is no longer $\sigma = F/A$ and it is replaced by the effective stress $\bar{\sigma}$:

$$\bar{\sigma} = \frac{F}{A - A_D} = \frac{\sigma}{(1 - D)} \tag{2.2}$$

The extension of the concept to multi-axial stress state with scalar damage variable is straightforward since damage, in this case, does not depend on the direction. Therefore, the following relation still holds:

$$\bar{\sigma}_{ij} = \frac{\sigma_{ij}}{(1 - D)} \tag{2.3}$$

where σ_{ij} and $\bar{\sigma}_{ij}$ are now the stress and effective stress tensors, respectively.

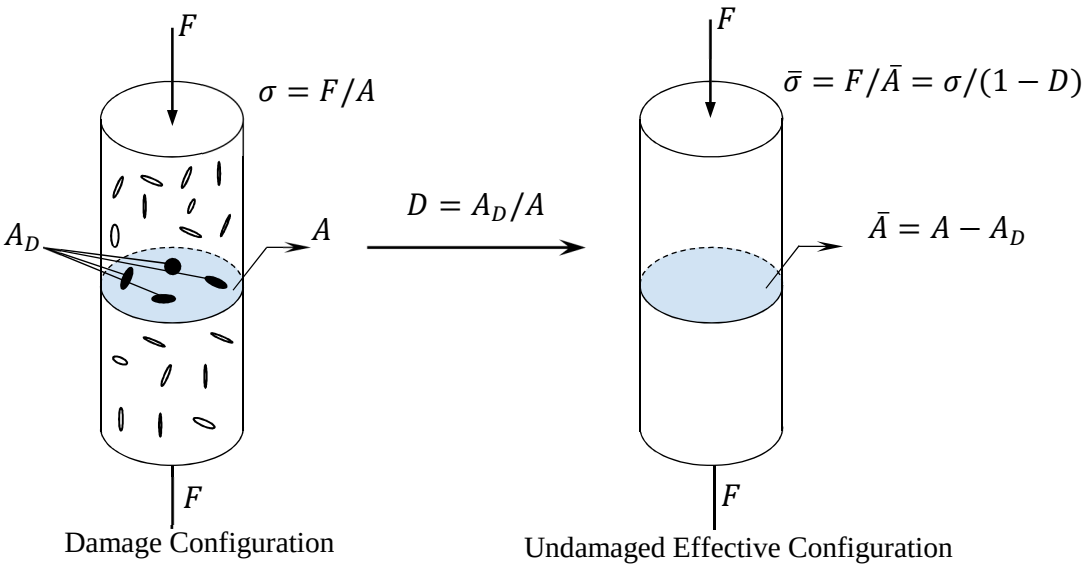

Figure 2.13: Schematic representation of the physical concept of damage

The principle of strain equivalence [146] follows directly from the effective stress concept and, in many cases, paves the way for the application of alternative approaches instead of a full micromechanical analysis [147]. The principle of strain equivalence states that "*Any strain constitutive equation for a damaged material may be derived in the same way as for a virgin material except that the usual stress is replaced by the effective stress*". Application of the strain equivalence hypothesis results in the state coupling between damage and elasticity [147]. This coupling is in accordance with the observed behaviour of damaged materials where damage, as an average interpretation of the breakage of bonds in

the material, causes deterioration in the elastic properties of materials. This coupling can be expressed as the following constitutive relation:

$$\sigma_{ij} = D_{ijpq} C_{pqkl} \varepsilon_{kl} \tag{2.4}$$

In the case of damage being represented by a scalar variable, the above expression can simply be written as:

$$\sigma_{ij} = (1 - D) C_{pqkl} \varepsilon_{kl} \tag{2.5}$$

Continuum damage models, similar to plasticity models, can be developed using either strain-based or stress-based formulation. In the strain-based formulation, damage is characterised through the effective stress concept along with the hypothesis of strain equivalence. In a stress-based formulation, on the other hand, the by adopting the hypothesis of stress equivalence [141], the representation of damage is given through the effective strain concept, in which the effective strain tensor in the case of isotropic damage is $\bar{\varepsilon}_{ij} = (1 - D)\varepsilon_{ij}$. The hypothesis of stress equivalence [141] states that "*The stress associated with a damaged state under the applied strain is equivalent to the stress associated with its undamaged state under the effective strain*".

In principle, the choice of the damage variable *D* is arbitrary, provided that the laws of thermodynamics are strictly followed. Damage can be represented as a variable which characterises the material deterioration by considering the concepts of effective stress or effective strain [117, 118, 137, 139, 141, 148-154]. Alternatively, damage can be represented by means of a function. The definition of such functions can also be arbitrary (as long as the laws of thermodynamics are not violated) and they are usually defined as a function of the position of the loading surface in stress space between the initial and bounding surfaces [155] or even as an arbitrarily defined decreasing function [156]. Such representations of damage, however, can be hardly related to the physical representation of damage, as illustrated in Figure 2.13. In fact, in macroscopic constitutive modelling, physical interpretation of damage variables is not always straightforward [119]. However, the convincing physical interpretation of the damage variable *D* depends on the identification of the microscopic mechanisms which govern the observed macroscopic response.

Recent developments of continuum damage models based on the phase field approach [157, 158] offers the opportunity of better understanding the damage processes. The phase field method can also be used for modelling the evolution or propagation of a

discrete fracture in fracture mechanics [159-162]. The phase field method (PFM) is a powerful theoretical and computational approach that is used in many research areas to predict the microstructure evolution that consists of two or more different phases and the continuous transformation between the different phases. The Phase Field Method (PFM) provides an excellent tool for studying the effects of the microstructure evolution without the necessity of tracking the interface. Nevertheless, no phase field based continuum damage model has been introduced hitherto which can be applicable in practical large-scale modelling of geomaterials, as these models are usually very computationally demanding.

Similar to the models based on conventional plasticity, elastic-damage models can be used for modelling the material behaviour exclusively in the case of monotonic loading, as it can replicate the softening response of the material without taking the permanent deformations into proper consideration. Furthermore, due to neglecting the participation of plastic deformations in energy dissipation, the elastic-damage models ([34, 137, 139, 153, 154, 163-170]) overestimate the stiffness reduction of the damaged material. Nevertheless, capturing the stiffness reduction due to damage processes can still be viewed as an important feature to be reflected in the constitutive modelling of cohesive geomaterials materials, as the limitation of elastic-damage models becomes prominent only when an unloading-reloading cycle is to be considered.

The conclusion, drawn from the brief discussions presented in the current and preceding sections, points towards the fact that neither the elastoplastic models nor the elastic-damage models on their own are capable of reflecting the macroscopic behaviour of cohesive-frictional geomaterials, as outlined in Section 2.2.4. Therefore, the coupling between damage and plasticity seems to be necessary in order to take into account the fundamental aspects of the macroscopic behaviour of cohesive-frictional geomaterials, which are briefly presented at the beginning of this chapter.

2.3.3. Coupled Elastoplastic-Damage Models

Inelastic deformation of most engineering materials involves either simultaneous or consecutive occurrence of damage processes and plastic deformation. Accordingly, residual strains and stiffness reduction are both observed in the macroscopic response of engineering materials during the course of inelastic deformation (see Figure 2.8). Therefore, the specification of coupling and interaction between damage and plasticity in the formulation of constitutive models is of great necessity. Over the past few decades, numerous coupled

elastoplastic-damage models, with different levels of complexity, have been proposed for describing the behaviour of engineering materials.

One approach for the development of coupled damage-plasticity models is to control the evolution of damage and plastic deformations by means of two separate loading functions, e.g. [118, 151, 171-183]. In these models, the two mechanisms of damage and plasticity are linked through the constitutive relations or by expressing the plastic yield function in the effective configuration which describes the stresses in the undamaged material. Although successful in the phenomenological description of material behaviour, numerical implementation of such models is cumbersome, as additional iteration schemes may be required for stress updating at material level (or Gauss point in FEM). Furthermore, the coupled relations are usually complex and may result in unstable numerical algorithms which may cause an unrealistic representation of plastic behaviour during the implementation and iteration procedures [118].

Another approach for coupling damage and plasticity is to specify the evolution of damage as a function of volumetric plastic strain or a strain-like internal softening variable (e.g. [29, 184-188]). In such models, the evolution of damage begins only after the development of plastic strains and the model behaviour is immensely influenced by ad hoc assumptions and definitions involved in expressing damage evolution as a function of plastic strains. These models suffer from some limitations particularly in cases where the source of plastic deformations prior to damage is not clear. Examples of such cases may include quasi-brittle materials, such as concrete or rock, in which plastic deformations are commonly attributed to asperity interlocking and frictional sliding between the two surfaces of pervasive micro-cracks. In other words, in such materials, damage is the active mechanism of inelastic deformation followed by plasticity, the passive mechanism [189].

Apart from the above-mentioned limitations, most of the published models, which can be categorised in these two groups of coupled damage-plasticity models, have other limitations in regard to capturing the macroscopic behaviour of rocks. In particular, many of these models were primarily developed for concrete and thus paid little or no attention to the yielding conditions of rock material, as outlined in the beginning of this section. Among these models, the model proposed by Salari et al [179] was particularly developed for rocks. However, this model also used the linear Drucker-Prager yield function, which as discussed in Section 2.3.2 does not describe the yielding behaviour of rocks adequately. Furthermore,

the model was not validated against experimental data and hence the identification and determination of model parameters were not adequately addressed in the development of the model. More recently, Unteregger et al [29] proposed a coupled damage-plasticity model for intact rocks based on a damage-plastic model for concrete, proposed by Grassl and Jirásek [190]. Although this model shows relatively high capability in capturing the macroscopic stress-strain response of rocks, its capability in predicting the onset of localisation and the orientation of the localisation band has not been discussed.

Recent developments for describing the coupling between damage and plasticity are based on the hyperplasticity framework [19]. The principles of hyperplasticity, which allow for developing plasticity theories within a thermodynamic framework, are established in [19-21, 191]. It is shown later by [192] that damage can also be modelled using the hyperplasticity framework and so it led to the development of damage-hyperplastic models. In this sense, damage and plasticity are represented by introducing a damage internal variable and the plastic strain tensor as another internal variable. In damage-hyperplasticity approach, which was developed within the framework of generalised thermodynamics, the entire constitutive relations, including the evolution rules for internal variables, can be derived from merely two scalar functions. These functions include; the free energy potential and the dissipation rate function. In damage-hyperplastic models, the coupling between damage and plasticity is specified in the formulation of dissipation function which will, consequently, lead to obtaining a single generalised yield function through performing a degenerate Legendre transformation. This single generalised yield function controls the simultaneous evolution of all internal variables of the model, e.g. damage and plasticity [118, 144, 189, 193]. The final form of the yield function is determined by specifying the active mechanism of dissipation at micro/meso scale. Active mechanisms of dissipation are primary causes of irreversible deformations which consequently give rise to some secondary or passive dissipative processes. For instance, in quasi-brittle materials, such as rocks and concrete, damage is the active mechanism of dissipation while the subsequent frictional dissipation is passive. In contrast, grain boundary sliding, which causes macroscopic plastic strain in metallic materials, is the active mechanism leading to the debonding process, which is, thus, passive to the sliding [189].

The use of a single generalised yield, which controls the simultaneous evolution of all internal variables, facilitates the numerical implementation of this class of damage-plastic models. Nevertheless, these models also suffer from some limitations, especially, in

modelling the non-associated flow and dilatant and/or contractive behaviour commonly observed in geomaterials. In order to alleviate these problems, recently Vu et al [23] proposed a damage-hyperplasticity approach with a slightly different form of the dissipation function. The proposed form of the dissipation function in Vu et al [23] facilitates further controlling the plastic flow vector in stress space and, consequently, allows for more control over the dilatant and/or contractive behaviour. However, the proof for thermodynamic admissibility (non-negativeness of the dissipation rate function) in this approach may be cumbersome in some cases. Details of this approach are presented in Appendix A.

2.4. Bifurcation Analysis and Modes of Localisation

Inelastic deformation and failure of geomaterials, such as rocks or concrete, is associated with localisation of deformation within a band of finite width. Therefore, it is required for any constitutive model developed for describing the behaviour of rocks to be capable of predicting the orientation of the localisation band as well as the stress state at which the localisation of deformation takes place. The localised deformation limits the formability of materials and will often quickly lead to failure with continued loading. Upon formation of the localisation band or at the onset of bifurcation the homogeneity of kinematic fields is lost and the stress field is redistributed and is no longer uniform. Starting with phenomenological descriptions of the inelastic deformation, localisation theories aim to describe the conditions under which a uniform (or smoothly varying) stress field becomes non-unique in the sense that it may have two (or more) associated strain fields, one of which corresponds to the concentrated deformation in the localisation band [71, 194-196]. The mathematical analysis of the bifurcation of a homogeneous stress field into a non-unique stress state, as a result of a non-unique deformation field, has led to the introduction of a number of bifurcation criteria. These bifurcation criteria can, in general, be regarded as setting an upper limit to the stability of the material. Some of these bifurcation criteria are briefly presented subsequently.

2.4.1. General Bifurcation

Based on the Drucker's stability postulate [113] a material is stable (will remain in equilibrium) if (1) during the application of a set of stresses by an external agency the total work done on the material is positive and (2) the net work done by the external agency over a cycle of application and removal is zero or positive. If plastic (or inelastic) deformation is generated during the cycle, then the work done by the external agency must be non-zero.

Based on these statements, a necessary condition for loss of material stability, loss of uniqueness and any bifurcation in the solution can be given as the loss of positiveness of the second order work [113, 197]:

$$\dot{\sigma}_{ij}\dot{\varepsilon}_{ij} \geq 0 \tag{2.6}$$

where $\dot{\sigma}_{ij}$ and $\dot{\varepsilon}_{ij}$ are the stress and strain rates at some point or region in the body. This general bifurcation criterion can also be expressed as loss of positive definiteness of the symmetric part of the tangent stiffness tensor:

$$\dot{\varepsilon}_{ij}C^{Ts}_{ijkl}\dot{\varepsilon}_{kl} \geq 0 \tag{2.7}$$

where C^{Ts}_{ijkl} is the symmetric part of the tangent stiffness tensor, $C^{Ts}_{ijkl} = (C^{T}_{ijkl} + C^{T}_{klij})/2$. equation (2.7) indicates that general bifurcations may occur whenever C^{Ts}_{ijkl} is not positive definite. The general bifurcation criterion does not provide any information about the orientation of the localised zone, neither does it specify the mode of bifurcation as to whether or not it has a kinematically compatible form. In other words, the condition of equation (2.7) is satisfied in both diffuse and discontinuous modes of bifurcation. Diffuse mode of bifurcation (which is not kinematically compatible mode [32]) can occur only in a zone described as a point or surface, i.e. a domain of measure zero. Such a mode initiates smooth changes in the deformation field. A typical example of this type of bifurcation is the necking phenomenon in deformation of metals under tension. On the other hand, discontinuous bifurcation can be interpreted as a jump in the strain which can take place across a band of finite width (or certain volume) which is kinematically compatible with the surrounding material [32, 198].

2.4.2. Limit Point Bifurcation

General bifurcations are usually associated with non-zero stress rates both inside and outside the bifurcation zone. The subset of general bifurcations associated with zero stress rate occur only at the limit point when:

$$C^{T}_{ijkl}\dot{\varepsilon}_{kl} = 0 \quad \text{or} \quad \det\left(C^{T}_{ijkl}\right) = 0 \tag{2.8}$$

An alternative way of stating the above condition is that the limit point bifurcation occurs when the tangent stiffness tensor C^{T}_{ijkl} obtains its first zero eigenvalue. Valanis [199] states that loss of material stability should be associated with the limit point where the tangent modulus tensor obtains a zero eigenvalue. This may be appropriate if only statically

determinant specimens with force prescribed systems are considered. For materials with symmetric tangent modulus tensors, the Valanis [199] and Drucker [113] interpretations both identify the limit point as the point at which necessary conditions for loss of material stability are first satisfied. For materials with non-symmetric tangent stiffness tensors, loss of positive definiteness of the symmetric part of the tangent modulus tensor and satisfaction of the necessary condition for a general bifurcation can occur prior to the limit point. Similar to the general bifurcation criteria, the direction of the localisation band and the mode of bifurcation cannot be determined be means of the limit point bifurcation, as the condition of equation (2.8) is satisfied for both diffuse and discontinuous modes of bifurcation.

2.4.3. Classical Discontinuous Bifurcation

The classical discontinuous bifurcation criterion [195, 196, 200-202] determines a point in the loading process at which discontinuous bifurcation can occur such that subsequent strain rates become discontinuous across parallel planes of orientation n that separate a zone of localised deformation from the rest of the body. It should be noted that in discontinuous bifurcation the materials inside and outside the localisation band are kinematically compatible. Accordingly, Maxwell's compatibility conditions require that the strain rate in the localised zone, $\dot{\varepsilon}_{ij}^{l}$, be of the form:

$$\dot{\varepsilon}_{ij}^{l} = \dot{\varepsilon}_{ij}^{o} + \dot{\varepsilon}_{ij}^{k} = \dot{\varepsilon}_{ij}^{o} + \frac{1}{2}\left([\dot{u}]_i n_j + [\dot{u}]_j n_i\right) \tag{2.9}$$

where $\dot{\varepsilon}_{ij}^{o}$ is the strain rate outside the localised zone, $\dot{\varepsilon}_{ij}^{k}$ is a kinematically admissible discontinuous mode and $[\dot{u}]_i$ can be interpreted as a vector that represents the orientation of the relative velocity of regions on opposite sides of the localised deformation zone due to the introduction of the localised zone. Assume that the entire body is being plastically deformed, the stress and strain components are uniform throughout, and the body is at the onset of localisation. The stress increments inside and outside the localised zone are given by:

$$\dot{\sigma}_{ij}^{l} = C_{ijkl}^{Tl}\dot{\varepsilon}_{kl}^{l} \quad \text{and} \quad \dot{\sigma}_{ij}^{o} = C_{ijkl}^{To}\dot{\varepsilon}_{kl}^{o} \tag{2.10}$$

where C_{ijkl}^{Tl} and C_{ijkl}^{To} are the tangent stiffness tensors for material inside and outside the localised band, respectively. For continuing equilibrium, the traction rates must be continuous across the boundaries of the localised deformation zone:

$$\dot{T}_i^{l} = \dot{T}_i^{o} \quad \text{or} \quad \left(\dot{\sigma}_{ij}^{l} - \dot{\sigma}_{ij}^{o}\right)n_j = 0 \tag{2.11}$$

By combining these equations, Rice [195] shows that the requirement for continuing equilibrium is given by:

$$\left(C_{ijkl}^{Tl} - C_{ijkl}^{To}\right)\dot{\varepsilon}_{kl}^{o} n_j + A_{ij}[\dot{u}]_j = 0 \tag{2.12}$$

where A_{ij} is the acoustic or localisation tensor and it is defined by:

$$A_{ij} = C_{ijkl}^{T} n_k n_l \tag{2.13}$$

Suppose the body is loaded such that the strain rate $\dot{\varepsilon}_{ij}^{o}$ is constrained to evolve continuously. Then it is reasonable to assume that the tangent stiffness tensor for material outside the localised zone, C_{ijkl}^{To}, is identical to the tangent stiffness tensor for material inside the localised zone, C_{ijkl}^{Tl}, at the initiation of the bifurcation. The classical necessary condition for a discontinuous bifurcation is then obtained from equation (2.12) as:

$$A_{ij}[\dot{u}]_j = 0 \quad \text{or} \quad \det\left(A_{ij}\right) = 0 \tag{2.14}$$

Therefore, loss of material stability and localisation will not occur until the acoustic tensor obtains a zero eigenvalue [195, 196, 202]. In other words, the classical criterion for a discontinuous bifurcation is that the acoustic tensor, A_{ij}, has a zero eigenvalue, a necessary condition for loss of ellipticity [195]. The acoustic tensor is dependent on both an orientation vector and on the material. Localisation is associated with a strain rate jump within a planar band that does not lead to any kinematic incompatibilities with the surrounding material. Furthermore, evolution of the domain can only be controlled if additional constraints such as those provided by a non-local constitutive theory are present [203].

2.4.4. Loss of Strong Ellipticity

The classical discontinuous bifurcation criterion is based on two important assumptions. The first assumption is that the discontinuity in the strain rate (or velocity) field is constrained to have a special form so that material in the localised zone will remain kinematically compatible with the surrounding material. The second assumption is that the strain rates evolve continuously such that the tangent stiffness tensors for material inside and outside the localised zone are identical at the onset of localisation. The general bifurcation criterion requires neither of these assumptions. Specifically, a general bifurcation will not necessarily be associated with a mode which has the special form of $\dot{\varepsilon}_{ij}^{k}$, given in equation (2.9) and the active tangent modulus tensors for material inside and outside the bifurcation

zone will not necessarily be identical. The general bifurcation criterion, given by equation (2.9), is a necessary condition for any type of bifurcation. A necessary condition for a general bifurcation with a kinematically compatible mode, $\dot{\varepsilon}_{ij}^{k}$ is the loss of strong ellipticity criterion [198]:

$$\dot{\varepsilon}_{ij}^{k}\, C_{ijkl}^{Ts} \dot{\varepsilon}_{kl}^{k} = 0 \quad \text{or} \quad A_{ij}[\dot{u}]_i[\dot{u}]_j = 0 \tag{2.15}$$

In addition to the loss of positive definiteness of the acoustic tensor, loss of strong ellipticity can also be interpreted as the satisfaction of the general bifurcation condition with an associated strain rate which is of a form suitable for providing a kinematically compatible velocity field [198]. Loss of strong ellipticity of the governing differential equations will first occur when positive definiteness of the symmetric part of the acoustic tensor is lost [200]:

$$A_{ij}^{s}[\dot{u}]_j = 0 \quad \text{or} \quad \det\left(A_{ij}^{s}\right) = 0 \tag{2.16}$$

When the tangent stiffness tensor and thus the acoustic tensor are symmetric, the condition of equation (2.16), that is, loss of strong ellipticity and the classical necessary condition for a discontinuous bifurcation, equation (2.14), will first be satisfied at the same point. However, for non-symmetric acoustic tensors, loss of strong ellipticity will precede satisfaction of the necessary condition for a classical discontinuous bifurcation.

2.4.5. Determination of the Orientation and Onset of the Localisation

Regarding the prediction of the onset of occurrence and orientation of the localisation band, in addition to the properties of the constitutive model, the choice of the bifurcation criterion is also important. Based on the discussion in the previous section, it is clear that for determining the orientation of the localisation band in geomaterials, in which the localisation band is kinematically compatible with the surrounding bulk, either the classical bifurcation criterion (equation (2.14)) or the criterion of loss of strong ellipticity (equation (2.16)) should be used. Furthermore, In order to predict the onset of localisation, it is pivotal to have a rigorous and versatile constitutive model able to appropriately capture the fundamental aspects of the macroscopic behaviour of rocks. In particular, when used in conjunction with bifurcation analysis, the constitutive model should be able to predict the mode of localisation and failure and the critical conditions for the onset of instability. Predictions of the onset of localisation and the orientation of the localisation band are sensitively dependent on the

constitutive model and its parameters that have been chosen or developed to characterise the mechanical behaviour of rock material.

As was discussed earlier the localisation of deformation in compact rocks, under the pressures attainable in the present day laboratory experiments, take place in an inclined band often referred to as the shear band. Compaction bands have not hitherto been observed in compact rocks in experimental studies. On the other hand, porous rocks exhibit two distinct localisation modes: (1) shear localisation, which results in brittle faulting and dilative behaviour under low pressure; and (2) compaction (or shear-enhanced compaction) localisation, which gives rise to contractive behaviour and cataclastic flow under high pressures. It is important for a constitutive model to be able to predict the onset and the mode of localisation together with the post-localisation behaviour, in addition to the mechanical behaviour. However, the focus of the majority of the existing constitutive models has been mainly on the macroscopic responses of rocks under different loading conditions. Therefore, many of the existing models have some limitations in predicting the onset of localisation and the orientation of the localisation band, let alone the capability to capture the post-localisation behaviour in a physically meaningful way, given the loss of homogeneity beyond the onset of localisation. For instance, some models [e.g. 29, 202] can predict the onset of localisation only in the brittle regime. Some other models that are able to predict the occurrence of the onset and orientation of the localisation band under high pressure [e.g. 74, 75, 204] suffer from some limitations in predicting the onset of localisation at low pressure and in the brittle regime. Although some models, such as the cap model proposed by Grueschow and Rudnicki [125], are able to predict the onset and mode of localisation for a wide range of pressures (both shear and compaction), they may have some limitations in capturing other aspects of rock behaviour. For example, in the model by Grueschow and Rudnicki [125] the stiffness reduction due to damage is not taken into account. Additionally, in this model, the evolution of shape and size of the cap is expressed as a function of both volumetric and deviatoric plastic strains, which leads to increasing the number of model parameters.

Furthermore, it should be noted that for a constitutive model with non-associated flow rules and therefore non-symmetric tangent stiffness the condition of equation (2.16) is satisfied prior to the condition of equation (2.14). As was discussed earlier in Section 2.2.3, experimental observations of the onset of localisation in rocks have not been conclusive about whether the onset of localisation takes place prior to or after the peak stress. For

instance, acoustic emission (AE) measurements commonly indicate that the onset of localisation does not occur until the peak stress has been attained [94] while strain and surface deformation measurements and some microstructural observations seem to indicate the occurrence of pre-peak localisation [45, 205, 206].

In order to investigate the localisation properties of the constitutive models developed in this study, the classical bifurcation criterion is adopted. In these proposed models the flow rules are non-associated and thus the tangent stiffness tensors are not symmetric. Therefore, if the classical condition of localisation is satisfied by the model formulation the satisfaction of the criteria of loss of strong ellipticity is guaranteed. Nevertheless, if the localisation properties of the model are to be compared against experimental data, in order to enrich the procedure of calibration of model parameters, then care must be practised as to which localisation criteria is chosen. It is demonstrated in Chapters 4 and 5 that the proposed coupled elastoplastic-damage models are capable of predicting the onset and mode of localisation for a wide range of stress states in softening/dilation and hardening/compaction regimes.

2.4.6. Localisation, Softening and Deterministic Size Effect

The size effect is a problem of scaling and it is crucial to be taken into proper account when applying a constitutive model to simulate a structural response or even when developing a constitutive model. The size effect in solid mechanics is understood as the effect of the characteristic structure size on the nominal strength and on the post-peak load-displacement response of the structure. Over the past few decades, the size effect problem has been viewed from two perspectives often referred to as ‘statistical size effect’ and ‘deterministic size effect’ [31]. In a nutshell, based on the statistical size effect the larger structures (or specimens) have a smaller nominal strength because the probability of the presence of flaws and defects (e.g. voids and microcracks) increases with the size of the structure. The deterministic size effect hypothesis, on the other hand, attributes the smaller nominal strength and also the steeper post-peak load-displacement response (in the softening regime) of larger structures to the enhancement in the material inhomogeneity and stress redistributions due to the stable propagation of micro-cracks, localisation of damage and the inherent energy release. In this study, the focus is on investigating and addressing some issues related to the deterministic size effect.

Due to the localisation induced inhomogeneity within a structure, stress and strain fields lose their uniqueness and thus any continuum (or macroscopic) definition or measure of stress and strain is no longer physically meaningful. Upon the onset of localisation, the material inside the localisation band will be loaded inelastically, while the material outside the band will undergo inelastic unloading. Therefore, when the localisation zone is formed, the volume fraction of the material outside the localisation band starts to give up its stored elastic energy. It is obvious that the stored elastic energy within a structure scales up with its size. However, assuming an invariable width for the localisation band the effect of structure size on the post-peak load-displacement response can be demonstrated. In this case, the load-displacement curves pertaining to specimens with the same cross section and different length are compared with on one another in Figure 2.14. As the slenderness of the specimen increases the specimen shows a steeper post-peak load-displacement response until a snap-back is observed in the load-displacement response.

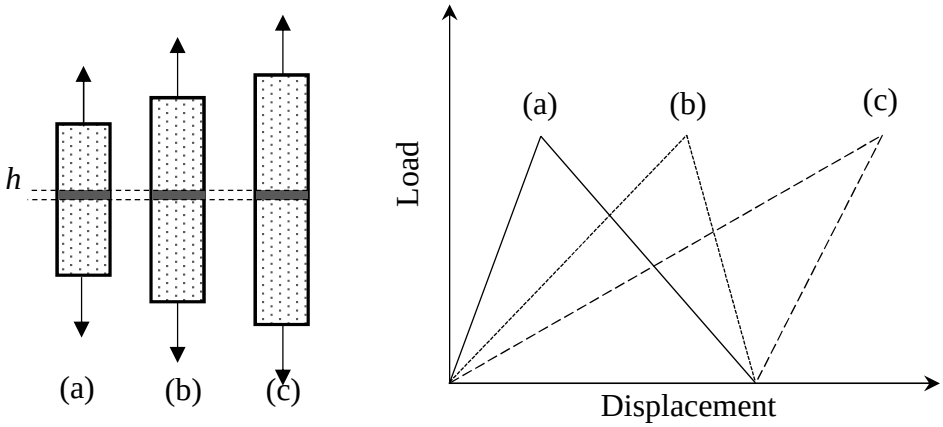

Figure 2.14: Schematic representation of the effect of the structure size on the post peak load-displacement

This phenomenon poses serious challenges to constitutive modelling based on the conventional continuum mechanics the most important of which is the ill-posedness of BVPs due to the loss of ellipticity of the governing constitutive equations (e.g. infinitely small softening zone and mesh-dependent solutions in FE analysis [33]). These problems can be alleviated by applying a regularisation scheme, such as non-local, gradient or rate-dependent regularisations. Recently a two-scale approach has been proposed by Nguyen et al. [37], which approximates the continuum response by specifying the kinematic interdependencies between the localisation band and the surrounding bulk. One important advantage of this model is that the post-localisation response can be modelled at the material level in a more

physically meaningful way compared to conventional continuum models. This approach will be further enhanced with a consistent thermodynamic formulation, and explored in this study.

2.5. Summary and Discussion

Analysis and study of the inelastic behaviour of rock material are of crucial importance in many practical problems encountered in mining and civil engineering projects. Typical examples of these problems include the analyses of rock-support interaction around underground excavations, or problems involving large deformations of rock material and rock masses such as mass caving or slope instability. Numerical simulations, in particular, finite element analysis, have been proven to be powerful tools for simulating the mechanical behaviour of many engineering materials, including rocks. The accuracy and robustness of these numerical simulations, however, rely heavily on the material or constitutive models which establish a relation between the applied stresses and the resultant deformations for a material point. The more realistically the constitutive model describes the mechanical behaviour of the material, the more reliable the results of a numerical simulation will be.

In general, the proper choice of constitutive models for an engineering application depends on the actual need and the loading circumstances. For instance, simple models, such as elastoplastic or elastic-damage models, can give satisfactory results in cases of monotonic loading. Nevertheless, each suffer from some limitation either in accounting for the stiffness reduction or for capturing the residual and permanent deformations. Therefore, more advanced and sophisticated constitutive models which can more accurately describe the observed macroscopic behaviour of the material are required. In particular, since the two dissipative mechanisms of damage and plasticity occur and evolve together during the inelastic deformation of most engineering materials, the coupling and interaction between these dissipative mechanisms should be reflected in the formulation of constitutive models. However, the development of coupled damage-plasticity models is non-trivial, as it concerns the macroscopic modelling of complex underlying phenomena at the microscopic scale, the experimental measurement of which is extremely difficult, if not impossible. An alternative approach would be a numerical microscopic analysis of the material behaviour in order to obtain some understanding of the underlying micromechanical phenomena. This approach, however, could be very computationally demanding. Such micromechanical approaches are outside the scope of this study.

Numerous coupled elastoplastic-damage models have been proposed during the past few decades. Nevertheless, since all constitutive models eventually suffer from some limitation, there is always space for new developments. The coupled damage-plasticity models proposed in this study are also no exception to this fact as they also have their own limitations. This study, however, attempts to focus on some aspects of constitutive modelling to which enough attention has not been paid. In particular, the complication and sometimes the use of *ad hoc* assumptions in the model formulation can be avoided by formulating the model within the well-established framework of thermodynamics. Since all the constitutive models in this study are developed within the framework of generalised thermodynamics, a separate chapter (Chapter 3) is devoted to the in-depth investigation of different features and potentials of the framework of generalised thermodynamics.

The combination of damage mechanics and plasticity theory within the framework of generalised thermodynamic will be focused on in the subsequent chapters. Thermodynamic principles will serve as a basis for the development of constitutive models and it facilitates the incorporation of the mechanisms of deformation into the model formulation in a rigorous and consistent manner. In the development of coupled elastoplastic-damage models in this study, an attempt is made to capture the most fundamental features of the rock material behaviour, such as strength and stiffness degradation due to damage evolution, permanent deformation, brittle to ductile transition and dilational and contractive responses. The identification and determination of model parameters will also be addressed and discussed in detail.

In addition, both field and laboratory observations have revealed that the process of inelastic deformation and failure of rock involve localisation of deformation within a band of finite width. Depending on the microstructure of rock and also the stress state various modes of deformation, localisation and failure can occur in a rock specimen. Examples of these modes of mechanical responses are shear localisation and brittle faulting, shear-enhanced compaction and pure compaction and cataclastic flow or ductile deformation. As was discussed earlier in preceding sections of this brief review, it is desirable for a constitutive model (to be used along with bifurcation analysis) to reflect all the above mentioned observable macroscopic behavioural features of the material.

Constitutive models like the critical state and cap models and their various modified versions of these models [e.g. 121-124, 125, 126], have been extensively used to capture the

formation of the localisation band (in particular compaction band) in the past. These studies, however, are mostly focused on calibrating and adjusting the parameters of the constitutive model so that the onset and mode of localisation can be predicted, without paying much attention to how the same model with the same model parameters would predict the experimental stress-strain data. On the other hand, in some other studies [e.g. 29, 127, 128] only the macroscopic stress-strain response and evolution of yield envelopes are taken into consideration, without providing any information about the capability of the model in predicting the onset and model of localisation. Despite the valuable achievements of the previous studies, it is clear that theoretical works are still far from being able to accurately and realistically explain, capture and predict all aspects of the mechanical behaviour of the rock material. In this study, in addition to the development of constitutive models, procedures and strategies for identification and calibration of the model parameters are also proposed. In particular, it is demonstrated that by using a single set of parameters the proposed coupled elastoplastic-damage models are capable of reflecting both the stress-strain response and the onset and mode of localisation and failure.

Furthermore, localisation of deformation, which is characteristic of the inelastic deformation of cohesive-frictional geomaterials, causes the mechanical response of the structure to be dependent on it size. When the structure is loaded under conditions conducive to post-peak softening, the steeper post-peak load-displacement curves are the result of an increase in the size of the structure. This problem poses serious problems on constitutive modelling and numerical simulation based on conventional continuum mechanics. In order to tackle this problem regularisation schemes, such as nonlocal and gradient models have been widely used in the literature. In this study, however, a kinematically enhanced constitutive modelling framework is adopted in order to investigated and study the deterministic size effect problem at the material level. This kinematically enhanced modelling framework is indeed a two-scale approach which specifies the coupling and kinematical interdependencies of the localisation band with the surrounding bulk. Details of the formulation of this two-scale approach are discussed is Chapter 6 of this thesis.

CHAPTER 3

Constitutive Modelling within the Framework of Generalised Thermodynamics

3.1. Introduction

Analyses of boundary value problems (BVPs) in engineering applications require the determination of constitutive behaviour of the material (or materials) making the structure under consideration. The complex behaviour of natural (e.g. rocks and soils) and many of manmade materials (e.g. concrete and composites) motivates the development of sophisticated constitutive models with high capability in predicting the material behaviour. In principle, necessary components of a constitutive model, such as the yield function, hardening/softening rules, etc., can be defined separately, without necessarily specifying the link between the yielding condition and the dissipation properties of the material model. In this approach, the requirements for the thermodynamic admissibility (non-negativeness of the energy dissipation rate during the inelastic behaviour) are applied retrospectively after the completion of the model formulation. This approach may lead to introducing *ad hoc* assumptions in the formulation of the model as there is no specific link between the rate of energy dissipation and the attainable stress state (or yielding condition) during each step of inelastic loading. A more rigorous and consistent approach is to construct the constitutive model within a thermomechanical framework which establishes a direct link between the energy dissipation properties and yielding conditions.

The two disciplines of continuum mechanics and thermodynamics are closely connected and even inseparable. In this regard, it is important to distinguish between the classical thermodynamics and the modern thermodynamic field theory. The study of changes in the state of a system in classical thermodynamics is restricted to extremely slow processes in the vicinity of an equilibrium state. The modern thermodynamic field theory, on the other hand, considers infinitesimal elements of a system in which a process takes place, admitting

that the thermodynamic state is homogeneous throughout an element and it only differs from one element to another. This field theory facilitates the amalgamation of thermodynamics and continuum mechanics [21]. Over the past few decades, the principles of thermodynamics have been extensively used for the development of constitutive models, describing the mechanical behaviour of engineering materials. General accounts of the thermodynamics of elastoplastic materials can be found in the works of Ziegler [21], Lemaitre and Chaboche [152], Maugin [207, 208] and Houlsby and Puzrin [19]. Many other authors have also made some key contributes to the field [22, 144, 191, 209].

In regard to the development of constitutive models within a thermodynamic framework, an important step is to select the material element. Since, in general, the conservation condition holds for the mass of a material element, whereas the volume of the element is variable, it is clear that the object to be considered is an element of mass. Nevertheless, in small strain continuum mechanics, a unit volume element of material can be considered which considerably simplifies the formulation [19]. Hence, for all thermodynamic formalisms and constitutive model developments in this study, a unit volume element is considered. This volume element must be sufficiently small to allow for the application of thermodynamics as a field theory, yet large enough to be representative of the most fundamental features of the continuum body. Such volume element is referred to as the representative volume element (RVE).

In this chapter, key aspects of a well-established thermodynamic framework referred to as the generalised thermodynamics or thermodynamics with internal variables (TIV) are presented. The aim of this chapter is to provide a brief introduction to the generalised thermodynamic framework which is extensively used in the development of constitutive models in the successive chapters of this thesis. In this sense, the repetition of the general principles and formalisms will be avoided in the successive chapters and reference will be made to the relevant sections of the current chapter where necessary. In addition, while the basis of the framework is based on earlier works by Ziegler [21] and Houlsby and Puzrin [19], the author has made an attempt to interpret and reformulate it in a slightly different and, to the best of his knowledge, easier way that can be later used in the development of several models. In addition, a further exploration of the dissipation properties in Section 3.4 is also introduced to give more insights into the intrinsic characteristics of the framework.

3.2. Definitions and Terminologies

In this section, the definition of some common thermodynamics terminologies is provided. These definitions help the subsequent discussions to follow more smoothly. Necessary definitions for the discussions presented in this chapter include:

Independent state variables are those variables that can completely describe the thermodynamics state of a system, e.g. strain $\boldsymbol{\varepsilon}$ and absolute temperature θ

Dependent state variables (state functions) are those variables which are defined as functions of the independent state variables, e.g. internal energy, U and entropy S

It should also be noted that the definition of independent and dependent variables are relative. For instance, in a strain based formulation, the total strain tensor ε is an independent variable, while the stress $\boldsymbol{\sigma}$ is considered as a dependent variable and vice versa. Stress $\boldsymbol{\sigma}$ and strain $\boldsymbol{\varepsilon}$ are also referred to as work conjugate variables.

Internal variables are those variables which somehow record the history of changes of the state variables within a system.

Internal forces are those thermodynamic forces which are work conjugate with the internal variables.

The system in the present study refers to a unit volume element of a material under consideration.

A *closed system* is a system that can exchange heat but not matter with the environment.

An *isolated system* can exchange neither heat nor matter with the environment.

3.3. Thermodynamic State of a Unit Volume Element

The state of a system (e.g. an RVE) can be completely described by two independent state variables strain, $\boldsymbol{\varepsilon}$, and absolute temperature, θ. However, in the context of continuum mechanics, the state of a system (e.g. a unit volume element of a material) at time t is not merely a function of the instantaneous values of the independent state variables but also depends on the previous history of these parameters. In such cases, the previous history of the thermodynamic state can be described by defining the dependent state variables (internal energy, entropy, etc.) as functionals of the independent state variables. These functionals depend not only on the instantaneous values of the independent state variables but also on their values at all previous times. This approach is generally referred to as the rational

thermodynamics. Another approach, which will be used in this study, is to introduce a number of internal variables that somehow encompass the previous history of the state of a system. This approach is referred to as the generalised thermodynamics or thermodynamics with internal variable (TIV). In principle, an infinite number of internal variables would be needed for precisely describing the previous history of the state of a system. In practice, however, a fairly small number of internal variables would suffice to give close approximations to the actual state of a system if the essential mechanisms responsible for the changes in the state of a system are properly understood.

If the state of the RVE is altered by infinitesimal changes in the strain and absolute temperature, i.e. $\dot{\boldsymbol{\varepsilon}}$ and $\dot{\theta}$, then the elementary work increment done on the RVE can be given by:

$$\delta W = \boldsymbol{\sigma} : \dot{\boldsymbol{\varepsilon}} \tag{3.1}$$

where $\boldsymbol{\sigma}$ is the stress tensor, which is a dependent state variable in an strain-based formulation. In general, a change in the state of a system is also accompanied by a certain amount of work done by the microscopic forces. The expression of the elementary work increment, as stated by equation (3.1), does not contain any information about this microscopic work. Understanding the nature of this microscopic work and the microscopic forces involved is necessary, especially in more complex systems, where the state of the system is not only a function of the instantaneous values of the state variables but also depends on the previous history of these variables (see Section 3.4). Therefore, a more comprehensive definition of the elementary work increment is required. To this end, it is assumed that the elementary work increment done on a system changes its properties. Therefore, instead of directly defining the elementary work increment, δW, as in equation (3.1), its definition can be given through the changes it causes to the properties of a system. In general, these properties are defined as state functions and for now, it is assumed that they are functions of only state variables $\boldsymbol{\varepsilon}$ and θ. Two state functions that can be used for describing the properties of an RVE are specific internal energy, $u = u(\boldsymbol{\varepsilon}, \tilde{\alpha}_1, \dots, \tilde{\alpha}_N, \theta)$ and specific entropy, $s = s(\boldsymbol{\varepsilon}, \tilde{\alpha}_1, \dots, \tilde{\alpha}_N, \theta)$. The internal energy and entropy are defined as functions of independent state variables (the strain tensor, $\boldsymbol{\varepsilon}$, and the absolute temperature, θ) and internal variables. In the definition of u and s the set $(\tilde{\alpha}_1, \dots, \tilde{\alpha}_N)$ is a set of internal variables with each variable being associated with one particular irreversible process that can potentially occur within the system at any time between the consecutive thermodynamic

states. The symbol '∼' on top of each internal variable indicates that they can be a tensor of any order, depending on the physical phenomenon they represent. All second order tensors are denoted by bold letters and the inner product between the second order tensors is denoted by ":". Also, the inner product between two tensors of the same unknown dimension is denoted by "·". Now the changes in the state of a system can be studied by investigating the changes in its properties. For this purpose, The First and The Second Laws of Thermodynamics is used.

The First Law of thermodynamics states that changes in the internal energy of a system can be given as the summation of the elementary work increment done on a system and the microscopic work done by microscopic forces within the system:

$$\delta W + \delta Q = \dot{u} \tag{3.2}$$

In the above expression, δQ represents the microscopic work done by microscopic forces within the system and it is often, phenomenologically, interpreted as the heat supply. A more accurate description of the microscopic work can be given by using the other property of the system, which is entropy. Entropy can be defined as a thermodynamic property that measures the degree of randomisation or disorder at the microscopic level. A macroscopic feature which is associated with entropy production is a loss of ability to do useful work. Energy is degraded to a less useful form, and it is sometimes said that there is a decrease in the availability of energy. Entropy is produced in both reversible and irreversible processes. The Second Law of Thermodynamics states that entropy can be produced, but never destroyed. Therefore, according to the Second Law any entropy increment is necessarily non-negative. This leads to the expression of The Second Law of Thermodynamics in the following form:

$$\dot{s} = \dot{s}^r + \dot{s}^{ir} \geq \frac{\delta Q}{\theta} \tag{3.3}$$

In the above expression, $\dot{s}^r$ and $\dot{s}^{ir}$ represent entropy increments due to reversible and irreversible processes, respectively. In the absence of irreversible processes, $\dot{s}^{ir} = 0$ and equality holds in the expression of the Second Law, therefore:

$$\dot{s} = \dot{s}^r = \frac{\delta Q}{\theta} \tag{3.4}$$

Equation (3.4) in conjunction with the Second Law, as stated by inequality (3.3), requires that the irreversible entropy be necessarily non-negative, i.e. $\dot{s}^{ir} \geq 0$. Substituting δQ from

equation (3.4) into equation (3.2) and making use of equation (3.3) results in the following expression for the elementary work increment:

$$\delta W = \dot{u} - \theta \dot{s} + \theta \dot{s}^{ir} \tag{3.5}$$

It is acknowledged that equation (3.4) for reversible processes is used in the above equation, and despite its usefulness, its validity for irreversible cases has not been examined yet. Since the specific internal energy, u, and specific entropy, s, are state functions, their rates of change with respect to changes in state and internal variables can be given as:

$$\dot{u} = \frac{\partial u}{\partial \boldsymbol{\varepsilon}} : \dot{\boldsymbol{\varepsilon}} + \frac{\partial u}{\partial \tilde{\alpha}_1} \cdot \dot{\tilde{\alpha}}_1 + \cdots + \frac{\partial u}{\partial \tilde{\alpha}_N} \cdot \dot{\tilde{\alpha}}_N + \frac{\partial u}{\partial \theta} \dot{\theta} \tag{3.6}$$

$$\dot{s} = \frac{\partial s}{\partial \boldsymbol{\varepsilon}} : \dot{\boldsymbol{\varepsilon}} + \frac{\partial s}{\partial \tilde{\alpha}_1} \cdot \dot{\tilde{\alpha}}_1 + \cdots + \frac{\partial s}{\partial \tilde{\alpha}_N} \cdot \dot{\tilde{\alpha}}_N + \frac{\partial s}{\partial \theta} \dot{\theta} \tag{3.7}$$

Substituting the above expressions into the expression of the elementary work increment, given by equation (3.5), results in:

$$\begin{aligned} \delta W = & \left(\frac{\partial u}{\partial \boldsymbol{\varepsilon}} - \theta \frac{\partial s}{\partial \boldsymbol{\varepsilon}} \right) : \dot{\boldsymbol{\varepsilon}} \\ & + \left(\frac{\partial u}{\partial \tilde{\alpha}_1} - \theta \frac{\partial s}{\partial \tilde{\alpha}_1} \right) \cdot \dot{\tilde{\alpha}}_1 + \cdots + \left(\frac{\partial u}{\partial \tilde{\alpha}_N} - \theta \frac{\partial s}{\partial \tilde{\alpha}_N} \right) \cdot \dot{\tilde{\alpha}}_N + \left(\frac{\partial u}{\partial \theta} - \theta \frac{\partial s}{\partial \theta} \right) \dot{\theta} \\ & + \theta \dot{s}^{ir} \end{aligned} \tag{3.8}$$

From the above expression, it is inferred that that $\theta \dot{s}^{ir}$ has the form of an elementary work increment which is dissipative and can be denoted by $\delta\Phi$. The terms $(\partial u/\partial \tilde{\alpha}_i - \theta \partial s/\partial \tilde{\alpha}_i)$, $i = 1 \ldots N$ are referred to as non-dissipative or quasiconservative [21] part of the internal forces which are work conjugate with the internal variables $\dot{\tilde{\alpha}}_i, i = 1 \ldots N$ and they are denoted here by $-\tilde{\tilde{\chi}}_i,\ i = 1 \ldots N$. Therefore, for isothermal problems, which are the focus of this study, the elementary work increment of equation (3.8) can be rewritten as:

$$\delta W = \boldsymbol{\sigma}^q : \dot{\boldsymbol{\varepsilon}} - \tilde{\tilde{\chi}}_1 \cdot \dot{\tilde{\alpha}}_1 - \cdots - \tilde{\tilde{\chi}}_N \cdot \dot{\tilde{\alpha}}_N + \delta\Phi \tag{3.9}$$

In the above expression, $\boldsymbol{\sigma}^q = (\partial u/\partial \boldsymbol{\varepsilon} - \theta \partial s/\partial \boldsymbol{\varepsilon})$ represents the quasiconservative part of the stress tensor and $\tilde{\tilde{\chi}}_i, i = 1 \ldots N$ are the quasiconservative part of the internal forces conjugate to each internal variable $(\dot{\tilde{\alpha}}_i, i = 1 \ldots N)$. Given the appearance of the quasiconservative part, $\boldsymbol{\sigma}^q$, of the stress tensor in (3.8), it is assumed that the general form of the dissipation function, $\delta\Phi$, can be expressed as:

$$\delta\Phi\left(\dot{\boldsymbol{\varepsilon}}, \dot{\tilde{\alpha}}_1, \ldots, \dot{\tilde{\alpha}}_N\right) = \boldsymbol{\sigma}^d : \dot{\boldsymbol{\varepsilon}} + \tilde{\chi}_1 \cdot \dot{\tilde{\alpha}}_1 + \cdots + \tilde{\chi}_N \cdot \dot{\tilde{\alpha}}_N \geq 0 \tag{3.10}$$

where $\boldsymbol{\sigma}^d$ is the dissipative part of the total stress tensor. It is acknowledged that this assumption on the form of the dissipation may lead to a sub-set of all possibilities, the consequence of which is not explored yet and is also outside the scope of this thesis, given the main focus on the application of thermodynamics to the development of constitutive models for rocks. Using (3.10), the expression of the elementary work increment, as stated by equation (3.9), can be given as follows:

$$\delta W = (\boldsymbol{\sigma}^q + \boldsymbol{\sigma}^d) : \dot{\boldsymbol{\varepsilon}} + (\tilde{\chi}_1 - \bar{\tilde{\chi}}_1) \cdot \dot{\tilde{\alpha}}_1 + \cdots + (\tilde{\chi}_N - \bar{\tilde{\chi}}_N) \cdot \dot{\tilde{\alpha}}_N \tag{3.11}$$

In the above expressions, $\boldsymbol{\sigma}^d$ represents the dissipative part of the stress tensor and $\tilde{\chi}_i, , i = 1 \ldots N$ are the dissipative parts of the internal forces. Comparing the expressions of the elementary work increment given by equations (3.11) and (3.1) indicates that except for the first term, all other terms in equation (3.11) are zero and $\boldsymbol{\sigma} = \boldsymbol{\sigma}^q + \boldsymbol{\sigma}^d$. This decomposition of the stress tensor arises as a consequence of using the notion of quasiconservative stress for the first term in equation (3.8) (i.e. $\boldsymbol{\sigma}^q = (\partial u/\partial \boldsymbol{\varepsilon} - \theta \partial s/\partial \boldsymbol{\varepsilon})$) and also assuming that the dissipation function can be expressed by the general form given by equation (3.10). Furthermore, the terms $\tilde{\chi}_i - \bar{\tilde{\chi}}_i$ can be interpreted as sets of non-dissipative gyroscopic forces [21], which can be denoted as $\tilde{\Gamma}_i$, dependent in such a way on the rates of internal variables ($\dot{\tilde{\alpha}}_i$) that their power is always zero, i.e. $\tilde{\Gamma}_i \cdot \dot{\tilde{\alpha}}_i = 0$.

An immediate conclusion could be that vectors of gyroscopic forces, $\tilde{\Gamma}_i = \tilde{\chi}_i - \bar{\tilde{\chi}}_i$, are always orthogonal to their corresponding velocity vectors $\dot{\tilde{\alpha}}_i$. With this conclusion, the only way of defining the dissipative part of the stress and internal forces and, consequently, the dissipation function, is to provide an explicit definition for the gyroscopic forces, $\tilde{\Gamma}_i$. It should be noted that the quasiconservative parts of the stress tensor ($\boldsymbol{\sigma}^q$) and internal forces ($\bar{\tilde{\chi}}_i, i = 1..N$) are state functions and they can, in principle, be determined from the explicit definitions of the specific internal energy and entropy. In this sense, the irreversible processes could be treated by any number of functions (each defining the source of these gyroscopic forces) in addition to the definition of the two state functions, i.e. internal energy and entropy.. However, Ziegler [21] argues that although the gyroscopic forces can in principle occur (e.g. in rotating reference frames or in magnetic fields), they have never been observed, at least in reference to the deformation of a continua. Therefore, by excluding the gyroscopic forces, a more useful conclusion than the orthogonality of $\tilde{\Gamma}_i$ and $\dot{\tilde{\alpha}}_i$, would be drawn from postulating equality between the dissipative and quasiconservative parts of internal forces, i.e. $\tilde{\chi}_i = \bar{\tilde{\chi}}_i$. This constitutive postulate gives rise to a very important

principle referred to as the Ziegler' orthogonality principle. An important consequence of accepting the absence of the gyroscopic forces as a constitutive postulate is that it reverses the roles of the dissipation function $\delta\Phi$ and the dissipative forces. In this regard, the dissipation function is now considered as the primary function (or potential) from which the dissipative stresses are derived. Furthermore, an irreversible system is referred to as purely dissipative, wherever the dissipative forces are derivable from the dissipation potential [21], that is, if the condition of $\tilde{\chi}_i = \bar{\tilde{\chi}}_i$ is accepted as a constitutive postulate. Under such assumption all thermodynamic forces can be determined by explicitly defining the two state functions (i.e. internal energy and entropy) and the dissipation function, $\delta\Phi$.

In this study, it is assumed that the dissipation function, $\delta\Phi$, is a homogeneous function of order n in terms of all internal variables $\dot{\tilde{\alpha}}_i$ ($i = 1 \dots N$). This assumption restricts the focus of this study on a subset of all possibilities yet general enough to be applicable to a wide range of materials. With this assumption and by invoking the Euler's theorem for homogeneous functions, the dissipation function can be written as:

$$\delta\Phi = \frac{1}{n}\left(\frac{\partial\delta\Phi}{\partial\dot{\boldsymbol{\varepsilon}}} : \dot{\boldsymbol{\varepsilon}} + \frac{\partial\delta\Phi}{\partial\dot{\tilde{\alpha}}_1}\cdot\dot{\tilde{\alpha}}_1 + \cdots + \frac{\partial\delta\Phi}{\partial\dot{\tilde{\alpha}}_N}\cdot\dot{\tilde{\alpha}}_N\right) \geq 0 \tag{3.12}$$

Comparing the above expression with the general form assumed for the dissipation function in equation (3.10), the following results can be obtained:

$$\boldsymbol{\sigma}^d = \frac{1}{n}\frac{\partial\delta\Phi}{\partial\dot{\boldsymbol{\varepsilon}}} \tag{3.13}$$

$$\tilde{\chi}_i = \frac{1}{n}\frac{\partial\delta\Phi}{\partial\dot{\tilde{\alpha}}_i} \qquad i = 1 \dots N \tag{3.14}$$

On account of equations (3.13) and (3.14), it can be inferred that the dissipative part of the stress tensor and the dissipative force vectors corresponding to $\dot{\tilde{\alpha}}_i$ at time t are orthogonal to the dissipation surface $\delta\Phi = \delta\Phi_t$ in $\dot{\tilde{\alpha}}_i$-space and in the end points of $\dot{\tilde{\alpha}}_i$ (Figure 3.1). This orthogonality is referred to as the Ziegler's orthogonality principle. This principle can be viewed in a variety of ways, but the most useful way is to view it as a stronger statement than the Second Law of Thermodynamics [19]. Furthermore, $n \neq 1$ in equations (3.13) and (3.14) indicates the rate-dependent behaviour, where the stress and internal forces are functions of the strain rate and rates of internal variables. On the other hand, for rate-independent behaviour, dissipation function is a homogeneous function of order one in terms of the rates and hence $n = 1$.

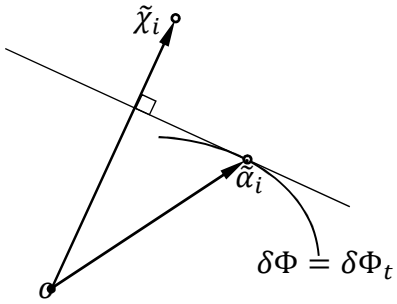

Figure 3.1: Orthogonality of the dissipative forces and the rates of internal variables (Ziegler [21])

Furthermore, instead of explicitly defining the internal energy and entropy, the quasiconservative parts of the stress tensor and the internal forces can be more straightforwardly obtained by introducing a free energy potential. Depending on the problem in hand, the free energy function can be either in the form of the Helmholtz free energy, $\Psi = \Psi(\boldsymbol{\varepsilon}, \tilde{\alpha}_1, \dots, \tilde{\alpha}_N, \theta)$, or in the form of the Gibbs free energy, $G = G(\boldsymbol{\sigma},\ \tilde{\alpha}_1, \dots, \tilde{\alpha}_N, \theta)$. By performing a Legendre transform (see [19]), the Helmholtz energy potential can be given as the dual function of the internal energy as follows:

$$\Psi = u - \theta s \tag{3.15}$$

Therefore, the rate of change of the Helmholtz free energy with respect to changes of dependent state variables (u and s) and the independent state variable (θ) is given as:

$$\dot{\Psi} = \dot{u} - \theta\dot{s} - s\dot{\theta} \tag{3.16}$$

Since in the development of all constitutive models in this study isothermal condition is assumed, the remainder of the current review will also focus on isothermal cases. For isothermal problems equation (3.16) reduces to:

$$\dot{\Psi} = \dot{u} - \theta\dot{s} \tag{3.17}$$

By substituting for $\dot{u}$ from the above equation into the expression of the First Law of thermodynamics, as stated by equation (3.2), the expression for the elementary work increment can be given as:

$$\delta W = \dot{\Psi} + \theta\dot{s} - \delta Q \tag{3.18}$$

Substituting for δQ from equation (3.4) and also accepting the assumption that was made immediately after equation (3.8), so that $\theta\dot{s}^{ir} = \delta\Phi$, the elementary work increment can be given as:

$$\delta W = \dot{\Psi} + \theta \dot{s}^{ir} = \dot{\Psi} + \delta\Phi \tag{3.19}$$

Furthermore, since the Helmholtz free energy is also a state function, the above expression for the elementary work increment can be further expanded to give:

$$\delta W = \dot{\Psi} + \delta\Phi = \frac{\partial \Psi}{\partial \boldsymbol{\varepsilon}} : \dot{\boldsymbol{\varepsilon}} + \frac{\partial \Psi}{\partial \tilde{\alpha}_1} \cdot \dot{\tilde{\alpha}}_1 + \cdots + \frac{\partial \Psi}{\partial \tilde{\alpha}_N} \cdot \dot{\tilde{\alpha}}_N + \delta\Phi \tag{3.20}$$

Comparing the above equation with equations (3.8) and (3.9), it follows that:

$$\frac{\partial \Psi}{\partial \boldsymbol{\varepsilon}} = \frac{\partial u}{\partial \boldsymbol{\varepsilon}} - \theta \frac{\partial s}{\partial \boldsymbol{\varepsilon}} = \boldsymbol{\sigma}^q \tag{3.21}$$

$$\frac{\partial \Psi}{\partial \tilde{\alpha}_i} = \theta \frac{\partial s}{\partial \tilde{\alpha}_i} - \frac{\partial u}{\partial \tilde{\alpha}_i} = -\tilde{\tilde{\chi}}_i \qquad i = 1 \ldots N \tag{3.22}$$

The specific definition of the free energy depends on the characteristic properties of the material, such as its microstructure and the physical mechanisms through which the energy is stored within the material. Substituting equation (3.12) into the expression of the elementary work increment, as stated by equation (3.20), results in:

$$\delta W = \left(\frac{\partial \Psi}{\partial \boldsymbol{\varepsilon}} + \frac{1}{n}\frac{\partial \delta\Phi}{\partial \dot{\boldsymbol{\varepsilon}}}\right) : \dot{\boldsymbol{\varepsilon}} + \left(\frac{\partial \Psi}{\partial \tilde{\alpha}_1} + \frac{1}{n}\frac{\partial \delta\Phi}{\partial \dot{\tilde{\alpha}}_1}\right) \cdot \dot{\tilde{\alpha}}_1 + \cdots + \left(\frac{\partial \Psi}{\partial \tilde{\alpha}_N} + \frac{1}{n}\frac{\partial \delta\Phi}{\partial \dot{\tilde{\alpha}}_N}\right) \cdot \dot{\tilde{\alpha}}_N \tag{3.23}$$

Again, comparing equations (3.23) and (3.1) the following set of equations is obtained:

$$\boldsymbol{\sigma} = \frac{\partial \Psi}{\partial \boldsymbol{\varepsilon}} + \frac{1}{n}\frac{\partial \delta\Phi}{\partial \dot{\boldsymbol{\varepsilon}}} \tag{3.24}$$

$$0 = \frac{\partial \Psi}{\partial \tilde{\alpha}_i} + \frac{1}{n}\frac{\partial \delta\Phi}{\partial \dot{\tilde{\alpha}}_i} \qquad i = 1 \ldots N \tag{3.25}$$

It is clear that if the explicit definition of the two scalar functions, namely, the free energy potential and the dissipation function are known, then the stress tensor and the dissipative parts of the internal forces can be obtained from the above sets of equations.

3.4. Rate-independent behaviour, loading function and evolution rules

Since the focus of this study is on the rate-independent behaviour of materials, the review of the generalised thermodynamic framework in this chapter is also restricted only to the rate-independent case. If the material behaviour is assumed to be rate-independent, then the dissipation function is a homogeneous first order function in rates. This implies that the coefficient of proportionality is one, i.e. $n = 1$. Therefore, for rate-independent behaviour

the set equations (3.24) and (3.25), and also equation (3.14) are modified to the following set of equations:

$$\boldsymbol{\sigma} = \frac{\partial \Psi}{\partial \boldsymbol{\varepsilon}} + \frac{\partial \delta\Phi}{\partial \dot{\boldsymbol{\varepsilon}}} \tag{3.26}$$

$$0 = \frac{\partial \Psi}{\partial \tilde{\alpha}_i} + \frac{\partial \delta\Phi}{\partial \dot{\tilde{\alpha}}_i} \tag{3.27}$$

$$\tilde{\chi}_i = \frac{\partial \delta\Phi}{\partial \dot{\tilde{\alpha}}_i} \qquad i = 1 \dots N \tag{3.28}$$

Several features of the behaviour of rate-independent materials follow from this special form of the dissipation function, i.e. a homogeneous first order function in rates. In particular, the existence of the yield or loading function arises as a direct consequence of the rate-independent behaviour [19]. The yield function can be derived by performing a Legendre transformation on the dissipation function. This transformation is a degenerate special case of the Legendre transformation because the dissipation function is homogeneous and first-order in the rates [19, 191]. The degenerate Legendre transformation of the dissipation function, $\delta\Phi\left(\boldsymbol{\varepsilon}, \tilde{\alpha}_1, \dots, \tilde{\alpha}_N, \dot{\tilde{\alpha}}_1, \dots, \dot{\tilde{\alpha}}_N\right)$, which is a homogeneous first-order function in terms of the rates of internal variables, is a function of state, internal and conjugate variables, $\tilde{\chi}_i$, and its value is always zero, i.e. $y = y(\boldsymbol{\varepsilon}, \tilde{\alpha}_1, \dots, \tilde{\alpha}_N, \tilde{\chi}_1, \dots, \tilde{\chi}_N) = 0$. It should, however, be noted that the additive form of the dissipation function, as given by equation (3.10), can give rise to the existence of n different yield functions corresponding to n internal variables [119]. Therefore, the evolution of the internal variables is controlled by n different yield functions. In order to obtain a single yield function which controls the simultaneous evolution of all internal variables a different form of the dissipation function is required. To this end, the dissipation function can be defined as a functional in the following general form:

$$\delta\Phi = F(\varphi_1, \dots, \varphi_N) \tag{3.29}$$

where φ_i $(i = 1 \dots N)$ are homogeneous first order functions in the rates of internal variables. These functions are related to the contribution of each of the dissipative mechanisms, associated with $\dot{\tilde{\alpha}}_i$'s, to the total dissipation rate. In general, any definition of F is acceptable as long as $\delta\Phi$ remains a homogeneous first-order function in terms of the rates of internal variables. To this end, it is required for F to satisfy the following condition (see [19, 144]):

$$\left\| \frac{\partial^2 F}{\partial \dot{\tilde{\alpha}}_i \cdot \partial \dot{\tilde{\alpha}}_i} \right\| = 0 \tag{3.30}$$

In order to clarify and simplify the discussion, a specific form of the functional $F(\varphi_1, \dots, \varphi_N)$ that has been adopted by many researchers [e.g. 144, 189, 204, 210, 211-213] is considered here, which is defined as:

$$\delta\Phi = \sqrt{{\varphi_1}^2 + \cdots + {\varphi_N}^2} \tag{3.31}$$

As mentioned earlier, functions $\varphi_1, \dots, \varphi_N$ are homogeneous firs-order functions in the rates of internal variables and they are related to the rate of energy dissipation due to each dissipation mechanism represented by an internal variable.

Assuming that each of φ_i's ($i = 1..N$) is a function of only one internal variable rate, i.e. $\varphi_i = \varphi_i(\dot{\tilde{\alpha}}_i)$, then the dissipative part of the internal force conjugate to the i^{th} internal variable, $\dot{\tilde{\alpha}}_i$, is given as follows:

$$\tilde{\chi}_i = \frac{\partial \delta\Phi}{\partial \dot{\tilde{\alpha}}_i} = \frac{\partial \delta\Phi}{\partial \varphi_i} \frac{\partial \varphi_i}{\partial \dot{\tilde{\alpha}}_i} = \frac{\varphi_i}{\delta\Phi} \frac{\partial \varphi_i}{\partial \dot{\tilde{\alpha}}_i} \tag{3.32}$$

For this particular form of the dissipation function the degenerate Legendre transformation is performed in the following manner to obtain the expression of the yield function in the dissipative stress space:

Starting with equation (3.32), the following result can be obtained:

$$\frac{\tilde{\chi}_i \cdot \tilde{\chi}_i}{\frac{\partial \varphi_i}{\partial \dot{\tilde{\alpha}}_i} \cdot \frac{\partial \varphi_i}{\partial \dot{\tilde{\alpha}}_i}} = \left(\frac{\varphi_i}{\delta\Phi}\right)^2 \tag{3.33}$$

Since $\sum_{i=1}^{N} (\varphi_i/\delta\Phi)^2 = 1$ (see equation (3.31)), the yield function in the dissipative stress space can be obtained as:

$$y^* = \sum\nolimits_{i=1}^{N} \frac{\tilde{\chi}_i \cdot \tilde{\chi}_i}{\frac{\partial \varphi_i}{\partial \dot{\tilde{\alpha}}_i} \cdot \frac{\partial \varphi_i}{\partial \dot{\tilde{\alpha}}_i}} - 1 \leq 0 \tag{3.34}$$

Furthermore, the evolution rules for internal variables are obtained from the properties of the degenerate Legendre transformation as:

$$\dot{\tilde{\alpha}}_i = \dot{\lambda} \frac{\partial y^*}{\partial \tilde{\chi}_i} \qquad i = 1 \dots N \tag{3.35}$$

A detailed explanation of the Legendre transformation can be found in [19]. Furthermore, using equation (3.32), the rate of energy dissipation due to a dissipative mechanism represented by the i^{th} internal variable is given as:

$$\delta\Phi_i = \tilde{\chi}_i \cdot \dot{\tilde{\alpha}}_i = \frac{\varphi_i}{\delta\Phi}\frac{\partial\varphi_i}{\partial\dot{\tilde{\alpha}}_i} \cdot \dot{\tilde{\alpha}}_i \tag{3.36}$$

Since it is assumed that φ_i is a first-order homogeneous function in $\dot{\tilde{\alpha}}_i$, by invoking the Euler's theorem, equation (3.36) can be rewritten as:

$$\delta\Phi_i = \tilde{\chi}_i \cdot \dot{\tilde{\alpha}}_i = \frac{{\varphi_i}^2}{\delta\Phi} \tag{3.37}$$

Therefore, the total dissipation rate can be given as the sum of all the dissipation rates due to each underlying dissipative mechanism:

$$\delta\Phi = \sum_{i=1}^{N} \delta\Phi_i = \sum_{i=1}^{N} \tilde{\chi}_i \cdot \dot{\tilde{\alpha}}_i \tag{3.38}$$

In regard to the relation between functions $\varphi_1, \dots, \varphi_N$ and dissipation functions $\delta\Phi_1, \dots, \delta\Phi_N$, the ratio between the rate of energy dissipation due to a dissipative mechanism associated with the i^{th} internal variable, $\delta\Phi_i$, and the total dissipation rate, $\delta\Phi$, is defined as:

$$\frac{\delta\Phi_i}{\delta\Phi} = {r_i}^2 \tag{3.39}$$

Comparing equations (3.39) and (3.38), it immediately follows that:

$$\sum_{i=1}^{N} {r_i}^2 = 1 \tag{3.40}$$

Substituting for $\delta\Phi_i$ form the ratios defined in equation (3.39), the following relations are established between φ_i, $\delta\Phi_i$ and $\delta\Phi$:

$$\varphi_i = r_i\delta\Phi \qquad \text{and} \qquad \delta\Phi_i = r_i\varphi_i \qquad i = 1 \dots N \tag{3.41}$$

Once r_i's and φ_i's ($i = 1 \dots N$) are defined the total dissipation can be calculated by integrating both sides of the first equation in (3.41) with respect to one of the internal variables. Additionally, integrating both sides of the second equation in (3.41) with respect to one of the internal variables yields the total dissipation due to a dissipative mechanism associated with the same internal variable.

3.5. Kinematic Interdependencies and Constrain Equations

In some models, kinematic variables are not entirely free or independent but are constrained or interdependent by some means. In general, these constraints or interdependencies might involve strains and/or the rate of internal variables. The development of such models can either be achieved by reducing the number of kinematic variables, through eliminating the dependent variables, or by introducing some constraint equations while keeping all the kinematic variables [19, 214]. The latter is a more powerful and general technique and hence will be adopted in this study. In principle, depending on the nature of the problem in hand any number of kinematic constraint equations can be introduced, in order to address the kinematic interdependencies between the state and internal variables of a model. For instance, for a model with N internal variables a set of K kinematic constraint equations can be introduced. If the constraints are on strains (e.g. incompressible behaviour), or in general the interdependency of the kinematic fields can be defined in the total form, rather than the incremental form, then the set of kinematic constraints can be given in the following generic form:

$$C_j' = C_j'(\boldsymbol{\varepsilon}, \tilde{\alpha}_1, \dots, \tilde{\alpha}_1) = 0 \qquad j = 1 \dots K \tag{3.42}$$

These constrain equations can then be used to supplement the free energy potential (e.g. the Helmholtz free energy potential, $\Psi(\boldsymbol{\varepsilon}, \tilde{\alpha}_1, \dots, \tilde{\alpha}_N)$) to obtain a new (but equivalent) function as:

$$\Psi' = \Psi(\boldsymbol{\varepsilon}, \tilde{\alpha}_1, \dots, \tilde{\alpha}_N) + \sum_{j=1}^{K} \Lambda_j \cdot C_j' \tag{3.43}$$

where, Λ_j are the Lagrangean multipliers, which are eliminated between the following sets of equations, obtained by modifying equations (3.26) and (3.27):

$$\boldsymbol{\sigma} = \frac{\partial \Psi'}{\partial \boldsymbol{\varepsilon}} + \frac{\partial \delta\Phi}{\partial \dot{\boldsymbol{\varepsilon}}} = \frac{\partial \Psi}{\partial \boldsymbol{\varepsilon}} + \frac{\partial \delta\Phi}{\partial \dot{\boldsymbol{\varepsilon}}} + \sum_{j=1}^{K} \Lambda_j : \frac{\partial C_j}{\partial \boldsymbol{\varepsilon}} \tag{3.44}$$

$$0 = \frac{\partial \Psi'}{\partial \tilde{\alpha}_i} + \frac{\partial \delta\Phi}{\partial \dot{\tilde{\alpha}}_i} = \frac{\partial \Psi}{\partial \tilde{\alpha}_i} + \frac{\partial \delta\Phi}{\partial \dot{\tilde{\alpha}}_i} + \sum_{j=1}^{K} \Lambda_j \cdot \frac{\partial C_j}{\partial \tilde{\alpha}_i} \qquad i = 1 \dots N \tag{3.45}$$

On the other hand, if the constraints are on the rates of state and internal variables, the generic form of the kinematic constraint equation can be given as:

$$C_j = C_j\left(\dot{\boldsymbol{\varepsilon}}, \dot{\tilde{\alpha}}_1, \dots, \dot{\tilde{\alpha}}_N\right) = 0 \qquad j = 1 \dots K \tag{3.46}$$

In this case, the development of the model involves supplementing the dissipation function:

$$\delta\Phi' = \delta\Phi\left(\boldsymbol{\varepsilon}, \tilde{\alpha}_1, \dots, \tilde{\alpha}_N, \dot{\boldsymbol{\varepsilon}}, \dot{\tilde{\alpha}}_1, \dots, \dot{\tilde{\alpha}}_N\right) + \sum_{j=1}^{K} \Lambda_j \cdot C_j \tag{3.47}$$

If the dissipation function is to be supplemented with the constraint equations, then each constraint equation must be introduced as a first order homogeneous function in rates of internal variables in accordance with the dissipation function. Accordingly, the sets of equations (3.26) and (3.27) are, modified as follows:

$$\boldsymbol{\sigma} = \frac{\partial\Psi}{\partial\boldsymbol{\varepsilon}} + \frac{\partial\delta\Phi'}{\partial\dot{\boldsymbol{\varepsilon}}} = \frac{\partial\Psi}{\partial\boldsymbol{\varepsilon}} + \frac{\partial\delta\Phi}{\partial\dot{\boldsymbol{\varepsilon}}} + \sum_{j=1}^{K} \Lambda_j : \frac{\partial C_j}{\partial\dot{\boldsymbol{\varepsilon}}} \tag{3.48}$$

$$0 = \frac{\partial\Psi}{\partial\tilde{\alpha}_i} + \frac{\partial\delta\Phi'}{\partial\dot{\tilde{\alpha}}_i} = \frac{\partial\Psi}{\partial\tilde{\alpha}_i} + \frac{\partial\delta\Phi}{\partial\dot{\tilde{\alpha}}_i} + \sum_{j=1}^{K} \Lambda_j \cdot \frac{\partial C_j}{\partial\dot{\tilde{\alpha}}_i} \qquad i = 1 \dots N \tag{3.49}$$

In addition to the specification of kinematic interdependencies between the state and internal variables of a model, another important application of kinematic constraint equations is that they can be used to introduce new internal variables into the model formulation. Regarding irreversible deformations, any internal variable in the model formulation represents, in principle, a dissipative mechanism. The evolutions of these dissipative mechanisms are not independent, but they interact with one another and influence each other's evolution. If the physics and underlying mechanisms of these interactions are understood they can be readily and straightforwardly incorporated into the model formulation by means of constraint equations.

The application of the kinematic constraint equations can be demonstrated through a simple example in this section, where the deformation of a unit volume of an elastoplastic material is considered under isothermal condition. In this case, the Helmholtz free energy is the same as the elastic strain energy and can be written as:

$$\Psi = C_{ijkl}\varepsilon^e_{kl}\varepsilon^e_{ij} \tag{3.50}$$

In the above expression, C_{ijkl} is the elastic stiffness tensor and ε^e_{ij} is the elastic strain tensor. If plastic deformations also take place within the unit volume of the material, then the rate of energy dissipation due to the plastic deformation can be given by the dissipation function as:

$$\delta\Phi = \chi_{ij}\dot{\varepsilon}^p_{ij} \tag{3.51}$$

Furthermore, the strain tensor can be decomposed into the elastic and plastic part as:

$$\varepsilon_{ij} = \varepsilon_{ij}^{e} + \varepsilon_{ij}^{p} \tag{3.52}$$

Also, the rate form of the above relation is given as:

$$\dot{\varepsilon}_{ij} = \dot{\varepsilon}_{ij}^{e} + \dot{\varepsilon}_{ij}^{p} \tag{3.53}$$

In this simple example, both equations (3.52) and (3.53) can be used to form the kinematic constraint equation, which, in this case, specifies the relation between the total strain tensor with its elastic and plastic part. However, as was outlined earlier, if equation (3.52) is used to form the constraint equation, then the constraint equation should be added to the expression of the free energy function given by equation (3.50). On the other hand, if the kinematic constraint is formed by the rate equation (3.53), then it should be used for supplementing the dissipation function. In the case of this example, equation (3.53) is used to form the kinematic constraint equation as:

$$C_{ij} = \dot{\varepsilon}_{ij} - \dot{\varepsilon}_{ij}^{e} - \dot{\varepsilon}_{ij}^{p} = 0 \tag{3.54}$$

The above kinematic constraint equation is then used to supplement the dissipation function of equation (3.51) as follows:

$$\delta\Phi' = \delta\Phi + \Lambda_{ij} C_{ij} \tag{3.55}$$

For this particular example, equations (3.48) and (3.49) can be written as the follows:

$$\sigma_{ij} = \frac{\partial\Psi}{\partial\varepsilon_{ij}} + \frac{\partial\delta\Phi'}{\partial\dot{\varepsilon}_{ij}} = \frac{\partial\Psi}{\partial\varepsilon_{ij}} + \frac{\partial\delta\Phi}{\partial\dot{\varepsilon}_{ij}} + \Lambda_{kl}\frac{\partial C_{kl}}{\partial\dot{\varepsilon}_{ij}} \tag{3.56}$$

$$0 = \frac{\partial\Psi}{\partial\varepsilon_{ij}^{e}} + \frac{\partial\delta\Phi'}{\partial\dot{\varepsilon}_{ij}^{e}} = \frac{\partial\Psi}{\partial\varepsilon_{ij}^{e}} + \frac{\partial\delta\Phi}{\partial\dot{\varepsilon}_{ij}^{e}} + \Lambda_{kl}\frac{\partial C_{kl}}{\partial\dot{\varepsilon}_{ij}^{e}} \tag{3.57}$$

$$0 = \frac{\partial\Psi}{\partial\varepsilon_{ij}^{p}} + \frac{\partial\delta\Phi'}{\partial\dot{\varepsilon}_{ij}^{p}} = \frac{\partial\Psi}{\partial\varepsilon_{ij}^{p}} + \frac{\partial\delta\Phi}{\partial\dot{\varepsilon}_{ij}^{p}} + \Lambda_{kl}\frac{\partial C_{kl}}{\partial\dot{\varepsilon}_{ij}^{p}} \tag{3.58}$$

Using equations (3.50), (3.51), (3.54) and (3.56) in conjunction with equations (3.56) – (3.58) the following results are obtained:

$$\sigma_{ij} = \Lambda_{ij} \tag{3.59}$$

$$0 = C_{ijkl}\varepsilon_{kl}^{e} - \Lambda_{ij} \tag{3.60}$$

$$0 = \chi_{ij} - \Lambda_{ij} \tag{3.61}$$

By eliminating Λ_{ij} between the above equations and also using equation (3.52) the stress tensor and the dissipative part of the internal forces conjugate to plastic deformations are obtain as:

$$\sigma_{ij} = \chi_{ij} = C_{ijkl}\varepsilon_{kl}^{e} = C_{ijkl}\left(\varepsilon_{kl} - \varepsilon_{kl}^{p}\right) \tag{3.62}$$

Further discussions and demonstrations of the use of kinematic constraint equations are presented in the development of constitutive models throughout this study. In particular, it is shown in Chapter 6 that how this technique can be used to further enhance the framework of the generalised thermodynamics to model the localised failure of geomaterials.

CHAPTER 4

A Coupled Damage-Plasticity Model for Porous Rocks

4.1. Introduction

The ability to predict the complex patterns of behaviour of porous rocks by means of numerical simulations would be of great value for various engineering applications that involve the extraction of hydrocarbons and the underground storage of fluid and solid waste. In such applications it is of crucial importance to model both pre- and post-failure deformations (e.g., for borehole stability assessment [215]), and to capture the variations in porosity associated with volumetric inelastic strains (e.g., to estimate the changes in permeability [26, 28]). In this context, prediction of the occurrence of compaction localisation is particularly important because of its detrimental effects on fluid flow [216]. Porous granular rocks can be described as multiphase materials that contain grains, intergranular cement and void spaces. The macroscopic behavioural features of these rocks under a certain loading condition are governed by the mechanical responses of all the material phases in their microscopic structure and the interaction between them. Different failure processes commonly observed in porous rocks may include grain crushing, cement debonding and pore collapse [28, 59]. Under low confining pressure, cement debonding is the predominate failure process and the grains or rock fragmentations have enough space to rotate and slip which may potentially give rise to shear induced dilatancy. Under high confining pressure, on the other hand, the rotation and slip of grains are inhibited due to pore collapse and the lack of available space. Additionally, grain crushing under high pressure and the subsequent rearrangement of rock fragments and debris further reduces the porosity and cause compaction [28, 59]. In general, porous rocks exhibit two types of mechanical response corresponding to the loading condition and/or applied pressure. These distinct behavioural features include (a) brittle faulting together with dilational behaviour under low pressure, and (b) cataclastic flow and contractive behaviour under high pressures pertaining to brittle-ductile transition and ductile regime.

Various modelling approaches have been proposed in order to describe the behaviour of porous rocks, ranging from critical state [121, 123, 124] and cap plasticity models [91, 100, 122, 125, 126] and their combination [127-129, 131-133] to more physically sophisticated models with focus on micro-mechanism of deformation such as cement debonding [130] and/or grain crushing [74, 75, 204] based on damage and breakage mechanics [217, 218]. Despite being successful in capturing some behavioural features of porous rocks, the main limitation of these models is that (with a single set of parameters) they can describe rock behaviour either in the brittle regime or in the ductile regime but not always in both. This may involve either inaccuracy in the prediction of stress-strain response and inelastic volumetric deformation or incapability of predicting the onset and the mode of localisation. For example, in the model proposed by Das et al [75] based on breakage mechanics theory, the micromechanics of grain crushing, mechanical behaviour and onset of localisation at high confinement is captured fairly well. However this model is unable to describe the responses under low confining when dilation and grain friction are dominant. It is, therefore, desirable to develop a constitutive model which is capable of describing the macroscopic behaviour of porous rocks, including the stress-strain response, volumetric deformation and localisation modes, in both brittle and ductile regimes with a single set of a few parameters.

In this chapter, a coupled damage-plasticity model is developed within the framework of generalised thermodynamics in order to describe the macroscopic behaviour of porous rocks. It is demonstrated that the model is capable of capturing some of the most fundamental features of the macroscopic response of porous rocks. These fundamental features include the transition from brittle to ductile response with increasing confining pressure, dilative and contractive responses and various modes of strain localisation and failure. The predictive capability of the proposed model in predicting the stress-strain response and the onset of localisation is extensively assessed at the material level. The proposed material model is then used to simulate the structural response of cylindrical rock specimens in drained triaxial tests by means of finite element (FE) analysis. In order to alleviate the numerical instabilities, which arise as a consequence of localisation of deformation, the proposed coupled damage-plasticity model is enhanced to a damage-viscoplastic formulation by means of a Perzyna type viscoplasticity [219] regularisation.

4.2. Preliminary Definitions and Basic Assumptions

In this section, some definitions and basic assumptions used in the formulation of a coupled damage-plasticity model, developed for describing the macroscopic behaviour of porous rocks are outlined. The model formulation is carried out using the notations appropriate for triaxial tests. Throughout the formulation process, compressive stresses and contractive strains are assumed to be positive. In this sense, given σ_{ij} and ε_{ij} as stress and strain tensors, respectively, the definitions of the mean pressure, p, the deviatoric stress, q, the volumetric strain, ε_v, and the effective shear strain, ε_s are given in Table 4.1.

Table 4.1: The definition of stresses and strains in triaxial notation

Quantity	Notation	Definition
Mean Pressure	p	$p = \sigma_{ii}/3$
Deviatoric stress	q	* $q = \sqrt{3J_2}$
Volumetric strain	ε_v	$\varepsilon_v = \varepsilon_{ii}$
Effective shear strain	ε_s	$\varepsilon_s = \sqrt{2e_{ij}e_{ij}/3}$ with ** $e_{ij} = \varepsilon_{ij} - \varepsilon_v\delta_{ij}/3$

* J_2 is the second invariant of the deviatoric stress tensor
** δ_{ij} is the Kronecker delta

It is important to note that the main objective of this study is to capture the macroscopic behaviour of porous rocks by means of a coupled damage-plasticity model. Therefore, underlying micro-mechanisms of deformation and energy dissipation, such as grain crushing and cement debonding are not directly described in the model formulation. These micro-mechanisms are, nevertheless, represented in the model formulation by means of macroscopic internal variables, i.e. damage variable and plastic strains. In order to use the proposed model also for describing the changes in porosity, it is necessary to establish a relation between the porosity change and volumetric deformations. This derivation follows closely that presented by Coussy [220].

The current volume of a representative volume element of a porous rock, V_t under compressive loading and at time t can be given as:

$$V_t = JV_o \tag{4.1}$$

where J represents the Jacobean of deformation and V_o is the initial volume of the RVE at time $t = t_0$. For small deformations, following the convention of compression positive, the above expression can be approximated as:

$$V_t \approx (1 - \varepsilon_v)V_o \tag{4.2}$$

The observable macroscopic volume deformation undergone by the RVE is due both to the change in porosity and to the volume deformation undergone by the solid matrix, although the latter is not accessible from purely macroscopic experiments. The current volume of the solid matrix is given by:

$$V_t^{matrix} = \left(1 - \varepsilon_v^{matrix}\right)V_o^{matrix} \tag{4.3}$$

Furthermore, the Lagrangian porosity, which refers the current porous volume to the initial volume, is defined as (see [220]) as follows:

$$\phi = \frac{V_t^{void}}{V_o} = \frac{V_t - V_t^{matrix}}{V_o} \tag{4.4}$$

The current volume of the solid matrix at time t (V_t^{matrix}) can also be given as:

$$V_t^{matrix} = V_t - \phi V_o \tag{4.5}$$

Furthermore, it rapidly follows from equations (4.4) and (4.5) that the initial volume of the solid matrix is given by:

$$V_o^{matrix} = (1 - \phi_o)V_o \tag{4.6}$$

where ϕ_o is the initial porosity of the RVE. Similar to strains, porosity change at any stage of loading can be given as the additive decomposition of reversible and irreversible porosity changes:

$$\phi = \phi_o + \phi^e + \phi^p \tag{4.7}$$

In the above expression, ϕ^e and ϕ^p represent the reversible and irreversible changes in porosity, respectively. Substitution for V_t and V_t^{matrix} from equations (4.2) and (4.3), respectively, into equation (4.5) and also making use of equation (4.6) gives:

$$\varepsilon_v = (1 - \phi_o)\varepsilon_v^{matrix} + (\phi_o - \phi) \tag{4.8}$$

$$\varepsilon_v = (1 - \phi_o)\varepsilon_v^{matrix} - \phi^e - \phi^p \tag{4.9}$$

Therefore, by virtue of equation (4.7), volumetric elastic and plastic strains for the RVE are given as follows:

$$\varepsilon_v^e = (1 - \phi_o)\left(\varepsilon_v^{matrix}\right)^e - \phi^e \tag{4.10}$$

$$\varepsilon_v^p = (1 - \phi_o)\left(\varepsilon_v^{matrix}\right)^p - \phi^p \tag{4.11}$$

In soil and rock mechanics the plastic volumetric deformations are mainly caused by the relative movement of the solid grains or fragmentations of the damaged material and hence, the volume change of the matrix due uniquely to plasticity is negligible in the absence of any porosity or micro-cracking. Therefore, by assuming $\left(\varepsilon_v^{matrix}\right)^p = 0$ the irreversible porosity and the plastic volumetric strain of the RVE can be used interchangeably in the model formulation, i.e.:

$$\varepsilon_v^p = \phi^p \tag{4.12}$$

Furthermore, it is envisaged that under compression in the elastic stage the elastically compressed solid matrix can potentially expand into the available porous space and give up its elastic energy while causing a reversible diminution in porosity. Therefore, the elastic volumetric strain and reversible porosity can also be assumed to be approximately the same, i.e. $\phi^e = \varepsilon_v^e$.

In general, the mode of volumetric deformation in porous rocks is determined as a result of competition between two underlying mechanisms. These underlying mechanisms are damaging in the cement matrix and the pore collapse phenomenon. Under deviatoric stressing of porous rocks, the collapse of porosity during deformation tends to counterbalance the tendency to dilatancy due to the growth of damage in the cement matrix. Therefore, porous rocks may exhibit compaction even at very low confining pressures [25, 27, 92].

4.3. Thermodynamics Formulation

In this section, the principles of generalised thermodynamics, in the form outlined in Chapter 3, are used to develop a coupled damage-plasticity model for describing the macroscopic behaviour of porous rocks. Constitutive modelling within the framework of generalised thermodynamics requires the knowledge of two thermodynamic potentials (the free energy and the dissipation functions) in order to determine the entire constitutive relations. These functions basically describe the mechanisms of energy storage and dissipation within a unit volume of material. Therefore, the predictive capability of constitutive models developed in this framework depends on how closely these functions represent the actual mechanisms of energy storage and energy dissipation

4.3.1. The free energy potential and the dissipation function

In the development of constitutive models for engineering materials, it is common to assume the small strain tensor as additive decomposition of elastic and plastic strain tensors. This decomposition leads to the development of material models whose instantaneous elastic moduli are independent of the internal variables [221-223]. These material models are often termed as decoupled material models [191]. Although in the context of constitutive modelling for porous rocks it is more appropriate, and perhaps more physically correct, to adopt a coupled material model, in which the instantaneous elastic modulus varies with the evolution of internal variables, it is demonstrated in this study that a decoupled model can also produce an adequate approximations to the observed behaviour of porous rocks. Collins and Houlsby [191] showed that the free energy function for a decoupled material model can be assumed as the summation of elastic and plastic parts. From a physical point of view, the elastic part of the free energy (Ψ^e) represents the stored elastic strain energy and the plastic part (Ψ^p) is related to that part of the plastic work which is not dissipated and is stored within the material (see [209, 212, 224, 225]). The general form of the Helmholtz free energy potential for a decoupled material can, therefore, be given as:

$$\Psi = \Psi^e\left(\varepsilon_{ij}^e\right) + \Psi^p\left(\varepsilon_{ij}^p\right) \tag{4.13}$$

In the above expression, Ψ^e is a function of only elastic strains and Ψ^p is a function of only plastic (or inelastic) strains. Furthermore, since the material is assumed to be decoupled, Ψ^p does not have any effect on the elastic response of the material.

The existence of the stored plastic work can be attributed to the non-homogeneous stress distribution at micro-scale. That part of the plastic work which does not contribute to dissipation is stored within the material and it can be recovered upon reverse dilatational volumetric plastic deformations, and therefore, it should be included in the definition of the continuum free energy potential. The concept of stored plastic work can be further clarified by considering the mechanisms of energy storage and energy dissipation within a non-homogeneous material under isotropic compressive loading and unloading. During the compressive loading, the elastic part of the free energy potential, Ψ^e, represents the elastic energy stored within the elastically compressed constituents (e.g. grains, crystals, etc.). Inelastic deformations, depending on the material micro-structure, may involve frictional sliding, plastic deformation in ductile and fracturing in brittle constituents. Therefore, the applied work (or the total energy budget for deformation) can be divided into recoverable,

elastic and irrecoverable or dissipated parts. Division of the applied work is not, however, that straightforward during unloading. When the compressed material is unloaded, some of the elastically compressed constituents will be able to expand into the available space and give up their stored elastic energy which, in turn, causes the RVE to tend to dilate elastically. However, many of the elastically compressed particles will be surrounded and trapped by the compacted neighbouring constituents, and can expand and give up their stored elastic energy only if some of these surrounding constituents are simultaneously rearranged (see [224, 225]). This rearrangement involves frictional dissipation and may also induce some volumetric plastic strains. The micro-elastic energy associated with these trapped particles can hence be recovered only if reversed inelastic dilational strains occur. At the continuum level, the proportion of this trapped micro-elastic energy can be determined by measuring the magnitude of the plastic strains induced due to the particle rearrangement and frictional sliding during the compression phase [see 225]. This trapped or frozen elastic energy is termed as stored plastic work, and it is denoted by Ψ^p. In contrast to isotropic compression, since shearing may induce dilatancy, which, in turn, would release some of the pre-existing frozen energy, no significant storage of plastic work is expected to take place due to shearing [225].

Shearing-induced dilatancy can be explained by assuming a simple sawtooth mechanism, e.g. between the contacting grains or between the rough surfaces of micro-cracks and cracks (Figure 4.1). The shear-induced dilatational plastic strain (ε_v^{ps}) can be defined as:

$$\varepsilon_v^{ps} = -\mu(D)\varepsilon_s^p \tag{4.14}$$

In the above expression $\mu(D)$ is defined as a function of the scalar damage variable, D. Initiation and propagation of damage within the material encourage the relative movement and slide of the grains and microcracks under sharing. Therefore, it is assumed that the possibility for the shearing-induced dilation to take place increases as damage grows within the material. It is also assumed that a critical state, with zero dilation, is reached when the material is fully damaged, i.e. $D = 1$. With these assumptions the following form of the function $\mu(D)$ is proposed:

$$\mu(D) = D^a(1 - D)^b\mu_0 \tag{4.15}$$

In the above expression μ_0 , a and b are material parameters. Parameter μ_0 can be interpreted as the coefficient of friction between the two surfaces of micro-cracks. Since during shearing

some of the stored plastic work is resealed owing to the expansion of the material into the available space (Figure 4.1), the stored plastic energy can be given as:

$$\Psi^p = \rho\left(\varepsilon_v^p - \varepsilon_v^{ps}\right) = \rho\left(\varepsilon_v^p + \mu(D)\varepsilon_s^p\right) \tag{4.16}$$

It will be shown later that in the above expression ρ and $\rho\mu(D)$ are two components of a shift stress vector between the dissipative and true stress spaces. The constant shift stress parameter ρ in (4.16) indicates that the model have different absolute values for initial yield under isotropic compression and extension (or decompression) in true stress space. The second component of the shift stress vector $\rho\mu(D)$, which varies with damage evolution, indicates the kinematic hardening with rotation of the yield surface in dissipative and true stress spaces. The details will be revealed later. For isothermal problems, the Helmholtz free energy potential can be given in the following form:

$$\Psi = \frac{1}{2}(1-D)K\varepsilon_v^{e\,2} + \frac{3}{2}(1-D)G\varepsilon_s^{e\,2} + \rho\left(\varepsilon_v^p + \mu(D)\varepsilon_s^p\right) \tag{4.17}$$

In the above expression, K and G are bulk and shear moduli, respectively, and D is the scalar damage variable.

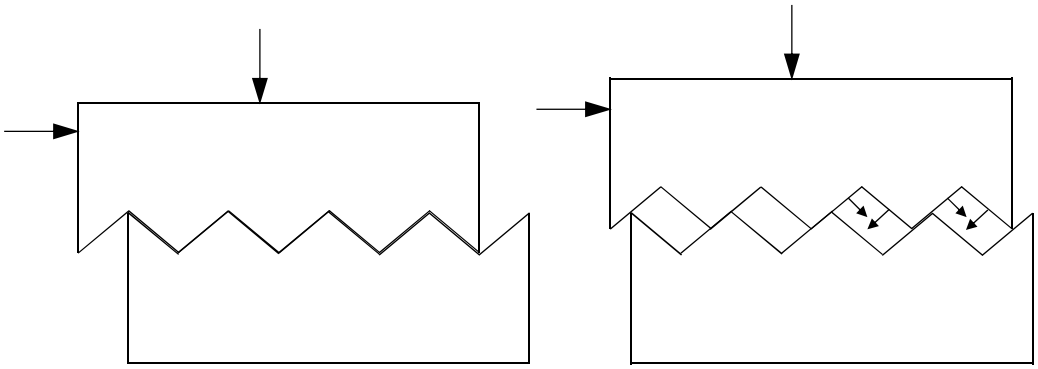

Figure 4.1: Schematic shear-induced dilation in a sawtooth mechanism. Small arrows indicate the expansion of the elastically compressed material into the available space

For rate independent behaviour, the dissipation function is a homogeneous first order function in the rates of internal variables. For a coupled damage-plasticity model the following form of the dissipation function is adopted ([144, 189]):

$$\delta\Phi = \sqrt{\varphi_v{}^2 + \varphi_s{}^2 + \varphi_D{}^2} \geq 0 \tag{4.18}$$

In the above expression, φ_v, φ_s and φ_D are homogeneous first order functions in terms of the rates of internal variables. These functions are associated with the contribution of each individual dissipative mechanism in the total dissipation rate (see also [189]). The general forms of the functions φ_v, φ_s and φ_D are proposed as follows:

$$\varphi_v = F_v\left(\dot{\varepsilon}_v^p + \mu(D)\dot{\varepsilon}_s^p\right) \tag{4.19}$$

$$\varphi_s = F_s\dot{\varepsilon}_s^p \tag{4.20}$$

$$\varphi_D = F_D\dot{D} \tag{4.21}$$

This form of coupling between different dissipative mechanisms is advantageous compared to the recent developments by Tengattini et al. [226] and Vu et al. [23], as the non-negativeness of the total dissipation rate is strictly enforced in the model formulation. Furthermore, it can be readily shown that the dissipation function of equation (4.18) is a homogeneous function of order one in terms of rates of internal variables. To this end, by invoking the Euler's theorem for homogeneous functions, the dissipation function of equation (4.18) can be written in the following from:

$$\delta\Phi = \frac{\partial\delta\Phi}{\partial\dot{\varepsilon}_v^p}\dot{\varepsilon}_v^p + \frac{\partial\delta\Phi}{\partial\dot{\varepsilon}_s^p}\dot{\varepsilon}_s^p + \frac{\partial\delta\Phi}{\partial\dot{D}}\dot{D} = \chi_v\dot{\varepsilon}_v^p + \chi_s\dot{\varepsilon}_s^p + \chi_D\dot{D} = \delta\Phi_v + \delta\Phi_s + \delta\Phi_D \geq 0 \tag{4.22}$$

where $\delta\Phi_v$, $\delta\Phi_s$, and $\delta\Phi_D$ are dissipations due to plastic volumetric behaviour, plastic shear behaviour, and damage, respectively. It will be shown later that dilation behaviour can result in negative values of $\delta\Phi_v$, but thanks to the specific form of the dissipation function (equation (4.18)), the thermodynamic admissibility of the model is always preserved.

Additionally, the decomposition of the volumetric and the equivalent shear strains into elastic and plastic strains is incorporated in the model formulation by introducing the following two kinematic constraint equations:

$$C_1 = \dot{\varepsilon}_v - \dot{\varepsilon}_v^e - \dot{\varepsilon}_v^p = 0 \tag{4.23}$$

$$C_2 = \dot{\varepsilon}_s - \dot{\varepsilon}_s^e - \dot{\varepsilon}_s^p = 0 \tag{4.24}$$

The above constraint equations are used to supplement the dissipation function of equation (4.18) as follows:

$$\delta\Phi' = \delta\Phi + \Lambda_1\mathrm{C}_1 + \Lambda_2\mathrm{C}_2 = \chi_v\dot{\varepsilon}_v^p + \chi_s\dot{\varepsilon}_s^p + \chi_D\dot{D} + \Lambda_1\mathrm{C}_1 + \Lambda_2\mathrm{C}_2 \geq 0 \tag{4.25}$$

By invoking the First Law of thermodynamics and also the Second Law, in the form of the Ziegler's orthogonality principle, as demonstrated in Chapter 3, the following set of equations is obtained:

$$p = \frac{\partial\Psi}{\partial\varepsilon_v} + \frac{\partial\delta\Phi'}{\partial\dot{\varepsilon}_v} = \frac{\partial\Psi}{\partial\varepsilon_v} + \frac{\partial\delta\Phi}{\partial\dot{\varepsilon}_v} + \Lambda_1\frac{\partial C_1}{\partial\dot{\varepsilon}_v} + \Lambda_2\frac{\partial C_2}{\partial\dot{\varepsilon}_v} = \Lambda_1 \tag{4.26}$$

$$q = \frac{\partial \Psi}{\partial \varepsilon_s} + \frac{\partial \delta\Phi'}{\partial \dot{\varepsilon}_s} = \frac{\partial \Psi}{\partial \varepsilon_s} + \frac{\partial \delta\Phi}{\partial \dot{\varepsilon}_s} + \Lambda_1 \frac{\partial C_1}{\partial \dot{\varepsilon}_s} + \Lambda_2 \frac{\partial C_2}{\partial \dot{\varepsilon}_s} = \Lambda_2 \tag{4.27}$$

$$0 = \frac{\partial \Psi}{\partial \varepsilon_v^e} + \frac{\partial \delta\Phi'}{\partial \dot{\varepsilon}_v^e} = \frac{\partial \Psi}{\partial \varepsilon_v^e} + \frac{\partial \delta\Phi}{\partial \dot{\varepsilon}_v^e} + \Lambda_1 \frac{\partial C_1}{\partial \dot{\varepsilon}_v^e} + \Lambda_2 \frac{\partial C_2}{\partial \dot{\varepsilon}_v^e} = (1-D)K\varepsilon_v^e - \Lambda_1 \tag{4.28}$$

$$0 = \frac{\partial \Psi}{\partial \varepsilon_s^e} + \frac{\partial \delta\Phi'}{\partial \dot{\varepsilon}_s^e} = \frac{\partial \Psi}{\partial \varepsilon_s^e} + \frac{\partial \delta\Phi}{\partial \dot{\varepsilon}_s^e} + \Lambda_1 \frac{\partial C_1}{\partial \dot{\varepsilon}_s^e} + \Lambda_2 \frac{\partial C_2}{\partial \dot{\varepsilon}_s^e} = 3(1-D)G\varepsilon_s^e - \Lambda_2 \tag{4.29}$$

$$0 = \frac{\partial \Psi}{\partial \varepsilon_v^p} + \frac{\partial \delta\Phi'}{\partial \dot{\varepsilon}_v^p} = \frac{\partial \Psi}{\partial \varepsilon_v^p} + \frac{\partial \delta\Phi}{\partial \dot{\varepsilon}_v^p} + \Lambda_1 \frac{\partial C_1}{\partial \dot{\varepsilon}_v^p} + \Lambda_2 \frac{\partial C_2}{\partial \dot{\varepsilon}_v^p} = \rho + \chi_v - \Lambda_1 \tag{4.30}$$

$$0 = \frac{\partial \Psi}{\partial \varepsilon_s^p} + \frac{\partial \delta\Phi'}{\partial \dot{\varepsilon}_s^p} = \frac{\partial \Psi}{\partial \varepsilon_s^p} + \frac{\partial \delta\Phi}{\partial \dot{\varepsilon}_s^p} + \Lambda_1 \frac{\partial C_1}{\partial \dot{\varepsilon}_s^p} + \Lambda_2 \frac{\partial C_2}{\partial \dot{\varepsilon}_s^p} = \mu(D)\rho + \chi_s - \Lambda_2 \tag{4.31}$$

$$\begin{aligned} 0 = \frac{\partial \Psi}{\partial D} + \frac{\partial \delta\Phi'}{\partial \dot{D}} &= \frac{\partial \Psi}{\partial D} + \frac{\partial \delta\Phi}{\partial \dot{D}} + \Lambda_1 \frac{\partial C_1}{\partial \dot{D}} + \Lambda_2 \frac{\partial C_2}{\partial \dot{D}} \\ &= -\frac{1}{2}K\varepsilon_v^{e\,2} - \frac{3}{2}G\varepsilon_s^{e\,2} + \rho \frac{\partial \mu(D)}{\partial D}\varepsilon_s^p + \chi_D \end{aligned} \tag{4.32}$$

From (4.26) – (4.29) the mean pressure, p, and the deviatoric stress, q, are derived as:

$$p = (1-D)K\varepsilon_v^e \tag{4.33}$$

$$q = 3(1-D)G\varepsilon_s^e \tag{4.34}$$

Furthermore, from (4.30) – (4.32), the dissipative part of the internal forces χ_v and χ_s, conjugate to ε_v^p and ε_s^p, respectively, and the conjugate damage energy, χ_D, are given as:

$$\chi_v = p - \rho \tag{4.35}$$

$$\chi_s = q - \mu(D)\rho \tag{4.36}$$

$$\chi_D = \frac{1}{2}K\varepsilon_v^{e\,2} + \frac{3}{2}G\varepsilon_s^{e\,2} = \frac{p^2}{2K(1-D)^2} + \frac{q^2}{6G(1-D)^2} - \rho \frac{\partial \mu(D)}{\partial D}\varepsilon_s^p \tag{4.37}$$

It is clear form equation (4.37) that in principle it is possible to define the function $\mu(D)$ and select its associated parameters so that the conjugate damage energy, χ_D, becomes negative. In the absence of any healing process the negativeness of the damage energy is physically meaningless, despite the warranted positiveness of the total dissipation. Therefore, preserving the non-negativeness of the conjugate damage energy can be viewed as a restrictive condition which has to be acknowledged in the definition of the function $\mu(D)$ and selecting its parameters.

4.3.2. The yield function

The yield function in the dissipative stress space (not the true stress space) can be derived by performing a Legendre transformation on the dissipation function. Since for rate-independent behaviour, the dissipation function is a homogeneous first-order function in rates, this transformation is a degenerate special case of Legendre transformation [19, 191]. The degenerate Legendre transformation of a first-order function of rates of internal variables ($\Phi = \Phi\left(\dot{\varepsilon}_v^p, \dot{\varepsilon}_s^p, \dot{D}\right)$) is a function of dissipative internal forces corresponding to these internal variables, that is the yield function $y^* = y^*(\chi_v, \chi_s, \chi_D)$. By making use of equations (4.18) – (4.21), the dissipative parts of internal forces are given as follows:

$$\chi_v = \frac{\partial \delta\Phi}{\partial \dot{\varepsilon}_v^p} = \frac{\partial \delta\Phi}{\partial \varphi_v}\frac{\partial \varphi_v}{\partial \dot{\varepsilon}_v^p} = \frac{\varphi_v}{\sqrt{{\varphi_v}^2 + {\varphi_s}^2 + {\varphi_D}^2}}\frac{\partial \varphi_v}{\partial \dot{\varepsilon}_v^p} \tag{4.38}$$

$$\begin{aligned}\chi_s = \frac{\partial \delta\Phi}{\partial \dot{\varepsilon}_s^p} &= \frac{\partial \delta\Phi}{\partial \varphi_s}\frac{\partial \varphi_s}{\partial \dot{\varepsilon}_s^p} + \frac{\partial \delta\Phi}{\partial \varphi_v}\frac{\partial \varphi_v}{\partial \dot{\varepsilon}_s^p} \\ &= \frac{\varphi_s}{\sqrt{{\varphi_v}^2 + {\varphi_s}^2 + {\varphi_D}^2}}\frac{\partial \varphi_s}{\partial \dot{\varepsilon}_s^p} + \frac{\varphi_v}{\sqrt{{\varphi_v}^2 + {\varphi_s}^2 + {\varphi_D}^2}}\frac{\partial \varphi_v}{\partial \dot{\varepsilon}_s^p}\end{aligned} \tag{4.39}$$

$$\chi_D = \frac{\partial \delta\Phi}{\partial \dot{D}} = \frac{\partial \delta\Phi}{\partial \varphi_D}\frac{\partial \varphi_D}{\partial \dot{D}} = \frac{\varphi_D}{\sqrt{{\varphi_v}^2 + {\varphi_s}^2 + {\varphi_D}^2}}\frac{\partial \varphi_D}{\partial \dot{D}} \tag{4.40}$$

The expression of the yield function in dissipative stress space (see Section 3.5) is, therefore, given as:

$$y^* = \left(\frac{\chi_v}{\partial \varphi_v / \partial \dot{\varepsilon}_v^p}\right)^2 + \left(\frac{\chi_s - \mu(D)\chi_v}{\partial \varphi_s / \partial \dot{\varepsilon}_s^p}\right)^2 + \left(\frac{\chi_D}{\partial \varphi_D / \partial \dot{D}}\right)^2 - 1 \leq 0 \tag{4.41}$$

By making use of equations (4.19) – (4.21) the above expression is simplified to give:

$$y^* = \left(\frac{\chi_v}{F_v}\right)^2 + \left(\frac{\chi_s - \mu(D)\chi_v}{F_s}\right)^2 + \left(\frac{\chi_D}{F_D}\right)^2 - 1 \leq 0 \tag{4.42}$$

As illustrated in Figure 4.2, the yield function of equation (4.42) represents an ellipsoid in the dissipative stress space (χ_v, χ_s, χ_D) space, for $\mu(D) = 0$. For $\mu(D) > 0$, the ellipsoid rotates around the origin of the dissipative stress space.

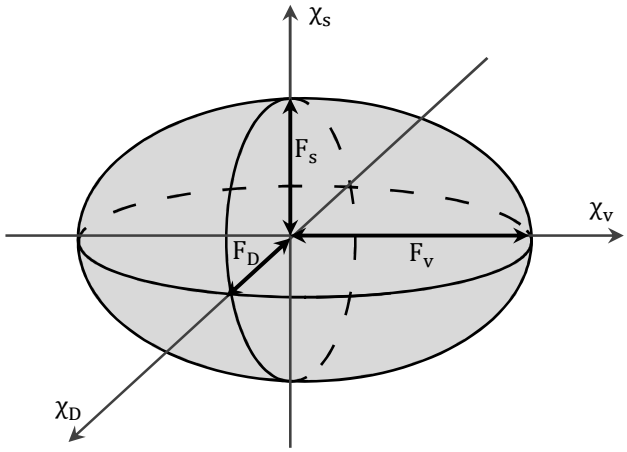

Figure 4.2: Geometric representation of the yield potential in dissipative stress space

The introduction of shear-induced dilation into the model formulation will necessarily result in rotational hardening, which can be physically interpreted as shear hardening. Due to this shear hardening, which is commonly observed in dense sand and rocks, the material behaviour becomes anisotropic. It is envisaged, therefore, that the phenomena of dilatancy and anisotropy are linked [214]. The simple sawtooth model of dilatancy (Figure 4.1), for instance, implies dilation due to shearing in one direction and contraction in the other. This means that dilation can only take place if the sliding surfaces are oriented in a preferential direction [214]. Figure 4.3 illustrates the projection of the ellipsoid of equation (4.42) on the $\chi_v - \chi_s$ plane. For $\mu\,(D) > 0$ at a certain damage state ($0 < D_t < 1$), $\mu(D_t)$ can be represented in the dissipative stress space as; $\mu = \tan\theta$, where the angle θ is the angle between the χ_v axis and the current normal consolidation line (Figure 4.3). Therefore, for non-zero values of $\mu(D)$ the model exhibits rotational hardening. In this sense, as damage grows within the material, the material behaviour immediately becomes anisotropic. However, when the material is fully damaged or when the damage variable approaches unity (at the critical state), it is assumed that no shear induced dilation is taking place.

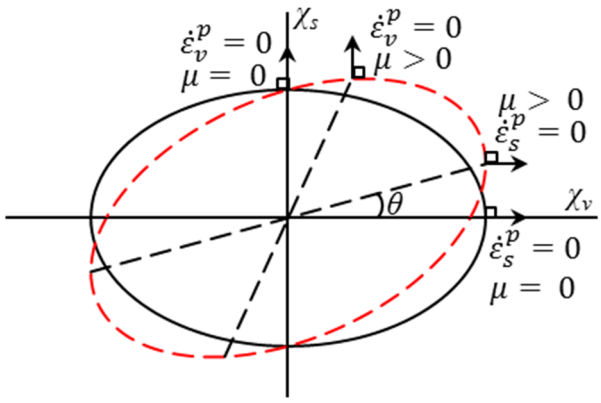

Figure 4.3: Rotation of the yield surface in dissipative stress space for $\mu > 0$

Since geomaterials, including porous rocks, exhibit different yielding behaviour under isotropic compression and decompression, it is necessary to adopt a kinematic hardening approach and introduce a shift stress into the model formulation [191, 212]. According to equations (4.35) and (4.36), the shift stress links the coordinates of the true stress space and the dissipative stress space (see also Figure 4.4). The true stresses can be viewed as the sum of dissipative stresses and a shift (quasiconservative) stress. It should be noted that while the plastic work increment can be given as the sum of the products of true stresses (p and q) with the plastic strain increments ($\dot{\varepsilon}_v^p$ and $\dot{\varepsilon}_s^p$), the plastic dissipation the product of the dissipative stresses (χ_v and χ_s) with plastic strain increments. The products of the shift stress components (ρ along the χ_v-axis and $\mu(D)\rho$ along the χ_s-axis (Figure 4.4)) with the plastic strain increments do not contribute to the dissipation and it is stored within the material.

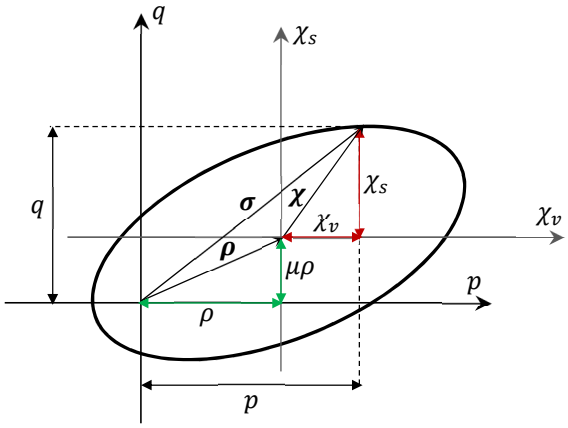

Figure 4.4: Relation between true stress, shift stress and dissipative stress

Furthermore, in order to obtain a closed teardrop-shaped yield surface in true stress space, similar to that proposed by Collins and Hilder [212], the definitions of functions F_v, F_s and

F_D which appear in the formulation of the yield function in the dissipative stress space (equation (4.42)) are proposed as follows:

$$F_v = \frac{1}{r_v}\left(\frac{(1-\gamma)p_c - p_t}{(1-D)(p_c+p_t)}p + \frac{\gamma}{2}p_c\right) \tag{4.43}$$

$$F_s = \frac{M}{r_s}\left(p - \alpha\sqrt{(1-D)}(p-\rho)\right) \tag{4.44}$$

$$F_D = \frac{\chi_D}{\sqrt{({r_D}^2 + {r_s}^2)\left(\frac{\chi_v}{r_v F_v}\right)^2 + ({r_D}^2 + {r_v}^2)\left(\frac{\chi_s - \mu(D)\chi_v}{r_s F_s}\right)^2}} \tag{4.45}$$

Substitution of the above expression into equation (4.42) will result in:

$$y^* = ({r_v}^2 + {r_s}^2 + {r_D}^2)\left[\left(\frac{\chi_v}{\frac{(1-\gamma)p_c - p_t}{(1-D)(p_c+p_t)}p + \frac{\gamma}{2}p_c}\right)^2 + \left(\frac{\chi_s - \mu(D)\chi_v}{M\left(p - \alpha\sqrt{(1-D)}(p-\rho)\right)}\right)^2 - 1\right] \leq 0 \tag{4.46}$$

For simplicity the effect of parameters r_v, r_s and r_D on the shape of the yield function in true stress space is eliminated by imposing the condition ${r_v}^2 + {r_s}^2 + {r_D}^2 = 1$. It is recognised that this may seem a strong assumption. Nevertheless, since these parameters also appear in the expressions of flow rules and thereby they influence the model behaviour, this simplification is found to be beneficial. Therefore, the expression of the yield function in the true stress space is obtained as:

$$y = \left(\frac{p-\rho}{\frac{(1-\gamma)p_c - p_t}{(1-D)(p_c+p_t)}p + \frac{\gamma}{2}p_c}\right)^2 + \left(\frac{q - \mu(D)p}{M\left(p - \alpha\sqrt{(1-D)}(p-\rho)\right)}\right)^2 - 1 \leq 0 \tag{4.47}$$

In the above expressions, parameters α and γ are material constants which control the shape of the yield surface in true stress space. This definition of functions F_v and F_s will result is a closed shape yield function similar to that introduce by Collins and Hilder [212]. For $\alpha = \gamma = 1$ the yield surface reduces to the elliptical modified Cam-Clay. For values of α and γ less than unity the yield surface adopts a tear drop shape in the true stress space (Figure 4.5 (a)). Furthermore, parameter M, in equation (4.44), represents the slope of the final failure envelope and p_c and p_t are yield stresses under isotropic compression and extension (or

decompression), respectively (Figure 4.5 (b)). The shift stress, ρ, is also defined in terms of p_c, p_t and γ as:

$$\rho = \frac{(4-\gamma)p_c p_t + \gamma {p_c}^2}{2(p_c + p_t)} \tag{4.48}$$

The incorporation of damage in the formulation of yield function in true stress space (equation (4.47)) allows for the transformation of the initial yield surface to a final failure envelope as the damage variable grows from zero to unity (Figure 4.5 (a)). The evolution of yield behaviour has also been observed in laboratory experiments on porous sandstones [91, 95, 227]. In many models developed for describing the behaviour of porous rocks [100, 122, 125, 228] brittle and ductile modes of behaviour are produced through separately introducing hardening/softening laws. The proposed model, however, is capable of capturing the brittle and ductile modes of behaviour, as well as the brittle-ductile transition, without any need for separately introducing hardening/softening laws. This is a significant feature of the proposed model which is resulted from the evolution of the initial yield surface to a final failure envelope due to the evolution of the internal variables of the model. In fact, this transformation of the initial yield surface to the final failure envelope describes the yielding and failure as consecutive processes, during which hardening/softening behaviour is naturally produced. This issue will be further discussed through demonstration of the model behaviour in Section 4.4 of the current chapter.

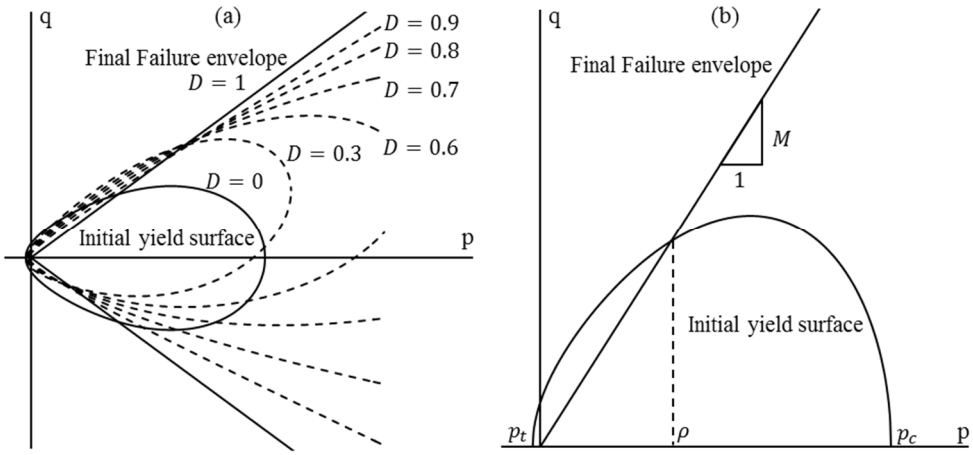

Figure 4.5: (a) Evolution of the yield surface to the failure envelope with damage growth; (b) Schematic representation of the parameters on the initial yield surface and final failure envelope

4.3.3. Evolution rules of the internal variables

Plastic deformation of many materials, such as ductile metals, can be described by means of an associated flow rule. In materials obeying this rule, the work done by each stress component can be regarded as being solely associated with the production of an incremental strain component having the same direction as the stress component, relative to the same Cartesian axes. If the yielding behaviour of such materials is defined by means of a surface in stress space, the plastic flow vectors are going to be normal to this surface. However, this, in general, is not true for frictional geomaterials including concrete, soil and rocks. Experimental observations have revealed that for these materials the plastic flow vectors are not normal to the initial yield surface defined in stress space. Furthermore, it can be proven that for frictional materials flow rules are necessarily non-associated [19, 191].

Within the framework of generalised thermodynamics, the evolution rules for the internal variables of the model are defined using the definition of the yield potential in dissipative stress space. The existence of the yield potential in generalised dissipative stress space is a direct consequence of rate-independent behaviour and it is derived directly from the dissipation function. Therefore, by using the expression of the yield function in dissipative stress space and by making use of equations (4.35) and (4.36) the evolution rules for the internal variables are obtained as follows:

$$\dot{\varepsilon}_v^p = \dot{\lambda}\frac{\partial y^*}{\partial \chi_v} = 2\dot{\lambda}\left(\frac{\chi_v}{{F_v}^2} - \frac{\mu(D)(\chi_s - \mu(D)\chi_v)}{{F_s}^2}\right) = 2\dot{\lambda}\left(\frac{(p-\rho)}{{F_v}^2} - \frac{\mu(D)(q - \mu(D)p)}{{F_s}^2}\right) \quad (4.49)$$

$$\dot{\varepsilon}_s^p = \dot{\lambda}\frac{\partial y^*}{\partial \chi_s} = 2\dot{\lambda}\frac{(\chi_s - \mu(D)\chi_v)}{{F_s}^2} = 2\dot{\lambda}\frac{(q - \mu(D)p)}{{F_s}^2} \quad (4.50)$$

$$\dot{D} = \dot{\lambda}\frac{\partial y^*}{\partial \chi_D} = 2\dot{\lambda}\frac{\chi_D}{{F_D}^2} \quad (4.51)$$

Further discussion on non-associated flow is presented in Section 4.4.2, where the model behaviour is investigated in more detail.

4.4. Integration of the Rate Constitutive Equations

Numerical implementations of constitutive models require the stress state to be updated for a given strain increment. For infinitesimal increments in strains, stresses can be updated explicitly using the tangent stiffness and by adopting, for example, a forward-Euler scheme. Unless the stresses are corrected and returned onto the new yield surface, the

forward-Euler scheme may produce erroneous values for stresses at the materials point which, in turn, may result in the divergence of the numerical scheme applied for satisfying equilibrium equations at the structural level. Hence, a form of the backward-Euler scheme is adopted here to return the stresses onto the new yield surface following an elastic trial predictor. Returning procedures, which involve returning the trial stresses onto a new yield surface (in cases of hardening or softening), are activated only if the trial stresses lie outside the yield surface.

4.4.1. Tangent stiffness tensor

The formulation of tangent stiffness tensor is given in this section since apart from its application in the explicit integration of rate constitutive equations, it is necessary for localisation analysis, presented in the subsequent sections. For this purpose, the elastic stress tensor, σ_{ij}, is given as:

$$\sigma_{ij} = (1 - D)C_{ijkl}\left(\varepsilon_{kl} - \varepsilon_{kl}^{p}\right) \tag{4.52}$$

where C_{ijkl} is the elastic stiffness tensor and D and ε_{kl}^{p} are the scalar damage variable and the plastic strain tensor, respectively. The incremental form of the stress tensor is, therefore, given as:

$$\dot{\sigma}_{ij} = (1 - D)C_{ijkl}\left(\dot{\varepsilon}_{kl} - \dot{\varepsilon}_{kl}^{p}\right) - \frac{\sigma_{ij}}{(1 - D)}\dot{D} \tag{4.53}$$

The increment of the plastic strain tensor, $\dot{\varepsilon}_{ij}^{p}$, can also be given by making use of equations (4.49) and (4.50) and applying chain rule as:

$$\dot{\varepsilon}_{ij}^{p} = \dot{\lambda}\frac{\partial y^{*}}{\partial \chi_{ij}} = \dot{\lambda}\left(\frac{\partial y^{*}}{\partial \chi_{v}}\frac{\partial \chi_{v}}{\partial p}\frac{\partial p}{\partial \sigma_{kl}}\frac{\partial \sigma_{kl}}{\partial \chi_{ij}} + \frac{\partial y^{*}}{\partial \chi_{s}}\frac{\partial \chi_{s}}{\partial q}\frac{\partial q}{\partial \sigma_{kl}}\frac{\partial \sigma_{kl}}{\partial \chi_{ij}}\right) \tag{4.54}$$

In addition, the consistency condition for the yield function, $y = y(p, q, D)$, in true stress is written as:

$$\dot{y} = \frac{\partial y}{\partial \sigma_{ij}}\dot{\sigma}_{ij} + \frac{\partial y}{\partial D}\dot{D} = 0 \tag{4.55}$$

Substituting equation (4.53) in the consistency condition of equation (4.55) and making use of the evolution rules of equations (4.49) – (4.51), the damage-plastic multiplier $\dot{\lambda}$ is obtained as:

$$\dot{\lambda} = M_{kl}\dot{\varepsilon}_{kl} \tag{4.56}$$

where the second order tensor M_{kl} is defined as follows:

$$M_{kl} = \frac{\frac{\partial y}{\partial \sigma_{ij}}(1-D)C_{ijkl}}{\frac{\partial y}{\partial \sigma_{ij}}(1-D)C_{ijkl}\frac{\partial y^*}{\partial \chi_{kl}} + \frac{\partial y}{\partial \sigma_{ij}}\frac{\sigma_{ij}}{(1-D)}\frac{\partial y^*}{\partial \chi_D} - \frac{\partial y}{\partial D}\frac{\partial y^*}{\partial \chi_D}} \tag{4.57}$$

Using the evolution rules, given by equations (4.49) – (4.51), and also by making use of equations (4.56) and (4.57), the incremental stress-strain relationship is given as follows:

$$\dot{\sigma}_{ij} = \left[(1-D)C_{ijkl} - (1-D)C_{ijpq}\frac{\partial y^*}{\partial \chi_{pq}}M_{kl} - \frac{\sigma_{ij}}{(1-D)}M_{kl}\frac{\partial y^*}{\partial \chi_D}\right]\dot{\varepsilon}_{kl} = C^T_{ijkl}\dot{\varepsilon}_{kl} \tag{4.58}$$

where C^T_{ijkl} represents the tangent stiffness tensor.

4.4.2. Semi-implicit stress return algorithm

In numerical simulation of structures, the strain field within a structure is not usually uniform and also the strain increments at material points (e.g. Gauss points in FEM) may not be infinitesimal throughout the body. Consequently, the updated stresses may drift away from the yield surface is an explicit integration scheme is used. Therefore, a return mapping is required to return the stresses onto the new yield surface. The new yield surface can be approximated using a first order Taylor expansion as follows:

$$y^{n+1} = y^{trial} + \left.\frac{\partial y}{\partial \sigma_{ij}}\right|^{trial} \Delta\sigma^{re}_{ij} + \left.\frac{\partial y}{\partial D}\right|^{trial} \Delta D = 0 \tag{4.59}$$

In the above expression, the return stresses, $\Delta\sigma^{re}_{ij}$, are given as normal to the trial yield surface (Figure 4.6) and, therefore, the internal variables (damage variable and plastic strain tensor) at the trial point will be; $D^{n+1}_{trial} = D^n$ and $\left(\varepsilon^p_{kl}\right)^{n+1}_{trial} = \left(\varepsilon^p_{kl}\right)^n$. The return stresses can be given as:

$$\Delta\sigma^{re}_{ij} = \sigma^{n+1}_{ij} - \sigma^{trial}_{ij} \tag{4.60}$$

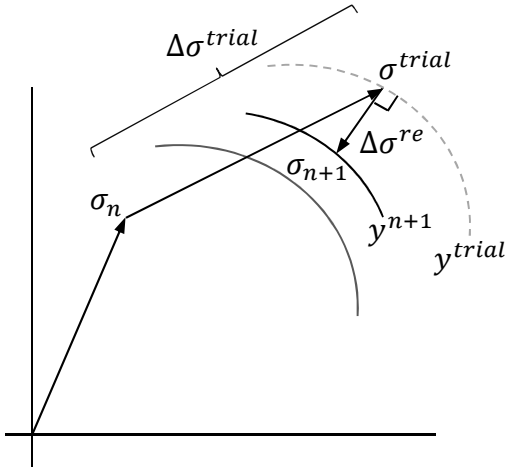

Figure 4.6: Return mapping from the trial yield surface onto the new yield surface corresponding to the semi-implicit integration scheme

Expanding the expression of equation (4.60) gives:

$$\Delta\sigma_{ij}^{re} = (1 - D^{n+1})C_{ijkl}\left(\varepsilon_{kl}^{n+1} - \varepsilon_{kl}^{p\,n+1}\right) - (1 - D^{n})C_{ijkl}\left(\varepsilon_{kl}^{n+1} - \varepsilon_{kl}^{p\,n}\right) \tag{4.61}$$

Since $D^{n+1} = D^n + \Delta D$ and $\left(\varepsilon_{kl}^{p}\right)^{n+1} = \left(\varepsilon_{kl}^{p}\right)^{n} + \Delta\varepsilon_{kl}^{p}$, the above expression can be rewritten in the following form:

$$\begin{aligned}\Delta\sigma_{ij}^{re} = &-(1 - D^{n})C_{ijkl}\left(\Delta\varepsilon_{kl}^{p}\right) - \Delta D C_{ijkl}\left(\varepsilon_{kl}^{n} - \varepsilon_{kl}^{p\,n}\right) \\ &- \Delta D C_{ijkl}\left(\Delta\varepsilon_{kl} - \Delta\varepsilon_{kl}^{p}\right)\end{aligned} \tag{4.62}$$

Ignoring the higher order term will result in the following expression:

$$\Delta\sigma_{ij}^{re} = -(1 - D^{n})C_{ijkl}\left(\Delta\varepsilon_{kl}^{p}\right) - \Delta D C_{ijkl}\left(\varepsilon_{kl}^{n} - \varepsilon_{kl}^{p\,n}\right) \tag{4.63}$$

Since the higher order term is ignored in equation (4.62), this integration procedure can be interpreted as a semi-implicit, as opposed to the fully implicit, backward-Euler scheme. In this sense, this stress return algorithm is different from a full backward-Euler scheme, in which $\Delta\sigma_{ij}^{re}$ are calculated as normal to the new yield surface (y^{n+1}) by applying an iterative scheme. For more detail see [229-231]. Substitution of equation (4.63) into equation (4.59) and making use of evolution rules of equations (4.49) – (4.51), the incremental damage-plastic multiplayer $\Delta\lambda$ is given as follows:

$$\Delta\lambda = \frac{y^{trial}}{\dfrac{\partial y}{\partial\sigma_{ij}}\left((1 - D)C_{ijkl}\left(\dfrac{\partial y^{*}}{\partial\chi_{kl}}\right) + \dfrac{\sigma_{ij}}{(1 - D)}\left(\dfrac{\partial y^{*}}{\partial\chi_{D}}\right)\right) - \dfrac{\partial y}{\partial D}\left(\dfrac{\partial y^{*}}{\partial\chi_{D}}\right)} \tag{4.64}$$

The updated returned stresses are, therefore, given as:

$$\sigma_{ij}^{n+1} = \sigma_{ij}^{trial} + \Delta\sigma_{ij}^{re} = \sigma_{ij}^{trial} - (1 - D^n)C_{ijkl}\Delta\lambda\frac{\partial y^*}{\partial \chi_{kl}} - \frac{{\sigma_{ij}}^n}{(1 - D^n)}\Delta\lambda\frac{\partial y^*}{\partial \chi_D} \qquad (4.65)$$

4.5. Model Behaviour

In this section, the capability of the proposed model in capturing various aspects of the mechanical behaviour of porous rocks, such as brittle to ductile transition, dilation and compaction and various modes of localisation of deformation are discussed in detail. In particular, it is demonstrated that these features of macroscopic material response are captured owing to the inherent and essential features of the proposed model, rather than through separately introducing additional controlling features, such as hardening and/or softening rules.

4.5.1. Brittle, ductile and brittle to ductile transition

As was discussed earlier in Section 4.2.2.1, the initial yield surface of the proposed model, in true stress space, is transformed to a failure function, as the scalar damage variable grows from zero to one. This inherent feature of the proposed model facilitates capturing the effect of confining pressure on brittle, ductile and brittle to ductile transition responses, without any need for separately introducing hardening/softening rules. It should also be noted that the rotational hardening, exhibited by the model, is due to the incorporation of shear-induced dilatancy in the model formulation and, therefore, is an intrinsic feature of the proposed model.

Along with the evolution of damage, the yield function rotates in the true stress space, as the function $\mu(D)$, (equation (4.15)), increases from zero to a maximum. Before the maximum value of $\mu(D)$ is reached, the model exhibits strain hardening response for both low and high confining pressures. This aspect of the model behaviour is illustrated in Figure 4.7 (a) for two loading paths AB and $A'B'$. The evolution of the yield function continues with the growing damage variable until it transforms to a final frictional failure surface. As illustrated in Figure 4.7 (b), the loading paths followed to reach the final failure state are different under low and high confining pressures. Under low confining pressure, or in the softening regime, the rotated yield surface moves downwards (loading path BC in Figure 4.7 (b)) until it converges to the final failure surface. This reverse rotation and contraction of the yield surface produces a brittle/softening response, as illustrated in Figure 4.7 (c). Under high confining pressures, on the other hand, damage evolution gives rise to further upward

movement of the yield function (loading path $B'C'$ in Figure 4.7 (b)) which, in turn, causes the model to exhibit a ductile response (Figure 4.7 (d)).

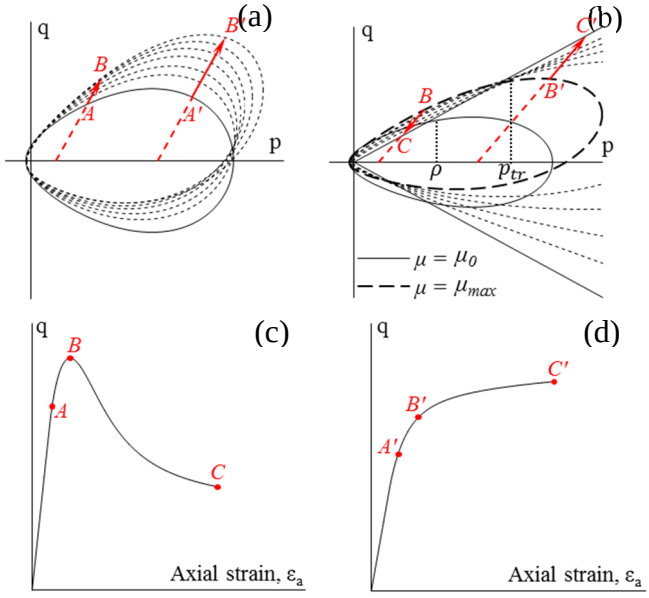

Figure 4.7: (a) rotational hardening of the yield be for the maximum value of μ (b) evolution of the initial yield after the maximum of μ is reached (c) and (d) brittle and ductile responses of the proposed model as a result of rotation and evolution of the yield surface.

Furthermore, for low confining pressures the model shows a profound brittle/softening behaviour characterised by a steep slope after the peak stress. For intermediate to relatively high pressures the steepness of the post-peak slope diminishes until it reaches a plateau associated with the gradual transition from a profoundly brittle behaviour to a completely ductile one. Figure 4.8 illustrates the effect of confining pressure on brittle to ductile responses of the proposed model.

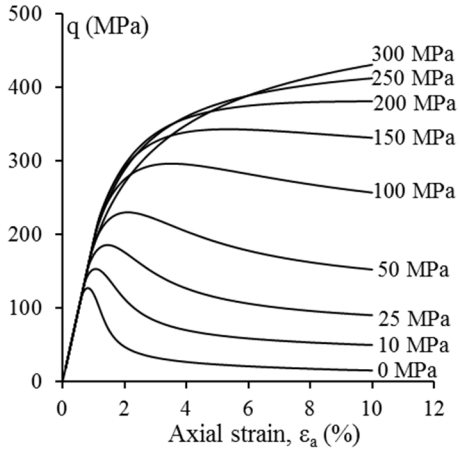

Figure 4.8: Brittle to ductile response of the model with model input parameters as; E = 20 GPa, ν = 0.27, p_c = 400 MPa, p_t = -10 MPa, M = 1.25, α = 0.5, γ = 0.8, μ_0 = 1.5, $r_v = r_s$ = 0.7

Furthermore, stiffness reduction due to damage growth and residual strain due to the accumulation of plastic deformations can also be observed in the model behaviour upon unloading (Figure 4.9 (a) and (b)). As can be seen in Figure 4.9, even at considerably large strains (about 25 %) the stiffness of the material is not completely lost. This is thanks to the residual frictional strengths at different confining pressures, as the stress condition at failure must respect this frictional behaviour.

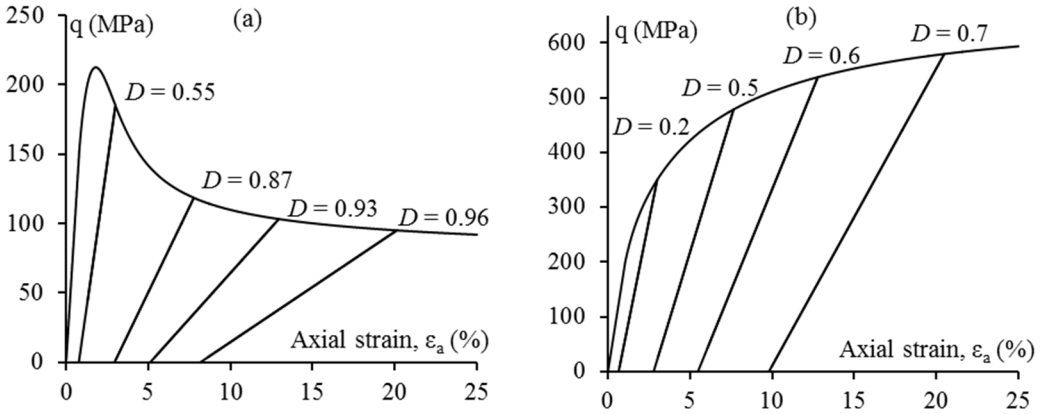

Figure 4.9: Stiffness reduction and residual strain upon unloading (a) 30 MPa and (b) 300 MPa confining pressure

Furthermore, as illustrated in Figure 4.10, damage growth is inhibited with the increase in confining pressure. This is a promising feature of the proposed model since, as also discussed in Chapter 2, the ductile behaviour of rocks under high confining pressure can be attributed to the inhibition of damage and stabilisation of micro-cracking processes [30].

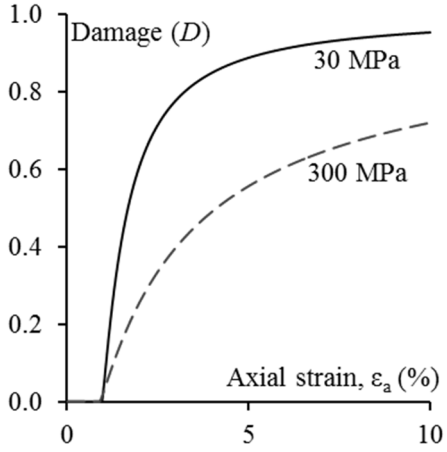

Figure 4.10: The effect of confining pressure on damage evolution for 10% axial strain

4.5.2. Non-associated Plastic Flow

In contrast to conventional plasticity, where a plastic potential is defined in true stress space to make the conventional plasticity formulation applicable to frictional materials for

which the flow rules are non-associated, in plasticity theories based on the generalised thermodynamics (termed as hyperplasticity [19]) plastic flow vectors are defined as normal vectors to the yield potential in dissipative stress space. In order to demonstrate the significance of the thermomechanical approach in modelling the non-associated flow, it would be convenient to show the relation between yield potentials, in dissipative stress space and in true stress space, at a given yield stress point. Corresponding to any yield point on the initial yield surface in true stress space, there exists an ellipsoidal yield potential, y^*, in dissipative stress space (χ_v, χ_s, χ_D) which can be obtained, from equation (4.42). These yield potentials in the dissipative stress space are analogous to the concept of plastic potential in conventional plasticity. However, unlike the arbitrarily defined plastic potentials, they have a strong connection with the underlying mechanisms of deformation and energy dissipation. Figure 4.11 illustrates the projection of a number of these ellipsoidal potentials on $\chi_D = 0$ plane, corresponding to a few yield points in true stress space.

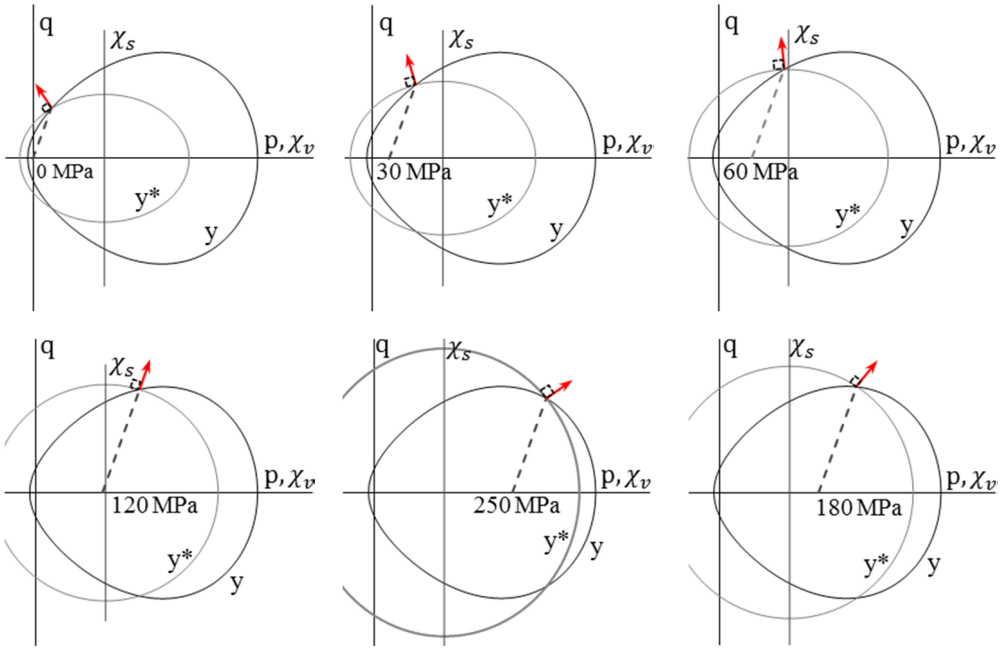

Figure 4.11: Initial yield loci in dissipative stress space, y^*, and in true stress space, y, with directions of non-associated flow vectors

As illustrated in Figure 4.11, plastic flow vectors are always normal to the yield potential in dissipative stress space, but they are not necessarily normal to the yield surface in true stress space. The plastic flow vectors in Figure 4.11 are pertaining to the case of zero damage and, thus, prior to the development of anisotropy. As the damage variable grows to values greater than zero the model response becomes anisotropic and the yield surfaces in both true and dissipative stress spaces will rotate. Correspondingly, the plastic flow vector

also rotates in true stress space, so that it remains normal to the yield potential y^* in the dissipative stress space, until it becomes parallel to the q axis when the damage variable is unity (Figure 4.12). Therefore, no plastic volumetric deformation is expected to take place on the final failure line. This feature of the model, which can also be inferred from the evolution rules of equations (4.15) and (4.49), implies that the proposed coupled damage-plasticity model can be classified as a critical state model, in which the critical state of zero volumetric deformation takes place when the material is fully damaged, i.e. $D = 1$. It should be noted that at the critical state (i.e. $D = 1$), the yield surface in the dissipative stress space becomes an extremely elongated ellipse, a section of which is shown in Figure 4.12 as two parallel lines.

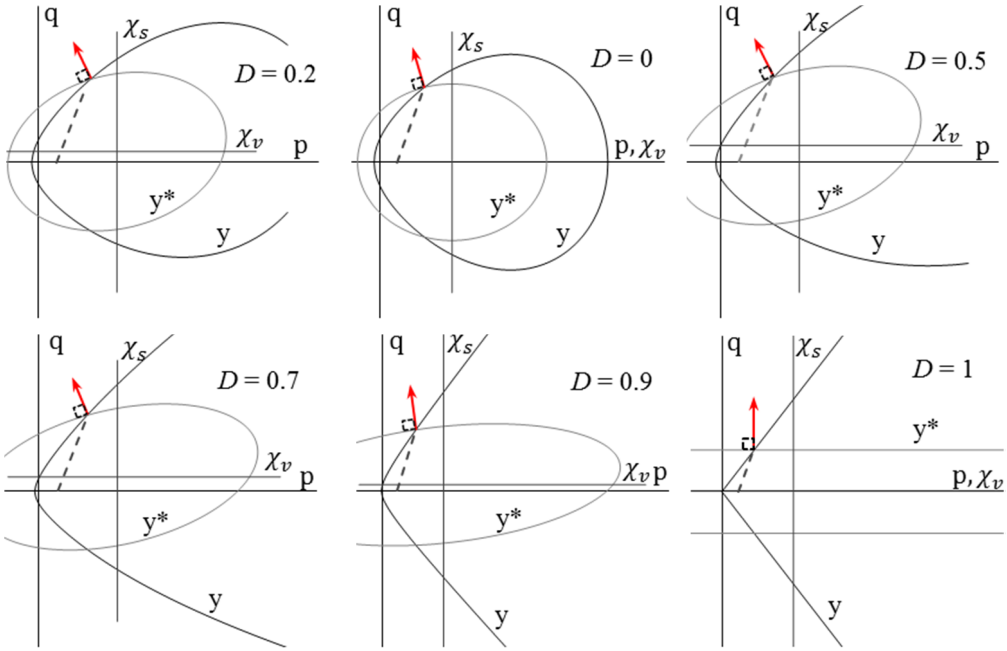

Figure 4.12: Evolution of the plastic flow direction with damage growth for 30 MPa confining pressure

4.5.3. Dilation and Compaction

Dilative and contractive responses of the proposed model depend on both direction and magnitude of the non-associated plastic flow vector. The evolution rule for the volumetric plastic strain, as stated by equation (4.49), indicates that under low confining pressure, the plastic volumetric strain rate is negative and, therefore, the behaviour is dilatational, considering the convention of compression/compaction positive. Furthermore, the second term in equation (4.49) represents the contribution of shear induced dilatancy to the rate of volumetric plastic deformation. In general, the overall model behaviour is dilative

if the magnitude of the plastic part of the volumetric strain rate is greater than its elastic part. Figure 4.13 illustrates dilative and contractive responses of the proposed model.

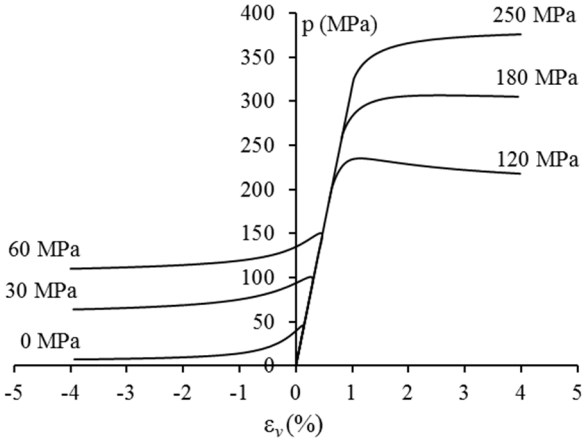

Figure 4.13: Dilative and contractive behaviour of the model with model input parameters as; E = 20 GPa, v = 0.27, p_c = 400 MPa, p_t = -10 MPa, M = 1.25, α = 0.5, γ = 0.8, μ_0 = 1.5, $r_v = r_s$ = 0.7

4.5.4. Bifurcation Analysis and Modes of Localisation

In this section, the capacity of the proposed coupled damage-plasticity model in predicting the onset of localisation of deformation as well as the orientation of the localisation band is assessed at the material level. Bifurcation from the homogeneous state in cohesive-frictional geomaterials is usually associated with the occurrence of discontinuity in the strain field, in the form of a velocity (displacement rate) jump, across the localisation band which is kinematically compatible with the surrounding material [32]. This type of localisation is referred to as the discontinuous bifurcation. A classical criterion for discontinuous bifurcation, which has been widely used in localisation analysis of geomaterials [37, 75, 179, 186, 204, 232-235], is given as the loss of positive definiteness of the localisation (or acoustic) tensor, A_{ij}, [195, 196, 200-202]. According to the classical bifurcation criterion, the material bifurcates from the homogeneous state when:

$$\det\left(A_{ij}\left(\theta, C^T_{ijkl}\right)\right) \leq 0 \tag{4.66}$$

Localisation (or acoustic) tensor is a tensor-valued function of material tangent stiffness tensor, C^T_{ijkl}, and the orientation of the planar localisation band, θ, and it is given as:

$$A_{ij} = C^T_{ijkl} n_k n_l \tag{4.67}$$

In the above expression, n_i (θ) is the unit vector normal to the boundary of the planar localisation band and the angle θ is measured from the direction of the maximum principal

stress. As illustrated in Figure 4.14, a steeper localisation band corresponds to a larger angle θ, measured between the normal to the localisation band and the axial stress.

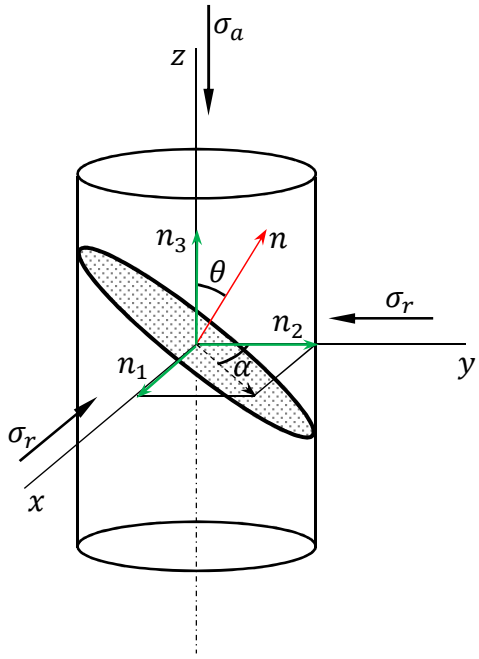

Figure 4.14: Schematic planar localisation band and the unit normal vector $\vec{n}$, indicating the orientation of the localisation band

Localisation will take place when the condition (4.66) is first satisfied. Since the acoustic tensor, A_{ij}, is a function of material tangent stiffness tensor, satisfaction of the localisation criterion of equation (4.66) is strongly dependent on the parameters of the constitutive model. In the case of the proposed model, the prediction of onset of localisation, more than any other model, parameter is sensitive to the ratios r_v , r_s and r_D. These ratios are related to the proportion of energy dissipation pertaining to each individual dissipation mechanism. As can be seen in the expression of the evolution rules, as stated by equations (4.49) – (4.51), these ratios also control the evolution of damage and plastic strains. In general, these parameters can be defined as functions of stresses and internal variables. Nevertheless, in the context of this study, for simplicity, they are kept as constants.

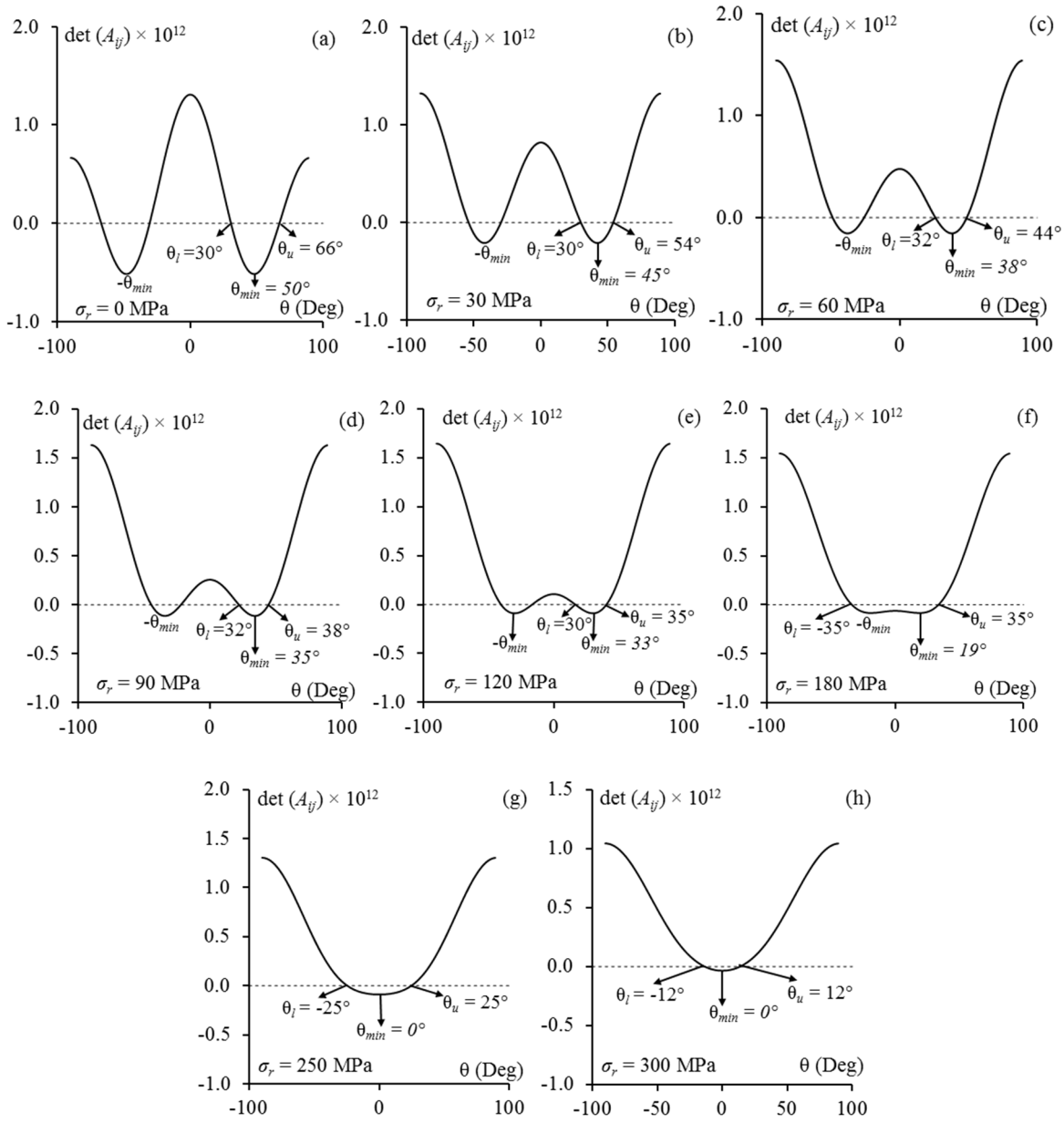

Figure 4.15: Determinant of the acoustic tensor, A_{ij}, plotted as a function of the localisation band angle at the onset of localisation, with model input parameters as; E = 20 GPa, ν = 0.27, p_c = 400 MPa, p_t = -10 MPa, M = 1.25, α = 0.5, γ = 0.8, μ_0 = 0.1, $r_v = r_s$ = 0.3

Furthermore, the orientation of the localisation band can be determined as an orientation perpendicular to a unit normal vector which satisfies the localisation condition (equation (4.66)). The unit normal vector $\vec{n}$ for a planar localisation band, as illustrated in Figure 4.14, is given as:

$$n_i = \begin{Bmatrix} \sin\theta \sin\alpha \\ \sin\theta \cos\alpha \\ \cos\theta \end{Bmatrix} \tag{4.68}$$

In fact, when the condition of equation (4.66) is first satisfied, it is possible not only for a single, unique orientation but for a range of an infinite number of orientations that satisfy the condition of equation (4.66). As illustrated in Figure 4.15, this range consists of a lower boundary and an upper boundary and the domain enclosed between these two boundaries. The upper and lower boundaries are denoted by their associated orientation as θ_u and θ_l, respectively, in Figure 4.15. Although any angle within this domain is a possible orientation of the localisation zone, the most probable direction along which the localisation zone will form is that for which $\det(A_{ij})$ is minimum. Furthermore, as illustrated in Figure 4.15, at low confining pressures the proposed model predicts two shear bands and towards higher confining pressures shear-enhanced compaction (for $\sigma_r = 180$ MPa) and finally pure compaction band (for $\sigma_r = 250$ MPa and 300 MPa) .

4.6. Numerical Examples

In this section, different aspects of the model behaviour, as discussed in the previous section, are assessed against experimental data from drained triaxial tests on porous sandstones available in the literature. To this end, comparison and validation are carried out at material level to demonstrate that the proposed coupled damage-plasticity model is adequately following the general trend observed in laboratory experiments. However, it should be noted that the available experimental data sets are not purely representative of the intrinsic material behaviour but a mixture of structural and material response. In order to take theses structural effects into consideration, cylindrical rock specimens with the same size as that used in triaxial tests are simulated using the finite element (FE) method in Section 4.7.

4.6.1. Identification of Model Parameters and the Calibration Procedure

An accurate prediction of the material behaviour by means of any phenomenological constitutive model depends, to a great extent, on assigning realistic values to model parameters that somehow represent a property or a behavioural feature of the material. Therefore, prior to comparing the model behaviour with experimental data, the effect of different model parameters on the model behaviour is briefly investigated and the adopted calibration procedure is also outlined in this section.

4.6.1.1. Parametric study on the model parameters

The proposed model employs two sets of parameters including; the parameters appearing in the formulation of the initial yield i.e. α, γ, μ_0, M, p_c and p_t, which control the shape of the initial yield surface in true stress space and parameters r_v, r_s and r_D, appearing in the formulation of flow rules, and influence the evolution of the internal variables. Parameters of the initial yield function enable the model to mimic a wide variety of experimentally observed initial yield behaviour. This flexibility is an important feature of the proposed model, as it allows the model to be applicable not only to porous rocks but also to a wide range of cohesive-frictional geomaterials with significantly different initial yield behaviour. The effect of different values of parameters α, γ, M, on the shape of the initial yield function is demonstrated in Figure 4.16. In order to further clarify the effect of each parameter on the shape of the initial yield surface, a yield surface which is calibrated for a set of experimental data (form Bentheim Sandstone [80]) is used as a benchmark for comparison.

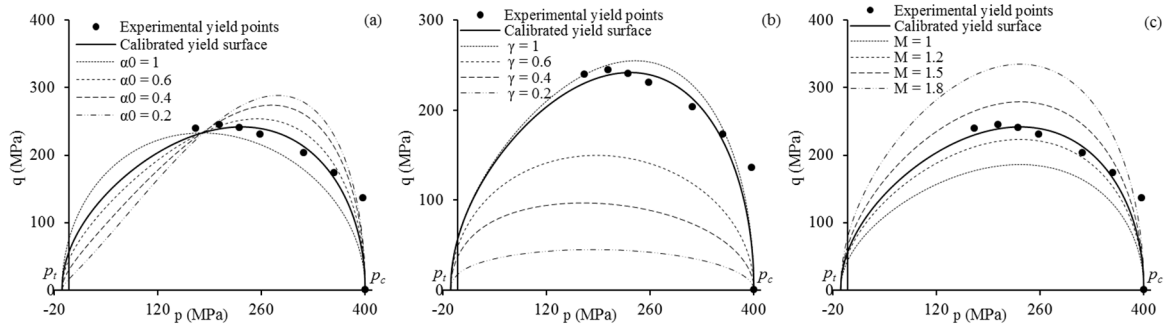

Figure 4.16: The effect of parameters α, γ and M on the shape of the initial yield surface

As illustrated in Figure 4.17 (a), under low confining pressures within the softening domain, assuming a higher evolution rate for the plastic volumetric strain, through assigning a larger value to parameter r_v (see equations (4.49) – (4.51)), will result in a more profound softening behaviour. This is because in the softening regime plastic volumetric strain is dilative (and therefore of negative sign) which causes a steeper post-peak slope through reducing the tangent stiffness (see equations (4.54), (4.57) and (4.58)). In the hardening domain, on the other hand, where the plastic volumetric strain is contractive, greater values of parameter r_v hinders the hardening response (Figure 4.17 (b)) by inhibiting the damage growth. It should be noted that the hardening and softening responses of the proposed model is automatically produced through the evolution of the initial yield surface in true stress space, which is, in turn, governed by the evolution of the scalar damage variable (see Section

4.3.2). Therefore, in general, inhibition of damage growth results in a less profound softening and/or hardening response. Accordingly, for larger values of r_s, associated with larger rates of shear plastic deformation, the post-yield response tends to shift towards the perfectly plastic behaviour in both dilation/softening and compaction/hardening domains (Figure 4.17 (c) and (d)).

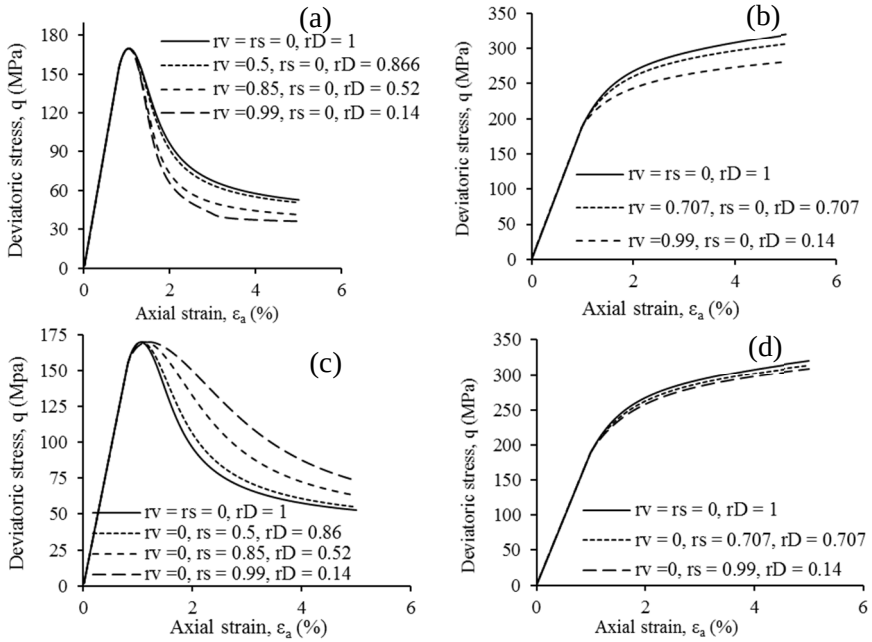

Figure 4.17: The effect of ratios r_s, r_v and r_D on the stress-strain response of the model

4.6.1.2. Calibration of model parameters

The calibration of the parameters of the proposed model involves calibration of two sets of parameters, namely the initial yield parameters (α, γ, μ_0, M, p_c and p_t) and parameters r_v, r_s and r_D. In general, it is desirable that the adopted calibration strategy extracts as much information as possible from the available experimental data. The initial yield parameters can be calibrated using experimentally observed initial yielding points at various levels of confinement in drained triaxial tests (Figure 4.18). If enough data are available, no further steps are required for calibrating the initial yield parameters. In cases where not enough data from the yielding behaviour the material are available, the stress-strain response of the material can be considered for further optimising these parameters. To this end, two sets of stress-strain data, ideally one from the softening regime and the other from the hardening regime can be selected for calibration. These data sets can also be used to calibrate the parameters r_v, r_s and r_D in conjunction with the initial yield parameters so that the model response follows the trend of behaviour of the two selected sets of stress-strain data. Thereafter, it is expected that the model can predict the material stress-strain response under any other confining pressure.

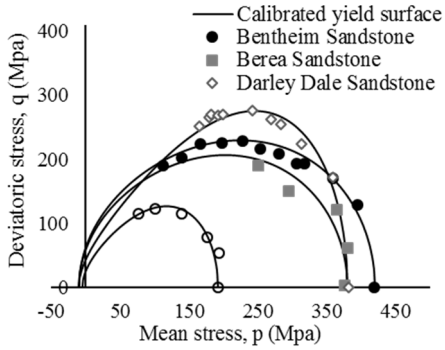

Figure 4.18: Calibration of the initial yield parameters experimental data from [28, 80, 91, 92, 232]

In addition to initial yield stresses and stress-strain data, experimental data from the onset of localisation, as well as the observations of the mode of localisation, (shear dilation or shear enhanced compaction) can be used for enriching the calibration procedure and further optimisation of the model parameters [232]. Since the localisation properties of the proposed model is sensitive to parameters r_v, r_s and r_D, the values of these parameters can be further optimised using the information extracted from experimentally observed localisation properties of rock samples. The model predictions of the stress states at which the onset of localisation takes place are compared with experimental observations for some porous sandstones in Figure 4.19. The localisation domains predicted by means of the proposed model are plotted as thick solid lines on top of the yield surfaces in true stress space.

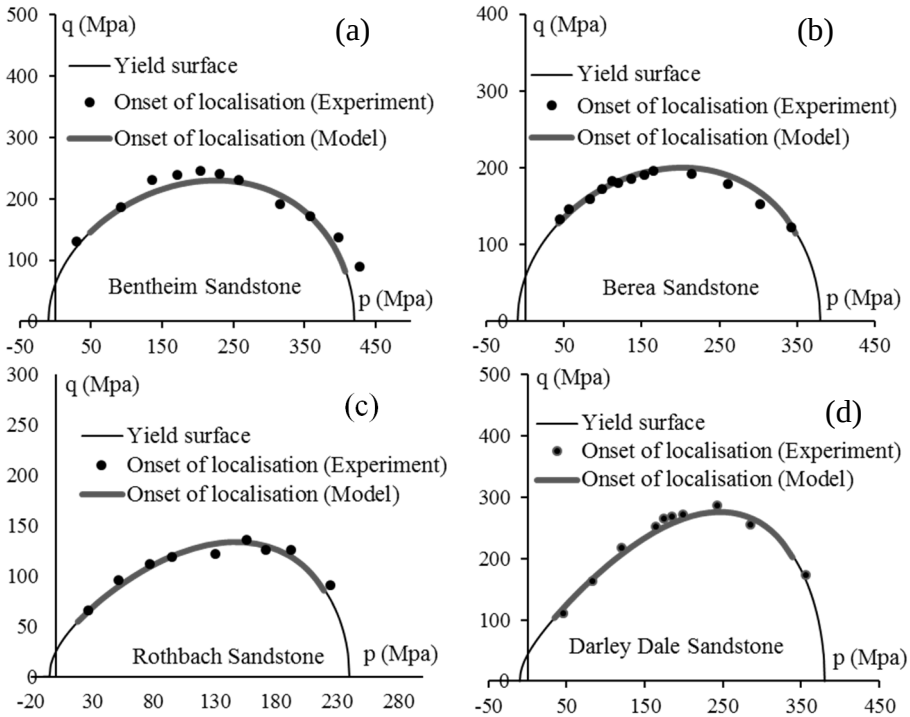

Figure 4.19: Localisation domain in stress space for Bentheim, Berea, Darley Dale and Rothbach sandstones; experimental data from [92].

If in addition to the stress state corresponding to the onset of localisation, experimental observations of the mode of localisation are also available, they may as well serve as extra information for further optimising the model parameters. For instance, predictions of the proposed model of the mode of localisation for Berea sandstone, as illustrated in Figure 4.20, could be compared and validated against experimental data.

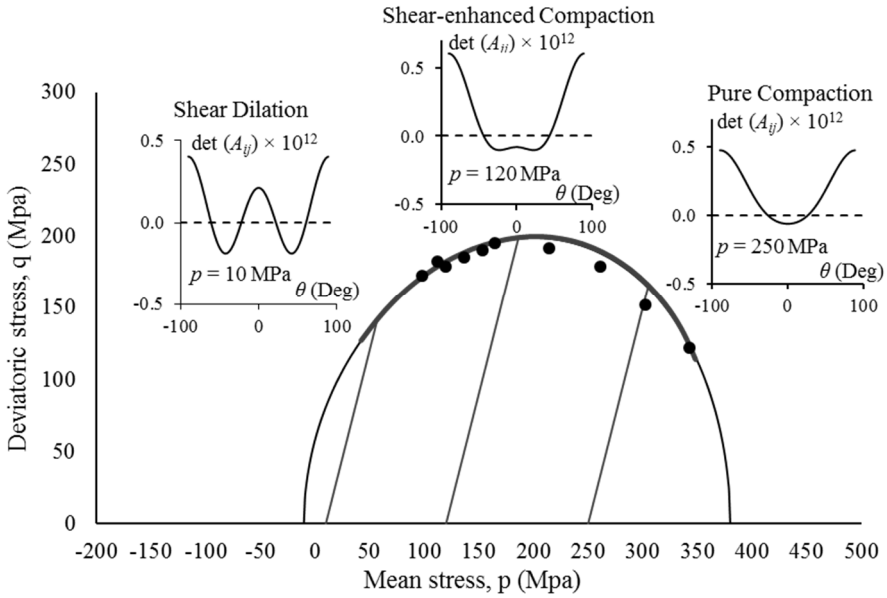

Figure 4.20: Model prediction of different localisation modes for Berea sandstone (Experimental data from Baud et al. [92]).

The procedure of calibration of model parameters is summarised in the flowchart of Figure 4.21. Model parameters calibrated for six different porous sandstones used for model validation at the material level in the subsequent section are listed in Table 4.2.

Table 4.2: Calibrated values of model parameters for the selected sets of experimental data

Rock type	E (GPa)	ν	α	γ	μ_0	M	p_c (MPa)	p_t (MPa)	r_v	r_s
Benthiem sandstone	19.25	0.27	0.85	0.95	0.10	1.20	420.00	-12.00	0.85	0.20
Berea sandstone	14.00	0.20	0.90	1.00	0.05	1.10	380.00	-10.00	0.85	0.20
Darley Dale sandstone	17.00	0.28	0.50	0.88	0.10	1.53	380.00	-10.00	0.85	0.20
Adamswiller sandstone	7.50	0.29	0.60	0.85	0.10	1.50	192.00	-6.00	0.85	0.20
Buleurswiller sandstone	10.00	0.28	1.00	1.00	0.20	1.10	120.00	-5.00	0.85	0.20
Rothbach sandstone	7.65	0.28	0.60	0.85	0.10	1.25	240.00	-7.00	0.85	0.20

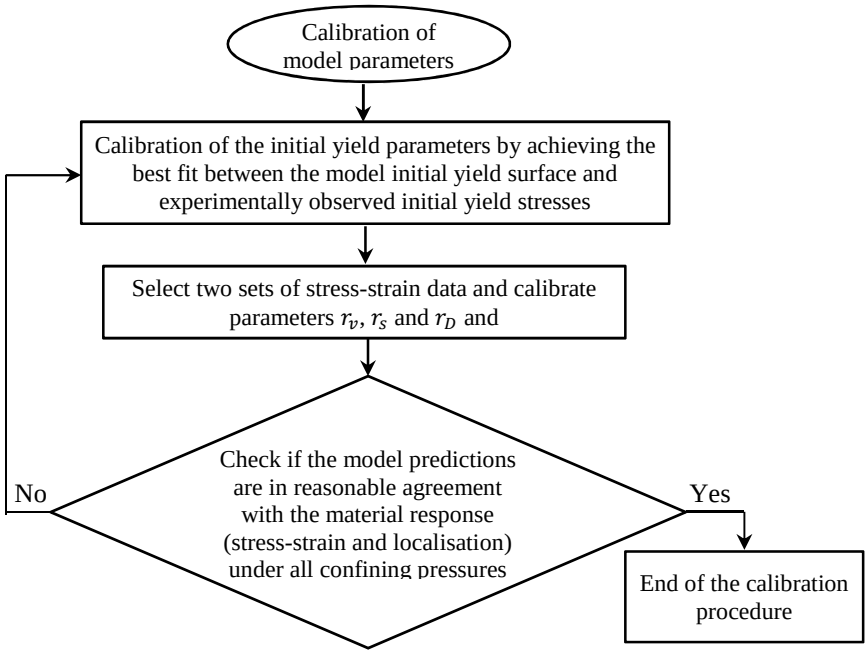

Figure 4.21: Summary of calibration procedure

4.6.2. Model Validation at Material Level

In order to demonstrate the capacity of the proposed model in presiding the stress-strain response of porous rocks, the model predictions are compared with the experimentally observed response of some porous sandstones, with porosities ranging from 13 – 24%. Experimental data selected for this study are from Adamswiller [28], Bentheim [80, 92], Darley Dale [92], Berea [91], Rothbach and Bleurswiller [232] sandstones. These experimental data sets consist of measurements of deviatoric stress, q, versus axial strain, ε_a, and mean pressure, p, against volumetric strain, ε_v, under various levels of confining pressure in drained triaxial tests on cylindrical rock specimens. In cases where the changes in volumetric strain due to the applied pressure are not available in the selected data sets (e.g. for Adamswiller sandstone), the information regarding the change in porosity is interpreted as the associated volume change. The relation between volumetric deformation and porosity change is outlined in Section 4.2. For predicting the stress-strain behaviour of the selected porous rocks, the calibrated model parameters, given in Table 4.2 are used. The stress-strain data sets used in the process of calibrating the model parameters are shown as empty circles in Figure 4.22 – Figure 4.27.

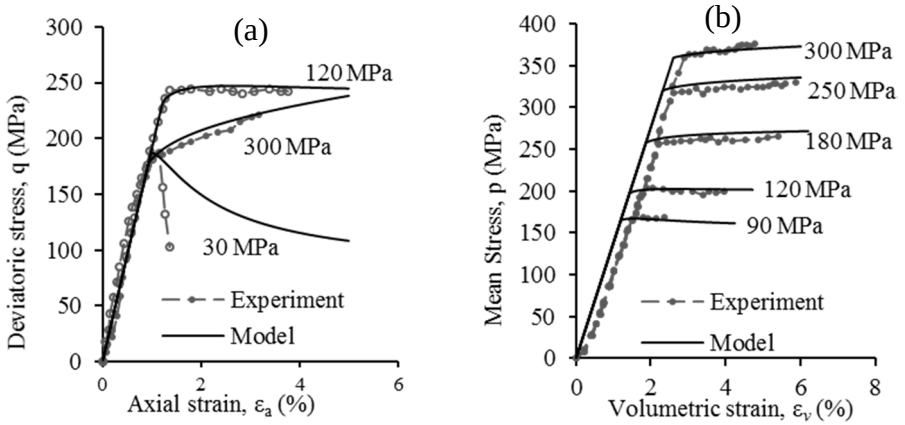

Figure 4.22: Mechanical response of Bentheim sandstone [80] and model predictions

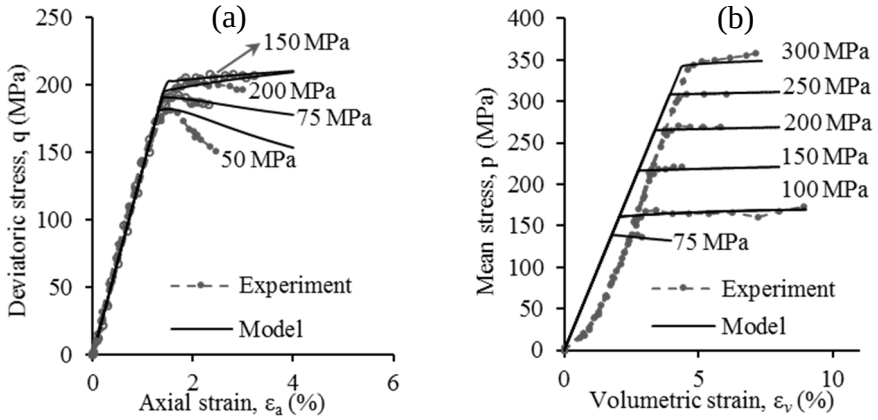

Figure 4.23: Mechanical response of Berea sandstone [91] and model predictions

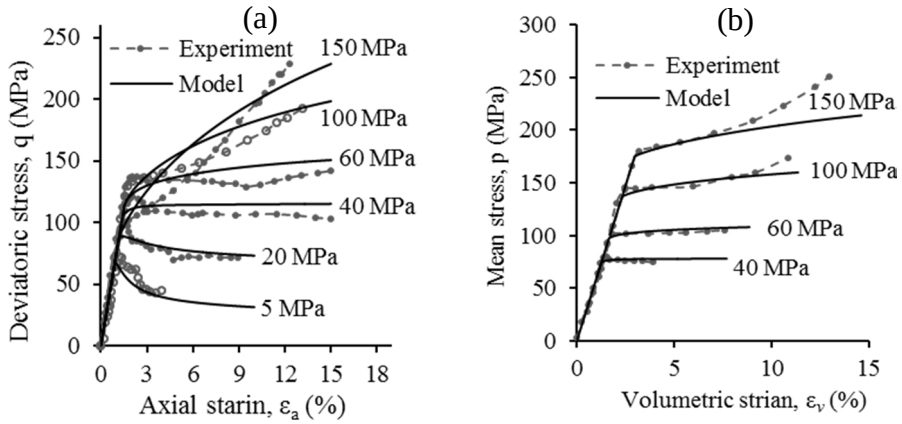

Figure 4.24: Mechanical response of Adamswiller sandstone [28] and model predictions

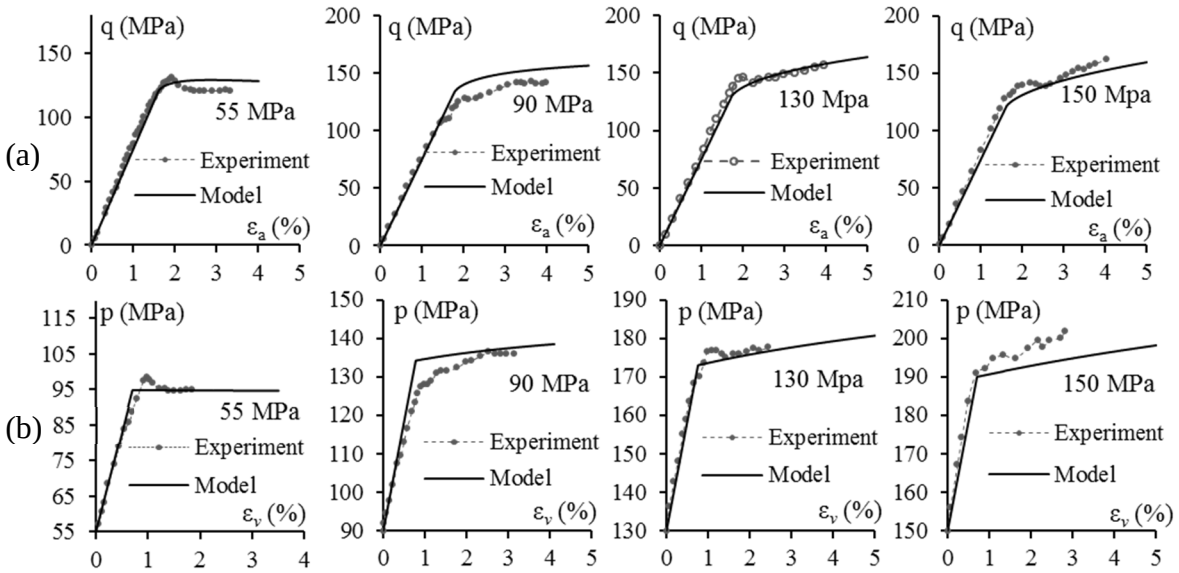

Figure 4.25: Mechanical response of Rothbach sandstone [232] and model predictions

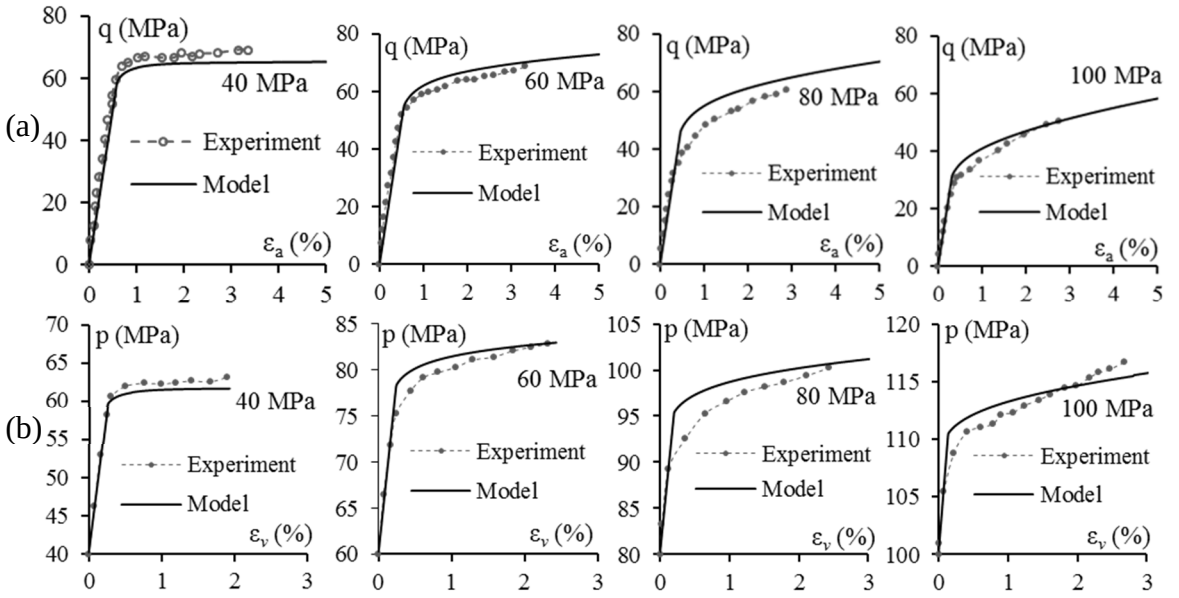

Figure 4.26: Mechanical response of Buleurswiller sandstone [232] and model predictions

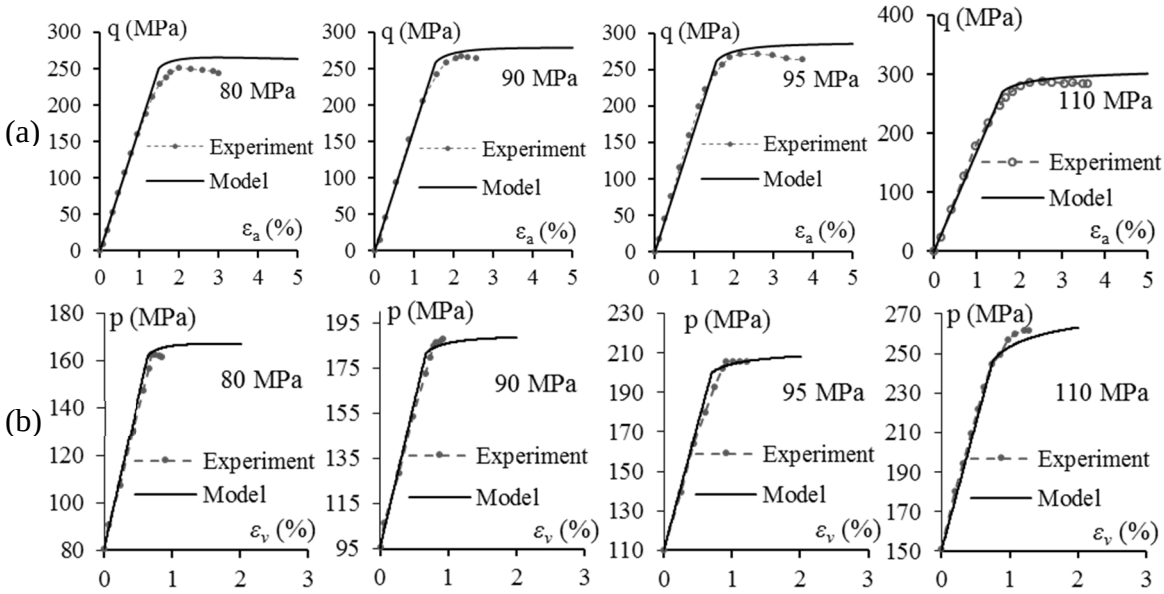

Figure 4.27: Mechanical response of Darley Dale sandstone [92] and model predictions

As illustrated in Figure 4.22 – Figure 4.27, the reasonable agreement between the model predictions and experimentally observed material response, highlights the predictive capability and versatility of the proposed model. It is, however, important to note that in calibrating the model parameters the specimens from which the experimental data are extracted are assumed to be a material point (RVE of a larger structure) in which the strain and stress fields assumed to be uniform. However, this is a rough assumption as due to localised failure, in the form of shear or compaction bands in these rocks, the characteristic sizes of the specimens would influence their mechanical response. In fact, the observed mechanical responses of laboratory specimens are combinations of structural and material responses. In particular, the effect of specimen size on the mechanical response, which is more profound under low confining pressures [31], may cause a misfit between the material model predictions and the experimental data (see Figure 4.22 (a) and Figure 4.23 (a)). This size effect, which is also referred to as the 'deterministic size effect', is even more profound in cases where the thickness of the (strain or damage) localisation zone is considerably smaller than the characteristic size of the specimen or structure. In cases where the thickness of the localisation band is considerably small compared to the characteristic size of the specimen, a snap-back is observed in the load-displacement response under quasi-static loading. This phenomenon, however, is mostly observed in hard and/or compact rocks, in which localisation of micro-cracks or damage usually take place in a band of vanishing thickness. In order to investigate the structural effect on the mechanical response of rock specimens, finite element simulation of cylindrical rock specimens in drained triaxial

condition is carried out in the subsequent section, after enhancing the current rate-independent model by means of a rate-dependent regularisation scheme.

4.7. Analysis of the Structural Behaviour

In the previous section, the capability of the proposed coupled damage-plasticity model in predicting the macroscopic behaviour of porous sandstones and the onset and mode of localisation was investigated at the material level. In this section, the proposed material model is used for analysing the structural behaviour of cylindrical sandstone specimens involving the initiation and propagation of the localisation band. The investigation of the localisation features of the proposed model at the material level (Section 4.5.4 and Section 4.6.1.2) indicates that the occurrence of localisation at the material level and, consequently, the loss of ellipticity of the governing constitutive equations will lead to numerical instability of the boundary value problem. This numerical instability of the proposed rate-independent model can be alleviated by means of a regularisation scheme. In this study, the regularisation of the rate-independent coupled damage-plasticity model is based on the development of a simple Perzyna type viscoplasticity rate-dependent enhancement. Through this analysis, an algorithmic tangent stiffness tensor, pertaining to the rate-dependent model, is derived and the rate-dependent, as well as rate-independent responses of the coupled damage-plasticity model, are investigated. Subsequently, finite element (FE) simulation of cylindrical rock specimens under drained triaxial tests enables the study of the formation and propagation of localisation bands. Furthermore, the structural effect (e.g. the effect of the size of the specimen) on the overall mechanical response of the specimen, can be investigated. In particular, it should be noted that at the onset of localisation, the homogeneity of stress and strain fields within the structure is lost. Accordingly, any definition and measure of macroscopic stress and strain will no longer be physically meaningful. After bifurcating from the homogenous state and redistribution of the stress and strain fields, the material inside the localisation band undergoes further inelastic deformation, while the material outside the band will be unloaded. A combination of these two features of behaviour will eventually determine the overall mechanical response of the specimen as recorded in laboratory experiments.

4.7.1. Rate-Dependent Regularisation

A rate-dependent enhancement of the proposed coupled damage-plasticity model is presented in this section. For this purpose, the strain rate effects on the model response are

incorporated into the rate-independent coupled damage-plasticity model by means of the Perzyna type viscoplastic regularisation [219]. The model enhancement is carried out by explicitly defining the Lagrange multiplier of equation (4.56) such that:

$$\dot{\lambda} = \frac{\langle y \rangle}{\eta} dt \tag{4.69}$$

In the above expressions, η is the viscosity parameter, having the unit s/pa (and the dimension $M^{-1}LT^3$) and $\langle y \rangle$ is a dimensionless overstress function derived from the yield function of the rate-independent model. The McCauley brackets $\langle . \rangle$ in equation (4.69) imply that:

$$\langle y \rangle = \begin{cases} y & if \quad y \geq 0 \ \ (inelastic\ response) \\ 0 & if \quad y < 0 \quad (elastic\ response) \end{cases}$$

The evolution laws of damage and plastic strains of equation (4.49) – (4.51) are, therefore, modified to give the viscoplastic strain and damage rates in the following manner:

$$\dot{\varepsilon}_v^{vp} = \dot{\lambda} \frac{\partial y^*}{\partial \chi_v} = 2 \frac{\langle y \rangle}{\eta} \left(\frac{{r_v}^2 (p - \rho)}{{F_v}^2} - \frac{{r_s}^2 \mu \ (q - \mu p)}{{F_s}^2} \right) dt \tag{4.70}$$

$$\dot{\varepsilon}_s^{vp} = \dot{\lambda} \frac{\partial y^*}{\partial \chi_s} = 2 \frac{\langle y \rangle}{\eta} \frac{{r_s}^2 (q - \mu p)}{{F_s}^2} dt \tag{4.71}$$

$$\dot{D} = \dot{\lambda} \frac{\partial y^*}{\partial \chi_D} = 2 \frac{\langle y \rangle}{\eta} \frac{{r_D}^2 \chi_D}{{F_D}^2} dt \tag{4.72}$$

Furthermore, by applying the chain rule, the viscoplastic strain tensor is given as:

$$\dot{\varepsilon}_{ij}^{vp} = \dot{\lambda} \frac{\partial y^*}{\partial \chi_{ij}} = 2 \frac{\langle y \rangle}{\eta} \left(\frac{\partial y^*}{\partial \chi_v} \frac{\partial \chi_v}{\partial p} \frac{\partial p}{\partial \sigma_{kl}} \frac{\partial \sigma_{kl}}{\partial \chi_{ij}} + \frac{\partial y^*}{\partial \chi_s} \frac{\partial \chi_s}{\partial q} \frac{\partial q}{\partial \sigma_{kl}} \frac{\partial \sigma_{kl}}{\partial \chi_{ij}} \right) dt \tag{4.73}$$

Figure 4.28 (a) shows the comparison between the rate-independent and rate-dependent model responses for different values of the viscosity parameter, η and for different strain rates, $\dot{\varepsilon}$. The model response collapses to rate-independent behaviour for small values of the viscosity parameter and/or lower strain rates. Furthermore, as illustrated in Figure 4.28 (a) and (b), for higher strain rates and/or greater values of the viscosity parameter the maximum attainable stress increases and the transition from elastic to inelastic response is smoother. Furthermore, as illustrated in Figure 4.28 (c) and (d), higher values of the viscosity parameter and/or greater strain rates inhibit the damage growth. This response of the proposed model is in accordance with the experimentally observed behaviour of rocks which

is often reported as an increase in the rock strength under tension and compression at higher strain rates [236-240].

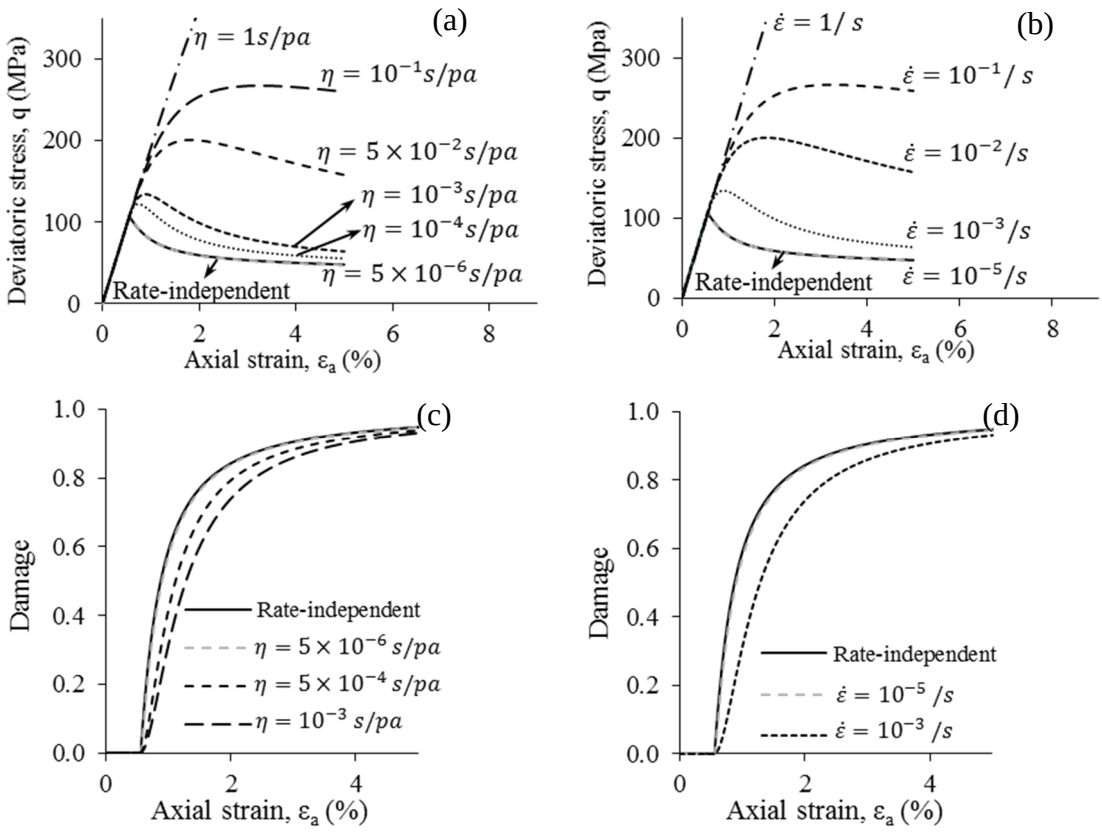

Figure 4.28: The influence of (a) viscosity parameter (with $\dot{\varepsilon} = 10^{-5}/\mathrm{s}$) and (b) strain rate (with $\eta = 5\times10^{-6}\,s/pa$) on (a) and (b) the stress-strain response and (c) and (d) of the evolution of damage

Furthermore, at higher strain rates rocks show a tendency towards more ductile behaviour, while in quasi-static loading, under the same confining pressure, the behaviour can be completely brittle [95, 241-243]. From a physical point of view, deformation processes in rocks are mostly time/rate-dependent at the microscopic scale. This, consequently, gives rise to the macroscopically observed rate-dependent behaviour of rocks. Examples of such time/rate-dependent micro-mechanisms may be given as time dependency of static friction and the evolution of frictional strength with the loading rate [244-247] and/or time dependent micro-crack growth [241, 248].

A constitutive model would not exhibit any bifurcation instability as long as its associated acoustic tensor is positive definite. Therefore, in order to demonstrate the numerical stability of the enhanced rate-dependent model, the formulation of the tangent stiffness tensor of the damage-viscoplastic model is required for localisation analysis. It should be noted, however, that since there is no consistency condition for the coupled

damage-viscoelasticity model, the algorithmic tangent stiffness is given as; $L_{ijk}^{vp} = d\sigma_{ij}/d\varepsilon_{kl}$ (see [249]). In this sense, the $(n+1)^{\text{th}}$ increment of the stress tensor is given as:

$$\Delta\sigma_{ij}^{n+1} = \sigma_{ij}^{n+1} - \sigma_{ij}^{n} \tag{4.74}$$

The stress tensor at step $n+1$ can be approximated by means of the first order Taylor expansion as:

$$\sigma_{ij}^{n+1} = \sigma_{ij}^{n} + \frac{\partial\sigma_{ij}}{\partial\varepsilon_{kl}}\Delta\varepsilon_{kl}^{n+1} + \frac{\partial\sigma_{ij}}{\partial D}\Delta D^{n+1} \tag{4.75}$$

Also, the elastic stress tensor of the coupled damage-viscoelasticity model is given as:

$$\sigma_{ij} = (1-D)C_{ijkl}\left(\varepsilon_{kl} - \varepsilon_{kl}^{vp}\right) \tag{4.76}$$

Therefore, the increment of the stress tensor of equation (4.74) can be rewritten as:

$$\Delta\sigma_{ij}^{n+1} = (1-D)C_{ijkl}\Delta\varepsilon_{kl}^{n+1} - (1-D)C_{ijkl}\Delta\varepsilon_{kl}^{vp\,n+1} - \frac{\sigma_{ij}}{(1-D)}\Delta D^{n+1} \tag{4.77}$$

The above expression can also be written in the following form:

$$\Delta\sigma_{ij}^{n+1} = (1-D)C_{ijkl}\Delta\varepsilon_{kl}^{n+1} - \left[(1-D)C_{ijkl}Q_{kl}^{n+1} + \frac{\sigma_{ij}}{(1-D)}\right]\Delta D^{n+1} \tag{4.78}$$

where Q_{ij} is the ratio between the increment of the viscoplastic strain tensor and the increment of the scalar damage variable:

$$Q_{ij}^{n+1} = \frac{\Delta\varepsilon_{ij}^{vp\,n+1}}{\Delta D^{n+1}} = \frac{\left(\frac{\partial y^*}{\partial\chi_v}\frac{\partial\chi_v}{\partial p}\frac{\partial p}{\partial\sigma_{kl}}\frac{\partial\sigma_{kl}}{\partial\chi_{ij}} + \frac{\partial y^*}{\partial\chi_s}\frac{\partial\chi_s}{\partial q}\frac{\partial q}{\partial\sigma_{kl}}\frac{\partial\sigma_{kl}}{\partial\chi_{ij}}\right)}{\frac{\partial y^*}{\partial\chi_D}} \tag{4.79}$$

In addition, the increment of stress residual is defined as follows:

$$\Delta R_{ij}^{n+1} = (1-D)C_{ijkl}\Delta\varepsilon_{kl}^{n+1} - \left[(1-D)C_{ijkl}Q_{kl}^{n+1} + \frac{\sigma_{ij}}{(1-D)}\right]\Delta D^{n+1} - \Delta\sigma_{ij}^{n+1} \tag{4.80}$$

In order to derive the analytical form of the consistent tangent stiffness tensor, the stress residual must be zero after each time step. Therefore, the root of $\Delta R_{ij}^{n+1} = 0$ can be determined by means of an iterative scheme, such as Newton-Raphson. To this end, the value of the stress residual at the end of the iterative solution is approximated using the first order Taylor expansion as:

$$\Delta R_{ij}^{n+1}\big|_{new} = \Delta R_{ij}^{n+1}\big|_{old} + d\Delta R_{ij}^{n+1} \tag{4.81}$$

In the above expression, $d\Delta R_{ij}^{n+1}$ is defined as:

$$d\Delta R_{ij}^{n+1} = \frac{\partial \Delta R_{ij}^{n+1}}{\partial \varepsilon_{kl}} d\varepsilon_{kl} + \frac{\partial \Delta R_{ij}^{n+1}}{\partial \sigma_{kl}} d\sigma_{kl} + \frac{\partial \Delta R_{ij}^{n+1}}{\partial D} dD \tag{4.82}$$

where

$$\frac{\partial \Delta R_{ij}^{n+1}}{\partial \varepsilon_{kl}} = (1-D)C_{ijkl} \tag{4.83}$$

$$\frac{\partial \Delta R_{ij}^{n+1}}{\partial \sigma_{kl}} = -\left[(1-D)C_{ijkl}\frac{\partial Q_{ij}}{\partial \sigma_{kl}} + \frac{\delta_{ik}\delta_{jl}}{(1-D)}\right]\Delta D - \delta_{ik}\delta_{jl} \tag{4.84}$$

$$\begin{aligned}\frac{\partial \Delta R_{ij}^{n+1}}{\partial D} = &-C_{ijkl}\varepsilon_{kl} - \left[-C_{ijkl}Q_{kl} + (1-D)C_{ijkl}\frac{\partial Q_{kl}}{\partial D} + \frac{\sigma_{ij}}{(1-D)^2}\right]\Delta D \\ &- \left[(1-D)C_{ijkl}Q_{kl} + \frac{\sigma_{ij}}{(1-D)}\right]\end{aligned} \tag{4.85}$$

Furthermore, by virtue of equation (4.72), the increment of the scalar damage variable, ΔD, can be written as:

$$\Delta D = 2\frac{\langle y \rangle}{\eta}\frac{\partial y^*}{\partial \chi_D}\Delta t \tag{4.86}$$

Therefore, the damage increment during each step of the Newton-Raphson iteration scheme can be obtained, by making use of equation (4.86), in terms of the increment of stress tensor as follows:

$$dD = \frac{2\frac{\Delta t}{\eta}\frac{\partial\left(y\frac{\partial y^*}{\partial \chi_D}\right)}{\partial \sigma_{ij}}}{1 - 2\frac{\Delta t}{\eta}\frac{\partial\left(y\frac{\partial y^*}{\partial \chi_D}\right)}{\partial D}} d\sigma_{ij} = \mathrm{X}_{ij} d\sigma_{ij} \tag{4.87}$$

By substitution of the above expression back into equation (4.82) and enforcing $d\Delta R_{ij}^{n+1} = 0$ at the end of the Newton-Raphson iterative scheme:

$$0 = \frac{\partial \Delta R_{ij}^{n+1}}{\partial \varepsilon_{kl}} d\varepsilon_{kl} + \frac{\partial \Delta R_{ij}^{n+1}}{\partial \sigma_{kl}} d\sigma_{kl} + \frac{\partial \Delta R_{ij}^{n+1}}{\partial D} \mathrm{X}_{kl} d\sigma_{kl} \tag{4.88}$$

the formulation of the consistent tangent stiffness tensor is obtained as follows:

$$L_{ijkl}^{vp} = \frac{d\sigma_{ij}}{d\varepsilon_{kl}} = -\frac{\partial \Delta R_{ij}^{n+1}}{\partial \varepsilon_{kl}}\left[\frac{\partial \Delta R_{ij}^{n+1}}{\partial \sigma_{kl}} + \frac{\partial \Delta R_{ij}^{n+1}}{\partial D}\mathrm{X}_{kl}\right]^{-1} \tag{4.89}$$

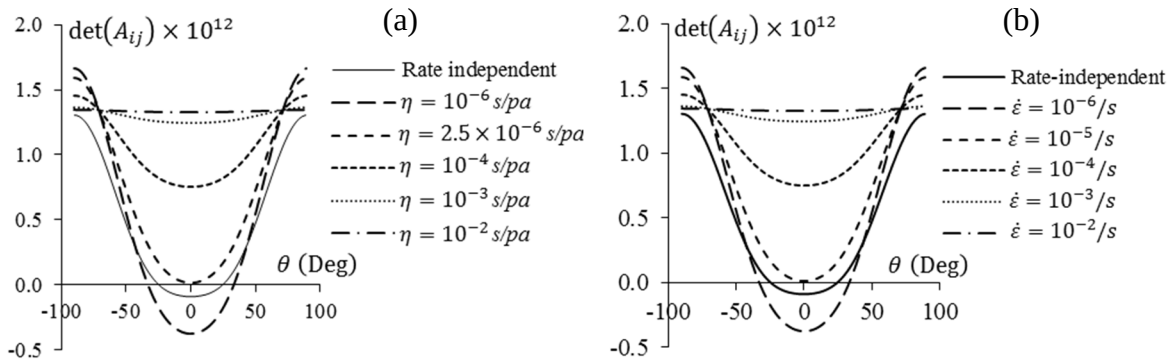

Figure 4.29: The influence of (a) the viscosity parameter (with $\dot{\varepsilon} = 10^{-5}/s$) and (b) strain rate (with $\eta = 2.5 \times 10^{-5} s/pa$) on the determinant of the acoustic tensor for Bentheim sandstone under 300 MPa confining pressure

The rate-dependent effects on the determinant of the acoustic tensor are shown in Figure 4.29, where the determinant of the acoustic tensor at the onset of yielding is plotted against the band orientation. It can be seen that for the rate-dependent model the determinant of the acoustic tensor can drop below zero, even beyond the rate-independent behaviour for certain combinations of the viscosity parameter, η and strain rate, $d\varepsilon/dt$. This is due to the difference in the way the acoustic tensors are derived in the two rate-independent and rate-dependent cases. The continuum tangent stiffness is used in the former (Section 4.4.1), while in derivation of the latter the consistent tangent stiffness (equation (4.89)) is adopted, which generally yields a smaller determinant of the stiffness tensor [250, 251].

As illustrated in Figure 4.29, for certain combinations of the viscosity parameter and strain rate ($\dot{\varepsilon}_a = 10^{-5}/s$ and $\eta = 2.5 \times 10^{-5}\ s/pa$ for Bentheim sandstone) the determinant of acoustic tensor ($\det(A_{ij})$) is non-negative for all possible orientations of the localisation band and the minimum value of $\det(A_{ij})$ lies just above zero. Therefore, it is expected that, owing to the rate-dependent enhancement, the numerical instabilities of the rate-independent model due to its localisation properties are eliminated. Furthermore, in order to calibrate the parameters of the rate-dependent model, the strategy adopted here is to keep the strain rate constant and similar to that applied in laboratory experiments and then calibrate and adjust the viscosity parameter, η. The basis for calibrating the viscosity parameter, η, is to, firstly, guarantee the non-negativeness of the determinant of the acoustic tensor of the rate-dependent model for all possible band orientations and, secondly, to match the stress-strain response of the model with that of the experiment. In experimental practice [93, 252], the range of axial strain rates used for triaxial tests on sandstone specimens varies between $10^{-6}/s$ and $10^{-4}/s$ [80, 92, 96], thus, for the present study the viscosity parameter, η, is

calibrated considering a constant axial strain rate of $\dot{\varepsilon}_a = 10^{-5}/s$. For example, for Bentheim sandstone, it was found that corresponding to a strain rate of $\dot{\varepsilon}_a = 10^{-5}/s$, the viscosity parameter $\eta = 2.5 \times 10^{-5} s/pa$ gives rise to a positive definite acoustic tensor in all directions and also to a good match between stress-strain response of the model and that of the experiment (Figure 4.30). This calibrated values of the viscosity parameter at the material level is used as a starting point for the calibration procedures at structural level in FE simulations.

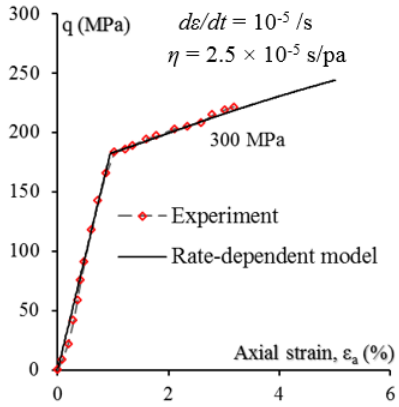

Figure 4.30: Calibration of the viscosity parameter at material level for Bentheim sandstone under 300 MPa confining pressure (Experimental data from Wong et al. [80])

4.7.2. Finite element analysis

In this section, numerical simulations of drained triaxial tests, involving shearing of cylindrical samples, are performed employing different FE discretisation. This simulations demonstrate the application of the proposed damage plasticity model to structural analyses in conjunction with the presented regularisation technique (Section 7.1). The aim of such numerical simulation (i.e. the use of different FE discretisation) is to investigate the mesh sensitivity of the model due to the localisation of deformation in the shear band. The FE-program ABAQUS/Standard 6.14 is employed for the FE-simulations. To this end, the proposed coupled damage-plasticity model has been implemented into ABAQUS as a user defined material subroutine UMAT along the lines of the stress update algorithm presented in Section 4.2. Drained triaxial compression tests on Bentheim sandstone with material and model parameters according to Table 2 are simulated for different levels of lateral confinement. The setup of the tests is similar to the triaxial tests described in [96]. The diameter and the height of the samples are 20 mm and 40 mm, respectively. Vertical displacements are only constrained at the bottom face of the specimen. The horizontal displacements are constrained at the centre of the bottom face to avoid lateral instability. The rotational motion of the bottom boundary about the vertical axis is also restricted, in order

to avoid any rotational instability that may arise due to the localisation of deformation. The specimens are first isotropically compressed and then the shearing process is initiated by means of a prescribed vertical displacement with a constant strain rate ($\dot{\varepsilon} = 10^{-5}/s$). In order to trigger the localisation, a local defect is introduced as a weak element at about the centre of each specimen to slightly disturb the homogeneity of the stress field. The isotropic compressive strength, p_c, of the weak element is assumed to be 99.5% of the value of this parameter for other elements. Three different FE meshes are employed in the numerical simulations. The coarse mesh consists of 600 linear hexahedral finite elements with reduced numerical integration. The medium mesh and the fine mesh are obtained by consistent refinement of the coarse mesh and they consist of 2500 and 7700 elements, respectively.

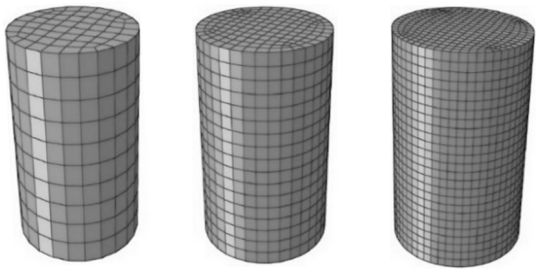

Figure 4.31: FE discretization of cylindrical rock specimens (a) 600 elements, (b) 2500 elements and (c) 7700 elements.

Figure 4.32 illustrates the deformed meshes after development of distinct shear bands in the samples, as well as the distribution of the scalar damage variable D. A similar approach to that adopted for calibrating η at the material level is also adopted in the FE analysis. In this sense, the strain rate is chosen to be the same as that applied in real laboratory tests ($10^{-4} - 10^{-6}/s$ [80, 92, 96]) and the viscosity parameter is calibrated in order to obtain identical responses from all FE meshes under identical loading conditions. In this study the axial strain rate $\dot{\varepsilon}_a = 10^{-5}/s$ is chosen. As illustrated in Figure 4.32, identical responses are achieved for different FE discretisation for the viscosity parameter being calibrated as $\eta = 3.0 \times 10^{-5}\ s/pa$ for a cylindrical specimen of Bentheim sandstone. Hence, the rate-dependent regularisation of the proposed model eliminates the mesh dependency of the numerical solution and thus, allows for predicting the structural response, including the formation of the shear band, independently of the employed FE-mesh.

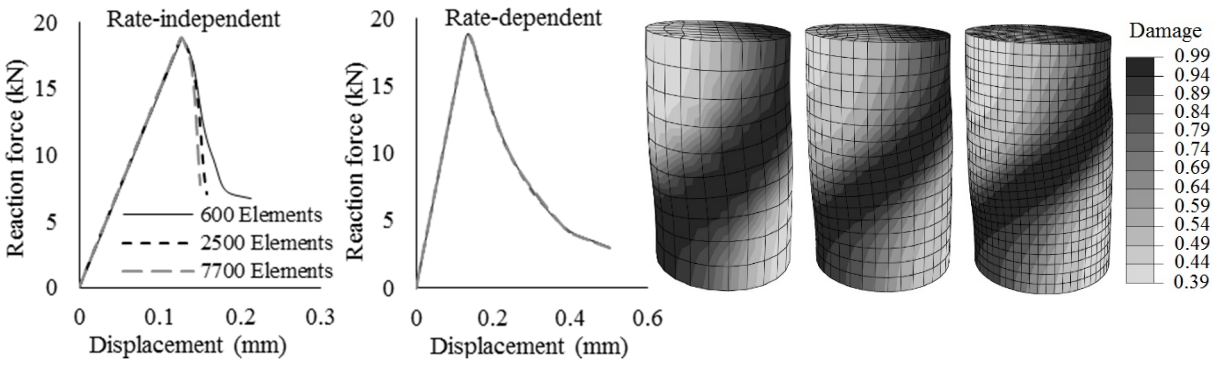

Figure 4.32: The effect of the FE discretisation on the global load-displacement of the rate-independent model and the results of the rate-dependent regularisation with distrubition of the scalar damage variable

As can be observed in Figure 4.32, the calibrated value of the viscosity parameter, η, for the converged solution, leads to a relatively thick localisation band. This is due to the stabilising effect of the rate-dependent model. In plasticity-based models, for instance, it can be proven that for any positive values of viscosity parameter η, the magnitude of inelastic strains are always smaller than their corresponding counterparts in a rate-independent model at any stress state [249]. This is also true for the values of the damage variable. Furthermore, higher values of the viscosity parameter cause the damage variable to grow at a slower rate compared to the rate-independent model. The numerical stabilisation effect of the rate-dependent enhancement can, therefore, be interpreted as the stabilisation effect it has on the evolution of internal variables, damage and plasticity.

In order to assess the predictive capability of the model, both the orientation of the localisation band (localisation or failure mode) and the stress-strain response of the FE simulations are compared with the macroscopic observations from the laboratory experiments. Figure 4.33 illustrates the orientation of the localisation bands and/or failure planes predicted by means of the classical bifurcation criterion, at the material level, and FE simulations, at the structural level, in comparison with those observed in drained triaxial experiments on Bentheim sandstone [96]. The contours in Figure 4.33 indicate the distribution of the scalar damage variable. A relatively good agreement is observed between the results of FE simulation and laboratory experiments. However, the model predicts a slightly less steep failure plane compared to that observed in experiments. This discrepancy is acknowledged as a limitation of the proposed model which may have arose as a consequence of simplifying assumptions in the phenomenological descriptions of the essential deformation mechanisms. With increasing confining pressure the inclination of the localisation band diminishes until at substantially high confining pressure, it transforms to a

horizontal pure compaction band. The theoretical analysis of Section 4.5.4 suggests that under substantially high confining pressures, pure compaction bands, i.e. horizontal planes with $\theta = 0$, can form within the specimen. Both experimental observations and FE simulations show that, in fact, multiple compaction bands form within a specimen of porous sandstone under high confining pressure in triaxial tests [92]. The FE simulation of multiple compaction bands in comparison with experimental observation form a Bentheim sandstone specimen [92] is also shown in Figure 4.33.

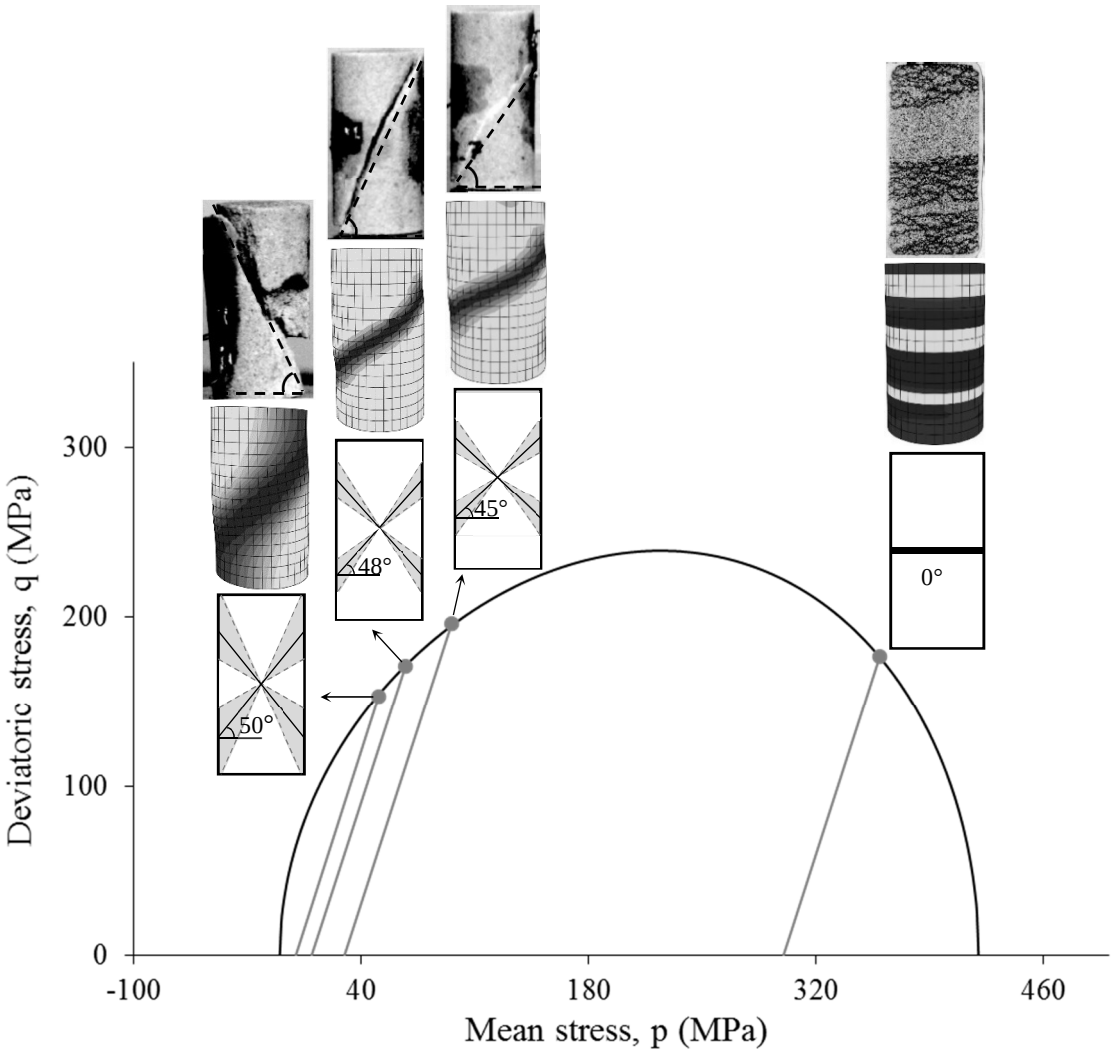

Figure 4.33: Orientation of the localisation band in experimental observations along with predictions of FE simulations and the classical bifurcation criterion

Furthermore, positive values of the viscosity parameter, η, also inhibit the evolution of damage and, therefore, cause the width of the localisation to become thicker. The effect of the viscosity parameter on the thickness of the localisation zone is illustrated in Figure 4.34.

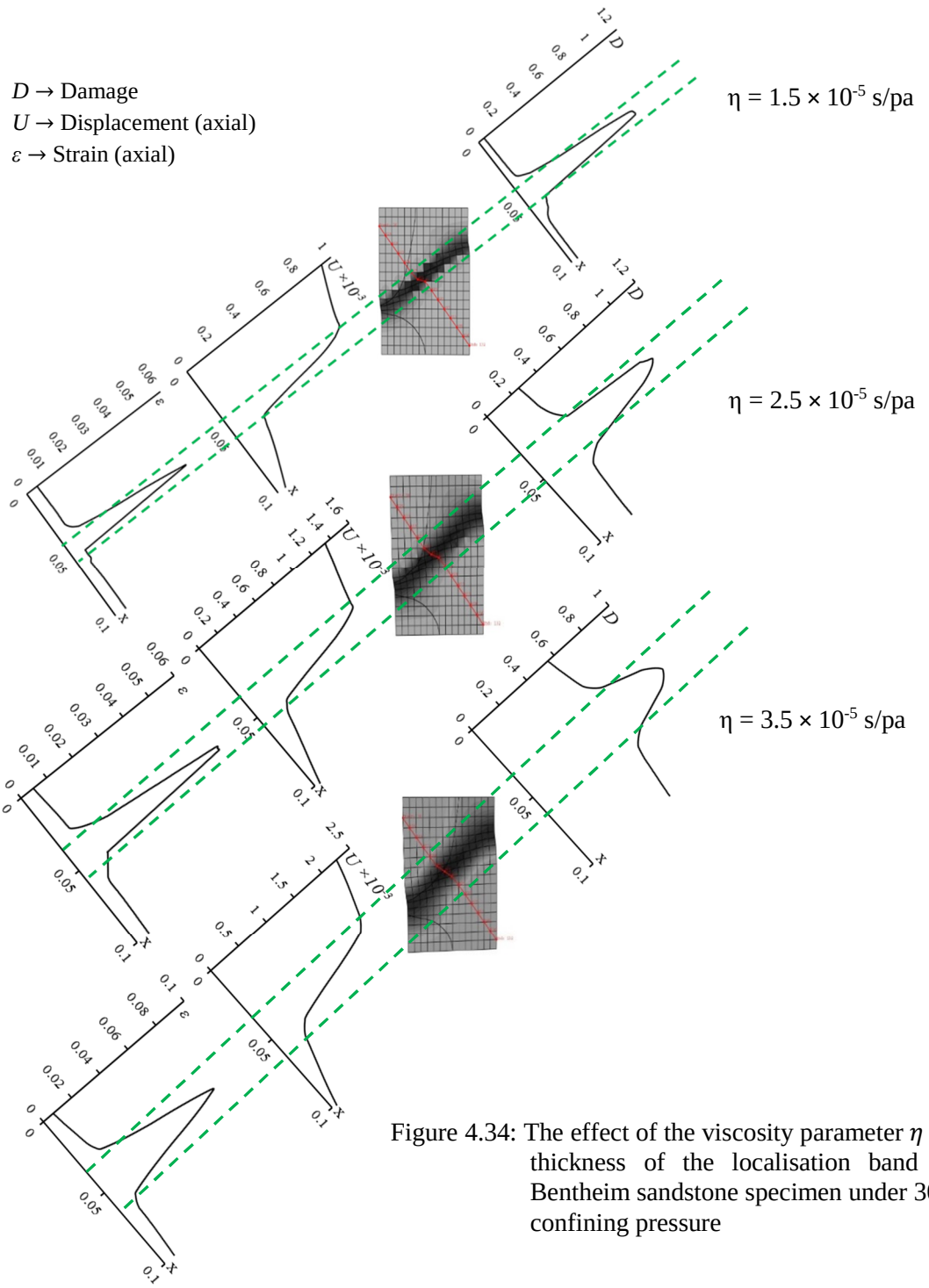

Figure 4.34: The effect of the viscosity parameter η on the thickness of the localisation band for a Bentheim sandstone specimen under 30 MPa confining pressure

Higher values of the viscosity parameter cause the damage variable to grow at a slower rate compared to the rate-independent model. This inhibitive effect of the viscosity parameter on damage evolution is demonstrated in Figure 4.35, where damage is plotted against the axial strain for two elements of identical locations in the spatial discretization of FE simulation with rate-independent and rate-dependent material models. The numerical stabilisation

effect of the rate-dependent enhancement can, therefore, be interpreted as the stabilisation effect it has on the evolution of internal variables, damage and plasticity.

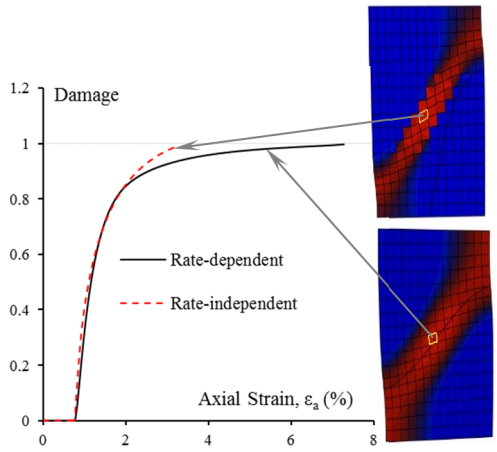

Figure 4.35: The effect of viscosity parameter on damage growth in FE simulation

Relatively good agreement between the stress-strain response of Bentheim sandstone [80] and FE simulation, as illustrated in Figure 4.36, highlights the high predictive capability of the model. It should be noted that the stress-strain response, as illustrated in Figure 4.36, are average quantities. In this sense, the average stress is calculated as the axial reaction force divided by the cross section area of the specimen. Also, the axial strain is defined as the total displacement divided by the length of the specimen. It is also important to note that in softening regime (i.e. under 30 MPa confining pressure) the prediction of FE simulation of stress-strain response of Bentheim sandstone is considerably closer to the experimental data compared to that of the material model in which the structural effects on the observed mechanical response is not taken into consideration (see Figure 4.22 (a)). In the hardening region, on the other hand, the FE and material model predictions are almost the same. This is because the effect of the size of the specimen on its mechanical behaviour is more profound if the specimen is loaded under conditions conducive to softening behaviour [31].

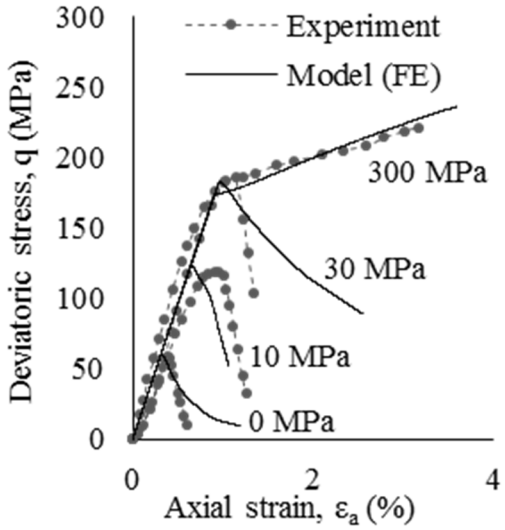

Figure 4.36: The stress-strain response of Bentheim sandstone [80, 92] under drained triaxial tests

As was discussed earlier in the current chapter and also in Chapter 2, the size effect arises as a consequence of bifurcation of stress and strain fields from the homogeneous state due to the localisation of deformation. Owing to this localisation-induced inhomogeneity material points at various locations within the specimen show different mechanical response. In particular, as illustrated in Figure 4.37, upon the onset of localisation, the material inside the localisation band undergoes further inelastic loading while the material outside the band is unloaded. Therefore, any definition and measurement of stress and strain pertaining to the specimen are not physically meaningful, unless as an average. The average stress-strain response of the model is also shown in Figure 4.37. It is inferred from Figure 4.37 that damage is first distributed uniformly throughout the specimen. After localisation, damage evolution continues within the localisation band while the damage level remains unaltered in the bulk outside the band.

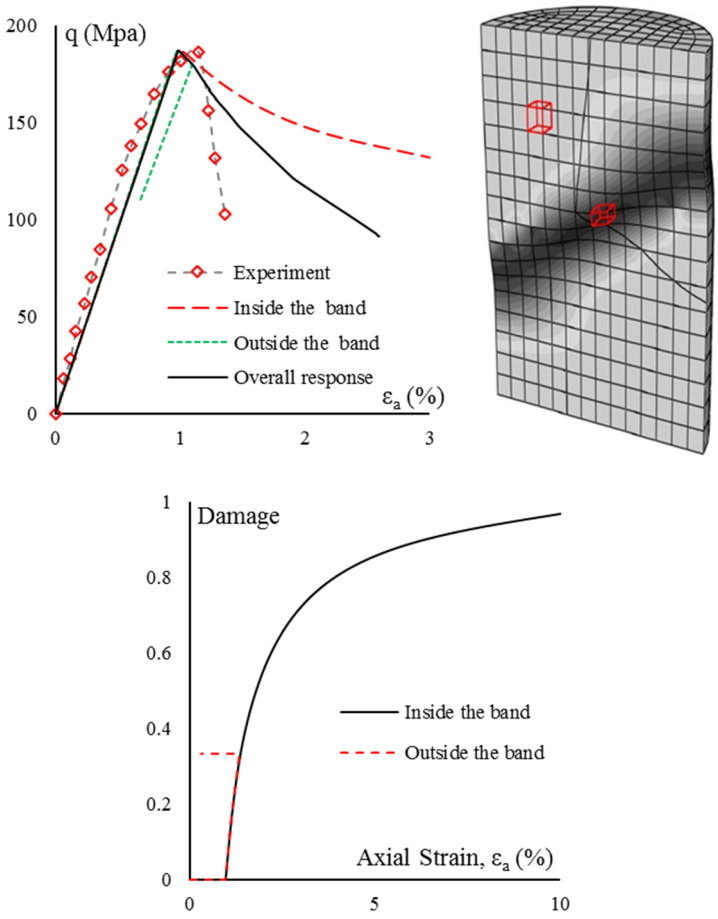

Figure 4.37: Average stress-strain response of the specimen along with the stress-strain response and damage evolution for materials inside and outside the localisation band

4.8. Summary and Discussion

The main objective of the developments in this chapter is to construct a coupled damage-plasticity model to describe the macroscopic behaviour of porous rocks. The development of the model is carried out within a well-established thermodynamic framework to guarantee the thermodynamic admissibility of the model. The proposed model is then used for finite element (FE) simulations of the mechanical response of porous sandstone specimens under drained triaxial loading. The motivation for FE simulation of rock specimens is that experimental data from triaxial tests do not merely reflect the intrinsic material response and they are also affected by the size and probably the geometry of the specimen. The results of FE simulations confirms that the structural effects on the mechanical response of rock specimens are more profound under loading conditions conducive to softening behaviour and brittle failure.

The proposed coupled damage-plasticity model is capable of predicting the onset of localisation and the orientation of the localisation band for a wide range of stress states in true stress space. It is demonstrated in this chapter that the orientations of the localisation bands in FE simulations are almost the same as the orientations at which the rate-independent material model exhibits localisation (see Section 4.5.4). In general, the FE simulations show a good agreement with experiments in both predicting the average stress-strain response and the orientation of the localisation band and failure mode. In order to alleviate the numerical instabilities pertaining to the rate-independent coupled damage-plasticity model, Perzyna type viscoplasticity [219] is used for rate-dependent regularisation of the rate-independent model. In FE simulations of the triaxial tests, the strain rate is kept constant and the same at that applied in the actual tests. The viscosity parameter η is then calibrated to converge to a solution. As was discussed earlier, positive values of the viscosity parameter cause the internal variables of the model to grow at a slower rate. Similar to the effect of confining pressure, a slower and more stable damage growth would cause the width of the localisation band to increase. Furthermore, no direct link can be established between the viscosity parameter and the width of the localisation band. It is, therefore, desirable to incorporate the essential features of the localised deformation in the constitutive equations. This will, in particular, involve the insertion of the width of the localisation band as a length scale into the constitutive model. This issue will be discussed in detail in Chapter 6 through developing a thermodynamics approach which facilitates the modelling of localised deformation in geomaterials in a consistent manner.

The coupled damage-plasticity model developed in this chapter exhibits a remarkable capability in predicting the macroscopic behaviour of porous rocks. However, this model does not directly take into account the micromechanisms of deformation and energy dissipation. Therefore, the proposed model is unable to explain the different microstructural evolutions (grain crushing, pore collapse, etc.) which take place in porous rocks during inelastic deformation. This is acknowledged as a weakness of the proposed approach. However, it should be noted that the focus of this model development is on capturing the overall macroscopic mechanical behaviour and the localisation of deformation under a wide range of confining pressure.

CHAPTER 5

A Coupled Damage-Plasticity Model for Compact Rocks

5.1. Introduction

At room temperature, compact rocks mostly exhibit brittle behaviour even under substantially high confining pressure. In addition, compact rocks often exhibit dilatancy prior to macroscopic fracture when the rock is loaded under conditions conducive to brittle fracture. Dilatancy can be attributed to the occurrence of pervasive micro-cracking prior to the macroscopic failure. Nevertheless, in some compact rocks, such as quartzite, norite and marble, dilational behaviour begins prior to the peak force and continues markedly also in the post-peak region (see e.g. [29, 253-255]). The effect of confining pressure on the magnitude of dilatancy prior to macroscopic fracture varies considerably from one type of rock to another. In this sense, while an increase in confining pressure causes a diminution in dilatancy in porous rocks, such as dolomite and sandstone [256, 257], it does not give rise to a marked decrease in dilatancy in compact rocks like marble and granite [258].

In this chapter, a coupled damage-plasticity model is developed to describe the mechanical behaviour of compact, non-porous rocks, in particular, the marked dilational behaviour commonly observed in these rocks in the brittle field. Under compressive loading, unlike the pore collapse phenomenon in porous rocks which causes the specimen to compact, it is envisaged that micro-crack opening, either in the form of tension cracks or wing cracks, gives rise, to a dilational response at the macroscopic scale. Accordingly, the focal point of the constitutive modelling in the current chapter is to capture the damage-induced dilation. The thermodynamic formulation presented in this chapter shares many essential features with that presented in Chapter 4 for modelling the behaviour of porous rocks. The main improvement here is to enhance the model by incorporating the kinematics of elastoplastic-damage deformation, in particular, damage-induced volumetric deformations, by means of kinematic

constraint equations as outlined in Chapter 3.

5.2. Definitions and Basic Assumptions

Under compressive loading conditions conducive to post-peak softening behaviour or brittle failure, the initiation and propagation of microcracks within the structure of compact rocks, are predominantly parallel to the direction of the maximum principal stress [99, 258-264]. In general, these microcracks can be assumed to be either in the form of axial splitting tension microcracks (Mode I) [265-268] or in the form of shear wing microcracks (Mode II) [269-273] (Figure 5.1). Furthermore, in triaxial compression, the observed increase in linear compressibility of rock specimens in the lateral direction [258] further implies that the opening microcracks are predominantly oriented parallel to the specimen axis. These observations imply that the damage-induced deformations are dilative in nature. Therefore, considering a representative volume element (RVE) of a damaged specimen in compressive loading, the macroscopic volumetric deformation is a combination of a dilative damage-induced deformation and the volumetric deformation of the solid or intact volume fraction which can be either dilative or contractive.

As was previously discussed in Chapter 4, in porous rocks the dilational effects of damage growth within the cement matrix is compensated for by pore collapse phenomenon, which may even take place under very low pressures [25, 27, 92]. Therefore, the mode of volumetric deformation (dilative/contractive) of porous rocks is mainly determined through a competition between damage processes and the pore collapse phenomenon. In compact or non-porous rocks, however, due to the lack of enough pore space, micro-cracking (or damage) is the predominate mechanism which governs the mode of volumetric deformation. These underlying mechanisms of volumetric deformation are schematically depicted in Figure 5.1. It should be noted that this discussion is, for now, restricted to underlying mechanisms responsible for dilational volumetric deformation under low confining pressure, where no significant inelastic intragranular deformation (e.g. crystal plasticity and grain crushing) is expected to take place.

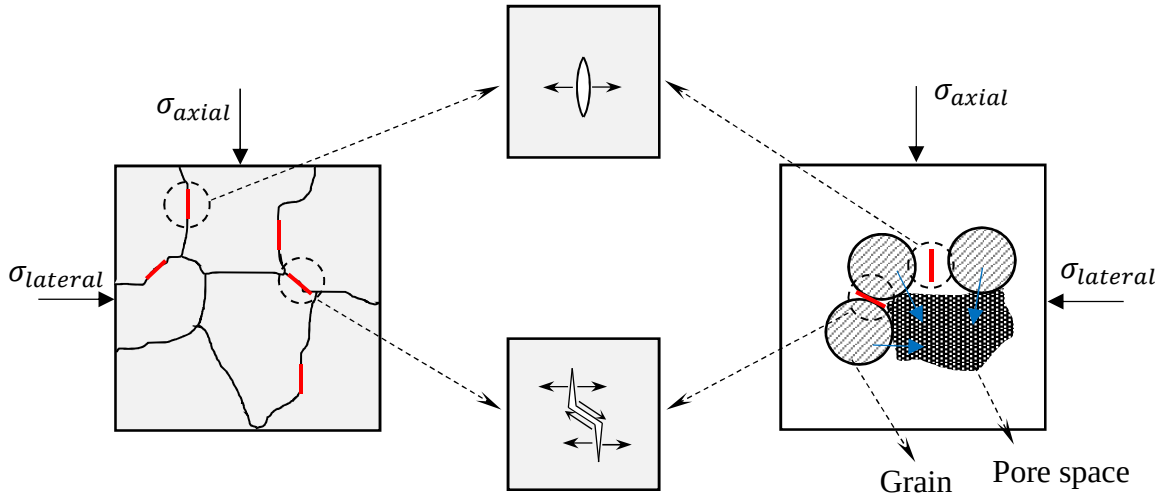

Figure 5.1: Schematic comparison of microstructure of porous (right) and compact rocks (left): the underlying mechanisms that influence the mode of volumetric behaviour (pore collapse axial splitting and shear wing cracks).

During compressive loading of compact rocks, a part of the energy budget is stored within the solid grains and some of the energy is dissipated due to micro-crack initiation and frictional sliding between the surfaces of micro-cracks. During unloading, the elastically compressed grains tend to expand and give up their elastic energy. This elastic expansion is accompanied by micro-crack closure due to the relative movement of neighbouring grains. This relative movement is either normal (in the case of axial splitting cracks) or tangential (in the case of shear wing cracks) to the micro-crack surfaces. As was pointed out earlier in Chapter 4, using a simple sawtooth mechanism, shear sling between the two rough surfaces of micro-cracks may give rise to dilation which further encourages the release of the stored elastic energy. However, not all micro-crack can be completely closed or slide back to their initial configuration. This may occur due to the presence of rock fragments between the two faces of micro-cracks or due to asperity interlocking or crack miss-fit [274, 275] (Figure 5.2). Under such conditions, some of the stored elastic energy cannot be released during unloading and will be trapped within the material. In addition, micro-cracks which are locked open cause some permanent dilation to the material element. In this study, this permanent dilational deformation is referred to as damage-induced dilation.

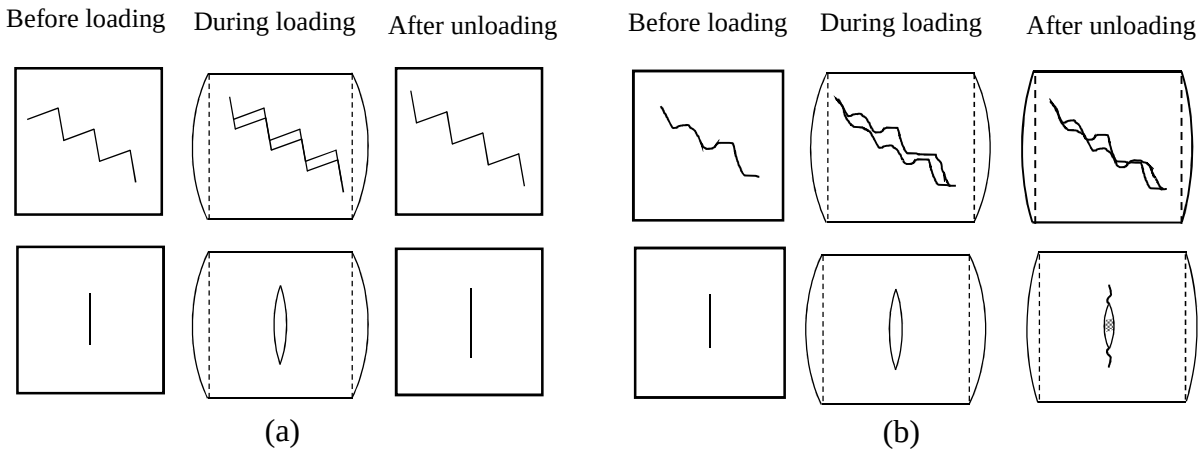

Figure 5.2: Schematic demonstration of (a) reversible damage-induced deformation and (b) irreversible damage-induced deformation.

The macroscopic reversible deformation of an RVE of a compact rock (ε^r) can be assumed to consist of a reversible damage-induced deformation (ε^{Dr}) and an elastic deformation (ε^e) in the solid material (Figure 5.3). The reversible part of the damage-induced deformation (ε^{Dr}) can be directly obtained from macroscopic experiments, regarding the effect of damage on the material stiffness degradation (Figure 5.3). However, the irreversible part of the damage-induced deformation (ε^{Di}) cannot be, in general, measured directly from purely macroscopic experiments. In fact, ε^{Di} is encapsulated within the macroscopic irreversible strain which refers to that part of the strain which remains when the stress is returned to its original value. This macroscopic residual strain is commonly represented by plastic strain ε^p. This study, however, distinguishes between the irrecoverable damage-induced deformations and the permanent deformations caused by other underlying mechanisms (e.g. crystal plasticity, frictional sliding, etc.). Furthermore, as illustrated in Figure 5.3, due to the existence of irreversible damage-induced deformations (ε^{Di}) it seems that the material requires less amount of elastic energy to be loaded to the same stress state form which unloading started. This is because some elastic energy is already trapped within the material due to the presence of micro-cracks which are locked open. Therefore, the irreversible damage-induced deformation (ε^{Di}) can be interpreted as that part of the plastic strain which influences the instantaneous elastic moduli. Although the damage process is an irreversible, dissipative process, damage induced deformations can be partially or completely recovered upon unloading, due to micro-cracks closure. Nevertheless, it should be noted that the recovery of damage induced deformation does not mean the healing of damage.

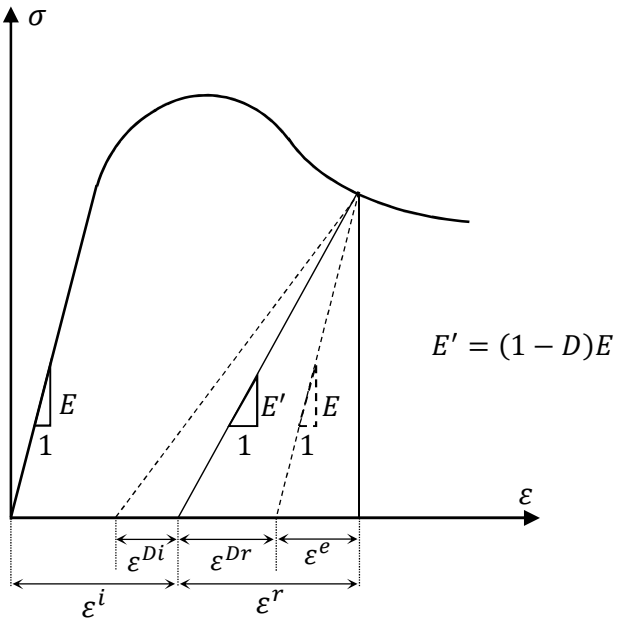

Figure 5.3: Schematic representation of elastoplastic-damage deformations for uniaxial loading

In almost all coupled damage-plasticity models (including the model developed in Chapter 4) only the effect of reversible damage-induced deformations (ε^{Dr}) on the instantaneous elastic moduli is taken into account. Hence, it is implicitly assumed in these models that the instantaneous elastic moduli are not affected by any type of irreversible deformation. Since the irreversible strains are usually represented by plastic strains, these models can be referred to as elasto-plastically decoupled models (see [191]). Neglecting the effects of irreversible damage-induced deformation on the instantaneous elastic moduli may renders the model inadequate in describing the volumetric deformations of non-porous, quasi-brittle materials. From the phenomenological point of view, tuning the parameters of such a model can help reproduce the experimentally observable dilation behaviour of compact rock under shearing at high confining pressure. Therefore, it is necessary to address the elasto-plastic coupling by specifying the effects of irreversible damage-induced deformations on the instantaneous elastic moduli.

In this chapter, however, it is demonstrated that an alternative approach can be adopted to take into account the effect of irreversible damage-induced deformation, especially, on the mode of volumetric deformation of non-porous compact rocks. To this end, the model is kept elasto-plastically decoupled, while the effects of irreversible damage-induced deformations are taken into account through specifying the role they play in trapping the elastic energy within the material. For this purpose, the evolution rule of the irreversible

damage-induced deformation (ε^{Di}) is explicitly specified and incorporated in the model formulation through introducing a kinematic constraint equation which is, subsequently, used to supplement the dissipation function. Apart from successfully capturing the observed volumetric deformation of compact rocks, the proposed coupled damage-plasticity model can also serve as an example to demonstrate how new internal variables can be introduced into the formulation of constitutive models by means of kinematic constraint equations.

5.3. Thermodynamic formulation

In this section, aiming to describe the macroscopic behaviour of compact rocks, a detailed thermodynamic formulation of a coupled-damage plasticity model is presented, using the notations appropriate for triaxial tests. The definitions of the pressure or the mean stress, p, the deviatoric stress, q, the volumetric and equivalent shear strain (ε_v and ε_s) are given in Table 4.1. Throughout the model formulation in this section, all reversible deformations are referred to as elastic deformations and are denoted as ε^e. In addition, all irreversible deformations are denoted by the plastic strain, ε^p, noting that they also include the irreversible damage-induced deformations ε_v^{Di}.

5.3.1. The free energy potential and the dissipation rate function

The Helmholtz energy function for an elasto-plastically decoupled model can be written as the sum of reversible and irreversible parts:

$$\Psi = \Psi^r(D, \varepsilon_v^e, \varepsilon_s^e) + \Psi^{ir}\left(\varepsilon_v^p, \varepsilon_s^p, \varepsilon_v^{Di}\right) \tag{5.1}$$

In the above expression, Ψ^r is a function of damage and elastic strains and Ψ^{ir} is a function of plastic and irreversible damage-induced deformation. In equation (5.1), the second term (Ψ^{ir}) represents that part of the plastic work which is stored within the material and dose not contribute to dissipation. Under isotropic compression, from the volumetric plastic work increment (δW_v^p) done on a unit volume of material, some part is dissipated ($\delta\Phi_v$) and some is stored ($\rho\dot{\varepsilon}_v^p$) within the material:

$$\delta W_v^p = \delta\Phi_v + \rho\dot{\varepsilon}_v^p = \chi_v\dot{\varepsilon}_v^p + \rho\dot{\varepsilon}_v^p \tag{5.2}$$

where χ_v is the dissipative part of the internal force conjugate to ε_v^p and ρ is the back stress. The existence of the stored plastic work can be attributed to the non-homogeneous stress distribution at micro-scale due to inherent inhomogeneity of the material [225]. One can assume that the shear plastic work is completely dissipative, i.e. $\delta W_s^p = q\dot{\varepsilon}_s^p = \delta\Phi_s =$

$\chi_s \dot{\varepsilon}_s^p$. This could be true if the shearing does not induce dilation. In the presence of shear-induced dilation some of the stored plastic work can be released (the sawtooth mechanism presented in Chapter 4). This released plastic work should be subtracted from the total shear plastic work:

$$\delta W_s^p = \delta \Phi_s - \rho \dot{\varepsilon}_v^{ps} = \chi_s \dot{\varepsilon}_s^p - \rho \dot{\varepsilon}_v^{ps} \tag{5.3}$$

In the above expression, χ_s is the dissipative part of internal forces conjugate to ε_s^p. Following the same description as that presented in Chapter 4, it is assumed that shear-induced dilation can take place only due to the shear-sliding along the surfaces of micro-cracks. Therefore, the increment of the shear induced-dilation ($\dot{\varepsilon}_v^{ps}$) is defined as:

$$\dot{\varepsilon}_v^{ps} = -\mu(D) \dot{\varepsilon}_s^p \tag{5.4}$$

In the above expression, D represents the scalar damage variable. Therefore, the shear plastic work increment of equation (5.3) can be rewritten as:

$$\delta W_s^p = \chi_s \dot{\varepsilon}_s^p + \mu(D) \rho \dot{\varepsilon}_s^p \tag{5.5}$$

The definition of the function $\mu(D)$ is given (the same as that given in Chapter 4) by:

$$\mu(D) = D^a (1 - D) \mu_0 \tag{5.6}$$

where μ_0 and a are dimensionless parameters. As was discussed in the previous section, in contrast to the shear-induced dilation, $\varepsilon_v^{ps} = -\mu(D) \varepsilon_s^p$, which causes some of the stored elastic energy to be released, the irreversible damage-induced volumetric deformation cause the elastic energy to be trapped within the material. Therefore, the volumetric plastic work increment (δW_v^p), given by equation (5.2), can be modified to:

$$\delta W_v^p = \delta \Phi_v + \rho \dot{\varepsilon}_v^p = \chi_v \dot{\varepsilon}_v^p + \rho \left(\dot{\varepsilon}_v^p + \dot{\varepsilon}_v^{pD} \right) \tag{5.7}$$

The increment of damage-induced dilation, $\dot{\varepsilon}_v^{pD}$, can be defined as:

$$\dot{\varepsilon}_v^{pD} = -f(D) \dot{\varepsilon}_v^{Di} \tag{5.8}$$

In the above expression, function $f(D)$ is a function of the scalar damage variable. It is assumed that the possibility for the irreversible damage-induced dilation to take place increases as damage grows within the material. Therefore, function $f(D)$ can be defined as a monotonically increasing function of the scalar damage variable. In the context of this

study, it will be shown that the following definition of $f(D)$ would result in adequately predicting the macroscopic behaviour of compact rocks:

$$f(D) = \sqrt{D} \tag{5.9}$$

Following the above discussion, and by virtue of equations (5.5), (5.7) and (5.8), that part of the total plastic work increment that is stored within the material and does not contribute to dissipation can be given as:

$$(\delta W^p)^{stored} = \Psi^{ir} = \rho\left(\dot{\varepsilon}_v^p + \mu(D)\dot{\varepsilon}_s^p - f(D)\dot{\varepsilon}_v^{Di}\right) \tag{5.10}$$

The expression of the Helmholtz free energy potential is, therefore, given as:

$$\Psi = \Psi^r + \Psi^{ir} = \frac{1}{2}(1-D)\left[K\varepsilon_v^{e2} + 3G\varepsilon_s^{e2}\right] + \rho\left(\varepsilon_v^p + \mu(D)\varepsilon_s^p - f(D)\varepsilon_v^{Di}\right) \tag{5.11}$$

In the above expression K and G are the material bulk and shear moduli, ε_v and ε_s are volumetric and equivalent shear strains, respectively, and D and ε_v^{Di} are the scalar damage variable and the irreversible damage-induced dilation, respectively.

Another thermodynamic function that needs to be specified to complete the formulation is the dissipation function. For a coupled damage-plasticity model the following form of the dissipation function is adopted [144, 189]:

$$\delta\Phi = \sqrt{{\varphi_v}^2 + {\varphi_s}^2 + {\varphi_D}^2} \geq 0 \tag{5.12}$$

In the above expression, φ_v, φ_s and φ_D are homogeneous first order functions in terms of the rates of internal variables, representing the contribution of each individual dissipative mechanism in the total dissipation rate (see [189]). Hence, the interaction between damage and plasticity is specified by controlling the amount of available energy budget being dissipated due to each mechanism. Furthermore, the definition of functions φ_v, φ_s and φ_D are given as follows:

$$\varphi_v = F_v\left(\dot{\varepsilon}_v^p + \mu(D)\dot{\varepsilon}_s^p + f(D)\dot{\varepsilon}_v^{Di}\right) \tag{5.13}$$

$$\varphi_s = F_s\dot{\varepsilon}_s^p \tag{5.14}$$

$$\varphi_D = F_D\dot{D} \tag{5.15}$$

Within the framework of generalised thermodynamics evolution rules for internal variables are specified using the formulation of the yield function in dissipative stress space. This yield function is obtained by performing a degenerate Legendre transform on the

dissipation function. However, in this study, in order to simplify the model formulation and also to provide an example of the application of the kinematic constraint equations, the evolution of the irreversible damage-induced dilation ($\dot{\varepsilon}_v^{Di}$) is explicitly defined as a function of the damage increment ($\dot{D}$). This function is then used to form a constraint equation which will be used to supplement the dissipation function. For this purpose, information from experimental observations of macroscopic behaviour of compact rocks can be used. In particular, compact rocks exhibit dilational behaviour even at pressures beyond the brittle-ductile transition. In addition, at high pressure, due to the stabilising effect of confining pressure on micro-crack growth, damage evolution is slow, whereas at low pressure damage grows at higher rate. Therefore, the following expression is proposed for the increment of the irreversible damage-induced dilation ($\dot{\varepsilon}_v^{Di}$):

$$\dot{\varepsilon}_v^{Di} = \frac{\beta p}{\rho}\dot{D} \tag{5.16}$$

where β is a dimensionless fitting parameter. It should also be noted that the definition of equation (5.16) is not unique and any form of this function can be proposed. However, as will be shown later the proposed evolution rule, given by equation (5.16) helps to adequately describe the macroscopic behaviour of compact rocks. Although the main purpose here is to provide an example of the application of kinematic constraint equations, this simplification in the model formulation is acknowledged as a weakness of this model. By virtue of equation (5.17) the definition of the function φ_v, given by equation (5.13), can be modified and rewritten as follows:

$$\varphi_v = F_v\left(\dot{\varepsilon}_v^p + \mu\dot{\varepsilon}_s^p + f(D)\frac{\beta p}{\rho}\dot{D}\right) \tag{5.17}$$

Furthermore, the evolution rule of equation (5.16) along with other kinematic dependencies, i.e. decomposition of the macroscopic strains, can be incorporated in the model formulation through defining the following set of kinematic constraint equations:

$$C_1 = \dot{\varepsilon}_v - \dot{\varepsilon}_v^e - \dot{\varepsilon}_v^p = 0 \tag{5.18}$$

$$C_2 = \dot{\varepsilon}_s - \dot{\varepsilon}_s^e - \dot{\varepsilon}_s^p = 0 \tag{5.19}$$

$$C_3 = \dot{\varepsilon}_v^{Di} - \frac{\beta p}{\rho}\dot{D} = 0 \tag{5.20}$$

The above constraint equations are used to supplement the dissipation function of equation (5.12) to give:

$$\delta\Phi' = \sqrt{{\varphi_v}^2 + {\varphi_s}^2 + {\varphi_D}^2} + \Lambda_i C_i \geq 0 \qquad i = 1 \dots 3 \tag{5.21}$$

Using the thermodynamics principles, outlined in Chapter 3, and the definition of two scalar thermodynamic functions of equations (5.11) and (5.21) the following set of equations ensues:

$$p = \frac{\partial\Psi}{\partial\varepsilon_v} + \frac{\partial\delta\Phi'}{\partial\dot{\varepsilon}_v} = \frac{\partial\Psi}{\partial\varepsilon_v} + \frac{\partial\delta\Phi}{\partial\dot{\varepsilon}_v} + \Lambda_i \frac{\partial C_i}{\partial\dot{\varepsilon}_v} = \Lambda_1 \qquad i = 1 \dots 3 \tag{5.22}$$

$$q = \frac{\partial\Psi}{\partial\varepsilon_s} + \frac{\partial\delta\Phi'}{\partial\dot{\varepsilon}_s} = \frac{\partial\Psi}{\partial\varepsilon_s} + \frac{\partial\delta\Phi}{\partial\dot{\varepsilon}_s} + \Lambda_i \frac{\partial C_i}{\partial\dot{\varepsilon}_s} = \Lambda_2 \tag{5.23}$$

$$0 = \frac{\partial\Psi}{\partial\varepsilon_v^e} + \frac{\partial\delta\Phi'}{\partial\dot{\varepsilon}_v^e} = \frac{\partial\Psi}{\partial\varepsilon_v^e} + \frac{\partial\delta\Phi}{\partial\dot{\varepsilon}_v^e} + \Lambda_i \frac{\partial C_i}{\partial\dot{\varepsilon}_v^e} = (1-D)K\varepsilon_v^e - \Lambda_1 \tag{5.24}$$

$$0 = \frac{\partial\Psi}{\partial\varepsilon_s^e} + \frac{\partial\delta\Phi'}{\partial\dot{\varepsilon}_s^e} = \frac{\partial\Psi}{\partial\varepsilon_s^e} + \frac{\partial\delta\Phi}{\partial\dot{\varepsilon}_s^e} + \Lambda_i \frac{\partial C_i}{\partial\dot{\varepsilon}_s^e} = 3(1-D)G\varepsilon_s^e - \Lambda_2 \tag{5.25}$$

From equations (5.22) and (5.23) the Lagrangian multipliers Λ_1, Λ_2 are calculated as follows:

$$\Lambda_1 = p \tag{5.26}$$

$$\Lambda_2 = q \tag{5.27}$$

Substituting equations (5.26) and (5.27) into equations (5.24) and (5.25), respectively, and also making use of equations (5.18) and (5.19), the mean and deviatoric stresses are given as follows:

$$p = (1-D)K\varepsilon_v^{eD} = (1-D)K\left(\varepsilon_v - \varepsilon_v^p\right) \tag{5.28}$$

$$q = 3(1-D)G\varepsilon_s^{eD} = 3(1-D)G\left(\varepsilon_s - \varepsilon_s^p\right) \tag{5.29}$$

Furthermore, in order to derive the dissipative part of internal forces, χ_v and χ_s, and the conjugate damage energy, χ_D, the following set of equations can be written by applying the standard thermodynamic principles, as outlined in Chapter 3:

$$0 = \frac{\partial\Psi}{\partial\varepsilon_v^p} + \frac{\partial\delta\Phi'}{\partial\dot{\varepsilon}_v^p} = \frac{\partial\Psi}{\partial\varepsilon_v^p} + \frac{\partial\delta\Phi}{\partial\dot{\varepsilon}_v^p} + \Lambda_i \frac{\partial C_i}{\partial\dot{\varepsilon}_v^p} = \rho + \chi_v - \Lambda_1 \qquad i = 1 \dots 3 \tag{5.30}$$

$$0 = \frac{\partial\Psi}{\partial\varepsilon_s^p} + \frac{\partial\delta\Phi'}{\partial\dot{\varepsilon}_s^p} = \frac{\partial\Psi}{\partial\varepsilon_s^p} + \frac{\partial\delta\Phi}{\partial\dot{\varepsilon}_s^p} + \Lambda_i \frac{\partial C_i}{\partial\dot{\varepsilon}_s^p} = \mu\rho + \chi_s - \Lambda_2 \tag{5.31}$$

$$0 = \frac{\partial\Psi}{\partial\varepsilon_v^{Di}} + \frac{\partial\delta\Phi'}{\partial\dot{\varepsilon}_v^{Di}} = \frac{\partial\Psi}{\partial\varepsilon_v^{Di}} + \frac{\partial\delta\Phi}{\partial\dot{\varepsilon}_v^{Di}} + \Lambda_i \frac{\partial C_i}{\partial\varepsilon_v^{Di}} = -\rho f(D) + \Lambda_3 \tag{5.32}$$

$$0 = \frac{\partial \Psi}{\partial D} + \frac{\partial \delta \Phi'}{\partial \dot{D}} = \frac{\partial \Psi}{\partial D} + \frac{\partial \delta \Phi}{\partial \dot{D}} + \Lambda_i \frac{\partial C_i}{\partial \dot{D}} = -\frac{1}{2}\left(K\varepsilon_v^{e\,2} + 3G\varepsilon_s^{e\,2}\right) + \rho\varepsilon_s^p \frac{d\mu(D)}{dD} - \rho\varepsilon_v^{Di}\frac{df(D)}{dD} + \chi_D - \frac{\beta p}{\rho}\Lambda_3 \tag{5.33}$$

From equations (5.32) the Lagrangian multipliers Λ_3 is obtained as:

$$\Lambda_3 = \rho f(D) \tag{5.34}$$

Furthermore, by substitution of equations (5.26) and (5.27) into equations (5.30) and (5.31), respectively, the dissipative parts of internal forces are given as:

$$\chi_v = p - \rho \tag{5.35}$$

$$\chi_s = q - \mu\rho \tag{5.36}$$

Also, from equation (5.33) and by virtue of equations (5.28), (5.29) and (5.34), the conjugate damage energy is obtained as:

$$\chi_D = \frac{p^2}{2K(1-D)^2} + \frac{q^2}{6G(1-D)^2} - \rho\varepsilon_s^p \frac{d\mu(D)}{dD} + \frac{df(D)}{dD}\rho\varepsilon_v^{Di} + f(D)\beta p \tag{5.37}$$

5.3.2. The yield function

The definition of the dissipation function of equation (5.12) results in the existence of a single generalised yield function which controls the simultaneous evolution of damage and plasticity. Following the principles of generalised thermodynamics, by performing a degenerate Legendre transformation on the dissipation rate function the yield function in the generalised dissipative stress space can be given as a function of the dissipative stresses and the conjugate damage energy. By making use of Ziegler's orthogonality principle for rate-independent behaviour the following relations ensues (see Sections 3.2.2 and 3.2.3):

$$\chi_v = \frac{\partial \delta\Phi}{\partial \dot{\varepsilon}_v^p} = \frac{\partial \delta\Phi}{\partial \varphi_v}\frac{\partial \varphi_v}{\partial \dot{\varepsilon}_v^p} = \frac{\varphi_v}{\sqrt{{\varphi_v}^2 + {\varphi_s}^2 + {\varphi_D}^2}}\frac{\partial \varphi_v}{\partial \dot{\varepsilon}_v^p} \tag{5.38}$$

$$\chi_s = \frac{\partial \delta\Phi}{\partial \dot{\varepsilon}_s^p} = \frac{\partial \delta\Phi}{\partial \varphi_s}\frac{\partial \varphi_s}{\partial \dot{\varepsilon}_s^p} + \frac{\partial \delta\Phi}{\partial \varphi_v}\frac{\partial \varphi_v}{\partial \dot{\varepsilon}_s^p} = \frac{\varphi_s}{\sqrt{{\varphi_v}^2 + {\varphi_s}^2 + {\varphi_D}^2}}\frac{\partial \varphi_s}{\partial \dot{\varepsilon}_s^p} + \frac{\varphi_v}{\sqrt{{\varphi_v}^2 + {\varphi_s}^2 + {\varphi_D}^2}}\frac{\partial \varphi_v}{\partial \dot{\varepsilon}_s^p} \tag{5.39}$$

$$\chi_D = \frac{\partial \delta\Phi}{\partial \dot{D}} = \frac{\partial \delta\Phi}{\partial \varphi_D}\frac{\partial \varphi_D}{\partial \dot{D}} + \frac{\partial \delta\Phi}{\partial \varphi_v}\frac{\partial \varphi_v}{\partial \dot{D}} = \frac{\varphi_D}{\sqrt{{\varphi_v}^2 + {\varphi_s}^2 + {\varphi_D}^2}}\frac{\partial \varphi_D}{\partial \dot{D}} + \frac{\varphi_v}{\sqrt{{\varphi_v}^2 + {\varphi_s}^2 + {\varphi_D}^2}}\frac{\partial \varphi_v}{\partial \dot{D}} \tag{5.40}$$

Therefore, by making use of equations (5.38) – (5.40), the general form of the yield function, (see Section 3.5), of the coupled damage-plasticity model in the dissipative stress space is given as:

$$y^* = \left(\frac{\chi_v}{\partial\varphi_v/\partial\dot{\varepsilon}_v^p}\right)^2 + \left(\frac{\chi_s - \chi_v\left(\frac{\partial\varphi_v/\partial\dot{\varepsilon}_s^p}{\partial\varphi_v/\partial\dot{\varepsilon}_v^p}\right)}{\partial\varphi_s/\partial\dot{\varepsilon}_s^p}\right)^2 + \left(\frac{\chi_D - \chi_v\left(\frac{\partial\varphi_v/\partial\dot{D}}{\partial\varphi_v/\partial\dot{\varepsilon}_v^p}\right)}{\partial\varphi_D/\partial\dot{D}}\right)^2 - 1 \leq 0 \qquad (5.41)$$

By virtue of equations (5.14), (5.15) and (5.17), the above expression can be simplified to give:

$$y^* = \left(\frac{\chi_v}{F_v}\right)^2 + \left(\frac{(\chi_s - \mu(D)\chi_v)}{F_s}\right)^2 + \left(\frac{(\chi_D - f(D)\beta p\chi_v/\rho)}{F_D}\right)^2 - 1 \leq 0 \qquad (5.42)$$

As was discussed earlier in Section 4.3.2, in order to obtain a closed teardrop-shaped yield surface in true stress space, the definitions of functions F_v, F_s and F_D which appear in the formulation of the yield function in the dissipative stress space (equation (5.42)) are proposed as follows:

$$F_v = \frac{1}{r_v}\left(\frac{(1-\gamma)p_c - p_t}{(1-D)(p_c + p_t)}p + \frac{\gamma}{2}p_c\right) \qquad (5.43)$$

$$F_s = \frac{M}{r_s}\left(p - \alpha\sqrt{(1-D)}(p-\rho)\right) \qquad (5.44)$$

$$F_D = \frac{\chi_D - f(D)\beta p\chi_v/\rho}{\sqrt{({r_D}^2 + {r_s}^2)\left(\frac{\chi_v}{r_v F_v}\right)^2 + ({r_D}^2 + {r_v}^2)\left(\frac{\chi_s - \mu(D)\chi_v}{r_s F_s}\right)^2}} \qquad (5.45)$$

Therefore, by substituting the above expression into the equation of yield function in dissipative stress space (equation (5.42)) and by making use of equations (5.35) and (5.36) the formulation of the yield function in true stress space is given as:

$$y = ({r_v}^2 + {r_s}^2 + {r_D}^2)\left[\left(\frac{p-\rho}{\frac{(1-\gamma)p_c - p_t}{(1-D)(p_c+p_t)}p + \frac{\gamma}{2}p_c}\right)^2 + \left(\frac{q - \mu(D)p}{M\left(p - \alpha\sqrt{(1-D)}(p-\rho)\right)}\right)^2\right] - 1 \leq 0 \qquad (5.46)$$

In order to restrict the effects of parameters r_v, r_s and r_d to the flow rules of the model and eliminate their effect on the shape of the yield surface in true stress space, similar approach

to that adopted in Chapter 4 is also adopted here by imposing $r_v^2 + r_s^2 + r_D^2 = 1$. Therefore, the expression of the initial yield surface in true stress space can be rewritten as follows:

$$y = \left(\frac{p - \rho}{\frac{(1-\gamma)p_c - p_t}{(1-D)(p_c + p_t)} p + \frac{\gamma}{2} p_c} \right)^2 + \left(\frac{q - \mu(D)p}{M\left(p - \alpha\sqrt{(1-D)}(p - \rho)\right)} \right)^2 - 1 \leq 0 \tag{5.47}$$

As can be seen from the above equation, the formulation of the yield function in true stress space is the same as that defined for porous rocks in Chapter 4. In this sense, the brittle to ductile response of the proposed coupled damage plasticity model for compact rocks is also captured owing to the evolution of the initial yield surface to a final failure envelope (see Figure 4.4). In the above expressions, parameters α and γ are material constants which control the shape of the yield surface in true stress space. Parameter M represents the slope of the final failure envelope and p_c and p_t are yield stresses under isotropic compression and extension (or decompression), respectively. The shift stress component along χ_v and/or p axes is also defined in terms of p_c, p_t and γ as:

$$\rho = \frac{(4-\gamma)p_c p_t + \gamma {p_c}^2}{2(p_c + p_t)} \tag{5.48}$$

It should be noted that the pivotal difference between the two proposed models for porous and compact rocks, presented in Chapter 4 and the current chapter, respectively, is in the description of energy dissipation and storage of energy within the material. This difference can be clearly seen in the formulation of the yield potentials of the two models in dissipative stress space, as well as their corresponding non-associated flow rules (see also Section 5.3.4). Non-associated flow rules for the coupled damage-plasticity model for compact rocks are discussed in the subsequent Section and also later in Section 5.4.

5.3.3. Non-associated flow rules

As was discussed earlier, within the framework of generalised thermodynamics the evolution rules for the model internal variables are defined using the formulation of the yield potential in generalised dissipative stress space. Therefore, by making use of equation (5.41) and equations (5.14), (5.15) and (5.17), the evolution rules for internal variables in true stress space are given as follows:

$$\dot{\varepsilon}_v^p = \dot{\lambda}\frac{\partial y^*}{\partial \chi_v} = \dot{\lambda}\left[2\frac{\chi_v}{\left(\partial\varphi_v/\partial\dot{\varepsilon}_v^p\right)^2} - 2\left(\frac{\partial\varphi_v/\partial\dot{\varepsilon}_s^p}{\partial\varphi_v/\partial\dot{\varepsilon}_v^p}\right)\left(\frac{\chi_s - \chi_v\left(\frac{\partial\varphi_v/\partial\dot{\varepsilon}_s^p}{\partial\varphi_v/\partial\dot{\varepsilon}_v^p}\right)}{\left(\partial\varphi_s/\partial\dot{\varepsilon}_s^p\right)^2}\right)\right.$$
$$\left. - 2\left(\frac{\partial\varphi_v/\partial\dot{D}}{\partial\varphi_v/\partial\dot{\varepsilon}_v^p}\right)\left(\frac{\chi_D - \chi_v\left(\frac{\partial\varphi_v/\partial\dot{D}}{\partial\varphi_v/\partial\dot{\varepsilon}_v^p}\right)}{\partial\varphi_D/\partial\dot{D}}\right)\right] \tag{5.49}$$
$$= 2\dot{\lambda}\left(\frac{(p-\rho)}{{F_v}^2} - \frac{\mu\,(q-\mu(D)p)}{{F_s}^2} - \frac{f(D)\beta p(\chi_D - \beta p\chi_v/\rho)}{\rho F_D^2}\right)$$

$$\dot{\varepsilon}_s^p = \dot{\lambda}\frac{\partial y^*}{\partial \chi_s} = 2\dot{\lambda}\left(\frac{\chi_s - \chi_v\left(\frac{\partial\varphi_v/\partial\dot{\varepsilon}_s^p}{\partial\varphi_v/\partial\dot{\varepsilon}_v^p}\right)}{\left(\partial\varphi_s/\partial\dot{\varepsilon}_s^p\right)^2}\right) = 2\dot{\lambda}\frac{(q-\mu(D)p)}{{F_s}^2} \tag{5.50}$$

$$\dot{D} = \dot{\lambda}\frac{\partial y^*}{\partial \chi_D} = 2\dot{\lambda}\left(\frac{\chi_D - \chi_v\left(\frac{\partial\varphi_v/\partial\dot{D}}{\partial\varphi_v/\partial\dot{\varepsilon}_v^p}\right)}{\left(\partial\varphi_s/\partial\dot{D}\right)^2}\right) = 2\dot{\lambda}\frac{(\chi_D - f(D)\beta p\chi_v/\rho)}{F_D^2} \tag{5.51}$$

The difference between the volumetric behaviour of the models proposed in Chapter 4 and the current chapter can be clearly seen in equation (5.49). The third term in equation (5.49) arises as a consequence of taking into account the dilational damage-induced deformations. This is, in particular, important for modelling the behaviour of compact rocks, such as marble and granite, as they tend to show a pronounced dilatational behaviour even under high confining pressures beyond the brittle-ductile transition [29, 30, 253-255]. The volumetric behaviour of the model is further discussed through demonstration of the model behaviour in Section 5.5.

5.4. Integration of the Rate Constitutive Equations

For the numerical implementation of the proposed model, it is necessary to specify the integration scheme by means of which stresses are updated for an infinitesimal strain increment. In this section (similar to Section 4.3), the formulation of the tangent stiffness tensor of the proposed coupled damage-plasticity for compact rocks is presented for it is a

pivotal component in localisation analysis. Furthermore, the semi-implicit integration scheme (Section 4.3.2) is used to integrate the rate constitutive equations.

5.4.1. Tangent stiffness tensor

The formulation of tangent stiffness tensor is given in this section since apart from its application in the explicit integration of rate constitutive equations, it is necessary for localisation analysis, presented in the subsequent Sections. For this purpose, the elastic stress tensor, σ_{ij}, is given as:

$$\sigma_{ij} = (1 - D)C_{ijkl}\left(\varepsilon_{kl} - \varepsilon_{kl}^{p}\right) \tag{5.52}$$

From the above damage-elastic constitutive law for the macroscopic stress tensor the increment of the stress tensor is given as:

$$\dot{\sigma}_{ij} = (1 - D)C_{ijkl}\left(\dot{\varepsilon}_{kl} - \dot{\varepsilon}_{kl}^{p}\right) - C_{ijkl}\left(\varepsilon_{kl} - \varepsilon_{kl}^{p}\right)\dot{D} \tag{5.53}$$

In the above expression C_{ijkl} is the elastic stiffness tensor and D is the scalar damage variable. Furthermore, using the chain rule, the rate of the plastic strain tensor is given as follows:

$$\dot{\varepsilon}_{ij}^{p} = \dot{\lambda}\frac{\partial y^{*}}{\partial \chi_{ij}} = \dot{\lambda}\left(\frac{\partial y^{*}}{\partial \chi_{v}}\frac{\partial \chi_{v}}{\partial p}\frac{\partial p}{\partial \sigma_{kl}}\frac{\partial \sigma_{kl}}{\partial \chi_{ij}} + \frac{\partial y^{*}}{\partial \chi_{s}}\frac{\partial \chi_{s}}{\partial q}\frac{\partial q}{\partial \sigma_{kl}}\frac{\partial \sigma_{kl}}{\partial \chi_{ij}}\right) \tag{5.54}$$

The consistency condition for the yield function of equation (5.47) is also written as:

$$\dot{y} = \frac{\partial y}{\partial \sigma_{ij}}\dot{\sigma}_{ij} + \frac{\partial y}{\partial D}\dot{D} = 0 \tag{5.55}$$

By substitution of equation (5.53) into the above expression and making use of the evolution rules of equations (5.49) – (5.51) and also equation (5.54), the damage-plastic multiplier $\dot{\lambda}$ is obtained as:

$$\dot{\lambda} = M_{kl}\dot{\varepsilon}_{kl} \tag{5.56}$$

where the second order tensor M_{kl} is specified by the following expression:

$$M_{kl} = \frac{\dfrac{\partial y}{\partial \sigma_{ij}}(1 - D)C_{ijkl}}{\dfrac{\partial y}{\partial \sigma_{ij}}(1 - D)C_{ijkl}\dfrac{\partial y^{*}}{\partial \chi_{kl}} + \dfrac{\partial y}{\partial \sigma_{ij}}\dfrac{\sigma_{ij}}{(1 - D)}\dfrac{\partial y^{*}}{\partial \chi_{D}} - \dfrac{\partial y}{\partial D}\dfrac{\partial y^{*}}{\partial \chi_{D}}} \tag{5.57}$$

The incremental stress-strain relationship is, therefore, given as:

$$\dot{\sigma}_{ij} = \left[(1-D)C_{ijkl} - (1-D)C_{ijpq}\frac{\partial y^*}{\partial \chi_{pq}}M_{kl} - \frac{\sigma_{ij}}{(1-D)}M_{kl}\frac{\partial y^*}{\partial \chi_D}\right]\dot{\varepsilon}_{kl} = C^T_{ijkl}\dot{\varepsilon}_{kl} \qquad (5.58)$$

where C^T_{ijkl} represents the tangent stiffness tensor.

5.3.2. Semi-implicit stress return algorithm

As was outlined in Section 4.3.2, for a given strain increment, if the trial elastic loading lies outside the current yield furnace, the return process of the semi-implicit integration scheme is activated to return the stresses onto the new yield surface. To this end, the new yield surface is approximated using the first order Taylor expansion as follows:

$$y^{n+1} = y^{trial} + \left.\frac{\partial y}{\partial \sigma_{ij}}\right|^{trial} \Delta\sigma^{re}_{ij} + \left.\frac{\partial y}{\partial D}\right|^{trial} \Delta D = 0 \qquad (5.59)$$

The return stress vector, $\Delta\sigma^{re}_{ij}$, is normal to the trial yield surface (Figure 4.7) and it is given as:

$$\Delta\sigma^{re}_{ij} = -(1-\mathrm{D})C_{ijkl}\left(\Delta\varepsilon^p_{kl}\right) - \Delta D\, C_{ijkl}\left(\varepsilon_{kl} - \varepsilon^p_{kl}\right) \qquad (5.60)$$

Furthermore, substitution of equation (5.60) into equation (5.59) and making use of flow rules of equations (5.49) – (5.51), the increment of the damage-plastic multiplayer $\Delta\lambda$ is given as follows:

$$\Delta\lambda = \frac{y^{trial}}{\frac{\partial y}{\partial \sigma_{ij}}\left((1-D)C_{ijkl}\left(\frac{\partial y^*}{\partial \chi_{kl}}\right) + \frac{\sigma_{ij}}{(1-D)}\left(\frac{\partial y^*}{\partial \chi_D}\right)\right) - \frac{\partial y}{\partial D}\left(\frac{\partial y^*}{\partial \chi_D}\right)} \qquad (5.61)$$

The updated returned stresses are, therefore, obtained as:

$$\sigma^{n+1}_{ij} = \sigma^{trial}_{ij} + \Delta\sigma^{re}_{ij} = \sigma^{trial}_{ij} - (1-\mathrm{D})C_{ijkl}\Delta\lambda\frac{\partial y^*}{\partial \chi_{kl}} - \frac{\sigma_{ij}}{(1-D)}\Delta\lambda\frac{\partial y^*}{\partial \chi_D} \qquad (5.62)$$

5.5. Model Behaviour

In this section, the capacity of the proposed model in capturing some important aspects of the macroscopic behaviour of compact rocks, such as brittle to ductile transition and dilation and compaction, are discussed. Similar to the model for porous rocks presented in Chapter 4, these macroscopic aspects of material response are captured owing to the inherent features of the proposed model, rather than through separately introducing additional hardening and/or softening rules. In particular, it is demonstrated in this section that the proposed coupled damage-plasticity model for compact rocks is capable of capturing

the dilational response of compact rocks even under substantially high confining pressures. This is owing to taking into account the dilational nature of damage-induced deformation in the model formulation.

Similar to the coupled damage-plasticity model for porous rocks (Chapter 4), brittle and ductile responses, as well as the transition from brittle to ductile in the current model is also produced naturally and only due to the transformation of the initial yield surface to a final failure envelope (see Figure 4.8 (a) and (b)) without any need for separately introducing hardening/softening rules. The stress-strain response of the model for a wide range of confining pressures is illustrated in Figure 5.4 (a).

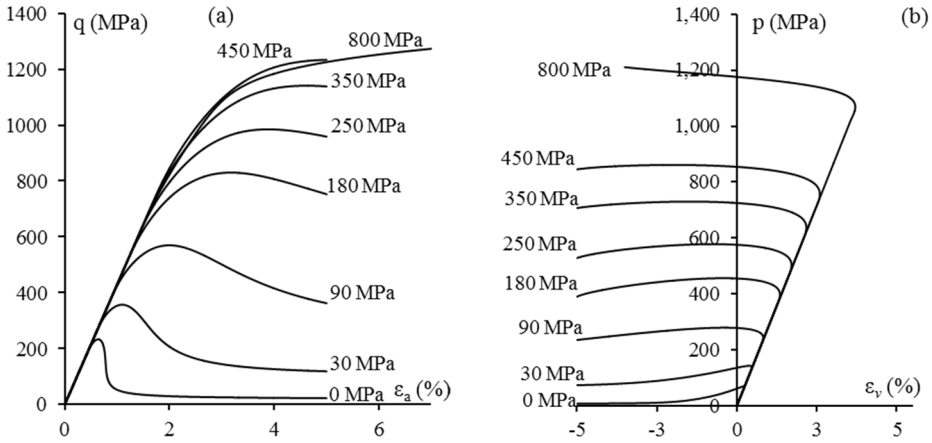

Figure 5.4: Model response; (a) deviatoric stress-axial strain and (b) mean stress-volumetric strain with model input parameters as; E = 40 GPa, v = 0.25, p_c = 1200 MPa, p_t = -12 MPa, M = 1.2, α = 0.5, γ = 0.9, μ_0 = 1.3, $r_v = r_s$ = 0.5

As illustrated in Figure 5.4 (b), the proposed coupled damage-plasticity model for compact rocks is capable of producing dilational behaviour even under substantially high confining pressure, which is characteristic of the mechanical behaviour of the compact rocks. This is due to the incorporation of dilational damage-induced deformations into the model formulation. It can be inferred from equation (5.49) that as damage grows, two dilative mechanisms of deformation start contributing to the irreversible volumetric deformation of the material. One of these mechanisms is the shear-induced dilation, represented by the second term in equation (5.49), noting that the function $\mu(D)$ is defined as a function of damage (equation (5.6)). The second dilational mechanism is the irreversible damage-induced deformation, described by the third term in equation (5.49). The first term in equation (5.49) encapsulates all other mechanisms responsible for irreversible volumetric deformations, which are dilative under low and contractive under high confining pressures. This aspect of the model is illustrated in Figure 5.5, where the plastic flow vector is initially

contractive at 400 MPa confining pressure and it eventually becomes dilative as damage grows within the material. The evolution of the volumetric deformation due to damage evolution is more clearly illustrated in Figure 5.6, where the volumetric deformation is plotted against axial strain, ε_a, and the scalar damage variable, D.

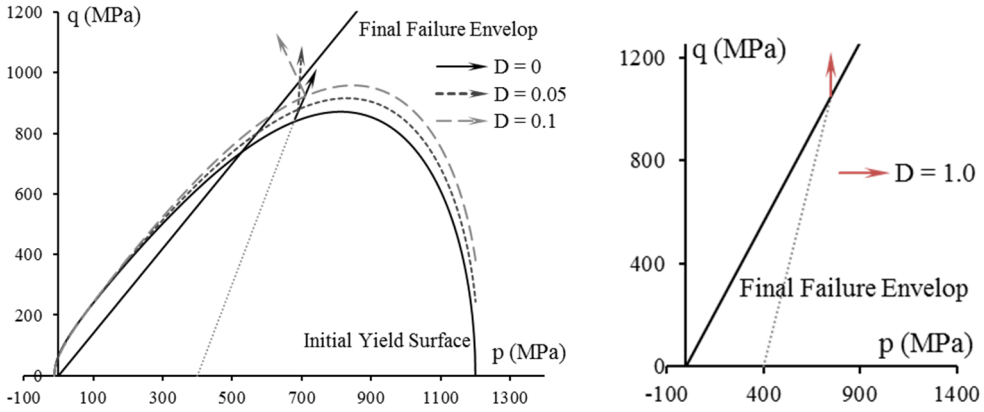

Figure 5.5: Changing the direction of plastic flow vector in true stress space from an initially contractive to a dilational flow due to damage evolution and the dilational nature of damage-induced deformation under triaxial shearing at 400 MPa confining pressure

Under high confining pressure, due to the stabilising effect of confining pressure on micro-crack growth the width of the localisation band increases until the whole volume is damaged uniformly [30, 47-49, 55, 276]. After the uniform spread of micro-cracks throughout the volume element, however, the material may no longer be a solid compact rock and it more resembles a granular domain, which can indeed exhibit compaction under a substantially high confining pressure. It should, however, be noted that unfortunately, no experimental data from hard rocks under substantially high pressure is available to support such intuition and assumption. Further discussion on the identification and calibration of model parameters is presented in Section 5.6.1.

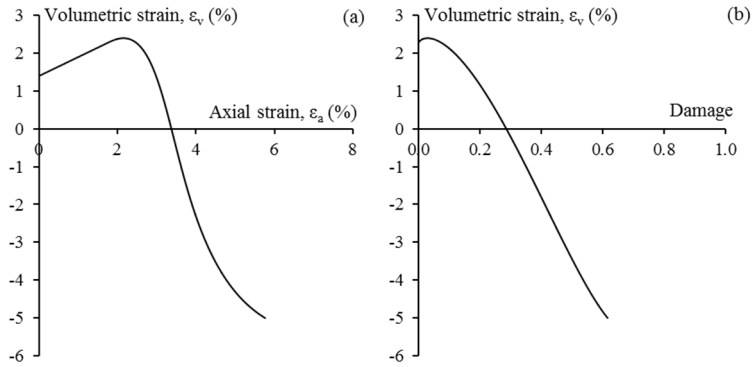

Figure 5.6: Evolution of the volumetric deformation (a) with increasing axial strain and (b) with the evolution of damage under 400 MPa confining pressure with model input parameters as; E = 40 GPa, ν = 0.25, p_c = 1200 MPa, p_t = -12 MPa, M = 1.2, α = 0.5, γ = 0.9, μ_0 = 1.3, r_v = r_s = 0.5

In accordance with the experimental observations, the stabilising effect of the confining pressure on damage growth is also captured by the proposed model. This aspect of model behaviour is illustrated in Figure 5.7.

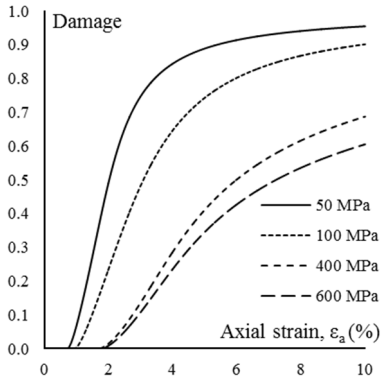

Figure 5.7: The effect of confining pressure on the evolution of the scalar damage variable, D.

5.6. Model Validation at Material Level

In this section, the predictive capability of the proposed model is assessed by comparing the model predictions at the material level with a few sets of experimental data from the drained triaxial test on compact, non-porous rocks (marble and granite [29]) or hard rocks with low porosity (Donbass sandstone [29]). As was discussed in Chapter 4, experimental data sets from rock specimens are not merely representative of the intrinsic material behaviour but they are also affected by structural characteristics of the specimens. Nevertheless, parameters of the proposed model can be adjusted so that in most cases a good agreement between the model predictions and experimental results is obtained, which demonstrates the flexibility and versatility of the proposed model.

5.6.1. Identification of model parameters

Prior to assessing the model performance by comparing it with experimental observations, the influence of each individual parameter on the model behaviour is briefly investigated in this section. The calibration procedure adopted in this section is the same as that outlined and used in Section 4.6.1. As illustrated in Figure 5.8 (a) – (d), for higher values of parameter β the model exhibits a more profound dilative behaviour.

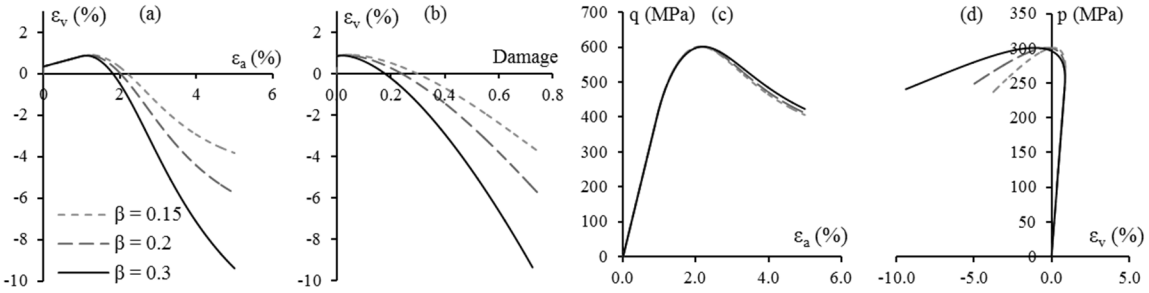

Figure 5.8: The effect of Parameters β on the volumetric response of the model under 100 MPa confining pressure

The effects of parameters r_v, r_s and r_D, on the volumetric response of the proposed model are illustrated in Figure 5.9. Higher values of r_D can be associated with more contribution of damage process to the total dissipation rate or a faster damage growth. Accordingly, for higher values of parameter r_D the model exhibits amore brittle behaviour. Therefore, for a high value of r_D, although the model initially exhibits a more profound dilational behaviour, the dilational response of the model will slow down for larger damage values close to the failure state (Figure 5.9). It should be noted that at final failure state no volumetric deformation takes place (Figure 5.5).

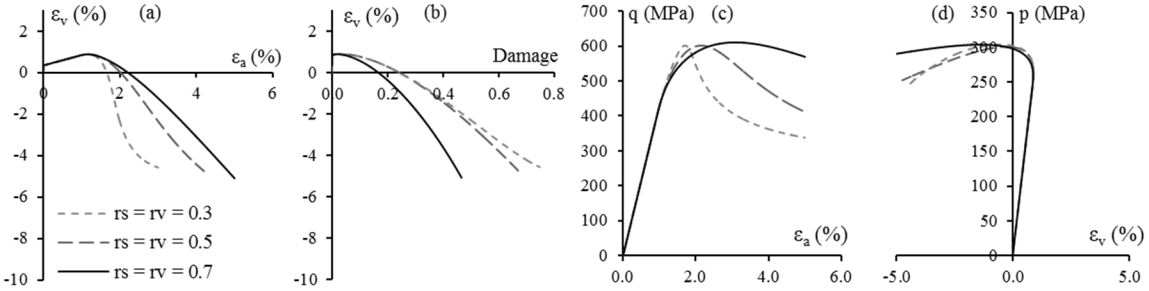

Figure 5.9: The effect of parameters r_v, r_s and r_D on the volumetric behaviour of the model (100 MPa confining pressure)

5.6.2. Parameter calibration and numerical examples

In this section, in order to demonstrate the predictive capability of the coupled damaged plasticity model proposed for compact rocks, the stress-strain response of the model is compared to those obtain from drained triaxial tests on three different rocks, i.e. Donbass sandstone, Karilya granite and Ural marble. Close agreement between the model predictions and observed material response, as illustrated in Figure 5.11 – Figure 5.13, demonstrates the capacity of the model replicating the actual material behaviour. In order to predict the stress-strain response for each rock the model parameters listed in Table 5.1 are used.

Table 5.1: Calibrated values of the model parameters for Kareliya granite, Ural marble and Donbass sandstone [29]

Rock	E (GPa)	ν	P_c (MPa)	P_t (MPa)	α	γ	M	μ_0	β	a	$r_v = r_s$
K. granite	43	0.25	1200	-12	0.45	0.9	1.25	1.2	0.2	0.5	0.5
U. marble	19.5	0.12	500	-10	0.6	0.85	1.2	1.0	0.5	1.0	0.5
D. sandstone	33.5	0.25	710	-7	0.5	0.95	1.15	1.5	0.2	0.5	0.5

The parameters of the initial yield surface (P_c, P_t, γ, α, M, μ_0) are determined and calibrated by finding the best fit between the initial yield surface of the model and the yield stresses measured in experiments (Figure 5.10). It should be noted, however, that these experimental data points are also affected by the structural size and geometry and are not completely representative of intrinsic material behaviour. Nevertheless, the good agreement between the model prediction at the material level and the experimental data demonstrates the flexibility and versatility of the proposed model.

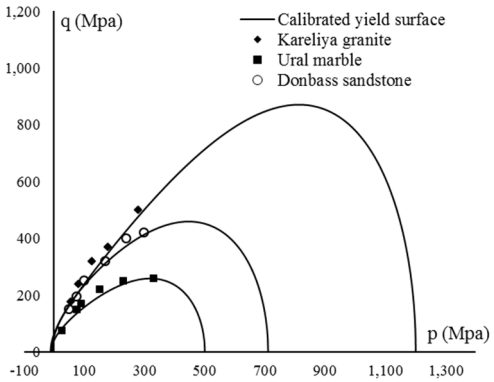

Figure 5.10: Calibration of parameters of the initial yield surface for Kareliya granite, Ural marble and Donbass sandstone [29]

The flexibility of the proposed model and its capability of replicating a wide range of behavioural features, observed in experimental studies on compact rocks, is further highlighted by more closely examining the model performance in predicting the mechanical response of marble (Figure 5.12). In particular, marble continues to dilate even in the hardening regime and at pressures well beyond the brittle-ductile transition. The present coupled damage-plasticity model is capable of capturing such behavioural features owing to the description and incorporation of dilational damage-induced deformation into the model formulation.

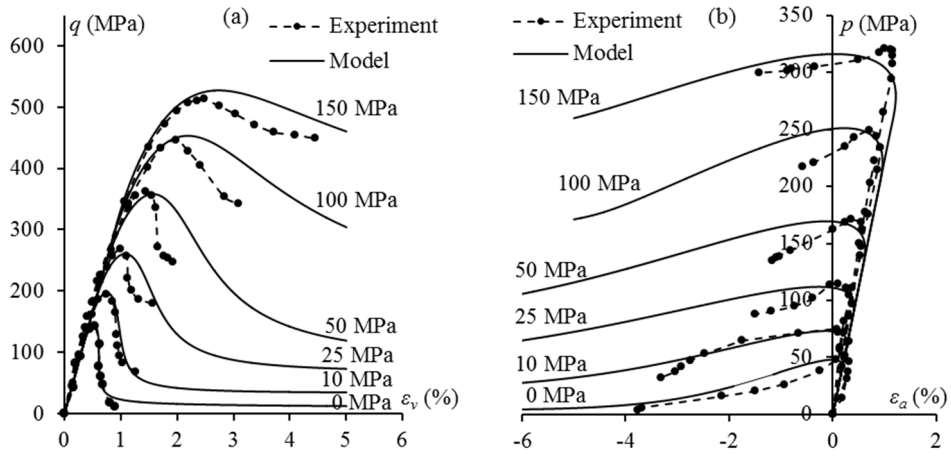

Figure 5.11: Comparison between the model predictions and experimental stress-strain data from drained triaxial test on Donbass sandstone [29]

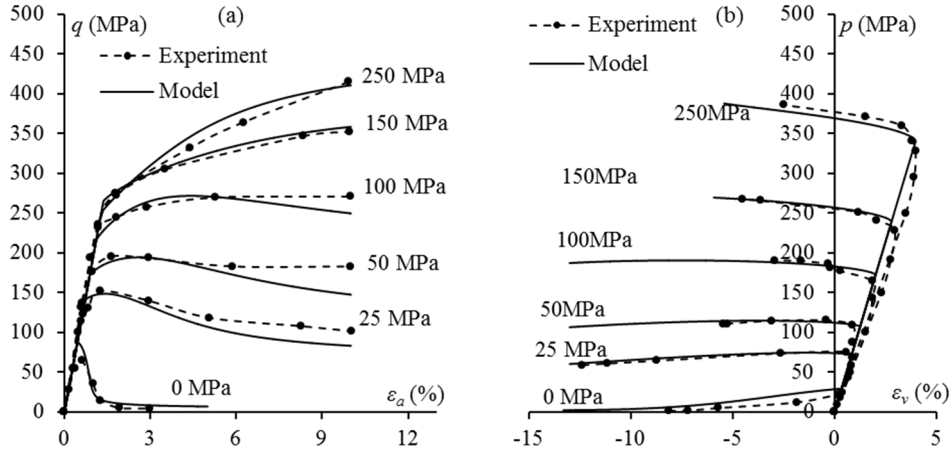

Figure 5.12: Comparison between the model predictions and experimental stress-strain data from drained triaxial test on Ural marble [29]

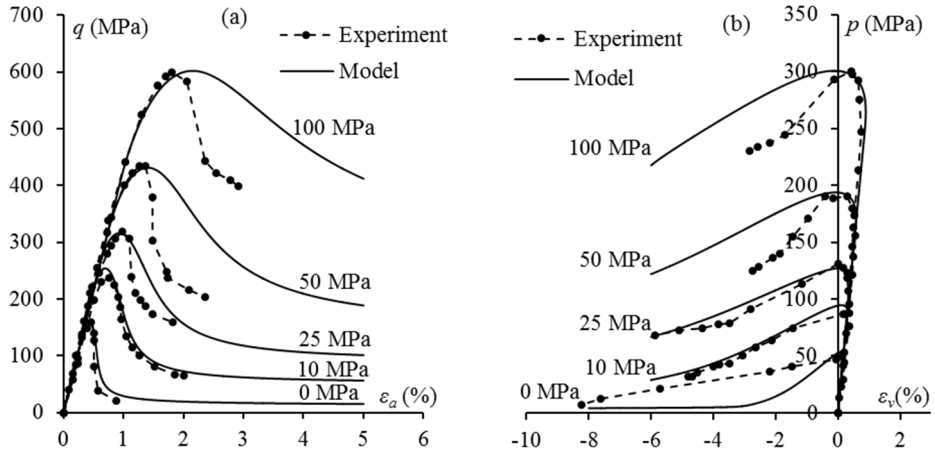

Figure 5.13: Comparison between the model predictions and experimental stress-strain data from drained triaxial test on Kareliya granite [29]

In experimental studies on marble under triaxial compression, up to 20% of axial deformation and at room temperature dilatancy is observed at confining pressures much

greater than the brittle-ductile transition pressure [42, 255, 277-280]. Furthermore, fluid flow measurements in marble [277] and also halite [281, 282] show that the permeability would increase while such a compact rock dilates and deforms in a ductile mode. Similar behavioural features are also expected to be observed in many other types of compact rocks, such as granite, norite, etc. if the laboratory facilities allow for pressurising these rocks well beyond their brittle-ductile transition pressure.

5.7. Localisation Analysis

The localisation properties of the proposed damaged plasticity model for compact rocks are assessed in this Section by adopting the classical bifurcation criterion. As was outlined in Chapter 4, according to the classical bifurcation criterion, the onset of localisation takes place when the acoustic tensor loses its positive definiteness (equation (4.70)). For convenience, the necessary condition for the occurrence of the onset of localisation is also repeated here as:

$$\det(A_{ij}) \leq 0 \qquad \text{with} \quad A_{ij} = C^T_{ijkl} n_k n_l \tag{5.63}$$

In the above expression A_{ij} is the acoustic tensor and C^T_{ijkl} is the tangent stiffness of the model, given by equation (5.58).

As illustrated in Figure 5.14, the proposed model predicts the onset of localisation for a wide range of stress states in true stress space for each rock type for a set of parameters listed in Table 5.1. The mode of localisation is predicted by the model to be predominantly the shear mode with two inclined shear bands, under low confining pressure and even up to relatively high confining pressures. With increasing confining pressure, however, the inclination of the shear bands decreases and they will become less steep. This can be clearly seen in Figure 5.14 where the determinant of the acoustic tensor is plotted against the orientation of the localisation band. At high confining pressures the probability of the occurrence of two distinct shear bands decreases and eventually a thick localisation band is formed. At even higher confining pressures no localisation takes place, which means that damage is uniformly distributed throughout the material volume. These features of the model are in agreement with experimental observations from failure modes of compact rocks. In general, experimental observations from triaxial tests on compact rocks, such as marble and granite, [30, 47-49, 55, 276], suggest that with increasing confining pressure, the width of the localisation band increases until at a substantially high pressure the whole volume of the specimen becomes damaged uniformly with no localisation taking place.

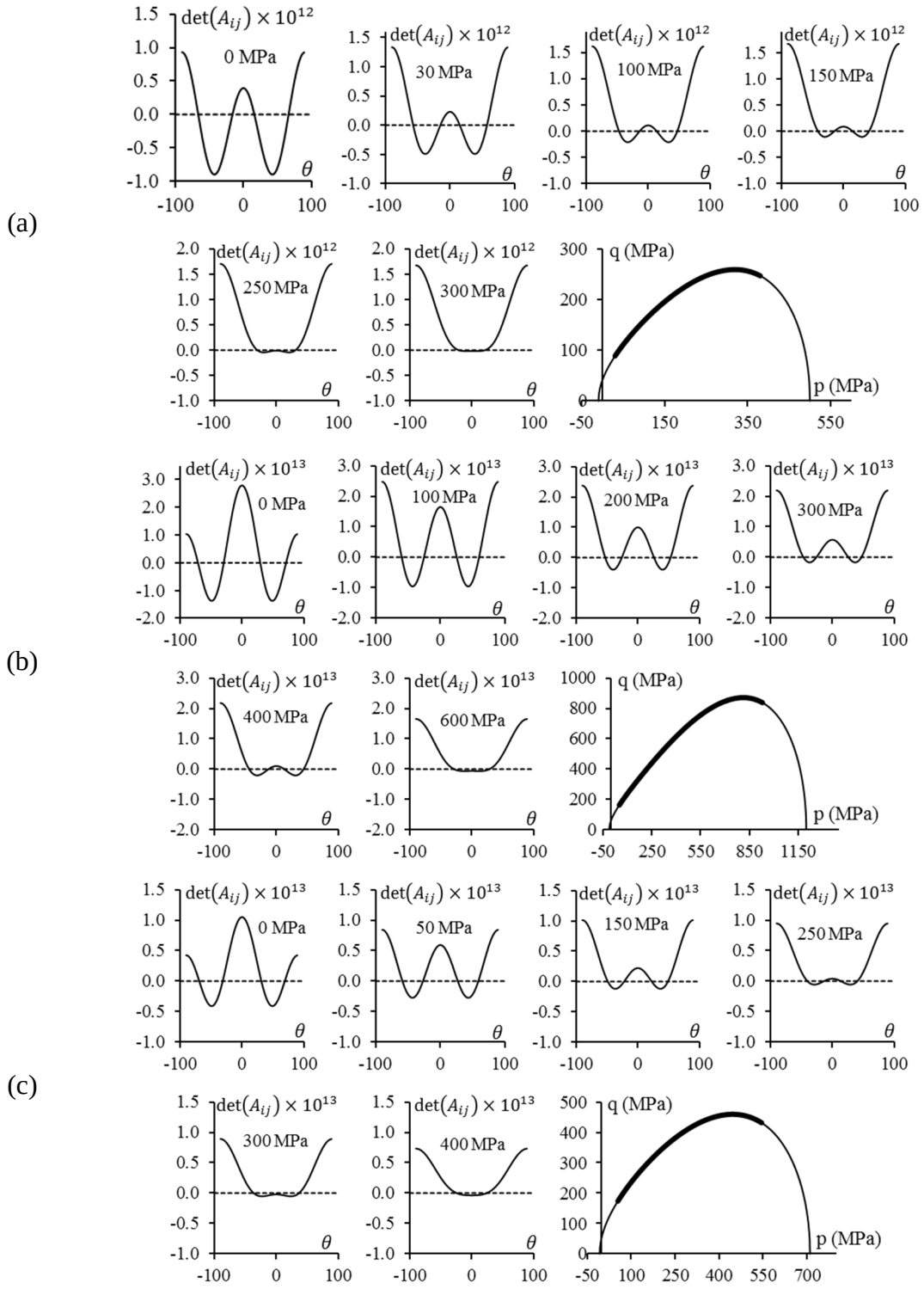

Figure 5.14: Prediction of the localisation mode and the localisation domain in true stress space for (a) Ural marble (b) Kareliya granite and (c) Donbass sandstone

5.8. Rate-dependent Regularisation

In the previous section, the capability of the proposed coupled damage-plasticity model in predicting the onset and mode of localisation was demonstrated. The occurrence of localisation at material level and, consequently, the loss of ellipticity of the governing

constitutive equations will, however, lead to the ill-posedness of BVPs, when the material model is used in numerical simulations, e.g. finite element. This numerical instability of the rate-independent coupled damage-plasticity model can be alleviated by means of a regularisation scheme. In this Section, similar to Section 4.7.1, the strain rate effects on the model response are incorporated into the proposed rate-independent coupled damage-plasticity model by means of the Perzyna [219] type viscoplastic regularisation. To this end, an algorithmic tangent stiffness tensor is derived and the effect of the rate-dependent enhancement on the localisation properties of the model is studied.

The model enhancement is carried out by explicitly defining the plastic multiplier of equation (5.56) such that:

$$\dot{\lambda} = \frac{\langle y \rangle}{\eta} dt \tag{5.64}$$

In the above expressions, η is the viscosity parameter, having the unit s/pa (and the dimension $M^{-1}LT^3$), $\langle y \rangle$ is a dimensionless overstress function, derived from the yield function of the rate-independent model, and $\langle . \rangle$ are the McCauley brackets. The evolution laws of damage and plastic strains of equations (5.49) – (5.51) are, therefore, modified to give the viscoplastic strain and damage rates as follows:

$$\dot{\varepsilon}_v^{vp} = \dot{\lambda}\frac{\partial y^*}{\partial \chi_v} = 2\frac{\langle y \rangle}{\eta}\left(\frac{{r_v}^2(p-\rho)}{{F_v}^2} - \frac{{r_s}^2\mu\,(q-\mu p)}{{F_s}^2} - \frac{{r_D}^2 f\beta p(\chi_D - f\beta p\chi_v/\rho)}{\rho F_D^2}\right)dt \tag{5.65}$$

$$\dot{\varepsilon}_s^{vp} = \dot{\lambda}\frac{\partial y^*}{\partial \chi_s} = 2\frac{\langle y \rangle}{\eta}\frac{{r_s}^2(q-\mu\rho)}{{F_s}^2}dt \tag{5.66}$$

$$\dot{D} = \dot{\lambda}\frac{\partial y^*}{\partial \chi_D} = 2\frac{\langle y \rangle}{\eta}\frac{{r_D}^2(\chi_D - f\beta p\chi_v/\rho)}{F_D^2}dt \tag{5.67}$$

Furthermore, by applying the chain rule, the viscoplastic strain tensor is given as:

$$\dot{\varepsilon}_{ij}^{vp} = \dot{\lambda}\frac{\partial y^*}{\partial \chi_{ij}} = 2\frac{\langle y \rangle}{\eta}\left(\frac{\partial y^*}{\partial \chi_v}\frac{\partial \chi_v}{\partial p}\frac{\partial p}{\partial \sigma_{kl}}\frac{\partial \sigma_{kl}}{\partial \chi_{ij}} + \frac{\partial y^*}{\partial \chi_s}\frac{\partial \chi_s}{\partial q}\frac{\partial q}{\partial \sigma_{kl}}\frac{\partial \sigma_{kl}}{\partial \chi_{ij}}\right)dt \tag{5.68}$$

As illustrated in Figure 5.16, with an increase in the viscosity parameter, η, and/or the strain rate, $\dot{\varepsilon}$, the maximum attainable stress increases until the model response approaches a completely elastic behaviour. Furthermore, the transition from elastic to inelastic response is smoother and more stable for higher values of the viscosity parameter and the strain rate. On the other hand, the model response collapses to the rate-independent behaviour for smaller values of the viscosity parameter and/or strain rate. This response of

the rate-dependent model resembles the experimentally observed behaviour of rocks, which is reported as an increase in the rock nominal strength under tension and compression at higher strain rates [236-240].

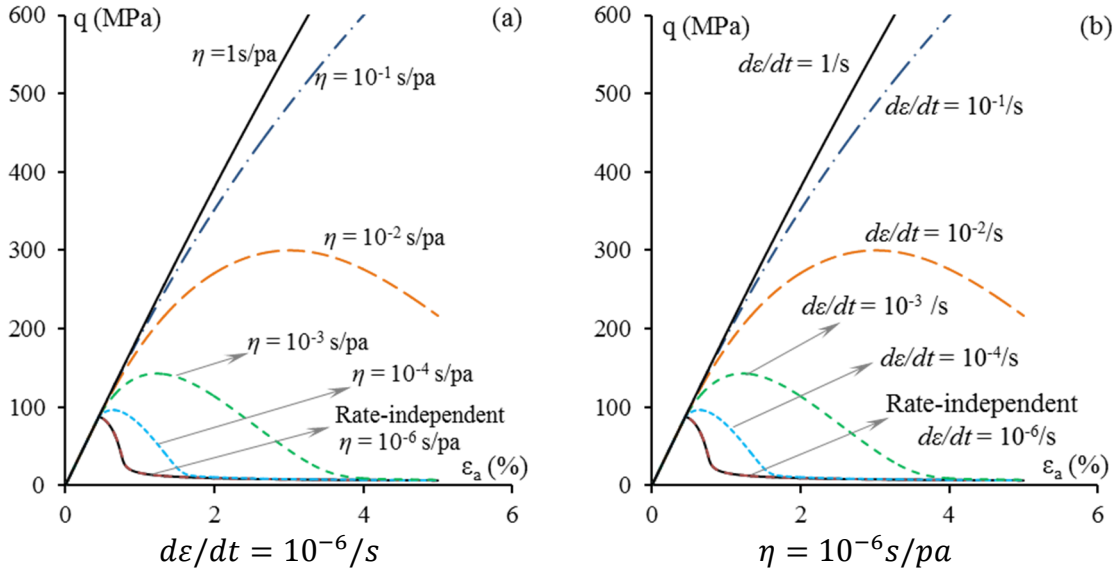

Figure 5.15: The influence of (a) viscosity parameter η and (b) strain rate on the stress-strain response of the model for uniaxial loading

Furthermore, for higher values of the viscosity parameter and strain rate the model exhibits a more profound dilation (Figure 5.16). This behaviour of the rate-dependent model is in accordance with the experimental observations in studies of the effect of the strain rate on volumetric deformation of rocks. Dilatancy has been observed to increase with time at a given applied force [257, 283-290]. Correspondingly, decrease in loading rate or strain rate gives rise to greater dilation at a given strain [258, 291, 292] (Figure 5.16 (c)).

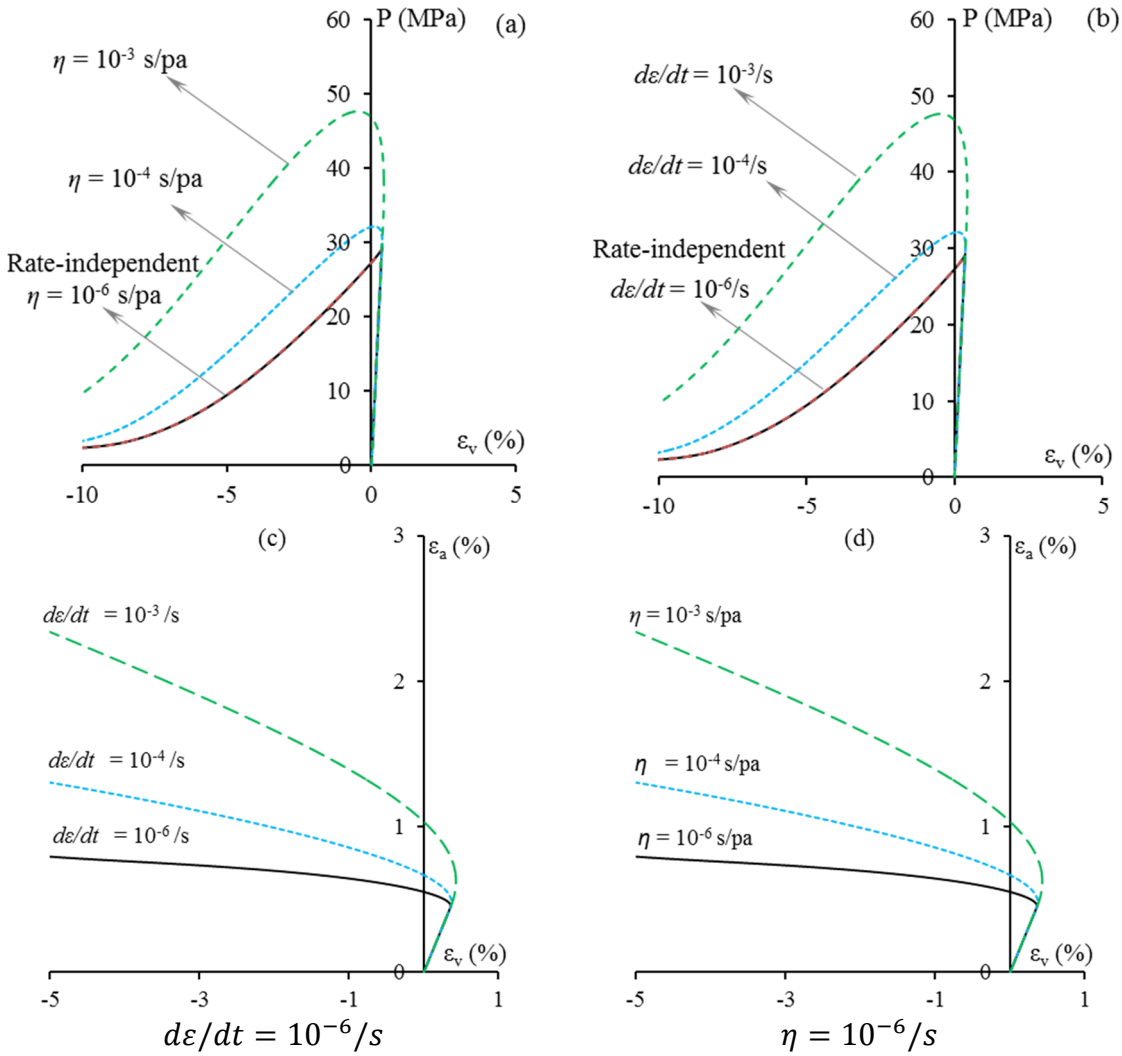

Figure 5.16: The influence viscosity parameter η and strain rate on dilational behaviour of the model; (a) and (b) stress-strain response and (c) and (d) axial strain against volumetric strain

At higher strain rates and/or higher values of the viscosity parameter damage grows at a slower rate. In coupled damage-plasticity models, on the other hand, the occurrence of localisation of deformation (or damage) is highly sensitive to the rate at which damage grows. In other words, localisation of deformation takes place if damage growth is fast [293]. Therefore, as was also discussed earlier in Chapter 4, the stabilising effect of the rate-dependent regularisation scheme can be clearly seen in a slower and more stable damage evolution.

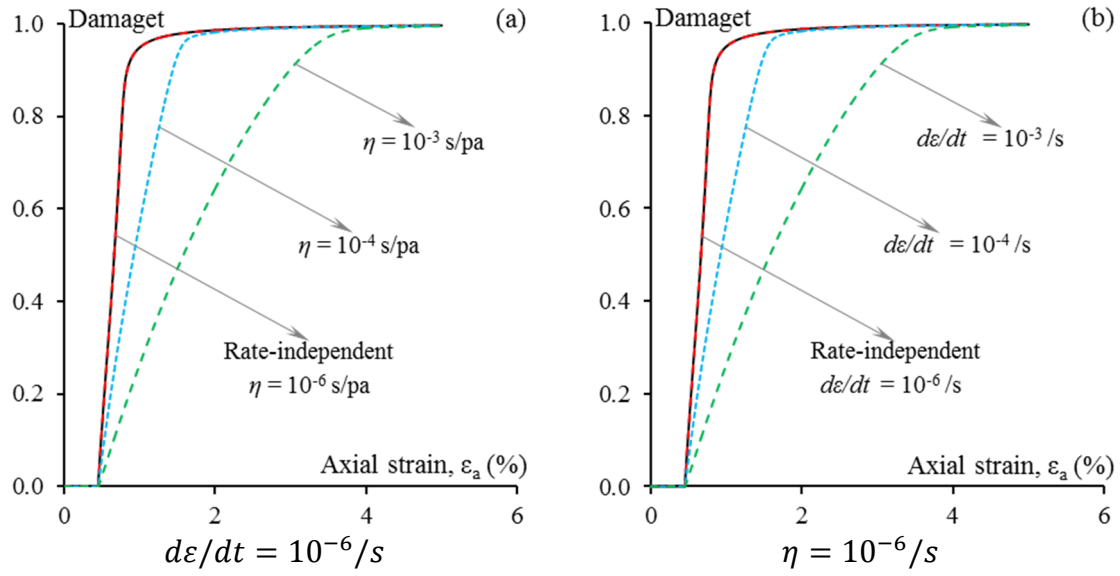

Figure 5.17: The influence of (a) viscosity parameter η and (b) strain rate on the evolution of damage

A constitutive model would not exhibit any bifurcation instability as long as its associated acoustic tensor is positive definite. Therefore, in order to demonstrate the numerical stability of the enhanced rate-dependent model, the formulation of the damage-viscoplastic tangent stiffness tensor is required for localisation analysis. It should be noted, however, that since there is no consistency condition for the coupled damage-viscoelasticity model, the tangent stiffness is given as; $L_{ijk}^{vp} = d\sigma_{ij}/d\varepsilon_{kl}$. In this sense, $(n+1)^{\text{th}}$ increment of the stress tensor is given as:

$$\Delta\sigma_{ij}^{n+1} = \sigma_{ij}^{n+1} - \sigma_{ij}^{n} \tag{5.69}$$

The stress tensor at step $n+1$ can be approximated by means of the first order Taylor expansion as:

$$\sigma_{ij}^{n+1} = \sigma_{ij}^{n} + \frac{\partial\sigma_{ij}}{\partial\varepsilon_{kl}}\Delta\varepsilon_{kl}^{n+1} + \frac{\partial\sigma_{ij}}{\partial D}\Delta D^{n+1} \tag{5.70}$$

Also, the elastic stress tensor of the coupled damage-viscoelasticity model is given as:

$$\sigma_{ij} = (1-D)C_{ijkl}\left(\varepsilon_{kl} - \varepsilon_{kl}^{vp}\right) \tag{5.71}$$

In the above expression C_{ijkl} is the elastic stiffness tensor, and D is the scalar damage variable. Therefore, the increment of the stress tensor of equation (5.69) can be rewritten as:

$$\Delta\sigma_{ij}^{n+1} = (1-D)C_{ijkl}\Delta\varepsilon_{kl}^{n+1} - (1-D)C_{ijkl}\Delta\varepsilon_{kl}^{vp\,n+1} - \frac{\sigma_{ij}}{(1-D)}\Delta D^{n+1} \tag{5.72}$$

The expression of equation (5.72) can also be written in the following form:

$$\Delta\sigma_{ij}^{n+1} = (1-D)C_{ijkl}\Delta\varepsilon_{kl}^{n+1} - \left[(1-D)C_{ijkl}Q_{kl}^{n+1} + \frac{\sigma_{ij}}{(1-D)}\right]\Delta D^{n+1} \tag{5.73}$$

where Q_{ij} is the ratio between the increment of the viscoplastic strain tensor, $\Delta\varepsilon_{ij}^{vp}$, and the increment of the scalar damage variable, ΔD:

$$Q_{ij}^{n+1} = \frac{\Delta\varepsilon_{ij}^{vp\,n+1}}{\Delta D^{n+1}} = \frac{\left(\frac{\partial y^*}{\partial \chi_v}\frac{\partial \chi_v}{\partial p}\frac{\partial p}{\partial \sigma_{kl}}\frac{\partial \sigma_{kl}}{\partial \chi_{ij}} + \frac{\partial y^*}{\partial \chi_s}\frac{\partial \chi_s}{\partial q}\frac{\partial q}{\partial \sigma_{kl}}\frac{\partial \sigma_{kl}}{\partial \chi_{ij}}\right)}{\frac{\partial y^*}{\partial \chi_D}} \tag{5.74}$$

Having known the stress state at step n and the stress increment at step $n+1$, the stress state at step $n+1$ can be obtained. However, a residual is always expected the increment of which is given as follows:

$$\Delta R_{ij}^{n+1} = (1-D)C_{ijkl}\Delta\varepsilon_{kl}^{n+1} - \left[(1-D)C_{ijkl}Q_{kl}^{n+1} + \frac{\sigma_{ij}}{(1-D)}\right]\Delta D^{n+1} - \Delta\sigma_{ij}^{n+1} \tag{5.75}$$

In order to derive the analytical form of consistent tangent stiffness tensor, the stress residual must be zero after each time step. Therefore, the root of $\Delta R_{ij}^{n+1} = 0$ can be determined by a Newton-Raphson iterative scheme. To this end, the value of the stress residual at the end of the iterative solution is approximated using the first order Taylor expansion as:

$$\Delta R_{ij}^{n+1}\big|_{new} = \Delta R_{ij}^{n+1}\big|_{old} + d\Delta R_{ij}^{n+1} \tag{5.76}$$

In the above expression $d\Delta R_{ij}^{n+1}$ is defined as:

$$d\Delta R_{ij}^{n+1} = \frac{\partial \Delta R_{ij}^{n+1}}{\partial \varepsilon_{kl}}d\varepsilon_{kl} + \frac{\partial \Delta R_{ij}^{n+1}}{\partial \sigma_{kl}}d\sigma_{kl} + \frac{\partial \Delta R_{ij}^{n+1}}{\partial D}dD \tag{5.77}$$

where

$$\frac{\partial \Delta R_{ij}^{n+1}}{\partial \varepsilon_{kl}} = (1-D)C_{ijkl} \tag{5.78}$$

$$\frac{\partial \Delta R_{ij}^{n+1}}{\partial \sigma_{kl}} = -\left[(1-D)C_{ijkl}\frac{\partial Q_{ij}}{\partial \sigma_{kl}} + \frac{\delta_{ik}\delta_{jl}}{(1-D)}\right]\Delta D - \delta_{ik}\delta_{jl} \tag{5.79}$$

$$\frac{\partial \Delta R_{ij}^{n+1}}{\partial D} = -C_{ijkl}\varepsilon_{kl} - \left[-C_{ijkl}Q_{kl} + (1-D)C_{ijkl}\frac{\partial Q_{kl}}{\partial D} + \frac{\sigma_{ij}}{(1-D)^2}\right]\Delta D - \left[(1-D)C_{ijkl}Q_{kl} + \frac{\sigma_{ij}}{(1-D)}\right] \tag{5.80}$$

Furthermore, by virtue of equation (5.67), the increment of the scalar damage variable, ΔD, can be written as:

$$\Delta D = 2\frac{\langle y \rangle}{\eta}\frac{\partial y^*}{\partial \chi_D}\Delta t \tag{5.81}$$

Therefore, damage increment during each step of the Newton-Raphson iteration can be obtained, by making use of equation (5.81) and some rearrangements, in terms of the increment of the stress tensor in the following manner:

$$dD = \frac{2\frac{\Delta t}{\eta}\frac{\partial\left(y\frac{\partial y^*}{\partial \chi_D}\right)}{\partial \sigma_{ij}}}{1 - 2\frac{\Delta t}{\eta}\frac{\partial\left(y\frac{\partial y^*}{\partial \chi_D}\right)}{\partial D}} d\sigma_{ij} = \mathrm{X}_{ij} d\sigma_{ij} \tag{5.82}$$

By substitution of the above expression back into equation (5.77) and enforcing $d\Delta R_{ij}^{n+1} = 0$ at the end of the Newton-Raphson iteration scheme:

$$0 = \frac{\partial \Delta R_{ij}^{n+1}}{\partial \varepsilon_{kl}} d\varepsilon_{kl} + \frac{\partial \Delta R_{ij}^{n+1}}{\partial \sigma_{kl}} d\sigma_{kl} + \frac{\partial \Delta R_{ij}^{n+1}}{\partial D} \mathrm{X}_{kl} d\sigma_{kl} \tag{5.83}$$

the formulation of the consistent tangent stiffness tensor is given as follows:

$$L_{ijkl}^{vp} = \frac{d\sigma_{ij}}{d\varepsilon_{kl}} = -\frac{\partial \Delta R_{ij}^{n+1}}{\partial \varepsilon_{kl}}\left[\frac{\partial \Delta R_{ij}^{n+1}}{\partial \sigma_{kl}} + \frac{\partial \Delta R_{ij}^{n+1}}{\partial D}\mathrm{X}_{kl}\right]^{-1} \tag{5.84}$$

The variation of the determinant of the acoustic tensor, derived from the tangent stiffness of the damage-viscoplastic model, with respect to the band orientation, is illustrated in Figure 5.18. As can be observed in Figure 5.18, for certain combinations of strain rate and viscosity parameter ($\dot{\varepsilon}_a = 10^{-6}/s$ and $\eta = 3 \times 10^{-6}\ s/pa$ for Ural marble), the determinant of acoustic tensor ($\det(A_{ij})$) is non-negative in all directions and the minimum value of $\det(A_{ij})$ lies just above zero. Therefore, it is expected that the numerical instabilities of the rate-independent model due to the localisation of deformation are eradicated due to the rate-dependent enhancement of the coupled damage-plasticity model.

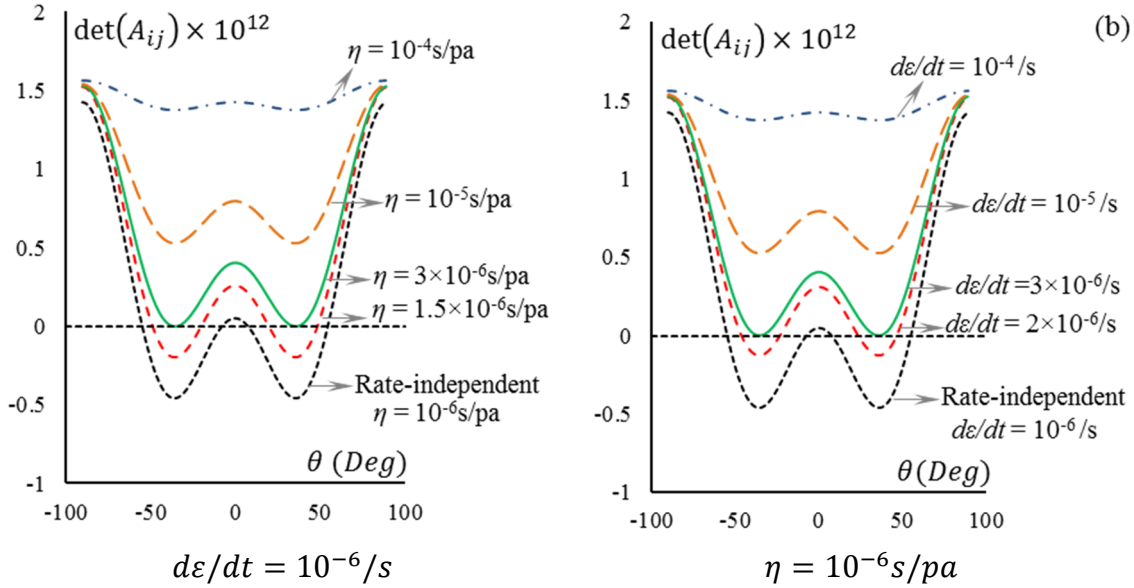

Figure 5.18: The influence of (a) viscosity parameter η (with $d\varepsilon/dt = 10^{-6}/s$) and (b) strain rate (with $\eta = 10^{-6}s/pa$) on the determinant of the acoustic tensor for Ural marble under triaxial shearing at 30 MPa confining pressure

In order to calibrate the parameters of the rate-dependent model at the material level, the strain rate is kept constant and similar to those applied in laboratory experiments and then the viscosity parameter, η is calibrated. The basis for calibration and adjustment of η is to firstly guarantee the non-negativeness of the determinant of the acoustic tensor for all possible band orientations and secondly to match the stress-strain response of the model with that of the experiment. In experimental practice [93, 252], the range of axial strain rates used for triaxial tests on sandstone specimens varies between $10^{-6}/s$ and $10^{-4}/s$, thus, for the present study the viscosity parameter η is calibrated considering a constant axial strain rate of $\dot{\varepsilon}_a = 10^{-6}/s$. For example, for Ural marble, it was found that a strain rate of $\dot{\varepsilon}_a = 10^{-6}/s$ along with a viscosity parameter of $\eta = 3 \times 10^{-6}s/pa$ gives rise to a positive definite acoustic tensor in all directions and also to a good match between stress-strain response of the model and that of the experiment, (Figure 5.19). The calibrated parameters of the rate-dependent model are given in

Table 5.2. The calibrated values of the strain rate and viscosity parameter at material level can later be used as a starting point for the calibration of these parameters at structural level in FE simulations.

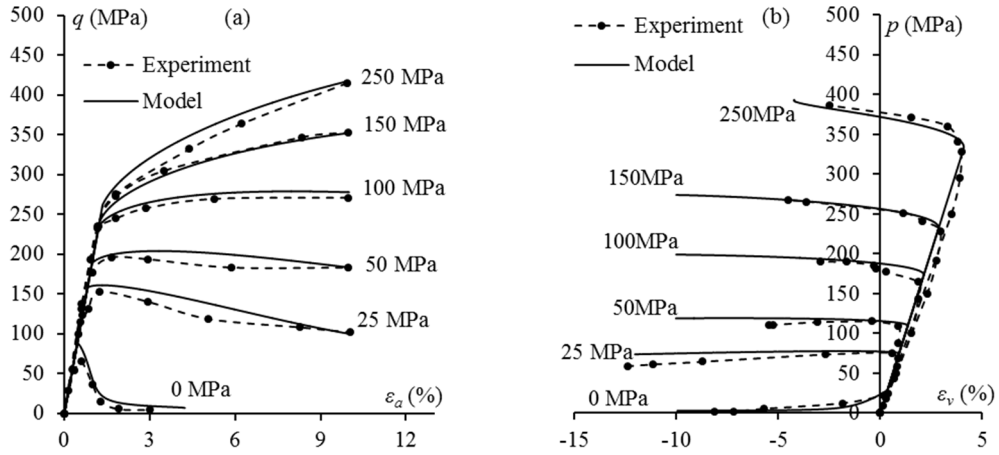

Figure 5.19: Rate-dependent model predictions of stress-strain response of Ural marble after calibrating the viscosity parameter as $\eta = 3 \times 10^{-6}\, s/pa$ and strain rate as $\dot{\varepsilon} = 10^{-6}/s$

Table 5.2: Rate-dependent model parameters, calibrated for predicting the stress-strain response of Ural marble

E (GPa)	ν	P_c (MPa)	P_t (MPa)	α	γ	M	μ_0	β	a	$r_v = r_s$	$d\varepsilon/dt$ (/s)	η (s/pa)
19.5	0.12	500	-10	0.6	0.85	1.2	1.0	0.5	1.0	0.5	10^{-6}	3×10^{-6}

5.9. Summary and Discussion

In this chapter, a coupled damage-plasticity model is developed to describe the macroscopic behaviour of compact, non-porous rocks. Since compact rocks exhibit dilational behaviour, even at pressures beyond that of the brittle-ductile transition, the focus of the constitutive model development is put on adequately capturing this dilational behaviour. To this end, the model development is based on the phenomenological description of damage-induced dilation. In addition, the model development is carried out within the framework of generalised thermodynamics in order to guarantee the thermodynamic admissibility of the results. The comparison between the stress-strain response of the proposed model (at the material level) and experimental data from drained triaxial tests on compact rocks indicates the high capability of the model in predicting the mechanical response of compact rocks. In particular, the significant dilational response of compact rocks at high pressures is successfully captured.

Furthermore, the proposed (rate-independent) model exhibits a good capability in predicting the onset of localisation for a wide range of stress states in true stress space. However, the localisation properties of the rate-independent model give rise to numerical instabilities when the model is used in the numerical analysis of a BVP. In order to alleviate

this problem, the rate-dependent enhancement of the rate-independent coupled damage-plasticity model is carried out by using the Perzyna [219] type viscoplastic regularisation.

The proposed model in this chapter have also some weaknesses and limitations. The main issue with this model is that the effect of irreversible damage deformations on the instantaneous elastic modulus has not been taken into account. This has led to making some assumptions which may not have enough physical justification. Nevertheless, the proposed coupled damage-plasticity model, in this chapter, can serve as an example to demonstrate how new internal variables, pertaining to different underlying physical phenomena, can be incorporated into the model formulation by making use of kinematic constraint equations within the framework of generalised thermodynamics (Chapter 3). In the subsequent chapter, it is demonstrated that the kinematic constraint equations can also be used to describe the interdependencies of kinematic fields through developing a thermodynamic approach to model the localised failure of geomaterials.

CHAPTER 6

A Thermodynamic Framework for Constitutive Modelling of Localised Failure

6.1. Introduction

Failure of geomaterials involves localisation of deformation within a band of finite width, referred to as the localisation band. Shear dilation and compaction bands observed in soils, porous and compact rocks are typical examples of this localised failure. Upon the onset of localisation, the uniform (or slightly varying) deformation field becomes non-unique, with discontinuity of displacement and other kinematic fields across the boundary of the localisation band. Under such conditions, the definitions of macroscopic stress and strain over a volume element containing a localisation band are not physically meaningful anymore. Phenomenological, classic constitutive models, which are developed based on the assumption of uniform distribution of stress and strain fields over a volume element, fail to give a meaningful measure of macroscopic stress and strain for a non-homogeneous volume element with a localisation band. The width of the localisation band under a given loading configuration is governed mainly by the material microstructure and also boundary condition. It can be assumed to be an intrinsic material property which should be included in the material constitutive description.

If the essential features of the localised deformation are not taken into proper consideration at the material level, identification and calibration of the model parameters may not be carried out in a consistent and physically meaningful manner. In particular, using the material model in the numerical simulation of any structure requires recalibration of the model parameters to deal with the effects of the structure size on its mechanical response under a certain loading condition. The size effect is a problem scaling, which is central to constitutive

modelling and numerical simulations. In geomaterials, localisation is associated with a strain rate jump within a band of certain width which is kinematically compatible with the surrounding material (discontinuous bifurcation [32]). Therefore, the essential features of localised deformation that should be incorporated in the constitutive equations include the characteristic size of the RVE, for which the constitutive equations are developed, the width of the localisation band, which appears within the RVE at the onset of bifurcation, and specification of kinematic dependencies between the localisation band and the surrounding material.

Several approaches have been proposed to tackle the problems pertaining to modelling the localised deformation in the analysis of solids and structures. In the context of constitutive modelling, these approaches range from the smeared crack approach [294] to mathematically sophisticated regularisations such as Cosserat [295] and nonlocal/gradient theories [151, 296-302]. The main feature of these approaches is the introduction of a length scale related to the localisation of deformation into the constitutive equations. In the smeared crack approach, the size of the finite element is incorporated into the constitutive equations and, accordingly, the constitutive behaviour is scaled with the resolution of the FE discretisation. This scaling is based on meeting some requirements on the energy dissipation, e.g. forcing the cracked elements to reproduce a dissipation invariant with respect to the size of the element. One important limitation of this approach is that no unique set of parameters can be found for the same material, due to the variation of the spatial resolution over the computational domain. In addition, if the elements are large numerical issues will arise due to spurious snap-back at the constitutive level (e.g. in quasi-brittle failure, this is the case in which the elastic strain energy in the element is larger than the dissipation the crack contained within it can produce). Enriching the constitutive models with a length scale in nonlocal/gradient regularisation is a mathematically and also physically rigorous approach to account for the size of the localisation zone. However, the numerical implementation of these models requires a finer numerical discretisation than the physical width of the localisation zone. The applications of such enhancements to very large scale problems are, therefore, restricted by the available computational resources. In substantially large scale problems of geotechnical and mining engineering, since the locations of failure zones are generally unknown within the domain under consideration, which can be several orders of magnitude larger than the characteristic width of the localisation zone, a very high resolution

discretisation required by non-local/gradient models renders the application of these models impracticable.

In cases where the width of the localisation band, h (fracture process zone (FPZ) in quasi-brittle materials, or shear/compaction bands in soils) is smaller than the size of numerical discretisation, H ($h < H$), numerical enhancements such as enhanced assumed strain (EAS) method (e.g. [303-306]) or the extended finite element method (XFEM) [307-310] have been widely used to model the localised failure. In these kinds of enhancement, the finite element shape functions are enriched to improve the kinematics of deformation the element can handle. This numerical enhancement is carried out by embedding the localisation zone, usually idealised as a strong discontinuity (i.e. discontinuous displacement filed) across the element. These approaches can appropriately capture some fundamental features of deformation, including crack opening/shearing and the shrinking of the elastic bulk, by introducing a separate constitutive law for the discontinuity, disconnected from the bulk continuum behaviour, to model the crack opening/shearing or behaviour inside the localisation band. Other similar approaches to improve the kinematics of finite elements by embedding a localisation zone (weak discontinuity, i.e. only strain field is discontinuous) within the finite element can be found in [311-315]. In these enhancements the embedded zone has a finite width and, accordingly, a continuum model is used to describe the inelastic material behaviour inside the localisation zone. Although these numerical enhancements have shown promising features in modelling a single discontinuity (either a single crack or a single fracture process zone) within an element, modelling multiple interacting discontinuities using these methods is cumbersome if not impossible. On example of these multiple interacting localisation bands can be given as the multiple compaction bands observed in porous rocks under substantially high pressure [92].

Accordingly, due to the above-mentioned limitations in modelling the localised deformation, especially for very large scale problems usually encountered in geotechnical and mining engineering, a more rigorous and practical approach is required. With this motivation, Nguyen et al. [36, 37] developed an approach in which the width of the localisation band is inserted into the description of the constitutive behaviour, and the constitutive descriptions include the responses at two scales: macro scale and the scale of the localisation band. The localisation band is then activated once the condition for the occurrence of the onset of localisation (equation (4.70)) is met. The interaction between the material inside and outside the localisation band is determined through satisfying the

continuity of traction across the boundaries of the localisation band. Details of the formulation of the two-scale approach can be found in [36, 37]. Due to the direct incorporation of the width of the localisation band and the characteristic size of the material volume element into the constitutive equations, the numerical implementation of the two scale approach does not require a finer numerical discretisation than the width of the localisation band. This important advantage of the two-scale approach makes its application desirable for substantially large scale problems of geotechnical and mining engineering. Furthermore, more recently Nguyen et. al [316] demonstrated that the two-scale approach can be enhanced to effectively capture the presence of multiple interacting localisation bands within a volume element.

Nevertheless, the requirements for the thermodynamic admissibility of the two-scale approach [36, 37] is applied retrospectively and after the completion of the model formulation. However, as was discussed earlier, a more rigorous and consistent approach is to construct the model within a well-established thermodynamic framework. It is, however, important to remember that the thermodynamic field theory is based on the assumption that the thermodynamic state is uniform within a material element and only varies from one element to another (this is different from the classical thermodynamics which deals only with extremely slow processes in the vicinity of a thermodynamic equilibrium state). Therefore, the original thermodynamics field theory should be enhanced to accommodate constitutive modelling for a material element which becomes non-homogeneous due to the localisation phenomenon. In this study, a thermodynamic approach is developed for modelling the localised failure of geomaterials. In addition to the homogenisation scheme, a pivotal assumption in this development is the kinematic compatibility between the localisation band and the surrounding material.

The coupled damage-plasticity models developed in Chapter 4 and Chapter 5, can be effectively used in conjunction with the results of the thermodynamic developments in this chapter to investigate the deterministic size effect problem. Previous developments of the two-scale approach [36, 37, 316] used simple material models and considered only some particular loading conditions. For example, [37] deals with the failure of quasi-brittle materials in the tensile regime and [316] used a breakage model [75] which can describe the behaviour of porous granular rocks only. The coupled damage-plasticity models developed in the previous chapters, although phenomenological, enable the description of the macroscopic behaviour of rocks under a wide range of loading conditions. In this chapter,

the coupled damage-plasticity model developed for porous rocks (Chapter 4) is used to investigate the deterministic size effect problem which is encountered in laboratory experiments and practical applications when the rock specimens or rock formations are loaded under conditions conducive to brittle failure.

6.2. A Thermodynamic Field Theory for Inhomogeneous Materials

The application of the thermodynamics field theory to continuum mechanics is essentially based on the assumption that no variation of the state variables takes place within the continuum element and they only differ from one element to another [21]. Therefore, in order for the thermodynamics field theory to be applicable to the development of constitutive relations for a non-homogeneous continuum element, consisting of different constituents, a homogenisation scheme should be adopted. At a smaller scale, however, the assumption of homogeneous element still holds for each individual constituent. Therefore, each individual constituent can have its own state and internal variables and also constitutive relations. In this sense, the homogenisation scheme can be interpreted as a measure for specifying the contribution of each constituent in the overall behaviour of the non-homogeneous continuum element at a larger scale. In addition, the interactions between different constituents comprising the non-homogeneous continuum element must be specified.

In generalised thermodynamics (or thermodynamics with internal variables), each internal variable is responsible for describing the evolution of a dissipation mechanism. Hence, the development of a fully micro-mechanical model, which takes into account all the details of deformation and energy dissipation at micro-scale, would require an infinitely large number of internal variables. In micromechanical models, the governing equations which describe the mechanism of deformation are given in the simplest form possible. Although the material behaviour can be predicted accurately by means of a micromechanical model, large-scale applications of these models could be restricted by its level of complexity and also by available computational resources. An alternative approach is, therefore, to select a small number of internal variables and enrich the governing equations which identify the essential mechanisms of deformation and energy dissipation. In addition to this, the interaction and interdependencies between these internal variables should be specified by means of some kinematic constraint equations.

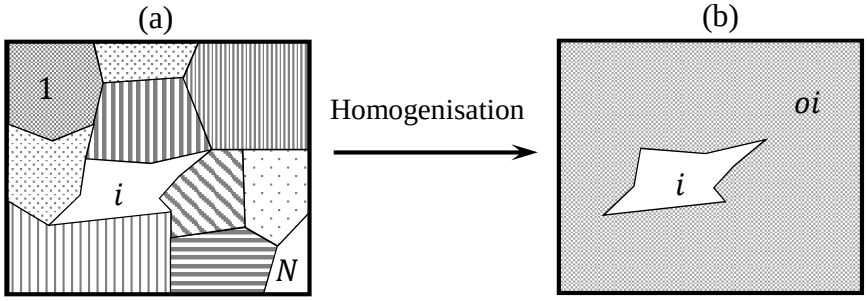

Figure 6.1: (a) A non-homogeneous RVE consisting of N constituents (b) Homogenisation of $N-1$ constituent outside the i^{th} constituent

As was discussed earlier in Section 3.3, in some models kinematic variables are not entirely free or independent but are constrained or interdependent by some means. In general, these constraints or interdependencies might involve strains and/or the rate of internal variables. The development of such models can either be achieved by reducing the number of kinematic variables, through eliminating the dependent variables, or by introducing some constraint equations while keeping all the kinematic variables [19, 214]. The latter is a more powerful and general technique and, hence, will be adopted in this study (see Section 3.3). Developing constitutive models for non-homogeneous RVEs (Figure 6.1) requires the determination of the contribution of each (micro) strain field, pertaining to each individual constituent, to the macroscopic strain field. In addition, it is required to specify the interaction and kinematic interdependencies between all the constituents. Therefore, for a unit volume of a heterogeneous material consisting of N different constituents, as illustrated in Figure 6.1, the first kinematic relationship, which specifies the contribution of each constituent to the macroscopic strain field, can be given as the weighted sum of the strain fields of all constituents as:

$$\dot{\boldsymbol{\varepsilon}} = f^1\dot{\boldsymbol{\varepsilon}}^1 + \cdots + f^N\dot{\boldsymbol{\varepsilon}}^N = \sum_{i=1}^{N} f^i\,\dot{\boldsymbol{\varepsilon}}^i \tag{6.1}$$

However, a more useful approach for modelling the localised failure is to give the macroscopic strain rate as the weighted sum of the strain rate of the i^{th} constituent and the volume-weighted average of all the strain rates pertaining to other constituents outside the boundaries of the i^{th} constituents (Figure 6.1):

$$\dot{\boldsymbol{\varepsilon}} = f^i\dot{\boldsymbol{\varepsilon}}^i + \left(1 - f^i\right)\dot{\boldsymbol{\varepsilon}}^{oi} \tag{6.2}$$

In the above expression, $\dot{\boldsymbol{\varepsilon}}^i$ is the strain rate inside the i^{th} constituent with the volume fraction f^i and $\dot{\boldsymbol{\varepsilon}}^{oi}$ represents the volume-weighted average of the strain rates outside the boundaries of the i^{th} constituent, which can be given as:

$$\dot{\boldsymbol{\varepsilon}}^{oi} = \frac{\left(\sum_{j=1}^{N} f^j \dot{\boldsymbol{\varepsilon}}^j\right) - f^i \dot{\boldsymbol{\varepsilon}}^i}{\left(\sum_{j=1}^{N} f^j\right) - f^i} \tag{6.3}$$

In addition, in the absence of strong discontinuities within the non-homogeneous RVE, Maxwell's compatibility condition requires that the strain rate in the i^{ih} constituent be of the form:

$$\dot{\boldsymbol{\varepsilon}}^i = \dot{\boldsymbol{\varepsilon}}^{oi} + \dot{\boldsymbol{\varepsilon}}^{ki} = \frac{\left(\sum_{j=1}^{N} f^j \dot{\boldsymbol{\varepsilon}}^j\right) - f^i \dot{\boldsymbol{\varepsilon}}^i}{\left(\sum_{j=1}^{N} f^j\right) - f^i} + \dot{\boldsymbol{\varepsilon}}^{ki} \tag{6.4}$$

In the above expression, $\dot{\boldsymbol{\varepsilon}}^{ki}$ represents a kinematically admissible discontinuous mode (e.g. velocity jump) over the boundaries of the i^{th} constituent. From equations (6.2) and (6.4) the macroscopic strain rate can be given in the two following forms:

$$\dot{\boldsymbol{\varepsilon}} = \dot{\boldsymbol{\varepsilon}}^{oi} + f^i \dot{\boldsymbol{\varepsilon}}^{ki} \tag{6.5}$$

$$\dot{\boldsymbol{\varepsilon}} = \dot{\boldsymbol{\varepsilon}}^{i} - \left(1 - f^i\right) \dot{\boldsymbol{\varepsilon}}^{ki} \tag{6.6}$$

Following the discussion in Chapter 3, the conditions of equations (6.5) and (6.6) can be given in the form of two kinematic constraint equations as follows:

$$\boldsymbol{C}_1 = \dot{\boldsymbol{\varepsilon}} - \dot{\boldsymbol{\varepsilon}}^{oi} - f^i \dot{\boldsymbol{\varepsilon}}^{ki} = 0 \tag{6.7}$$

$$\boldsymbol{C}_2 = \dot{\boldsymbol{\varepsilon}} - \dot{\boldsymbol{\varepsilon}}^{i} + \left(1 - f^i\right) \dot{\boldsymbol{\varepsilon}}^{ki} = 0 \tag{6.8}$$

Furthermore, the general form of the Helmholtz free energy potential can be given as the weighted sum of the Helmholtz free energy potentials for the material inside the i^{th} constituent and the Helmholtz free energy for the homogenised bulk outside the boundaries of the i^{th} constituent:

$$\Psi = f^i \Psi^i\left(\boldsymbol{\varepsilon}^i, \tilde{\alpha}_1^i, \dots, \tilde{\alpha}_n^i\right) + \left(1 - f^i\right) \Psi^{oi}\left(\boldsymbol{\varepsilon}^{oi}, \tilde{\alpha}_1^{oi}, \dots, \tilde{\alpha}_n^{oi}\right) \tag{6.9}$$

In the above expression, the strain tensor $\boldsymbol{\varepsilon}^i$ represents the strain field of the i^{th} constituent and $\left(\tilde{\alpha}_1^i, \dots, \tilde{\alpha}_n^i\right)$ is a set of n internal variables, which describe the history of deformation and energy dissipation within the i^{th} constituent. The symbol '$\sim$' at the top of each internal variable indicates that the internal variable can be a tensor of any order, including a scalar (which is a zero order tensor). The homogenised strain tensor $\boldsymbol{\varepsilon}^{oi}$ is the volume-weighted

average of the strain fields of all constituents outside the i^{th}constituent and it is given by equation (6.3). Furthermore, each of the internal variables in the set $\left(\tilde{\alpha}_1^{oi}, \dots, \tilde{\alpha}_n^{oi}\right)$ and also their rates $(\dot{\tilde{\alpha}}_1^{oi}, \dots, \dot{\tilde{\alpha}}_n^{oi})$ can be determined using the same method as that used for determining $\boldsymbol{\varepsilon}^{oi}$. For example the rate of the k^{th} internal variable in the homogenised zone outside the i^{th} constituent can be given as the volume-weighted average of the rate of the same internal variable in all constituents:

$$\dot{\tilde{\alpha}}_k^{oi} = \frac{\left(\sum_{j=1}^{N} f^j \dot{\tilde{\alpha}}_k^j\right) - f^i \dot{\tilde{\alpha}}_k^i}{\left(\sum_{j=1}^{N} f^j\right) - f^i} \tag{6.10}$$

Furthermore, the power of deformation produced by macroscopic stresses can also be given as the weighted sum of the power of deformation in the i^{th} constituent and the volume-weighted average of the powers of deformation produced by microscopic stresses within all other constituents:

$$\delta W = \boldsymbol{\sigma} : \dot{\boldsymbol{\varepsilon}} = f^i \boldsymbol{\sigma}^i : \dot{\boldsymbol{\varepsilon}}^i + \left(1 - f^i\right)\boldsymbol{\sigma}^{oi} : \dot{\boldsymbol{\varepsilon}}^{oi} = f^i \delta W^i + \left(1 - f^i\right)\delta W^{oi} \tag{6.11}$$

Therefore, by making use of equations (6.9) and (6.11) according to the First Law of thermodynamics, the dissipation function for the RVE can be given as:

$$\delta\Phi = \delta W - \dot{\Psi} = f^i\left(\delta W^i - \dot{\Psi}^i\right) + \left(1 - f^i\right)\left(\delta W^{oi} - \dot{\Psi}^{oi}\right) = f^i \delta\Phi^i + \left(1 - f^i\right)\delta\Phi^{oi} \tag{6.12}$$

In the above expression, $\delta\Phi^i = \delta\Phi^i\left(\tilde{\alpha}_1^i, \dots, \tilde{\alpha}_n^i, \dot{\tilde{\alpha}}_1^i, \dots, \dot{\tilde{\alpha}}_n^i\right)$ and $\delta\Phi^{oi} = \delta\Phi^{oi}\left(\tilde{\alpha}_1^{oi}, \dots, \tilde{\alpha}_n^{oi}, \dot{\tilde{\alpha}}_1^{oi}, \dots, \dot{\tilde{\alpha}}_n^{oi}\right)$ represent the dissipation functions for a unit volume of the material inside and outside the i^{th} constituent. The dissipation function of equation (6.12) can now be supplemented with the two kinematic constraint equations (6.7) and (6.8). Therefore, the supplemented dissipation function can be given as:

$$\delta\Phi' = \delta\Phi + \boldsymbol{\Lambda}_1 : \boldsymbol{C}_1 + \boldsymbol{\Lambda}_2 : \boldsymbol{C}_2 \geq 0 \tag{6.13}$$

where $\boldsymbol{\Lambda}_1$ and $\boldsymbol{\Lambda}_2$ are two Lagrangian multipliers. The Lagrangian multipliers can then be obtained from the following set of equations, which, as outlined in Chapter 3, are resulted from the First Law of thermodynamics and the Second Law in the form of Ziegler's orthogonality principle:

$$\boldsymbol{\sigma} = \frac{\partial\Psi}{\partial\boldsymbol{\varepsilon}} + \frac{\partial\Phi}{\partial\dot{\boldsymbol{\varepsilon}}} + \boldsymbol{\Lambda}_1 : \frac{\partial\boldsymbol{C}_1}{\partial\dot{\boldsymbol{\varepsilon}}} + \boldsymbol{\Lambda}_2 : \frac{\partial\boldsymbol{C}_2}{\partial\dot{\boldsymbol{\varepsilon}}} = \boldsymbol{\Lambda}_1 + \boldsymbol{\Lambda}_2 \tag{6.14}$$

$$0 = \frac{\partial \Psi}{\partial \boldsymbol{\varepsilon}^{oi}} + \frac{\partial \Phi}{\partial \dot{\boldsymbol{\varepsilon}}^{oi}} + \boldsymbol{\Lambda}_1 : \frac{\partial \boldsymbol{C}_1}{\partial \dot{\boldsymbol{\varepsilon}}^{oi}} + \boldsymbol{\Lambda}_2 : \frac{\partial \boldsymbol{C}_2}{\partial \dot{\boldsymbol{\varepsilon}}^{oi}} = \left(1 - f^i\right)\boldsymbol{\sigma}^{oi} - \boldsymbol{\Lambda}_1 \tag{6.15}$$

$$0 = \frac{\partial \Psi}{\partial \boldsymbol{\varepsilon}^{i}} + \frac{\partial \Phi}{\partial \dot{\boldsymbol{\varepsilon}}^{i}} + \boldsymbol{\Lambda}_1 : \frac{\partial \boldsymbol{C}_1}{\partial \dot{\boldsymbol{\varepsilon}}^{i}} + \boldsymbol{\Lambda}_2 : \frac{\partial \boldsymbol{C}_2}{\partial \dot{\boldsymbol{\varepsilon}}^{i}} = f^i\boldsymbol{\sigma}^{i} - \boldsymbol{\Lambda}_2 \tag{6.16}$$

$$0 = \frac{\partial \Psi}{\partial \boldsymbol{\varepsilon}^{ki}} + \frac{\partial \Phi}{\partial \dot{\boldsymbol{\varepsilon}}^{ki}} + \boldsymbol{\Lambda}_1 : \frac{\partial \boldsymbol{C}_1}{\partial \dot{\boldsymbol{\varepsilon}}^{ki}} + \boldsymbol{\Lambda}_2 : \frac{\partial \boldsymbol{C}_2}{\partial \dot{\boldsymbol{\varepsilon}}^{ki}} = \left(1 - f^i\right)\boldsymbol{\Lambda}_2 - f^i\boldsymbol{\Lambda}_1 \tag{6.17}$$

$$0 = \frac{\partial \Psi}{\partial \tilde{\alpha}_k^{oi}} + \frac{\partial \Phi}{\partial \dot{\tilde{\alpha}}_k^{oi}} + \boldsymbol{\Lambda}_1 : \frac{\partial \boldsymbol{C}_1}{\partial \dot{\tilde{\alpha}}_k^{oi}} + \boldsymbol{\Lambda}_2 : \frac{\partial \boldsymbol{C}_2}{\partial \dot{\tilde{\alpha}}_k^{oi}} = \left(1 - f^i\right)\frac{\partial \Psi^{oi}}{\partial \tilde{\alpha}_k^{oi}} + (1 - f^i)\tilde{\chi}_k^{oi} \tag{6.18}$$

$$0 = \frac{\partial \Psi}{\partial \tilde{\alpha}_k^{i}} + \frac{\partial \Phi}{\partial \dot{\tilde{\alpha}}_k^{i}} + \boldsymbol{\Lambda}_1 : \frac{\partial \boldsymbol{C}_1}{\partial \dot{\tilde{\alpha}}_k^{i}} + \boldsymbol{\Lambda}_2 : \frac{\partial \boldsymbol{C}_2}{\partial \dot{\tilde{\alpha}}_k^{i}} = f^i\frac{\partial \Psi^{i}}{\partial \tilde{\alpha}_k^{i}} + f^i\tilde{\chi}_k^{i} \qquad k = 1 \dots n \tag{6.19}$$

From equations (6.15) and (6.16) it rapidly follows that:

$$\boldsymbol{\Lambda}_1 = \left(1 - f^i\right)\boldsymbol{\sigma}^{oi} \tag{6.20}$$

$$\boldsymbol{\Lambda}_2 = f^i\boldsymbol{\sigma}^{i} \tag{6.21}$$

Therefore, by virtue of equations (6.14), (6.20) and (6.21), the macroscopic stress tensor is obtained as the weighted sum of the micro-stress tensor inside the i^{th} constituent and the volume-weighted average of all other micro-stress tensors outside the i^{th} constituent:

$$\boldsymbol{\sigma} = \left(1 - f^i\right)\boldsymbol{\sigma}^{oi} + f^i\boldsymbol{\sigma}^{i} \tag{6.22}$$

In addition, from equation (6.17) the following equilibrium condition is obtained between the i^{th} constituent and the surrounding homogenised domain:

$$\left(1 - f^i\right)\boldsymbol{\sigma}^{oi} = f^i\boldsymbol{\sigma}^{i} \tag{6.23}$$

The homogenisation scheme used in this section is a simple volume averaging. In principle, more sophisticated homogenisation techniques can be adopted to specify the connection between the microscopic and macroscopic strain fields. This would require further research and investigation on homogenisation methods applicable to inelastic deformation of inhomogeneous materials which is outside the scope of this study. Furthermore, the interaction between different phases, as stated by the Maxwell's compatibility condition in equation (6.4), in this general thermodynamics formulation needs further specification. For instance, it is required that the specific definition of the kinematically compatible mode, denoted as $\dot{\varepsilon}^k$ in equation (6.4), be determined. The next section is a simple illustration of such an interaction of a two-phase solid material, with a localisation band.

6.3. A Thermodynamic Formulation of Localised Deformation

For a volume element of material containing a localisation band, two separate homogeneous solutions can be developed to describe the constitutive behaviour of each of the two material phases inside and outside the localisation band. The contribution of each material phase in determining the overall behaviour of the volume element can then be specified by adopting a homogenisation scheme the same as that outlined in Section 6.2. In the development of a two-scale model, Nguyen et al [36, 37] adopted a similar homogenisation scheme and defined the volume fraction of the localisation zone, f, as (see Figure 6.2):

$$f = \frac{\Omega_i}{\Omega_i + \Omega_o} = \frac{hA}{(H-h)A + hA} = \frac{h}{H} \tag{6.24}$$

In the above expression Ω_i and Ω_o represent the volume of the localisation band and that of the surrounding material, respectively, H is the characteristic size of the RVE and h represents the width of the localisation band. It should be noted that in this formulation the width and orientation of the localisation band are considered as invariants. If the Helmholtz free energy potentials for a unit volume of the material inside and outside the localisation band are, respectively, denoted as Ψ^i and Ψ^o, the general form of the Helmholtz free energy for the macroscopic volume element, as illustrated in Figure 6.2, is given as follows:

$$\Psi = (1-f)\Psi^o\left(\varepsilon_{ij}^o, \tilde{\alpha}_1^o, \dots, \tilde{\alpha}_N^o\right) + f\Psi^i\left(\varepsilon_{ij}^i, \tilde{\alpha}_1^i, \dots, \tilde{\alpha}_N^i\right) \tag{6.25}$$

In the above expression, $f = h/H$ and $(1-f)$ are volume fractions of the material inside and outside the localisation zone, represented by superscript, i and o, respectively. Furthermore, $\tilde{\alpha}_1^i, \dots, \tilde{\alpha}_N^i$ and $\tilde{\alpha}_1^o, \dots, \tilde{\alpha}_N^o$ are sets of N internal variables pertaining to the material inside and outside the localisation band, respectively. These two sets of internal variables are responsible for recording the history of inelastic deformation and/or energy dissipation in each individual material phase. In cases when the internal variables for the material inside and outside the band are of the same nature (e.g. the case of a homogeneous material which is going to bifurcate from the homogeneous state) this homogenisation scheme will be switched on at the onset of localisation, when the evolutions of these internal variables and, subsequently, their total values for the material inside and outside the band become different. However, if the two sets of internal variables are identical in nature and have the same evolutions and total values, the whole formulation automatically collapses to the homogeneous case, i.e. $\Psi = \Psi^i = \Psi^o$.

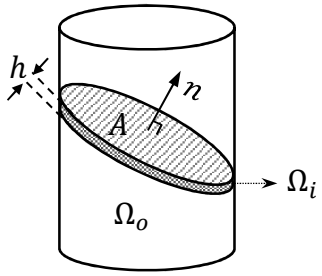

$$H = \frac{\Omega_o + \Omega_i}{A}$$

$\Omega_i \rightarrow$ Volume fraction of the material inside
$\Omega_o \rightarrow$ Volume fraction of the material outside
$A \rightarrow$ Area of the FPZ

Figure 6.2: Localisation band of width h embedded in a volume element of characteristic size H

Furthermore, as was discussed in Section 6.2, the power of deformation produced by macroscopic stresses can also be given as the weighted sum of the powers of deformation produced by microscopic stresses inside and outside the localisation zone (Hill-Mandel condition):

$$\delta W = \sigma_{ij}\dot{\varepsilon}_{ij} = (1-f)\sigma_{ij}^{o}\dot{\varepsilon}_{ij}^{o} + f\sigma_{ij}^{i}\dot{\varepsilon}_{ij}^{i} = (1-f)\delta W^{o} + f\delta W^{i} \tag{6.26}$$

Therefore, by making use of equations (6.25) and (6.26) according to the First Law of thermodynamics, the dissipation function can be given as:

$$\delta\Phi = \delta W - \dot{\Psi} = (1-f)\left(\delta W^{o} - \dot{\Psi}^{o}\right) + f\left(\delta W^{i} - \dot{\Psi}^{i}\right) = (1-f)\delta\Phi^{o} + f\delta\Phi^{i} \tag{6.27}$$

In the above expression $\delta\Phi^{i} = \delta\Phi^{i}\left(\tilde{\alpha}_1^{i}, \dots, \tilde{\alpha}_N^{i}, \dot{\tilde{\alpha}}_1^{i}, \dots, \dot{\tilde{\alpha}}_N^{i}\right)$ and $\delta\Phi^{o} = \delta\Phi^{o}\left(\tilde{\alpha}_1^{o}, \dots, \tilde{\alpha}_N^{o}, \dot{\tilde{\alpha}}_1^{o}, \dots, \dot{\tilde{\alpha}}_N^{o}\right)$ represent the dissipation functions for the unit volume of the material inside and outside localisation band, respectively.

As was discussed in Section 6.2, the development of a constitutive model for a non-homogeneous RVE, e.g. an RVE containing a localisation band, requires to, firstly, specify the relationship between the microscopic and macroscopic kinematic fields and, secondly, to specify the kinematic interdependency between different constituents within the RVE. Therefore, the first kinematic relationship gives the macroscopic strain rate ($\dot{\varepsilon}_{ij}$) as the weighted sum of the microscopic strains inside ($\dot{\varepsilon}_{ij}^{i}$) and outside ($\dot{\varepsilon}_{ij}^{o}$) the localisation band:

$$\dot{\varepsilon}_{ij} = (1-f)\dot{\varepsilon}_{ij}^{o} + f\dot{\varepsilon}_{ij}^{i} \tag{6.28}$$

The above kinematic relationship specifies the contribution of each constituent to the macroscopic strain field with respect to their volume fraction. In addition, bifurcation from the homogeneous state in geomaterials is associated with the occurrence of discontinuity in the strain field across the localisation band which is kinematically compatible with the surrounding material (discontinuous bifurcation [32]). Therefore, following the discussion

in section 6.2, the strain rate inside the localisation band ($\dot{\varepsilon}_{ij}^{i}$) can be given, from the Maxwell's compatibility condition, as the sum of the strain rate outside the localisation band ($\dot{\varepsilon}_{ij}^{o}$) and a kinematically admissible mode over the boundaries of the localisation band ($\dot{\varepsilon}_{ij}^{k}$) (equation (6.4)). For a localisation band with planar boundaries this kinematically admissible mode can be given as a velocity (displacement rate) jump between the two planar boundaries as [317, 318]:

$$\dot{\varepsilon}_{ij}^{k} = \frac{\left([\dot{u}]_i n_j\right)^s}{h} \tag{6.29}$$

In the above expression, $[\dot{u}]_i$ represents the velocity jump between the two sides of the localisation band and n_j is the unit vector normal to the orientation of the localisation band. The superscript s refers to the symmetric part of the 'directional velocity tensor'. Hence, the strain field for the material inside the localisation band is connected to the strain field outside the band by means of the Maxwell's compatibility condition, which is stated as:

$$\dot{\varepsilon}_{ij}^{i} = \dot{\varepsilon}_{ij}^{o} + \dot{\varepsilon}_{ij}^{k} = \dot{\varepsilon}_{ij}^{o} + \frac{\left([\dot{u}]_i n_j\right)^s}{h} \tag{6.30}$$

At the continuum level, the two microscopic strain tensors, $\dot{\varepsilon}_{ij}^{o}$ and $\dot{\varepsilon}_{ij}^{i}$ as well as the velocity jump vector, $[\dot{u}]_i$, play the role of internal variables and are termed here as macro-internal variables. In this sense, conditions of equations (6.28) and (6.30) specify the interaction and interdependency between the rates of macro-internal variables and also the macroscopic state variable, $\dot{\varepsilon}_{ij}$. The macro-internal variables also play the role of microscopic state variables for their associated constituent. In general, each constituent can have its own set of micro-internal variables and can exhibit a unique constitutive behaviour. For instance, in an RVE containing a localisation band under monotonic compressive loading the material inside the band undergoes further inelastic loading while the material outside the band will be unloaded. The overall behaviour of the RVE is then a combination of these two modes of behaviour.

Using equations (6.28) and (6.30), after some rearrangements, the macroscopic strain tensor ($\dot{\varepsilon}_{ij}$) can be given in the two following alternative forms:

$$\dot{\varepsilon}_{ij} = \dot{\varepsilon}_{ij}^{o} + \frac{f}{h}\left([\dot{u}]_i n_j\right)^s \tag{6.31}$$

$$\dot{\varepsilon}_{ij} = \dot{\varepsilon}_{ij}^{i} - \frac{(1-f)}{h}\left([\dot{u}]_i n_j\right)^s \tag{6.32}$$

Following the discussion in Chapter 3, the conditions of equations (6.31) and (6.32) can be given in the form of some kinematic constraint equations as follows:

$$\mathrm{C}_{ij}^{1} = \dot{\varepsilon}_{ij} - \dot{\varepsilon}_{ij}^{o} - \frac{f}{h}\left([\dot{u}]_i n_j\right)^s = 0 \tag{6.33}$$

$$\mathrm{C}_{ij}^{2} = \dot{\varepsilon}_{ij} - \dot{\varepsilon}_{ij}^{i} + \frac{(1-f)}{h}\left([\dot{u}]_i n_j\right)^s = 0 \tag{6.34}$$

As can be seen from equations (6.33) and (6.34), in accordance with the dissipation function, kinematic constraint equations are also homogeneous first order functions in terms of the rates of internal variables. Thereby, the dissipation function can be supplemented by the kinematic constraints of equations (6.33) and (6.34) as follows:

$$\delta\Phi' = \delta\Phi + \Lambda_{ij}^{1} C_{ij}^{1} + \Lambda_{ij}^{2} C_{ij}^{2} \geq 0 \tag{6.35}$$

Therefore, from equations (6.25) and (6.35) and by following the standard procedures of the generalised thermodynamics, as outlined in Chapter 3, the following set of equations can be written for an RVE containing a localisation band:

$$\sigma_{ij} = \frac{\partial\Psi}{\partial\varepsilon_{kl}} + \frac{\partial\Phi}{\partial\dot{\varepsilon}_{kl}} + \Lambda_{kl}^{1}\frac{\partial C_{ij}^{1}}{\partial\dot{\varepsilon}_{kl}} + \Lambda_{kl}^{2}\frac{\partial C_{ij}^{2}}{\partial\dot{\varepsilon}_{kl}} = \Lambda_{kl}^{1}\delta_{ik}\delta_{jl} + \Lambda_{kl}^{2}\delta_{ik}\delta_{jl} = \Lambda_{ij}^{1} + \Lambda_{ij}^{2} \tag{6.36}$$

$$0 = \frac{\partial\Psi}{\partial\varepsilon_{kl}^{o}} + \frac{\partial\Phi}{\partial\dot{\varepsilon}_{kl}^{o}} + \Lambda_{kl}^{1}\frac{\partial C_{ij}^{1}}{\partial\dot{\varepsilon}_{kl}^{o}} + \Lambda_{kl}^{2}\frac{\partial C_{ij}^{2}}{\partial\dot{\varepsilon}_{kl}^{o}} = (1-f)\sigma_{ij}^{o} - \Lambda_{kl}^{1}\delta_{ik}\delta_{jl} = (1-f)\sigma_{ij}^{o} - \Lambda_{ij}^{1} \tag{6.37}$$

$$0 = \frac{\partial\Psi}{\partial\varepsilon_{kl}^{i}} + \frac{\partial\Phi}{\partial\dot{\varepsilon}_{kl}^{i}} + \Lambda_{kl}^{1}\frac{\partial C_{ij}^{1}}{\partial\dot{\varepsilon}_{kl}^{i}} + \Lambda_{kl}^{2}\frac{\partial C_{ij}^{2}}{\partial\dot{\varepsilon}_{kl}^{i}} = f\sigma_{ij}^{i} - \Lambda_{kl}^{2}\delta_{ik}\delta_{jl} = f\sigma_{ij}^{i} - \Lambda_{ij}^{2} \tag{6.38}$$

$$\begin{aligned} 0 = \frac{\partial\Psi}{\partial[u]_k} + \frac{\partial\Phi}{\partial[\dot{u}]_k} + \Lambda_{ij}^{1}\frac{\partial C_{ij}^{1}}{\partial[\dot{u}]_k} + \Lambda_{ij}^{2}\frac{\partial C_{ij}^{2}}{\partial[\dot{u}]_k} &= \frac{(1-f)}{h}\Lambda_{ij}^{2}\delta_{ik}n_j - \frac{f}{h}\Lambda_{ij}^{1}\delta_{ik}n_j \\ &= \frac{(1-f)}{h}\Lambda_{kj}^{2}n_j - \frac{f}{h}\Lambda_{kj}^{1}n_j \end{aligned} \tag{6.39}$$

$$0 = \frac{\partial\Psi}{\partial\tilde{\alpha}_m^{o}} + \frac{\partial\Phi}{\tilde{\alpha}_m^{o}} + \Lambda_{kl}^{1}\frac{\partial C_{ij}^{1}}{\dot{\tilde{\alpha}}_m^{o}} + \Lambda_{kl}^{2}\frac{\partial C_{ij}^{2}}{\dot{\tilde{\alpha}}_m^{o}} = (1-f)\frac{\partial\Psi^{o}}{\partial\tilde{\alpha}_m^{o}} + (1-f)\tilde{\chi}_m^{o} \qquad m = 1 \ldots N \tag{6.40}$$

$$0 = \frac{\partial\Psi}{\partial\tilde{\alpha}_m^{i}} + \frac{\partial\Phi}{\tilde{\alpha}_m^{i}} + \Lambda_{ij}^{1}\frac{\partial C_{ij}^{1}}{\dot{\tilde{\alpha}}_m^{i}} + \Lambda_{ij}^{2}\frac{\partial C_{ij}^{2}}{\dot{\tilde{\alpha}}_m^{i}} = f\frac{\partial\Psi^{i}}{\partial\tilde{\alpha}_m^{i}} + f\tilde{\chi}_m^{i} \qquad m = 1 \ldots N \tag{6.41}$$

From equations (6.37) and (6.38) it rapidly follows that:

$$\Lambda_{ij}^{1} = (1-f)\sigma_{ij}^{o} \tag{6.42}$$

$$\Lambda_{ij}^2 = f\sigma_{ij}^i \tag{6.43}$$

where σ_{ij}^i and σ_{ij}^o are stress tensors for the localisation band and the surrounding material, respectively. Therefore, by virtue of equation (6.36), the macroscopic stress tensor is deduced as the weighted sum of the stress tensors inside and outside the localisation band as:

$$\sigma_{ij} = (1-f)\sigma_{ij}^o + f\sigma_{ij}^i \tag{6.44}$$

Furthermore, from equation (6.39) along with equations (6.42) and (6.43) the following result is obtained:

$$\frac{f(1-f)}{h}\left(\sigma_{ij}^i - \sigma_{ij}^o\right)n_j = 0 \tag{6.45}$$

For $0 < f < 1$, that is, for cases when the RVE contains a localisation band of width $0 < h < H$, the continuity of traction across the boundaries of the localisation band is deduced as:

$$\left(\sigma_{ij}^i - \sigma_{ij}^o\right)n_j = 0 \tag{6.46}$$

In order to complete the formulation, it is also essential to obtain the explicit expression of the velocity jump $[\dot{u}]_i$ in terms of the macroscopic strain increment, $\dot{\varepsilon}_{ij}$. To this end, the internal equilibrium or the continuity of traction across the localisation band, as stated by equation (6.46), is used in the rate form as:

$$\left(\dot{\sigma}_{ij}^i - \dot{\sigma}_{ij}^o\right)n_j = 0 \tag{6.47}$$

Furthermore, by virtue of equations (6.33) and (6.34), the microscopic strain increments for the material outside and inside the localisation band in terms of the total macroscopic strain increment and the velocity jump are given as:

$$\dot{\varepsilon}_{ij}^o = \dot{\varepsilon}_{ij} - \frac{f}{h}\left([\dot{u}]_i n_j\right)^s \tag{6.48}$$

$$\dot{\varepsilon}_{ij}^i = \dot{\varepsilon}_{ij} + \frac{1-f}{h}\left([\dot{u}]_i n_j\right)^s \tag{6.49}$$

Therefore, if the tangent stiffness tensors for the material inside and outside the localisation band are denoted as C_{ijkl}^{iT} and C_{ijkl}^{oT}, respectively, then the stress increments inside and outside the localisation band are given as:

$$\dot{\sigma}_{ij}^i = C_{ijkl}^{iT}\dot{\varepsilon}_{kl}^i = C_{ijkl}^{iT}\left(\dot{\varepsilon}_{kl} + \frac{(1-f)}{h}\left([\dot{u}]_k n_l\right)^s\right) \tag{6.50}$$

$$\dot{\sigma}_{ij}^{o} = C_{ijkl}^{oT}\dot{\varepsilon}_{kl}^{o} = C_{ijkl}^{oT}\left(\dot{\varepsilon}_{kl} - \frac{f}{h}([\dot{u}]_k n_l)^s\right) \tag{6.51}$$

Substitution of equations (6.50) and (6.51) into the rate form of the traction continuity condition (equation (6.47)), results in the following expression:

$$C_{ijkl}^{iT}\left(\dot{\varepsilon}_{kl} + \frac{1-f}{h}([\dot{u}]_k n_l)^s\right)n_j = C_{ijkl}^{oT}\left(\dot{\varepsilon}_{kl} - \frac{f}{h}([\dot{u}]_k n_l)^s\right)n_j \tag{6.52}$$

Rearrangement of the above expression gives:

$$\left((1-f)A_{ij}^{i} + fA_{ij}^{o}\right)[\dot{u}]_j = h\left(C_{ijkl}^{oT} - C_{ijkl}^{iT}\right)\dot{\varepsilon}_{kl}n_j \tag{6.53}$$

In the above expression A_{ij}^{i} and A_{ij}^{o} are the acoustic tensors pertaining to the material inside and outside the localisation band, respectively, and they are defined as follows:

$$A_{ij}^{i} = C_{ijkl}^{iT}n_k n_l \tag{6.54}$$

$$A_{ij}^{o} = C_{ijkl}^{oT}n_k n_l \tag{6.55}$$

Therefore, the velocity jump $[\dot{u}]_i$ across the boundaries of the localisation band is given in terms of the macroscopic strain increment by the following expression:

$$[\dot{u}]_i = h\left[(1-f)A_{ij}^{i} + fA_{ij}^{o}\right]^{-1}\left(C_{jklm}^{oT} - C_{jklm}^{iT}\right)\dot{\varepsilon}_{lm}n_k \tag{6.56}$$

Furthermore, the dissipative parts of the internal forces corresponding to the microscopic internal variables are obtained from equations (6.40) and (6.41) as follows:

$$\tilde{\chi}_n^o = -\frac{\partial\Psi^o}{\partial\tilde{\alpha}_n^o} - \left(\Lambda_{kl}^1\frac{\partial C_{ij}^1}{\dot{\tilde{\alpha}}_n^o} + \Lambda_{kl}^2\frac{\partial C_{ij}^2}{\dot{\tilde{\alpha}}_n^o}\right)/(1-f) = -\frac{\partial\Psi}{\partial\tilde{\alpha}_n^o} \qquad n = 1 \dots N \tag{6.57}$$

$$\tilde{\chi}_n^i = -\frac{\partial\Psi^i}{\partial\tilde{\alpha}_n^i} - \left(\Lambda_{ij}^1\frac{\partial C_{ij}^1}{\dot{\tilde{\alpha}}_n^i} + \Lambda_{ij}^2\frac{\partial C_{ij}^2}{\dot{\tilde{\alpha}}_n^i}\right)/f = -\frac{\partial\Psi}{\partial\tilde{\alpha}_n^i} \qquad n = 1 \dots N \tag{6.58}$$

For practical applications of the above formulation, it should be noted that this model describes the behaviour of an RVE which is initially homogeneous. After the onset of localisation has taken place, the RVE bifurcates from the homogeneous state and becomes non-homogeneous. One way of describing the behaviour of the RVE after localisation is to assume an elastic behaviour for the material outside the localisation band, while the material inside the band continues to deform elastically [37]. An alternative approach, which is used in this study, is assume a single mode of behaviour, i.e. inelastic behaviour for both the localisation band and the surrounding material. However, it should be noted that the

evolutions and the total values of the state and internal variables of the models will be different for the materials inside and outside the localisation band.

6.3.1. The Case of a Localisation Band of Vanishing Thickness ($h \to 0$)

For some quasi-brittle materials, such as hard rocks the thickness of the localisation band or the fracture process zone (FPZ) is very small compared to the characteristic size of the specimen or structure. In such cases, the constitutive behaviour of the FPZ can be described using a cohesive crack model or a cohesive-frictional interface (see Appendix B). For the case when the width of the localisation band is negligible, i.e. $h \to 0$, the volume averaged macroscopic strain tensor is obtained by virtue of equation (6.28) and (6.30) as follows:

$$\dot{\varepsilon}_{ij} = (1-f)\dot{\varepsilon}^o_{ij} + f\dot{\varepsilon}^i_{ij} = \left(1-\frac{h}{H}\right)\dot{\varepsilon}^o_{ij} + \frac{h}{H}\left(\dot{\varepsilon}^o_{ij} + \frac{\left([\dot{u}]_i n_j\right)^s}{h}\right) = \dot{\varepsilon}^o_{ij} + \frac{1}{H}\left([\dot{u}]_i n_j\right)^s \tag{6.59}$$

In addition, the increment of the macroscopic stress tensor, given by equation (6.44), reduces to:

$$\dot{\sigma}_{ij} = \dot{\sigma}^o_{ij} \tag{6.60}$$

Therefore, by making use of equation (6.59) the following expression is deduced for the increment of the macroscopic stress tensor:

$$\dot{\sigma}_{ij} = \dot{\sigma}^o_{ij} = C^{oT}_{ijkl}\left(\dot{\varepsilon}_{kl} - \frac{1}{H}\left([\dot{u}]_k n_l\right)^s\right) \tag{6.61}$$

where C^{oT}_{ijkl} is the tangent stiffness of the bulk outside the FPZ. If the tangent stiffness of the thin FPZ is denoted as K_{ij} then the traction continuity condition across the FPZ can be written as:

$$\dot{\sigma}^o_{ij} n_j = K_{ij}[\dot{u}]_j \tag{6.62}$$

Substitution of equation (6.61) into equation (6.62) after some rearrangement gives:

$$\left(\frac{1}{H}C^{oT}_{ijkl} n_k n_l + K_{ij}\right)[\dot{u}]_j = C^{oT}_{ijkl}\dot{\varepsilon}_{kl} n_j \tag{6.63}$$

Recalling that $A^o_{ij} = C^{oT}_{ijkl} n_k n_l$ is the acoustic tensor for the material outside the FPZ, the following expression for the velocity jump across the FPZ is deduced:

$$[\dot{u}]_i = \left(\frac{1}{H}A^o_{kl} + K_{kl}\right)^{-1} C^{oT}_{klmj} n_m \dot{\varepsilon}_{ij} \tag{6.64}$$

Substituting the above expression into equation (6.61) results in the following expression for the macroscopic stress tensor:

$$\dot{\sigma}_{ij} = \dot{\sigma}^{o}_{ij} = C^{oT}_{ijkl}\left(1 - \frac{1}{H}A^{-1}_{pq}C^{oT}_{pqrs}n_r n_s\right)\dot{\varepsilon}_{kl} \tag{6.65}$$

In the above expression, A^{-1}_{ij} is given from equation (6.64) as:

$$A^{-1}_{ij} = \left(\frac{1}{H}A^{o}_{ij} + K_{ij}\right)^{-1} \tag{6.66}$$

In cases where the thickness of the localisation band is infinitesimal ($h \to 0$), the constitutive model for the localisation band specifies the relationships between the tractions acting on the boundaries of the localisation band (or fracture process zone) and the corresponding displacements. An example of this case is provided in Appendix B, where a very thin fracture process zone is modelled as a cohesive-frictional interface. However, it should be noted that the case of an infinitesimal h as shown in the developments of this section is a special case of a more general formulation presented earlier. This new development makes it possible to describe the cohesive behaviour using a continuum model. In this sense, a single continuum model can be used for the RVE and after the onset of localisation the same continuum model can be used to describe the constitutive behaviour of a fracture process zone with infinitesimal thickness. An important aspect of the present developments is that it facilitates to take into account the stress triaxiality in cohesive crack modelling, a feature which is usually missing in conventional constitutive models developed for cohesive cracks.

6.3.2. Continuum Tangent Stiffness Tensor

From equation (6.44), the increment of the macroscopic stress tensor is given as:

$$\dot{\sigma}_{ij} = (1-f)\dot{\sigma}^{o}_{ij} + f\dot{\sigma}^{i}_{ij} \tag{6.67}$$

Substitution of equations (6.50) and (6.51) into the above expression will result in:

$$\dot{\sigma}_{ij} = (1-f)\left(C^{oT}_{ijkl}\left(\dot{\varepsilon}_{kl} - \frac{f}{h}([\dot{u}]_k n_l)^s\right)\right) + f\left(C^{iT}_{ijkl}\left(\dot{\varepsilon}_{kl} + \frac{(1-f)}{h}([\dot{u}]_k n_l)^s\right)\right) \tag{6.68}$$

By rearranging equation (6.68) the following expression for the increment of the macroscopic stress tensor is obtained:

$$\dot{\sigma}_{ij} = \left[(1-f)C^{oT}_{ijkl} + fC^{iT}_{ijkl}\right]\dot{\varepsilon}_{kl} - \frac{f(1-f)}{h}\left[C^{oT}_{ijkl} - C^{iT}_{ijkl}\right]([\dot{u}]_k n_l)^s \tag{6.69}$$

Substituting for the velocity jump, $[\dot{u}]_k$, from equation (6.56) into equation (6.69) results in the following expression for the increment of the macroscopic stress tensor:

$$\dot{\sigma}_{ij} = \left[(1-f)C^{oT}_{ijkl} + fC^{iT}_{ijkl}\right]\dot{\varepsilon}_{kl} - f(1-f)\left[C^{oT}_{ijkl} - C^{iT}_{ijkl}\right]\left(A^{-1}_{pq}\left(C^{oT}_{pqrs} - C^{iT}_{pqrs}\right)n_r n_s\right)\dot{\varepsilon}_{kl} \tag{6.70}$$

In the above expression the second order tensor A_{ij} is defined as (see equation (6.56)):

$$A_{ij} = (1-f)A^{i}_{ij} + fA^{o}_{ij} \tag{6.71}$$

Therefore, the macroscopic tangent stiffness tensor for the RVE is given as:

$$C^{T}_{ijkl} = \left[\left((1-f)C^{oT}_{ijkl} + fC^{iT}_{ijkl}\right) - f(1-f)\left(C^{oT}_{ijkl} - C^{iT}_{ijkl}\right)\left(A^{-1}_{pq}\left(C^{oT}_{pqrs} - C^{iT}_{pqrs}\right)n_r n_s\right)\right] \tag{6.72}$$

From the expression of the tangent stiffness tensor (equation (6.72)) it is clear that the model is neither an upper bound nor a lower bound solution but it lays between these two limits. This feature of the model is a direct consequence of specifying the kinematic relationships at two scales. Firstly, the macroscopic strain field is given as the weighted sum of the strain fields inside and outside the localisation band. Secondly, the kinematic relationship between the localisation band and the surrounding material is specified in the form of Maxwell's compatibility condition. The macroscopic stress is then obtained automatically within the thermodynamic formulation as the weighted sum of the two stress fields inside and outside the band. Furthermore, for the homogeneous state, e.g. before the onset of localisation, the tangent stiffness tensors are the same inside and outside the band, i.e. $C^{oT}_{pqrs} = C^{iT}_{pqrs}$ and the solution collapses to a homogeneous solution.

6.3.3. An explicit stress return algorithm

In this section, an explicit stress return algorithm for numerical implementation of the two-scale model is presented. This follows earlier developments in [27, 28]. Explicit stress return algorithms are easy to implement and can also serve the verification of other more complicated stress return algorithms if used with extremely small increments. The explicit algorithm in Section 6.2.2, requires the enforcement of traction continuity in incremental form (equation (6.47)) in order to obtain the velocity jump (equation (6.56)) for determination of tangent stiffness tensor. The enforcement of traction continuity in incremental form inevitably introduces error accumulation during the deformation and affects the accuracy of the numerical solutions. In order to improve the performance of the explicit algorithm an algorithm which uses the total form of the traction continuity is

developed in this section. Due to numerical error, the traction continuity ($\sigma_{ij}^{o} n_j = \sigma_{ij}^{i} n_j$) has a small residual as:

$$r_i = \sigma_{ij}^{o} n_j - \sigma_{ij}^{i} n_j \tag{6.73}$$

The first order Taylor expansion of the residual traction vector can be written as:

$$r_i^{new} = r_i^{old} + \Delta\sigma_{ij}^{o} n_j - \Delta\sigma_{ij}^{i} n_j \tag{6.74}$$

where r_i^{old} is the traction residual vector calculated from the stress states in the previous step:

$$r_i^{old} = \left(\sigma_{ij}^{o}\right)^{old} n_j - \left(\sigma_{ij}^{i}\right)^{old} n_j \tag{6.75}$$

The traction vectors for the material inside and outside the localisation band are given from equations (6.50) and (6.51) as follows:

$$\Delta\sigma_{ij}^{o} n_j = C_{ijkl}^{oT}\left(\Delta\varepsilon_{kl} - \frac{f}{h}\left(\Delta[u]_k n_l\right)^s\right) n_j = C_{ijkl}^{oT}\Delta\varepsilon_{kl} n_j - \frac{f}{h} C_{ijkl}^{oT} n_l n_j \Delta[u]_k \tag{6.76}$$

$$\begin{aligned}\Delta\sigma_{ij}^{i} n_j &= C_{ijkl}^{iT}\left(\Delta\varepsilon_{kl} + \frac{(1-f)}{h}\left(\Delta[u]_k n_l\right)^s\right) n_j \\ &= C_{ijkl}^{iT}\,\Delta\varepsilon_{kl} n_j + \frac{(1-f)}{h} C_{ijkl}^{iT} n_l n_j \Delta[u]_k\end{aligned} \tag{6.77}$$

Substituting equations (6.76) and (6.77) into equation (6.74) and rearranging the obtained expression will result in:

$$r_i^{new} = r_i^{old} + \left(C_{ijkl}^{oT} - C_{ijkl}^{iT}\right)\Delta\varepsilon_{kl} n_j - \left(\frac{f}{h} C_{ijkl}^{oT} n_l n_j + \frac{(1-f)}{h} C_{ijkl}^{iT} n_l n_j\right)\Delta[u]_k \tag{6.78}$$

The above expression can be rewritten as:

$$r_i^{new} = r_i^{old} + \left(C_{ijkl}^{oT} - C_{ijkl}^{iT}\right)\Delta\varepsilon_{kl} n_j - \left(\frac{f}{h} A_{ij}^{o} + \frac{(1-f)}{h} A_{ij}^{i}\right)\Delta[u]_k \tag{6.79}$$

where A_{ij}^{o} and A_{ij}^{i} are the acoustic tensors for the materials inside and outside of the localisation band. Enforcing the requirement of $r_i^{new} = 0$ and solving the obtained equation for the displacement jump increment $\Delta[u]_i$ leads to:

$$\Delta[u]_i = \left(\frac{f}{h} A_{ij}^{o} + \frac{(1-f)}{h} A_{ij}^{i}\right)^{-1}\left(r_j^{old} + \left(C_{ijkl}^{oT} - C_{ijkl}^{iT}\right)\Delta\varepsilon_{kl} n_i\right) \tag{6.80}$$

Once $\Delta[u]_i$ has been calculated, the strain increments can be obtained as:

$$\Delta\varepsilon_{ij}^{i} = \Delta\varepsilon_{ij} + \frac{1-f}{h}\left(\Delta[u]_i n_j\right)^s \tag{6.81}$$

$$\Delta\varepsilon_{ij}^{o} = \Delta\varepsilon_{ij} - \frac{f}{h}\left(\Delta[u]_i n_j\right)^s \tag{6.82}$$

Having the strain increments for the material inside and outside the localisation band their associated stress increment can be computed using a classical stress return algorithm [319, 320]. Then the macroscopic stress increment can be computed using equation (6.44). The aspects of the numerical implementation of the two-scale approach and its performance can be found in [36].

6.4. Analysis of the Deterministic Size Effect

As was discussed in Section 4.7, the observed mechanical responses of rock specimens in drained triaxial tests are a combination of structural and material responses. In general, whenever the consequence of failure is the post-peak softening or the lack of ductility, a size effect is expected [31]. The size effect is the most important practical consequence of fracturing phenomena and observation of the size effect is an effective way to calibrate the parameters of a constitutive model. Understanding the effect of the size of the specimen (or structure) on its mechanical response under a certain loading configuration is of paramount importance in engineering design and applications. The size effect is a problem of scaling which should be taken into proper consideration, especially, in areas such as geotechnical engineering, arctic engineering and geomechanics. In other areas of engineering, where the structural components can be tested at full size (e.g. aerospace engineering), the scaling problem is a relatively less pressing issue. In solid mechanics, the size effect is understood as the effects of the characteristic size (or dimension) of a specimen (or structure) on its mechanical response, i.e. nominal strength and the post peak load-displacement response. Theories developed for addressing the size effect problem can either be classified as statistical or as deterministic size effect theories. In the former, it is assumed that the size effect is caused by the randomness of material strength which increases with the dimension (or characteristic size) of the structure. In the later, on the other hand, the size effect is known to be caused by stress redistributions due to the stable propagation of a fracture process zone (or a localisation zone).

The overall response of a rock specimen is determined by the material behaviour inside and outside the band and also the orientation and thickness of the localisation band. In the context of the two-scale model, the orientation of the band is determined by means of a standard bifurcation analysis (e.g. loss of positive definiteness of the acoustic tensor).

Therefore, for a given set of parameters, the orientation of the localisation band under a certain loading condition is always the same. The thickness of the localisation band is governed by the material microstructure and also boundary conditions. In particular, experimental observations show that the band thickness is a physical quantity which can be linked to the grain size of the material (e.g. 8-20 times the mean grain diameter) in granular materials [194, 321, 322] or 3 times the maximum aggregate diameter in concrete [323]. Figure 6.3 illustrates the variations in the response of a model under triaxial compression at 30 MPa confining pressure, with respect to different widths of the localisation band, while all other model parameters are kept unchanged. The coupled damage-plasticity model for porous rocks, developed in Chapter 4, is used for this parametric study and the material model parameters are the same as those given in Table 4.2. The incorporation of a length scale, via parameter h, into the model formulation allows for correctly capturing the effect of size on the macroscopic response of a specimen at the constitutive level.

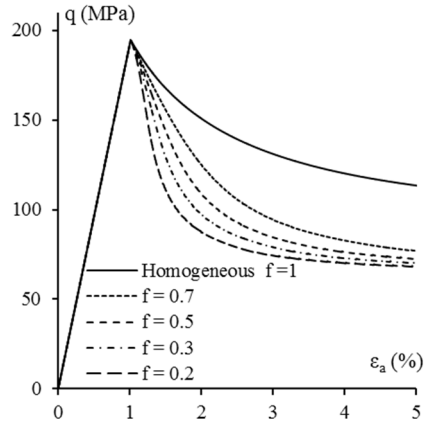

Figure 6.3: The effect of the width of the localisation band on the average stress-strain response of a specimen modelled by means of the two-scale model

In Section 4.7.2, the effect of the specimen size on the overall mechanical response of the specimen was investigated by means of finite element (FE) simulation of rock specimens in drained triaxial tests, using the material model for porous rocks developed and discussed in Sections 4.3 – 4.6. In this section, the two-scale model, detailed in Section 6.3, along with the coupled damage-plasticity model developed for porous rocks in Chapter 4 are used to investigate the effect of the deterministic size effect on the overall mechanical response recorded for rock specimens in experimental studies. As mentioned earlier, upon the onset of localisation the homogeneity of the material is lost and the material inside and outside the localisation band exhibit different responses to different stress (and kinematic) fields inside and outside the band. In particular, the dissipation mechanisms (e.g. damage

and plasticity) are active inside the localisation band, while they are deactivated outside the band. Therefore, the amount of total dissipated energy is mainly determined by the size of the fracture process zone or the shear localisation band. On the other hand, the amount of total elastic energy which is stored within the specimen prior to the formation of fracture process zone scales up with the specimen (or structure) size. Accordingly, specimens of the same cross section and different slenderness can store different amounts of elastic energy, but the amount of dissipated energy is the same for all cases as the width of the localisation band does not change with the size of the specimen. This, however, is only true if the aspect ratio of the specimen is large enough so that the stress distribution inside the specimen is not majorly affected by the end effects due to the interaction between the steel platens of the loading machine and the rock specimen. The effect of the specimen slenderness on the load-displacement response of specimens of unit cross section and different slenderness under uniaxial tension is illustrated in Figure 6.4. In Figure 6.4, the area under each load-displacement curve can be interpreted as fracture energy or the amount of energy which is dissipated during the course of inelastic deformation and fracturing. As can be seen in Figure 6.4, in all cases the same amount of energy is dissipated. However, the effect of the specimen slenderness can be clearly seen in the post-peak softening branch, which becomes progressively steeper for longer specimens.

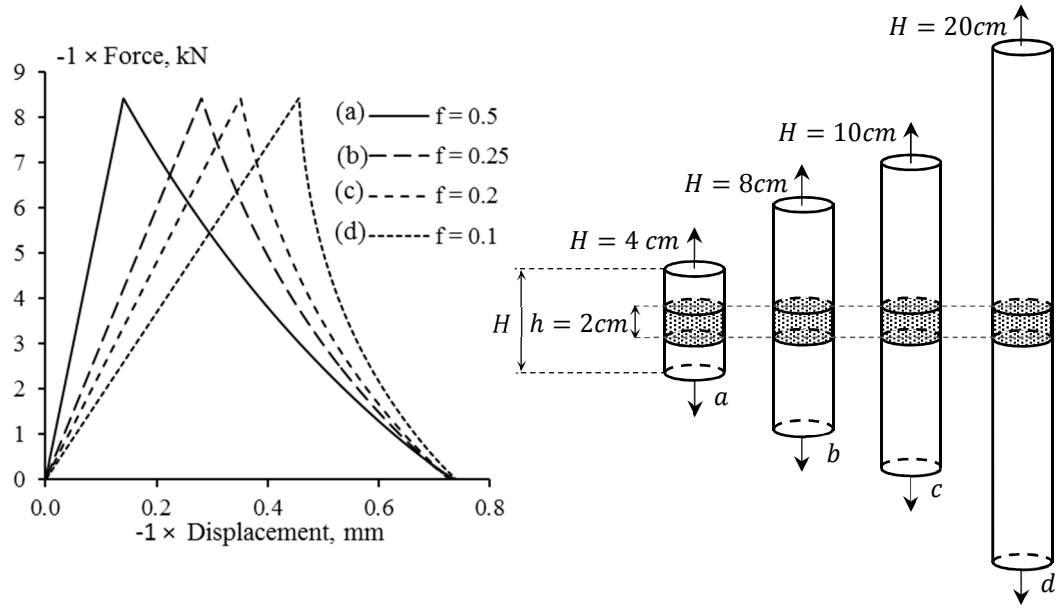

Figure 6.4: Analysis of size effect on the load-displacement response of rock specimens with the same cross-sectional area and different slenderness by means of the two-scale model

Due to the loss of homogeneity of stress and strain (and other kinematic) fields upon the onset of localisation the macroscopic stress and strains measured for rock specimens in

laboratory experiments are only meaningful as averages. Due to the localisation of deformation, material points inside a specimen, depending on whether they are located inside or outside the localisation band, exhibit different stress-strain responses. The overall average stress-strain response measured in tests is actually a combination of stress-strain responses of different material points within the specimen. This issue was addressed in finite element simulation of porous rock specimens in Section 4.7.2, where it was demonstrated that upon the onset of localisation, inelastic loading continues in the finite elements (integration points) inside the localisation band while those outside the band were unloaded. It was also shown and discussed that since the structural effects on the overall mechanical response are accounted for in FE simulation of rock specimens, a closer agreement between the simulated results and those from experiments can be achieved (Figure 4.42), compared to the case when the whole specimen is assumed as an RVE over which the stress and strain fields are assumed to be homogeneous (Figure 4.23).

Furthermore, the localisation features of the rate-independent coupled damage-plasticity model (Section 4.5.4) causes the BVPs to be ill-posed and, hence, the rate-dependent enhancement of the material model was carried out in Section 4.7.1, as a computationally efficient regularisation scheme, to alleviate the ill-posedness of the BVPs. In the application of the rate-dependent model, the basis for calibrating the viscosity parameter is that the axial strain rate is prescribed the same as that in the laboratory tests ($\dot{\varepsilon}_a = 10^{-6}$/s) and the viscosity parameter η is calibrated using stress-strain data and the localisation properties of the rate-dependent model (see Sections 4.7.1 and 4.7.2). It should be noted that although the viscosity parameter can be calibrated to replicate the load-displacement (or average stress-strain) response, there is no direct link between the width of the localisation band and the viscosity parameter. As illustrated in

Figure 6.5, identical load-displacement responses can be obtained for two different special discretisation by calibrating the viscosity parameter η. Therefore, despite the difference in the width of the localisation band the same amount of energy is dissipated in both cases. This can be explained by considering the strain profile across the localisation bands, which indicates a greater strain rate for the band of smaller width. Therefore, the discrepancy between the widths of the two localisation band is compensated for by the strain rate to produce the same amount of dissipation.

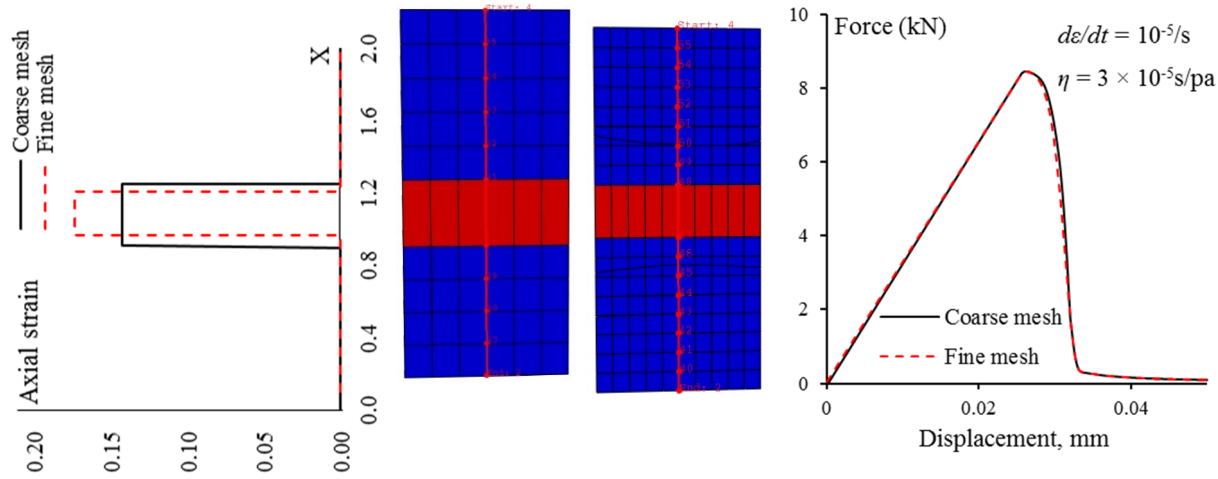

Figure 6.5: Load-displacement response and strain profile across the localisation band for two different mesh sizes

Figure 6.6 (a) illustrates the FE simulation of a Bentheim sandstone specimen under drained triaxial test with 30 MPa confining pressure. The overall stress-strain response of the specimen is calculated as the average of the stress-strain responses of the material inside and outside the band.

Figure 6.6 (a) also illustrates the stress-strain response for two elements inside and outside the localisation band. The same analysis can be carried out using the two-scale approach through activating the localisation band with a prescribed thickness which is embedded in an RVE. The localisation band is activated at the onset of bifurcation, which is determined by means of a bifurcation criterion (Equation 4.70). The classical bifurcation criterion, which is used throughout this study, determines the stress state and the orientation of the localisation bad for which the governing PDEs lose their ellipticity. This loss of ellipticity of the governing PDEs can be interpreted as the loss of material stability in a certain direction at which the acoustic tensor loses its positive definiteness [32]. Figure 6.6 (b) illustrates the overall structural response as well as the material responses inside and outside the localisation band captured by means of the two-scale model.

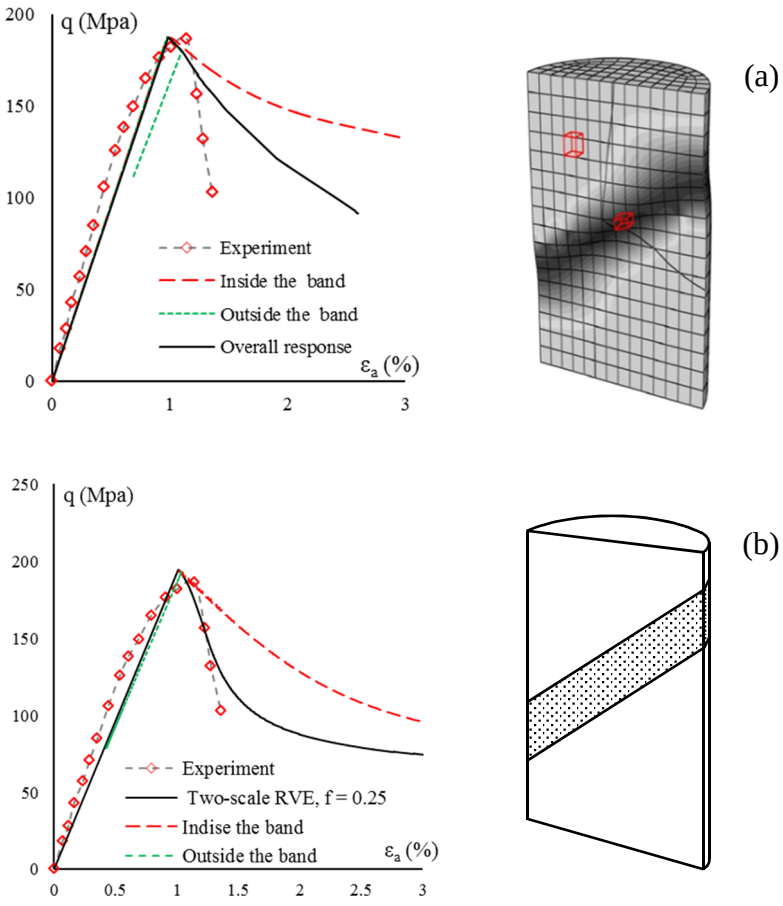

Figure 6.6: Average stress-strain response and the stress-strain responses for the material inside and outside the localisation band for a specimen of Bentheim sand stone under 30 MPa confining pressure analysed by means of (a) FE simulation (b) the two-scale model with $f = h/H = 0.25$.

As was discussed in Chapters 4 and 5, the simple rate-dependent regularisation (Perzyna viscoplasticity [219]) scheme alleviates the numerical instabilities of the coupled damage-plasticity models in a more computationally efficient way compared to non-local or gradient models. More specifically, rate-dependent regularisation can eliminate the mesh-dependency of the FE simulation (Figure 6.5). However, if in addition to numerical stabilisation, prediction of the thickness of the localisation band is also required, then the viscose regularisation may not be adequate, no direct link can be established between the viscosity parameter and the width of the localisation band (see Figure 6.5). It should, also, be noted that the application of the rate-dependent models still requires that the size of the finite elements be smaller than the width of the localisation band. Therefore, the application of these models for very large scale problems of geotechnical and mining engineering is still limited by the available computational resources. The two-scale approach, however, enables simulating substantially large scale problems by enriching the kinematics of the constitutive

models through incorporating the essential features of localised deformation and failure at the material level. As illustrated in Figure 6.7, the accuracy of the model in predicting the mechanical response (of the specimens) is significantly improved compared to the case of assuming a homogeneous RVE. Furthermore, the time of computation is significantly reduced while achieving similar results compared to the FE simulation.

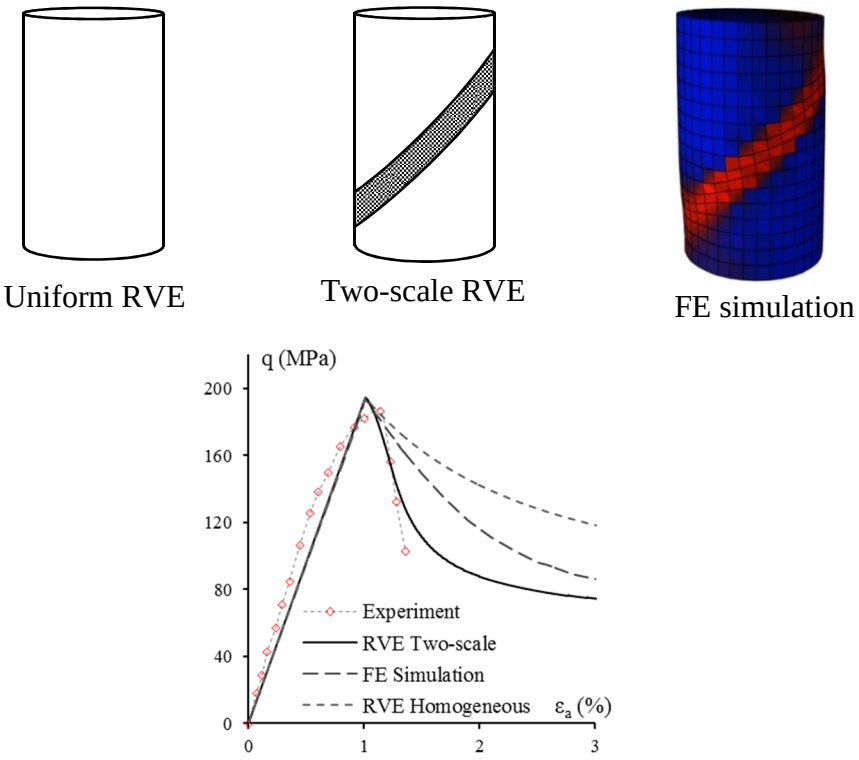

Figure 6.7: Comparison between the stress-strain response of a Bentheim sandstone specimen under 30 MPa confining pressure and the stress-strain responses produced by the homogeneous and two-scale models at the material level and FE simulation

Figure 6.7 shows a discrepancy between the results of FE simulation and that of the two scale model. This discrepancy is due to the simplifications in the two-scale model, which assumes two separate zones and a '"jump" in the behaviour. It should be recalled that the thickness of the localisation band, h, is specified as a constant parameter in the two-scale approach. In Figure 6.7, the volume fraction of the localisation band is specified ($f = h/H = 0.1$) so that the best fit with the experimental data can be achieved. However, it is emphasised here that the discussions and developments in this chapter are not aiming towards achieving best fits. The focus is rather on the development of an approach which is more physically correct compared to other approaches, which do not take into account the induced non-homogeneity at and beyond the onset of localisation at the material level. As illustrated in

Figure 6.8, the results of FE simulation and the two-scale model are in closer agreement when the same bandwidth as that in the FE simulation ($f = h/H \approx 0.3$) is used in the two-scale approach.

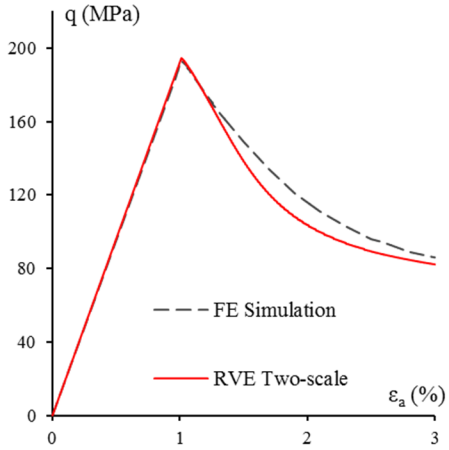

Figure 6.8: Comparison between the stress-strain response of the two-scale model and that of the FE simulation when the same bandwidth as that obtained in FE simulation is used for the two-scale model

Nevertheless, assuming a constant width for the localisation band poses some challenges in selecting the bandwidth h as an input parameter for the two-scale approach. No experimental procedure has been hitherto designed to effectively measure this length scale. A common strategy for measuring the length scale either in the two-scale model or in non-local or gradient models is to use the profile of strain across the localisation band. However, this profile shows a distribution with gradual variation across the localisation band. The main question is, therefore, how the length scale h can be defined from the distribution of kinematic fields (e.g. strain or displacement) across the localisation band? Providing an answer to this question, however, requires further experimental and numerical investigations at the grain scale which is outside the scope of this study.

The two-scale approach can effectively capture the deterministic size effect by taking into account the inhomogeneity of the stress and kinematic (strain and other kinematic internal variables) fields at the onset of localisation. It should, however, be noted that the two scale model assumes the width of the localisation band to be invariant throughout post-localisation phase of deformation. This assumption approximates the variations of the kinematic field within the localisation band and the surrounding bulk.

Figure 6.9 illustrates the displacement and strain profiles across the localisation band obtained from the FE simulation and the analysis by means of the two-scale model. Non-

local and gradient models can produce the gradual variation of the kinematic field across the localisation band. However, as mentioned earlier, the implementation of these models requires a discretisation size smaller than the width of the localisation band. If the location of the band is also unknown, then the whole domain under consideration should be discretised with the spatial resolution smaller than the bandwidth. This would severely limit the application of non-local and/or gradient models to very large scale problems of geotechnical and mining engineering. The two-scale model approximates the variation of the displacement and strain fields by assuming a constant bandwidth (h). This bandwidth is then directly incorporated in the constitutive equations and the interaction between the materials inside and outside the band at the constitutive level. Therefore, the application of the two-scale model does not require a smaller element size than the bandwidth. This feature of the two-scale model makes it desirable for large-scale modelling in geotechnical and mining engineering. However, for smaller scale problems non-local or gradient models produce more accurate results.

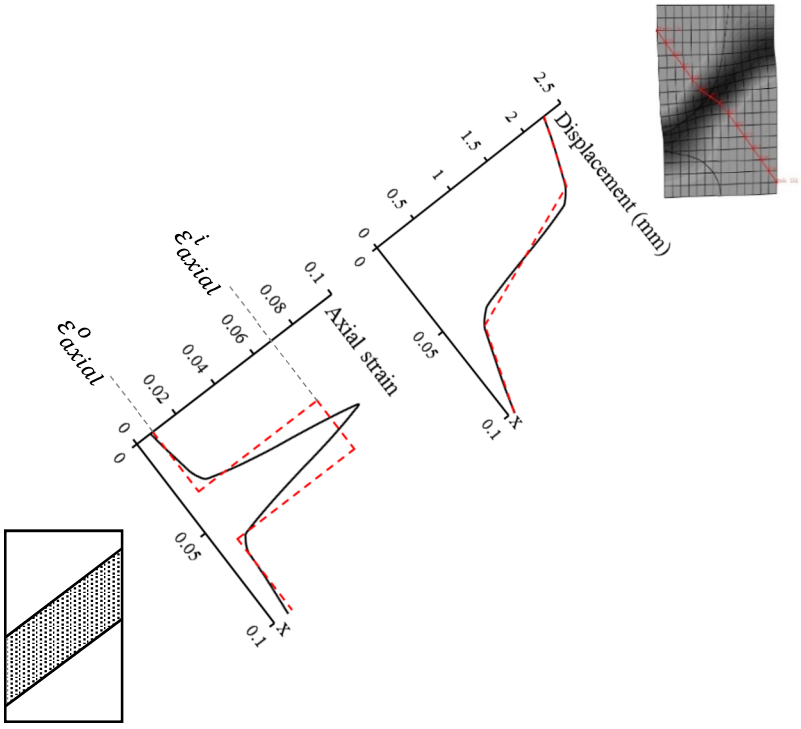

Figure 6.9: Variation of displacement and strain profiles across the localisation band captured by means of FE simulation and the two-scale model

6.5. Summary and Discussion

The main objective of this chapter is to develop a thermodynamic approach to constitutive modelling of localised failure. The two-scale approach [37] featuring two different responses upon the onset of localisation was the basis for this development. In order to apply the thermodynamic field theory to the constitutive modelling of localised failure, a homogenisation scheme is proposed in this study. This homogenisation scheme, although simplistic, enables the modelling of localised failure to be carried out in a consistent and coherent manner within the framework of generalised thermodynamics.

Furthermore, the application of the two-scale approach in capturing the deterministic size effect is briefly discussed in this chapter. Understanding the deterministic size effect on the mechanical response of structures is of paramount importance in any solid mechanics problem, especially, in areas such as geotechnical and mining engineering that conducting experiments on full-scale structures is not usually possible. The analysis of the deterministic size effect by means of the two-scale approach is considerably more efficient and computationally cheaper compared to other kinematically enhanced models such as non-local or gradient models since the numerical implementation of the two-scale model does not require a discretisation resolution finer than the width of the localisation zone. Furthermore, the two-scale model, detailed in Section 6.3, can be easily enhanced to accommodate more than a single crack or fracture process zone within a volume element.

It is also discussed in this chapter that the two-scale approach specifies the connection between the materials inside and outside the localisation band by approximating the kinematic fields across a band of an invariant width ($h = constant$). In other words, the localisation band which is activated at the onset of bifurcation has a fixed width (or thickness) throughout the entire course of post-localisation deformation. However, the results of FE analysis (and also experimental measurements [194, 321-323]) show that the thickness of the localisation band is not constant and it evolves from an initially thick band to a final fracture of negligible thickness ($h \to 0$). It should also be noted that although the width of the localisation band (h) can be incorporated in the constitutive equations as a length scale, the measurement or interpretation of this width from experimental observations may not be straightforward. This length scale is selected by approximating the profile of kinematic variables across the localisation band, usually by satisfying an energy balance criterion. Although the macroscopic load-displacement response of the experimental

samples can be replicated by calibrating the model parameters and selecting a length scale, there are more than just one unique length scale that saftisfy the energy balence criterion. The schematic representation of this discussion is depicted in Figure 6.10. The two strain profiles across the localisation band are resulted from selecting two different withs (h_1 and h_2) for the localisation band. In both cases the macroscopic load-displacemnt response and the dissipated energy are the same. This discussion also applies to non-local and gradient models. This issue is briefly addressed in Chapter 7 as a subject for future research.

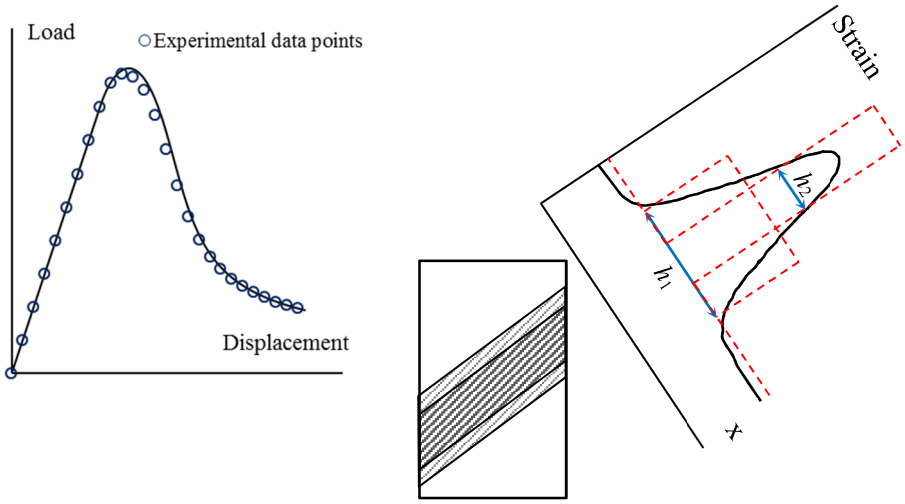

Figure 6.10: Schematic demonstration of two different bandwidth with the same load displacement response and different strain profiles across the localisation band

CHAPTER 7

Conclusions and Future Research

7.1. Summary and Conclusions

A thermodynamic approach has been adopted in this study to develop constitutive models for rocks, using continuum damage mechanics and plasticity theory. The focus of the constitutive model developments is on capturing the key features of the macroscopic behaviour of rock material. These features include brittle and ductile failure modes and the transition from brittle to ductile, dilation and compaction and localised failure. Emphasis is placed on the thermodynamic admissibility of the models by formulating the constitutive models within the generalised thermodynamic framework. In particular, a thermodynamic approach is developed for modelling the localised failure in geomaterials. In this section, the main contributions of this study together with the limitations and weaknesses of the proposed models in this study is briefly discussed. In the end, possible future research directions are proposed.

The main contributions of this research are:

- Development of constitutive models for two general rock types (porous and compact rocks) within the framework of generalised thermodynamics using damage mechanics and plasticity theory. The key feature that distinguishes these models from existing ones is their capability to capture both the mechanical behaviour and corresponding localisation modes of failure under both low and confining pressures. In particular, it is demonstrated that these coupled damage-plasticity models are capable of predicting the macroscopic behaviour of rocks (brittle, ductile, brittle-ductile transition, dilation and compaction) under a wide range of stress states (Chapters 4 and 5). Furthermore, the proposed coupled damage-plasticity models are able to predict the onset and orientation of localised deformation for a wide range of the applied confining pressures.

- Developing a thermodynamics formulation for modelling post-localisation at the material (constitutive) level. A general thermodynamic basis for constitutive modelling of localised failure in geomaterials is proposed, as an essential step that follows the thermodynamic formulation for homogeneous behaviour. In fact this formulation is a general one that covers both homogeneous and localised behaviour to facilitate the developments of constitutive models that can capture both pre- and post-localisation responses in a physically meaningful way. The proposed approach is then used to model the localised failure of geomaterials as an example (Chapter 6).

- An investigation of localised failure in geomaterials at both structural (specimen) and material levels. In particular, the regularised coupled damage-plasticity model for porous rocks, using rate-dependent enhancement, allows the finite element simulations of localised failure in cylindrical rock specimens under a wide range of confining pressures. Based on the results of FE simulations, the deterministic size effect is investigated and discussed (Chapter 4). In parallel with this, it is also demonstrated that once a correct mechanism of failure (in this study, localised modes of failure) is identified and embedded in a model, it is possible to investigate this size effect at the material level. In this regard, the constitutive model developed for porous rocks is also used in conjunction with the results from the thermodynamics development to analyse the deterministic size effect at the material level. This is physically meaningful and also more computationally efficient, compared to the full finite element simulation of rock specimens. This also has good potential for simulations of large scale issues.

In the subsequent sections, the above-mentioned contributions and findings of the present research will be further illustrated and discussed.

7.1.1. Constitutive model development for rock using damage and plasticity

Coupled damage plasticity models are developed in this study to describe the macroscopic behaviour of porous and compact rocks (Chapters 4 and 5). The development of the models was carried out within the framework of generalised thermodynamics. Within the framework of generalised thermodynamics, the entire constitutive relations can be obtained through explicitly defining two scalar functions, i.e. an energy potential and a dissipation function [19, 21, 22]. Coupling between damage and plasticity is specified in the formulation of the dissipation rate function, which, in turn, gives rise to the existence of a single yield function, which controls the simultaneous evolution of all internal variables, i.e.

the scalar damage variable and plastic strains. It is also demonstrated that owing to possessing a single generalised yield function that evolves to a failure function, under the effects of both damage and plastic deformation, the proposed model facilitates the simulation of rock behaviour under a wide range of confining pressures. In particular, unlike many existing models in the literature, no explicit hardening/softening laws are needed in this formulation. Instead, both hardening and softening together with their transition are contained in the evolution of the yield function from its initial state (onset of inelastic behaviour) to ultimate failure. This greatly simplifies the structure of the models, reduces the number of parameters, and can facilitate their use in practical applications.

An important feature that, to the best of my knowledge, has been overlooked in the development of constitutive models for geomaterials is the capability to predict correctly both the onset and orientation of localised deformation, in conjunction with the mechanical responses, under different confining pressures. Adding the requirements to predict correctly the onset and orientation of localisation bands to a model is, to some extent, like imposing more constraints that the model should conform to. As has been demonstrated in Chapters 4 & 5, the proposed coupled damage plasticity models are capable of predicting the onset and orientation of the localisation band for a wide range of confining pressures. Capturing all these behavioural features together is not trivial and is missing in most (if not all) constitutive models. Furthermore, it is demonstrated, through the development of two separate constitutive models for porous and compact rocks, how different deformation mechanisms can be taken into consideration by selecting and defining the internal variables in the formulation of thermodynamically admissible constitutive models. The main motivation for these developments is the observed differences between the dilational/contractive responses of porous and compact rocks.

7.1.2. Thermodynamics developments

It is essential for any constitutive model to be thermodynamically admissible. It is, in principle, possible to apply the requirements for the thermodynamic admissibility of a constitutive model retrospectively after the completion of the model formulation. This approach, however, may lead to introducing *ad hoc* assumptions in the formulation of the model. A more rigorous and consistent approach is, therefore, to construct the constitutive model within a well-established thermomechanical framework. Constitutive models in this study are all developed within the framework of generalised thermodynamics or thermodynamics with internal variables. Standard procedures and principles of the

generalised thermodynamic framework are summarised and presented in Chapter 3 of this thesis in a simple way which facilitates the application of the framework to the constitutive modelling of engineering materials.

More importantly, given localisation as an important feature of rock behaviour that should be correctly captured in a model, it is essential to establish a general thermodynamic formulation that can cover both homogeneous and localised modes of failure in a physically meaningful and consistent manner. To the best of my knowledge, no such thermodynamic frameworks exist in the literature, although there have been constitutive models capable of handling post-localisation responses and capturing size effects at the material level. This issue is addressed in Chapter 6, in which a thermodynamic approach for modelling the localised deformation and failure in geomaterials is developed. For this purpose, the original thermodynamics field theory is enhanced to accommodate constitutive modelling for geomaterials under both homogeneous and localised modes of failure. This enhancement, although simplistic, has proven to be useful in constitutive modelling of localised deformation, which is a special type of non-homogeneity being introduced to a homogeneous material element at the onset of localisation. Furthermore, this simple enhancement can also serve as a basis for further developments of the thermodynamics field theory for it to be applicable to constitutive modelling of materials with more complex modes of inhomogeneity.

7.1.3. Study of the deterministic size effect

Experimental data from triaxial tests do not merely reflect the intrinsic material response and they are also affected by the size and probably the geometry of the specimen. In order to investigate the effect of specimen size on its mechanical response finite element simulation of cylindrical rock specimens under drained triaxial loading condition is carried out in this study. The results of FE simulations confirms that the size effect on the mechanical response of rock specimens are more profound under loading conditions conducive to softening behaviour and brittle failure. Furthermore, in order to eliminate the numerical instabilities pertaining to the rate-independent coupled damage-plasticity model, Perzyna type viscoplasticity [219] is used for rate-dependent regularisation of the rate-independent models. In FE simulations of the triaxial tests, the strain rate is kept constant and the same at that applied in the actual tests. The viscosity parameter η is then calibrated to converge to a solution. However, despite a good match between experimental and numerical results, no direct link can be established between the viscosity parameter and the

width of the localisation band. This is due to the use of rate-dependent enhancement purely as a mathematical approach to regularise the constitutive behaviour for dealing with material instability issues in analysing boundary value problems.

It is desirable, therefore, to directly incorporate the width of the localisation band as a length scale into the constitutive equations. To this end, a thermodynamics framework is developed in this thesis to model the localised failure of geomaterials. The basis for this development is a two-scale approach proposed by Nguyen et al [36, 37]. The enhancement at the material level has a good physical justification, given the experimental observations of localised failure addressed in Chapter 2. This allows a computationally cheaper approach to size effect issues at the material level, while retaining all essential features of the model. In particular classical approach to dealing with localised failure and size effects is to enhance a model with a regularisation after the model development. In this sense, a regularisation, despite some physical justifications, is usually not well connected to a model and its behaviour, besides its intended use as a localisation limiter. It is therefore more physically meaningful to close that gap, although not completely yet in this study, by embedding physically meaningful mechanisms of failure directly in a constitutive model, as part of its development.

7.2. Limitations and Weaknesses of the Models Developed in This Study

In general, any constitutive model has some kind of limitation and/or potential weaknesses. As was pointed out by Houlsby and Puzrin [19]: "*the constitutive relations are simply approximations to the behaviour of real materials; none of which will behave exactly according to the idealisations employed. Thus constitutive relations are never "true" for a real material; they can only provide solutions that approximate what happens in reality to a certain degree of precision*". Like any other constitutive model, the constitutive models developed in this study also have their own limitations and potential weaknesses. The main limitations of the models developed in this study can be summarised as follows:

- Despite their remarkable capability in predicting the macroscopic behaviour of porous and compact rocks, the proposed coupled damage-plasticity models in this study do not directly take into account the micromechanisms of deformation and energy dissipation. Therefore, these models are unable to explain the different

microstructural evolutions (grain crushing, pore collapse, the interaction between micro-cracks, etc.) which take place in rock material during inelastic deformation.

- At the macro continuum level, the constitutive models in this study are of isotropic nature, due to the use of a scalar damage variable. In this sense, anisotropic behaviour, including unilateral effects under tension-compression transition, is not accounted for. As reasoning in Chapter 2, we consider this anisotropic behaviour, as a material characteristic, minor to that stronger one due to the onset and development of a localisation band. The latter one in this case is not purely a material behaviour but in our opinion a mix between material and structural ones and is treated using the two-scale approach. However the consequence of neglecting anisotropic nature of behaviour prior to localisation is an issue that should be explored in the future, together with possible enhancements to take anisotropy into account.

- The rate-dependent enhancements, used merely for the elimination of numerical instabilities of the rate-independent models. These enhancements do not have a clear physical link with the observed rate-dependent response of rocks and they are not derived from the thermodynamics principles, discussed and used throughout this study. In general, the mechanical response of rocks is sensitive to the rate of deformation [241, 242, 324, 325] (see also Appendix C). The rate-dependent nature of deformation, usually observed in rocks, is not taken into account in the constitutive models developed in this thesis.

- Through rate-dependent regularisation and finite element implementation of the proposed constitutive models, it was found that no direct link can be established between the width of the localisation band and the parameters of the homogeneous models. Therefore, a thermodynamics approach was developed to model the localised failure of geomaterials by inserting the width of the localisation band as a length scale into the constitutive equations. This thermodynamic formulation is based on a two-scale approach which assumes an invariant width and orientation for the localisation band throughout the post-localisation deformation. Therefore, the width and orientation of the localisation band are considered as material input parameters that can, in principle, be measured from experiments. However, no experimental procedure has been hitherto designed to effectively measure this length scale. A common strategy for measuring the length scale (either in the two-scale

model or in non-local or gradient models) is to use the profile of strain across the localisation band. However, this profile shows a distribution with gradual variation across the localisation band. One can, therefore, pose the question as to how this length scale can be defined using the smooth distribution of kinematic fields (e.g. strain or displacement) across the localisation band. However, the problem can be viewed from an entirely different angle. In this sense, the question can be put as: would further enhancements of the constitutive equations facilitate the identification of a single length scale from a distribution? To provide a convincing answer to this question necessitates further experimental, numerical and theoretical research and developments.

7.3. Future Research Directions

In this section, based on the limitations and potential weaknesses of the current developments, discussed in the previous section, some possible directions are proposed for the future research.

7.3.1. Micromechanical developments

Techniques and frameworks used in this study in the development of constitutive models need further enhancement so that micromechanisms of deformation and energy dissipation can be directly incorporated into model formulations in a straightforward and consistent manner. For this purpose, understanding the underlying micromechanisms of deformation and the mathematical description of essential mechanisms at micro-scale is necessary. In addition to this, innovative, sophisticated yet simple enough homogenisation schemes are required to map these micromechanisms to the macroscopic scale. One particular example of benefits of a micromechanical model is the elimination of the need for defining the yield function of the constitutive models based on laboratory tests on specimens. In generalised thermodynamics, each internal variable is responsible for describing the evolution of a dissipative mechanism during inelastic deformations. Instead of phenomenologically defining the internal variables (e.g. damage variable and plastic strain tensor) each internal variable can directly represent the evolution of a dissipative mechanism at the microscale, e.g. friction, micro-cracking in mode I and II, grain crushing, etc. Subsequently, the macroscopic dissipation function can be defined by combining all the microscopic dissipation functions. Then the yield function in the dissipative stress space, which is obtained by performing a degenerate Legendre transform on the dissipation

function, will specify the attainable stress domain for the material under a given loading configuration. The yield function in the true stress space can be obtained from the yield in the dissipative stress space (see Chapters 4 and 5). This yield function which is obtained from the micromechanical considerations can now be verified against the experimental observations of yielding the laboratory specimens. The main motivation for this development is that, as was discussed in Chapter 4, experimental measurements are carried out on laboratory specimens and, therefore, the recorded mechanical response is not merely representative of material behaviour but is also influenced by the size of the specimen.

7.3.3. Localisation of deformation in a band of varying width

The distribution of strain profile across the localisation band in FE simulations and also experimental observations [194, 321-323] reveals that the strain concentration gradually increases from a background value to a maximum, usually at the centre of the localisation band. Application of all models which incorporate the width of the localisation band as a length scale into their formulations involves selecting this length scale from a gradually varying strain profile. This is, in general, possible only by approximating the strain field inside the localisation band through satisfying some energy equivalence criterion and by fitting the model to the macroscopic load-displacement data (see Figure 4.39). Experimental procedures for determining the width of the localisation band also involve indirect and approximate measurements, e.g. by making links between the width of the localisation band and the grain size of the material (e.g. 8-20 times the mean grain diameter) in granular materials [194, 321, 322] or 3 times the maximum aggregate diameter in concrete [323].

In this section, it is briefly discussed that the introduction of the varying width of the localisation band may be feasible though further kinematic enhancements of the constitutive model. This may be achieved if instead of assuming an invariant width for the localisation band, it is assumed that the width of the localisation band varies with the evolution of inelastic deformations. In this sense, the width of the localisation band is inserted into the model formulation not as a material input parameter, but as an internal variable. This internal variable can evolve from an initial value (e.g. a very thick band) to a final macroscopic fracture with a negligible thickness (the case $h \to 0$). As the width of the localisation band reduces with the evolution of inelastic processes, the material outside the band becomes progressively non-homogeneous while the material inside the current localisation band can still be assumed as homogeneous. With this assumption, the generic thermodynamic framework developed for constitutive modelling of heterogeneous materials in Chapter 6

can be used to specify the kinematic relationship between the current active localisation band and the surrounding non-homogeneous material.

In order to further clarify the discussion, an RVE which has bifurcated form the homogeneous state under uniaxial tensile loading can be considered (Figure 7.1). As schematically demonstrated in Figure 7.1, it is assumed that the width of the localisation band is reduced with the evolution of inelastic processes. In addition, the strain profile suggests that the strain concentration also takes place within a progressively narrower band. For a discrete approach, the strain profile can be approximated by defining the width of the localisation band as a discrete and monotonically decreasing function of the total value of one of the internal variables pertaining to the material inside the currently active localisation band, e.g. $h = h(\tilde{\alpha}_k^i)$. Is this sense, once $\tilde{\alpha}_k^i$ has reached a certain value the solution is continued by adopting a new width for the localisation band, depending of the definition of $h = h(\tilde{\alpha}_k^i)$. In this sense, if the diminution of the width of the localisation from a thick band to a macro-fracture ($h \to 0$) is supposed to take place in N steps, then the total strain rate at the RVE level, $\dot{\boldsymbol{\varepsilon}}$, at the i^{th} step can be given as:

$$\dot{\boldsymbol{\varepsilon}} = f^i \dot{\boldsymbol{\varepsilon}}^i + \left(1 - f^i\right)\overline{\dot{\boldsymbol{\varepsilon}}^{oi}} \tag{7. 1}$$

In the above expression, $\dot{\boldsymbol{\varepsilon}}^i$ is the strain rate inside the i^{th} active localisation band with the width h_i and the volume fraction $f^i = h^i/H$. The term $\overline{\dot{\boldsymbol{\varepsilon}}^{oi}}$ represents the homogenised strain rate outside the i^{th} active localisation zone. The strain rate outside the i^{th} active zone is homogenised in order to obtain a single stress-strain relationship. This facilitates the application of the developments in Chapter 6. To this end, the volume-weighted average of the strain rates for the material outside the i^{th} active localisation band, $\overline{\dot{\boldsymbol{\varepsilon}}^{oi}}$, can be given as:

$$\begin{aligned}\overline{\dot{\boldsymbol{\varepsilon}}^{oi}} &= \frac{(1-f^1)\dot{\boldsymbol{\varepsilon}}^{o1} + \sum_{j=1}^{i-1}\left(f^j - f^{j+1}\right)\dot{\boldsymbol{\varepsilon}}^{oj+1}}{(1-f^1) + \sum_{j=1}^{i-1}(f^j - f^{j+1})} \\ &= \frac{(1-f^1)\dot{\boldsymbol{\varepsilon}}^{o1} + \sum_{j=1}^{i-1}\left(f^j - f^{j+1}\right)\dot{\boldsymbol{\varepsilon}}^{oj+1}}{(1-f^i)}\end{aligned} \tag{7. 2}$$

In addition, the kinematic relationship between the i^{th} active localisation band and the surrounding materials is given by Maxwell compatibility condition as:

$$\dot{\boldsymbol{\varepsilon}}^i = \overline{\dot{\boldsymbol{\varepsilon}}^{oi}} + \dot{\boldsymbol{\varepsilon}}^{ki} = \overline{\dot{\boldsymbol{\varepsilon}}^{oi}} + \frac{([\dot{\boldsymbol{u}}]\otimes\boldsymbol{n})^s}{h^i} \tag{7. 3}$$

In the above expression, $\dot{\boldsymbol{\varepsilon}}^{ki}$ is a kinematically admissible mode across the boundaries of the localisation band at the i^{th} step, $\boldsymbol{n}$ is an outward unit vector normal to the planar boundaries

of the active band and $[\dot{\boldsymbol{u}}]$ is the velocity jump across the active band. Similar to $\overline{\dot{\boldsymbol{\varepsilon}}^{oi}}$, the internal variables outside the i^{th} active band can also be given as the volume-weighted average of the internal variables of all the deactivated bands. For instance the volume-weighted average of the k^{th} internal variable outside the i^{th} active band is given as:

$$\overline{\tilde{\alpha}_k^{oi}} = \frac{(1-f^1)\tilde{\alpha}_k^{o1} + \sum_{j=1}^{i-1}\left(f^j - f^{j+1}\right)\tilde{\alpha}_k^{oj+1}}{(1-f^i)} \tag{7. 4}$$

From equations (7. **1**) and (7. 3) the following constraint equations are obtained (see Chapter 6):

$$\boldsymbol{C}_1 = \dot{\boldsymbol{\varepsilon}} - \overline{\dot{\boldsymbol{\varepsilon}}^{oi}} - f^i\frac{([\dot{\boldsymbol{u}}]\otimes\boldsymbol{n})^s}{h^i} = 0 \tag{7. 5}$$

$$\boldsymbol{C}_2 = \dot{\boldsymbol{\varepsilon}} - \dot{\boldsymbol{\varepsilon}}^i + \left(1-f^i\right)\frac{([\dot{\boldsymbol{u}}]\otimes\boldsymbol{n})^s}{h^i} = 0 \tag{7. 6}$$

where $\overline{\dot{\boldsymbol{\varepsilon}}^{oi}}$ is given by equation (7. 2). Therefore, the dissipation function can be supplemented by the above constraint equations as (see Chapter 6):

$$\delta\Phi' = \delta\Phi + \boldsymbol{\Lambda}_1 : \boldsymbol{C}_1 + \boldsymbol{\Lambda}_2 : \boldsymbol{C}_2 = f^i\delta\Phi^i + \left(1-f^i\right)\delta\Phi^{oi} + \boldsymbol{\Lambda}_1 : \boldsymbol{C}_1 + \boldsymbol{\Lambda}_2 : \boldsymbol{C}_2 \tag{7. 7}$$

where, $\delta\Phi^i = \delta\Phi^i\left(\tilde{\alpha}_1^i, \dots, \tilde{\alpha}_N^i, \dot{\tilde{\alpha}}_1^i, \dots, \dot{\tilde{\alpha}}_N^i\right)$ and $\delta\Phi^{oi} = \delta\Phi^{oi}\left(\overline{\tilde{\alpha}_1^{oi}}, \dots, \overline{\tilde{\alpha}_N^{oi}}, \overline{\dot{\tilde{\alpha}}_1^{oi}}, \dots, \overline{\dot{\tilde{\alpha}}_N^{oi}}\right)$ represent the dissipation functions for a unit volume of the material inside and outside the i^{th} active band.

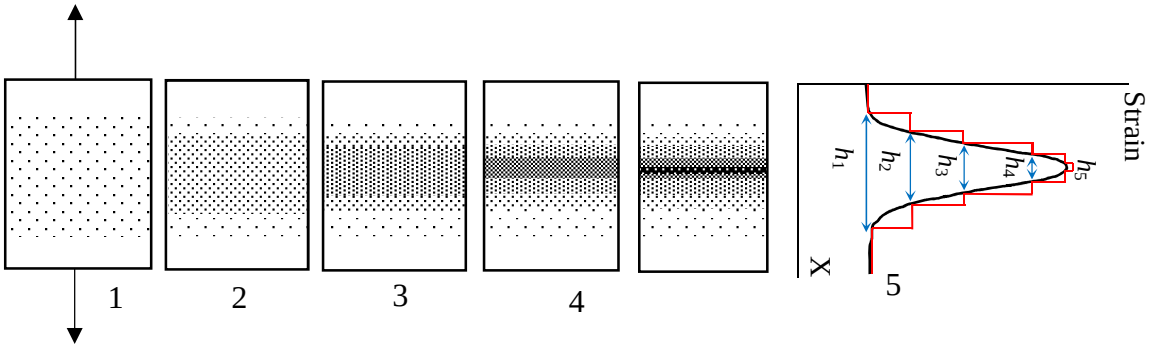

Figure 7.1: Schematic evolution of the width of the localisation band in uniaxial tension

Once the definition of $h\left(\tilde{\alpha}_k^i\right)$ is specified the following constraint equation can be written:

$$C_0 = h - h\left(\tilde{\alpha}_k^i\right) = 0 \tag{7. 8}$$

Subsequently, the Helmholtz free energy potential is supplemented with the above constraint equation:

$$\Psi' = \Psi + \Lambda_0 C_0 \; = f^i \Psi^i + \left(1 - f^i\right)\Psi^{oi} + \Lambda_0 C_0 \tag{7. 9}$$

where $\Psi^i = \Psi^i(\boldsymbol{\varepsilon}^i, \tilde{\alpha}_1^i, \dots, \tilde{\alpha}_N^i)$ is the Helmholtz free energy potentials for the material inside the i^{th} active band and the $\Psi^{oi} = \Psi^{oi}\left(\boldsymbol{\varepsilon}^{oi}, \tilde{\alpha}_1^{oi}, \dots, \tilde{\alpha}_N^{oi}\right)$ represents the Helmholtz free energy for the homogenised bulk outside the boundaries of the i^{th} active band. The rest of the constitutive relations can be obtained from the standard procedures of generalised thermodynamics as outlined in Chapter 3. In particular, following the discussion presented in Section 3-5 the following sets of equations are obtained:

$$\boldsymbol{\sigma} = \frac{\partial \Psi}{\partial \boldsymbol{\varepsilon}} + \frac{\partial \Phi}{\partial \dot{\boldsymbol{\varepsilon}}} + \boldsymbol{\Lambda}_1 : \frac{\partial \boldsymbol{C}_1}{\partial \dot{\boldsymbol{\varepsilon}}} + \boldsymbol{\Lambda}_2 : \frac{\partial \boldsymbol{C}_2}{\partial \dot{\boldsymbol{\varepsilon}}} + \Lambda_0 \frac{\partial C_0}{\partial \dot{\boldsymbol{\varepsilon}}} = \boldsymbol{\Lambda}_1 + \boldsymbol{\Lambda}_2 \tag{7. 10}$$

$$0 = \frac{\partial \Psi}{\partial \overline{\boldsymbol{\varepsilon}^{oi}}} + \frac{\partial \Phi}{\partial \overline{\dot{\boldsymbol{\varepsilon}}^{oi}}} + \boldsymbol{\Lambda}_1 : \frac{\partial \boldsymbol{C}_1}{\partial \overline{\dot{\boldsymbol{\varepsilon}}^{oi}}} + \boldsymbol{\Lambda}_2 : \frac{\partial \boldsymbol{C}_2}{\partial \overline{\dot{\boldsymbol{\varepsilon}}^{oi}}} + \Lambda_0 \frac{\partial C_0}{\partial \overline{\dot{\boldsymbol{\varepsilon}}^{oi}}} = \left(1 - f^i\right)\overline{\boldsymbol{\sigma}^{oi}} - \boldsymbol{\Lambda}_1 \tag{7. 11}$$

$$0 = \frac{\partial \Psi}{\partial \boldsymbol{\varepsilon}^i} + \frac{\partial \Phi}{\partial \dot{\boldsymbol{\varepsilon}}^i} + \boldsymbol{\Lambda}_1 : \frac{\partial \boldsymbol{C}_1}{\partial \dot{\boldsymbol{\varepsilon}}^i} + \boldsymbol{\Lambda}_2 : \frac{\partial \boldsymbol{C}_2}{\partial \dot{\boldsymbol{\varepsilon}}^i} + \Lambda_0 \frac{\partial C_0}{\partial \dot{\boldsymbol{\varepsilon}}^i} = f^i \boldsymbol{\sigma}^i - \boldsymbol{\Lambda}_2 \tag{7. 12}$$

$$0 = \frac{\partial \Psi}{\partial [\boldsymbol{u}]} + \frac{\partial \Phi}{\partial [\dot{\boldsymbol{u}}]} + \boldsymbol{\Lambda}_1 \cdot \frac{\partial \boldsymbol{C}_1}{\partial [\dot{\boldsymbol{u}}]} + \boldsymbol{\Lambda}_2 \cdot \frac{\partial \boldsymbol{C}_2}{\partial [\dot{\boldsymbol{u}}]} + \Lambda_0 \frac{\partial C_0}{\partial [\dot{\boldsymbol{u}}]} = \left(1 - f^i\right)\boldsymbol{\Lambda}_2 \cdot \boldsymbol{n} - f^i \boldsymbol{\Lambda}_1 \cdot \boldsymbol{n} \tag{7. 13}$$

$$\begin{aligned} 0 = {} & \frac{\partial \Psi}{\partial \overline{\tilde{\alpha}_k^{oi}}} + \frac{\partial \Phi}{\partial \overline{\dot{\tilde{\alpha}}_k^{oi}}} + \boldsymbol{\Lambda}_1 : \frac{\partial \boldsymbol{C}_1}{\partial \overline{\dot{\tilde{\alpha}}_k^{oi}}} + \boldsymbol{\Lambda}_2 : \frac{\partial \boldsymbol{C}_2}{\partial \overline{\dot{\tilde{\alpha}}_k^{oi}}} + \Lambda_0 \frac{\partial C_0}{\partial \overline{\dot{\tilde{\alpha}}_k^{oi}}} \\ & = \left(1 - f^i\right)\frac{\partial \Psi^{oi}}{\partial \overline{\tilde{\alpha}_k^{oi}}} + \left(1 - f^i\right)\overline{\tilde{\chi}_k^{oi}} \qquad k = 1 \dots n \end{aligned} \tag{7. 14}$$

$$\begin{aligned} 0 = {} & \frac{\partial \Psi}{\partial \tilde{\alpha}_k^i} + \frac{\partial \Phi}{\partial \dot{\tilde{\alpha}}_k^i} + \boldsymbol{\Lambda}_1 : \frac{\partial \boldsymbol{C}_1}{\partial \dot{\tilde{\alpha}}_k^i} + \boldsymbol{\Lambda}_2 : \frac{\partial \boldsymbol{C}_2}{\partial \dot{\tilde{\alpha}}_k^i} + \Lambda_0 \frac{\partial C_0}{\partial \dot{\tilde{\alpha}}_k^i} \\ & = f^i \frac{\partial \Psi^i}{\partial \tilde{\alpha}_k^i} + f^i \tilde{\chi}_k^i + \frac{\Lambda_0 \partial h}{\partial \dot{\tilde{\alpha}}_k^i} \qquad k = 1 \dots n \end{aligned} \tag{7. 15}$$

$$0 = \frac{\partial \Psi}{\partial h} + \frac{\partial \Phi}{\partial \dot{h}} + \boldsymbol{\Lambda}_1 : \frac{\partial \boldsymbol{C}_1}{\partial \dot{h}} + \boldsymbol{\Lambda}_2 : \frac{\partial \boldsymbol{C}_2}{\partial \dot{h}} + \Lambda_0 \frac{\partial C_0}{\partial \dot{h}} = \frac{1}{H}\left(\Psi^i - \Psi^o\right) + \Lambda_0 \tag{7. 16}$$

In equation (7. 14), $\overline{\tilde{\chi}_k^{oi}}$ represent the volume-weighted average of the dissipative parts of the internal forces for the material outside the i^{th} active localisation zone. Furthermore, from equation (7. 10) – (7. 12) the macroscopic stress tensor is given as the weighted sum of the micro-stress tensor inside the i^{th} active band and the volume-weighted average of the stress tensors outside the i^{th} active band:

$$\boldsymbol{\sigma} = \left(1 - f^i\right)\overline{\boldsymbol{\sigma}^{oi}} + f^i \boldsymbol{\sigma}^i \tag{7. 17}$$

Also, from equations (7. 11) – (7. 13) the continuity of traction across the boundaries of the currently active band is obtained as:

$$\left(\boldsymbol{\sigma}^{i} - \overline{\boldsymbol{\sigma}^{oi}}\right).\boldsymbol{n} = 0 \tag{7. 18}$$

For a continuum approach the width of the localisation band, h can be defined as a continuous and monotonically decreasing function of the total value of an internal variable inside the currently active band ($h = h\left(\tilde{\alpha}_k^i\right)$). Alternatively, if the rate of change of $\dot{h}$ is defined as a function of the rate of one internal variable inside the currently active band ($\dot{h} = h\left(\dot{\tilde{\alpha}}_k^i\right)$), then the dissipation function is supplemented with the following constraint equation:

$$C_0 = \dot{h} - h\left(\dot{\tilde{\alpha}}_k^i\right) = 0 \tag{7. 19}$$

In this case, the dissipation function of equation (7. 7) is further supplemented with the above constraint equation:

$$\delta\Phi' = f\delta\Phi^{i} + (1-f)\delta\Phi^{oi} + \boldsymbol{\Lambda}_1 : \boldsymbol{C}_1 + \boldsymbol{\Lambda}_2 : \boldsymbol{C}_2 + \Lambda_0 C_0 \geq 0 \tag{7. 20}$$

The procedure of driving the rest of the formulation is similar to that presented in the case of the discrete approach.

The simple thermodynamics formulation that presented in this section may facilitate the selection of the length scale for the two-scale model presented in Chapter 6. With this formulation, only an initial value for the width of the localisation band is needed. This width can be the thickest width that can be measured from the strain profile. Then this thick bandwidth is reduced to a negligible thickness at failure by explicitly defining the function $h = h\left(\tilde{\alpha}_k^i\right)$ (or the function $\dot{h} = h\left(\dot{\tilde{\alpha}}_k^i\right)$). Further clarification, enhancement and verification of the proposed formulation is reserved as the subject of the future studies.

References

[1] Bazant ZP, Oh BH. Microplane model for fracture analysis of concrete structures. NORTHWESTERN UNIV EVANSTON IL TECHNOLOGICAL INST; 1983.

[2] Bažant ZP, Gambarova PG. Crack shear in concrete: Crack band microflane model. Journal of Structural Engineering. 1984;110:2015-35.

[3] Bažant ZP, Oh BH. Microplane model for progressive fracture of concrete and rock. Journal of Engineering Mechanics. 1985;111:559-82.

[4] Bažant ZP, Prat PC. Creep of anisotropic clay: new microplane model. Journal of engineering mechanics. 1987;113:1050-64.

[5] Bažant ZP, Prat PC. Microplane model for brittle-plastic material: I. Theory. Journal of Engineering Mechanics. 1988;114:1672-88.

[6] Bazoant Z, Prat P. Microplane model for brittle plastic material: II. Verification. Journal of Engineering Mechanics. 1988;114:1689-99.

[7] Carol I, Bažant ZP, Prat PC. Geometric damage tensor based on microplane model. Journal of engineering mechanics. 1991;117:2429-48.

[8] Carol I, Prat PC, Bažant ZP. New explicit microplane model for concrete: theoretical aspects and numerical implementation. International Journal of Solids and Structures. 1992;29:1173-91.

[9] Cofer WF. Implementation of the nonlocal microplane concrete model within an explicit dynamic finite element program. Applied Mechanics Reviews. 1992;45:S132-S9.

[10] Ožbolt J, Bažant ZP. Microplane model for cyclic triaxial behavior of concrete. Journal of engineering mechanics. 1992;118:1365-86.

[11] Cofer W, Kohut S. A general nonlocal microplane concrete material model for dynamic finite element analysis. Computers & structures. 1994;53:189-99.

[12] Bažant ZP, Xiang Y, Prat PC. Microplane model for concrete. I: Stress-strain boundaries and finite strain. Journal of Engineering Mechanics. 1996;122:245-54.

[13] Bažant ZP, Xiang Y, Adley MD, Prat PC, Akers SA. Microplane model for concrete: II: data delocalization and verification. Journal of Engineering Mechanics. 1996;122:255-62.

[14] Bažant ZP, Adley MD, Carol I, Jirásek M, Akers SA, Rohani B et al. Large-strain generalization of microplane model for concrete and application. Journal of engineering mechanics. 2000;126:971-80.

[15] Bažant ZP, Caner FC, Carol I, Adley MD, Akers SA. Microplane model M4 for concrete. I: Formulation with work-conjugate deviatoric stress. Journal of Engineering Mechanics. 2000;126:944-53.

[16] Ozbolt J, Bazant ZP. Numerical smeared fracture analysis: nonlocal microcrack interaction approach. International Journal for Numerical Methods in Engineering. 1996;39:635-62.

[17] Kuhl E, Ramm E, de Borst R. Anisotropic gradient damage with the microplane model. Comput Model Concrete Struct Balkema, Badgastein, Austria. 1998:103-12.

[18] Carol I, Jirásek M, Bažant Z. A thermodynamically consistent approach to microplane theory. Part I. Free energy and consistent microplane stresses. International Journal of Solids and Structures. 2001;38:2921-31.

[19] Houlsby GT, Puzrin AM. Principles of hyperplasticity: an approach to plasticity theory based on thermodynamic principles: Springer Science & Business Media; 2007.

[20] Houlsby G, Puzrin A. A thermomechanical framework for constitutive models for rate-independent dissipative materials. International Journal of Plasticity. 2000;16:1017-47.

[21] Ziegler H. An Introduction to Thermomechanics,(1983), 268: North-Holland; 1983.

[22] Ziegler H, Wehrli C. The derivation of constitutive relations from the free energy and the dissipation function. Advances in applied mechanics. 1987;25:183-238.

[23] Vu VD, Mir A, Nguyen GD, Sheikh AH. A thermodynamics-based formulation for constitutive modelling using damage mechanics and plasticity theory. Engineering Structures. 2017;143:22-39.

[24] Mir A, Nguyen GD, Sheikh AH. A CONTINUUM MODEL WITH AN EMBEDDED FRACTURE PROCESS ZONE MODELLED AS A COHESIVE FRICTIONAL INTERFACE. Applied Mechanics & Materials. 2016;846.

[25] Vajdova V, Baud P, Wong Tf. Compaction, dilatancy, and failure in porous carbonate rocks. Journal of Geophysical Research: Solid Earth. 2004;109.

[26] Vajdova V, Baud P, Wong Tf. Permeability evolution during localized deformation in Bentheim sandstone. Journal of Geophysical Research: Solid Earth. 2004;109.

[27] Wong T, Baud P. Mechanical compaction of porous sandstone. Oil & Gas Science and Technology. 1999;54:715-27.

[28] Wong Tf, David C, Zhu W. The transition from brittle faulting to cataclastic flow in porous sandstones: Mechanical deformation. Journal of Geophysical Research: Solid Earth. 1997;102:3009-25.

[29] Unteregger D, Fuchs B, Hofstetter G. A damage plasticity model for different types of intact rock. International Journal of Rock Mechanics and Mining Sciences. 2015;80:402-11.

[30] Paterson MS, Wong T-f. Experimental rock deformation-the brittle field: Springer Science & Business Media; 2005.

[31] Bažant ZP, Cedolin L. Stability of structures: elastic, inelastic, fracture and damage theories: World Scientific; 2010.

[32] Neilsen M, Schreyer H. Bifurcations in elastic-plastic materials. International Journal of Solids and Structures. 1993;30:521-44.

[33] Jirásek M, Bazant ZP. Inelastic analysis of structures: John Wiley & Sons; 2002.

[34] Comi C. A non-local model with tension and compression damage mechanisms. European Journal of Mechanics-A/Solids. 2001;20:1-22.

[35] Peerlings RHJ. Enhanced damage modelling for fracture and fatigue: Eindhoven University of Technology, Eindhoven, The Netherlands; 1999.

[36] Nguyen GD, Nguyen CT, Nguyen VP, Bui HH, Shen L. A size-dependent constitutive modelling framework for localised failure analysis. Computational Mechanics. 2016;58:257-80.

[37] Nguyen GD, Korsunsky AM, Einav I. A constitutive modelling framework featuring two scales of behaviour: fundamentals and applications to quasi-brittle failure. Engineering Fracture Mechanics. 2014;115:221-40.

[38] Hajiabdolmajid V, Kaiser P. Brittleness of rock and stability assessment in hard rock tunneling. Tunnelling and Underground Space Technology. 2003;18:35-48.

[39] Hirth G, Tullis J. The brittle-plastic transition in experimentally deformed quartz aggregates. Journal of Geophysical Research: Solid Earth. 1994;99:11731-47.

[40] Hadizadeh J, Tullis J. Transition from brittle faulting to cataclastic flow for anorthosite: both P and T are required. EOS. 1986;67:372-3.

[41] Shimada M, Yukutake H. Fracture and deformation of silicate rocks at high pressures in a cubic press. High-Pressure Research in Geophysics, ed S Akimoto and MH Manghnani. 1982:193-205.

[42] Schock R, Heard H, Stephens D. Stress-strain behavior of a granodiorite and two graywackes on compression to 20 kilobars. Journal of Geophysical Research. 1973;78:5922-41.

[43] Alam AB, Niioka M, Fujii Y, Fukuda D, Kodama J-i. Effects of confining pressure on the permeability of three rock types under compression. International Journal of Rock Mechanics and Mining Sciences. 2014;65:49-61.

[44] Seo Y, Jeong G, Kim J, Ichikawa Y. Microscopic observation and contact stress analysis of granite under compression. Engineering Geology. 2002;63:259-75.

[45] Hallbauer D, Wagner H, Cook N. Some observations concerning the microscopic and mechanical behaviour of quartzite specimens in stiff, triaxial compression tests. International Journal of Rock Mechanics and Mining Sciences & Geomechanics Abstracts: Elsevier; 1973. p. 713-26.

[46] Hoshino K, Koide H. Process of deformation of the sedimentary rocks. International Society of Rock Mechanics, Proceedings. 1970;1.

[47] Mitra G. Ductile deformation zones and mylonites; the mechanical processes involved in the deformation of crystalline basement rocks. American Journal of Science. 1978;278:1057-84.

[48] Siddiqi G, Liu M, Evans B. Strengthening of marbles by stiff inclusions. EOS Trans AGU. 1997;78:F723.

[49] Dresen G, Evans B. Brittle and semibrittle deformation of synthetic marbles composed of two phases. Journal of Geophysical Research: Solid Earth. 1993;98:11921-33.

[50] Dell'Angelo LN, Tullis J. Textural and mechanical evolution with progressive strain in experimentally deformed aplite. Tectonophysics. 1996;256:57-82.

[51] Ibanez WD, Kronenberg AK. Experimental deformation of shale: Mechanical properties and microstructural indicators of mechanisms. International journal of rock mechanics and mining sciences & geomechanics abstracts: Elsevier; 1993. p. 723-34.

[52] Tullis J, Yund R. The brittle-ductile transition in feldspar aggregates: An experimental study. International Geophysics. 1992;51:89-117.

[53] Tullis J. Experimental studies of deformation mechanisms and microstructures in quartzo-feldspathic rocks. Deformation processes in minerals, ceramics and rocks: Springer; 1990. p. 190-227.

[54] Boland J, Tullis T. Deformation behavior of wet and dry clinopyroxenite in the brittle to ductile transition region. Mineral and Rock Deformation: Laboratory Studies: The Paterson Volume. 1986:35-49.

[55] Thill RE. Acoustic methods for monitoring failure in rock. The 14th US Symposium on Rock Mechanics (USRMS): American Rock Mechanics Association; 1972.

[56] Wawersik W, Fairhurst C. A study of brittle rock fracture in laboratory compression experiments. International Journal of Rock Mechanics and Mining Sciences & Geomechanics Abstracts: Elsevier; 1970. p. 561IN7565-564IN14575.

[57] Louis L, Wong T-f, Baud P, Tembe S. Imaging strain localization by X-ray computed tomography: discrete compaction bands in Diemelstadt sandstone. Journal of Structural Geology. 2006;28:762-75.

[58] Milliken KL, Laubach SE. Brittle deformation in sandstone diagenesis as revealed by scanned cathodoluminescence imaging with application to characterization of fractured reservoirs. Cathodoluminescence in geosciences: Springer; 2000. p. 225-43.

[59] Menéndez B, Zhu W, Wong T-F. Micromechanics of brittle faulting and cataclastic flow in Berea sandstone. Journal of structural geology. 1996;18:1-16.

[60] Antonellini MA, Aydin A, Pollard DD. Microstructure of deformation bands in porous sandstones at Arches National Park, Utah. Journal of structural geology. 1994;16:941-59.

[61] Bernabe Y, Brace W. Deformation and fracture of Berea sandstone. The brittle-ductile transition in rocks. 1990:91-101.

[62] Hirth G, Tullis J. The effects of pressure and porosity on the micromechanics of the brittle-ductile transition in quartzite. Journal of Geophysical Research: Solid Earth. 1989;94:17825-38.

[63] Hadizadeh J, Rutter E. The low temperature brittle-ductile transition in a quartzite and the occurrence of cataclastic flow in nature. Geologische Rundschau. 1983;72:493-509.

[64] Aydin A. Small faults formed as deformation bands in sandstone. Rock Friction and Earthquake Prediction: Springer; 1978. p. 913-30.

[65] Wong T-f, David C, Menendez B. Mechanical compaction. INTERNATIONAL GEOPHYSICS SERIES. 2004;89:55-114.

[66] Chuhan FA, Kjeldstad A, Bjørlykke K, Høeg K. Porosity loss in sand by grain crushing—Experimental evidence and relevance to reservoir quality. Marine and Petroleum Geology. 2002;19:39-53.

[67] Wu XY, Baud P, Wong T-f. Micromechanics of compressive failure and spatial evolution of anisotropic damage in Darley Dale sandstone. International Journal of Rock Mechanics and Mining Sciences. 2000;37:143-60.

[68] Zhang J, Wong TF, Davis DM. Micromechanics of pressure-induced grain crushing in porous rocks. Journal of Geophysical Research: Solid Earth. 1990;95:341-52.

[69] Shimada M. Mechanism of deformation in a dry porous basalt at high pressures. Tectonophysics. 1986;121:153-73.

[70] Shimada M, Cho A, Yukutake H. Fracture strength of dry silicate rocks at high confining pressures and activity of acoustic emission. Tectonophysics. 1983;96:159-72.

[71] Bésuelle P, Rudnicki JW. Localization: shear bands and compaction bands. INTERNATIONAL GEOPHYSICS SERIES. 2004;89:219-322.

[72] El Bied A, Sulem J, Martineau F. Microstructure of shear zones in Fontainebleau sandstone. International Journal of Rock Mechanics and Mining Sciences. 2002;39:917-32.

[73] Mair K, Main I, Elphick S. Sequential growth of deformation bands in the laboratory. Journal of Structural Geology. 2000;22:25-42.

[74] Das A, Nguyen GD, Einav I. The propagation of compaction bands in porous rocks based on breakage mechanics. Journal of Geophysical Research: Solid Earth. 2013;118:2049-66.

[75] Das A, Nguyen GD, Einav I. Compaction bands due to grain crushing in porous rocks: a theoretical approach based on breakage mechanics. Journal of Geophysical Research: Solid Earth. 2011;116.

[76] Sibson RH. Earthquakes and rock deformation in crustal fault zones. Annual Review of Earth and Planetary Sciences. 1986;14:149-75.

[77] Byerlee J. A review of rock mechanics studies in the United States pertinent to earthquake prediction. Rock Friction and Earthquake Prediction: Springer; 1978. p. 586-602.

[78] Scholz CH, Sykes LR, Aggarwal YP. Earthquake prediction: A physical basis. Science. 1973;181:803-10.

[79] Nur A. Dilatancy, pore fluids, and premonitory variations of ts/tp travel times. Bulletin of the Seismological society of America. 1972;62:1217-22.

[80] Wong Tf, Baud P, Klein E. Localized failure modes in a compactant porous rock. Geophysical Research Letters. 2001;28:2521-4.

[81] Marshall J, Bull P, Morgan R. Energy regimes for aeolian sand grain surface textures. Sedimentary Geology. 2012;253:17-24.

[82] Cheung CS, Baud P, Wong Tf. Effect of grain size distribution on the development of compaction localization in porous sandstone. Geophysical Research Letters. 2012;39.

[83] Brzesowsky R, Spiers C, Peach C, Hangx S. Failure behavior of single sand grains: theory versus experiment. Journal of Geophysical Research: Solid Earth. 2011;116.

[84] Xiao X, Evans B. Shear-enhanced compaction during non-linear viscous creep of porous calcite–quartz aggregates. Earth and Planetary Science Letters. 2003;216:725-40.

[85] Fortin J, Stanchits S, Dresen G, Guéguen Y. Acoustic emission and velocities associated with the formation of compaction bands in sandstone. Journal of Geophysical Research: Solid Earth. 2006;111.

[86] Eichhubl P, Hooker JN, Laubach SE. Pure and shear-enhanced compaction bands in Aztec Sandstone. Journal of Structural Geology. 2010;32:1873-86.

[87] Holcomb D, Rudnicki JW, Issen KA, Sternlof K. Compaction localization in the Earth and the laboratory: state of the research and research directions. Acta Geotechnica. 2007;2:1-15.

[88] Sternlof K, Chapin J, Pollard D, Durlofsky L. Permeability effects of deformation band arrays in sandstone. AAPG bulletin. 2004;88:1315-29.

[89] Mollema P, Antonellini M. Compaction bands: a structural analog for anti-mode I cracks in aeolian sandstone. Tectonophysics. 1996;267:209-28.

[90] Hill RE. Analysis of deformation bands in the Aztec sandstone, Valley of Fire State Park, Nevada. Geological Society of America, Abstracts with Programs;(United States). 1993;25.

[91] Baud P, Vajdova V, Wong Tf. Shear-enhanced compaction and strain localization: Inelastic deformation and constitutive modeling of four porous sandstones. Journal of Geophysical Research: Solid Earth. 2006;111.

[92] Baud P, Klein E, Wong T-f. Compaction localization in porous sandstones: spatial evolution of damage and acoustic emission activity. Journal of Structural Geology. 2004;26:603-24.

[93] Vajdova V, Wong TF. Incremental propagation of discrete compaction bands: Acoustic emission and microstructural observations on circumferentially notched samples of Bentheim. Geophysical Research Letters. 2003;30.

[94] Lockner D, Byerlee J, Kuksenko V, Ponomarev A, Sidorin A. Observations of quasistatic fault growth from acoustic emissions. International Geophysics. 1992;51:3-31.

[95] Wong T-f, Baud P. The brittle-ductile transition in porous rock: A review. Journal of Structural Geology. 2012;44:25-53.

[96] Klein E, Reuschlé T. A model for the mechanical behaviour of Bentheim sandstone in the brittle regime. Thermo-Hydro-Mechanical Coupling in Fractured Rock: Springer; 2003. p. 833-49.

[97] Moore DE, Lockner D. The role of microcracking in shear-fracture propagation in granite. Journal of Structural Geology. 1995;17:95113-111114.

[98] Wong T-F. Micromechanics of faulting in Westerly granite. International journal of rock mechanics and mining sciences & geomechanics abstracts: Elsevier; 1982. p. 49-64.

[99] Wong T-F, Biegel R. Effects of pressure on the micromechanics of faulting in San Marcos gabbro. Journal of structural geology. 1985;7:737-49.

[100] Carroll M. A critical state plasticity theory for porous reservoir rock. Recent Advances in Mechanics of Structured Continua. 1991;117:1-8.

[101] Jiang M, Yan H, Zhu H, Utili S. Modeling shear behavior and strain localization in cemented sands by two-dimensional distinct element method analyses. Computers and Geotechnics. 2011;38:14-29.

[102] Katsman R, Aharonov E. A study of compaction bands originating from cracks, notches, and compacted defects. Journal of Structural Geology. 2006;28:508-18.

[103] Katsman R, Aharonov E, Scher H. Numerical simulation of compaction bands in high-porosity sedimentary rock. Mechanics of materials. 2005;37:143-62.

[104] Marketos G, Bolton M. Compaction bands simulated in discrete element models. Journal of structural Geology. 2009;31:479-90.

[105] Wang B, Chen Y, Wong Tf. A discrete element model for the development of compaction localization in granular rock. Journal of Geophysical Research: Solid Earth. 2008;113.

[106] Lisjak A, Grasselli G. A review of discrete modeling techniques for fracturing processes in discontinuous rock masses. Journal of Rock Mechanics and Geotechnical Engineering. 2014;6:301-14.

[107] Nguyen NH, Bui HH, Nguyen GD, Kodikara J. A cohesive damage-plasticity model for DEM and its application for numerical investigation of soft rock fracture properties. International Journal of Plasticity. 2017.

[108] Duan K, Kwok C, Tham L. Micromechanical analysis of the failure process of brittle rock. International Journal for Numerical and Analytical Methods in Geomechanics. 2015;39:618-34.

[109] Haghighat E, Pietruszczak S. On modeling of discrete propagation of localized damage in cohesive-frictional materials. International Journal for Numerical and Analytical Methods in Geomechanics. 2015;39:1774-90.

[110] Weerasekara N, Powell M, Cleary P, Tavares LM, Evertsson M, Morrison R et al. The contribution of DEM to the science of comminution. Powder technology. 2013;248:3-24.

[111] Hentz S, Daudeville L, Donzé FV. Identification and validation of a discrete element model for concrete. Journal of engineering mechanics. 2004;130:709-19.

[112] Donzé FV, Richefeu V, Magnier S-A. Advances in discrete element method applied to soil, rock and concrete mechanics. Electronic Journal of Geotechnical Engineering. 2009;8:44.

[113] Drucker DC. Some implications of work hardening and ideal plasticity. Quarterly of Applied Mathematics. 1950;7:411-8.

[114] Chen W-F, Han D-J. Plasticity for structural engineers: J. Ross Publishing; 2007.

[115] Grassl P, Lundgren K, Gylltoft K. Concrete in compression: a plasticity theory with a novel hardening law. International Journal of Solids and Structures. 2002;39:5205-23.

[116] Kang HD, Willam KJ. Localization characteristics of triaxial concrete model. Journal of engineering mechanics. 1999;125:941-50.

[117] Lee J, Fenves GL. A plastic-damage concrete model for earthquake analysis of dams. Earthquake engineering & structural dynamics. 1998;27:937-56.

[118] Lee J, Fenves GL. Plastic-damage model for cyclic loading of concrete structures. Journal of engineering mechanics. 1998;124:892-900.

[119] Nguyen GD. A thermodynamic approach to constitutive modelling of concrete using damage mechanics and plasticity theory: Citeseer; 2005.

[120] Imran I, Pantazopoulou S. Plasticity model for concrete under triaxial compression. Journal of engineering mechanics. 2001;127:281-90.

[121] Schofield A, Wroth P. Critical state soil mechanics. 1968.

[122] DiMaggio FL, Sandler IS. Material model for granular soils. Journal of Engineering Mechanics. 1971.

[123] Gerogiannopoulos N, Brown E. The critical state concept applied to rock. International Journal of Rock Mechanics and Mining Sciences & Geomechanics Abstracts: Elsevier; 1978. p. 1-10.

[124] Shah KR. An elasto-plastic constitutive model for brittle-ductile transition in porous rocks. International Journal of Rock Mechanics and Mining Sciences. 1997;34:283. e1-. e13.

[125] Grueschow E, Rudnicki JW. Elliptic yield cap constitutive modeling for high porosity sandstone. International Journal of Solids and Structures. 2005;42:4574-87.

[126] Fossum AF, Fredrich JT. Cap plasticity models and compactive and dilatant pre-failure deformation. 4th North American Rock Mechanics Symposium: American Rock Mechanics Association; 2000.

[127] Sheldon H, Barnicoat A, Ord A. Numerical modelling of faulting and fluid flow in porous rocks: an approach based on critical state soil mechanics. Journal of Structural Geology. 2006;28:1468-82.

[128] Schultz R, Siddharthan R. A general framework for the occurrence and faulting of deformation bands in porous granular rocks. Tectonophysics. 2005;411:1-18.

[129] Cuss R, Rutter E, Holloway R. The application of critical state soil mechanics to the mechanical behaviour of porous sandstones. International Journal of Rock Mechanics and Mining Sciences. 2003;40:847-62.

[130] Navarro V, Alonso J, Calvo B, Sánchez J. A constitutive model for porous rock including effects of bond strength degradation and partial saturation. International Journal of Rock Mechanics and Mining Sciences. 2010;47:1330-8.

[131] Castellanza R, Gerolymatou E, Nova R. Experimental observations and modelling of compaction bands in oedometric tests on high porosity rocks. Strain. 2009;45:410-23.

[132] Nova R, Castellanza R, Tamagnini C. A constitutive model for bonded geomaterials subject to mechanical and/or chemical degradation. International Journal for Numerical and Analytical Methods in Geomechanics. 2003;27:705-32.

[133] Vatsala A, Nova R, Murthy BS. Elastoplastic model for cemented soils. Journal of Geotechnical and Geoenvironmental Engineering. 2001;127:679-87.

[134] Lagioia R, Nova R. An experimental and theoretical study of the behaviour of a calcarenite in triaxial compression. Géotechnique. 1995;45:633-48.

[135] Gens A, Nova R. Conceptual bases for a constitutive model for bonded soils and weak rocks. Geotechnical engineering of hard soils-soft rocks. 1993;1:485-94.

[136] KACHANOV LM. Rupture time under creep conditions. 1958.

[137] Jirasek M, Rolshoven S, Grassl P. Size effect on fracture energy induced by non-locality. International Journal for Numerical and Analytical Methods in Geomechanics. 2004;28:653-70.

[138] Geers Md, De Borst R, Peerlings R. Damage and crack modeling in single-edge and double-edge notched concrete beams. Engineering Fracture Mechanics. 2000;65:247-61.

[139] Peerlings RHJ. Enhanced damage modelling for fracture and fatigue. 1999.

[140] Singh U, Digby P. A continuum damage model for simulation of the progressive failure of brittle rocks. International Journal of Solids and Structures. 1989;25:647-63.

[141] Simo J, Ju J. Strain-and stress-based continuum damage models—I. Formulation. Mathematical and Computer Modelling. 1989;12:378.

[142] Mazars J, Pijaudier-Cabot G. Continuum damage theory—application to concrete. Journal of Engineering Mechanics. 1989;115:345-65.

[143] Krajcinovic D, Fonseka G. The continuous damage theory of brittle materials. J appl Mech. 1981;48:809-24.

[144] Einav I, Houlsby G, Nguyen G. Coupled damage and plasticity models derived from energy and dissipation potentials. International Journal of Solids and Structures. 2007;44:2487-508.

[145] Burlion N, Gatuingt F, Pijaudier-Cabot G, Daudeville L. Compaction and tensile damage in concrete: constitutive modelling and application to dynamics. Computer methods in applied mechanics and engineering. 2000;183:291-308.

[146] Lemaitre J. Evaluation of dissipation and damage in metals submitted to dynamic loading. Mechanical behavior of materials. 1972:540-9.

[147] Lemaitre J. A course on damage mechanics: Springer Science & Business Media; 2012.

[148] Liu S, Ning JG, Tan YL, Gu QH. Damage constitutive model based on energy dissipation for intact rock subjected to cyclic loading. International Journal of Rock Mechanics & Mining Sciences. 2016;85:6.

[149] Nguyen GD, Korsunsky AM, Belnoue JP-H. A nonlocal coupled damage-plasticity model for the analysis of ductile failure. International Journal of Plasticity. 2015;64:56-75.

[150] Nguyen GD, Korsunsky AM, Belnoue J. Coupled damage-plasticity modelling of ductile failure in an aluminium alloy. Applied Mechanics and Materials: Trans Tech Publications; 2015. p. 266-73.

[151] Nguyen GD, Korsunsky AM. Development of an approach to constitutive modelling of concrete: isotropic damage coupled with plasticity. International Journal of Solids and Structures. 2008;45:5483-501.

[152] Lemaitre J, Chaboche J-L. Mechanics of solid materials: Cambridge university press; 1994.

[153] Lemaitre J. A course on damage mechanics. Second ed: Springer Science & Business Media; 1992.

[154] Mazars J, Pijaudier-Cabot G. Continuum damage theory-application to concrete. Journal of Engineering Mechanics. 1989;115:345-65.

[155] Li Q, Ansari F. Mechanics of damage and constitutive relationships for high-strength concrete in triaxial compression. Journal of engineering mechanics. 1999;125:1-10.

[156] Addessi D, Marfia S, Sacco E. A plastic nonlocal damage model. Computer methods in applied mechanics and engineering. 2002;191:1291-310.

[157] Mozaffari N, Voyiadjis GZ. Phase field based nonlocal anisotropic damage mechanics model. Physica D: Nonlinear Phenomena. 2015;308:11-25.

[158] Voyiadjis GZ, Mozaffari N. Nonlocal damage model using the phase field method: Theory and applications. International Journal of Solids and Structures. 2013;50:3136-51.

[159] Miehe C, Hofacker M, Welschinger F. A phase field model for rate-independent crack propagation: Robust algorithmic implementation based on operator splits. Computer Methods in Applied Mechanics and Engineering. 2010;199:2765-78.

[160] Miehe C, Welschinger F, Hofacker M. Thermodynamically consistent phase-field models of fracture: Variational principles and multi-field FE implementations. International Journal for Numerical Methods in Engineering. 2010;83:1273-311.

[161] Amor H, Marigo J-J, Maurini C. Regularized formulation of the variational brittle fracture with unilateral contact: numerical experiments. Journal of the Mechanics and Physics of Solids. 2009;57:1209-29.

[162] Borden MJ, Verhoosel CV, Scott MA, Hughes TJ, Landis CM. A phase-field description of dynamic brittle fracture. Computer Methods in Applied Mechanics and Engineering. 2012;217:77-95.

[163] Lyakhovsky V, Zhu W, Shalev E. Visco-poroelastic damage model for brittle-ductile failure of porous rocks. Journal of Geophysical Research: Solid Earth. 2015;120:21.

[164] Pituba J, Fernandes G. Anisotropic damage model for concrete. Journal of Engineering Mechanics. 2011;137:610-24.

[165] Kahn A, Al-Gadhib A, Baluch M. Elasto-damage model for high strength concrete subjected to multiaxial loading. International Journal of Damage Mechanics. 2007.

[166] Comi C, Perego U. Fracture energy based bi-dissipative damage model for concrete. International Journal of Solids and Structures. 2001;38:6427-54.

[167] Kattan PI, Voyiadjis GZ. A coupled theory of damage mechanics and finite strain elasto-plasticity—I. Damage and elastic deformations. International Journal of Engineering Science. 1990;28:421-35.

[168] Mazars J. A description of micro- and macroscale damage of concrete structures. Engineering Fracture Mechanics. 1986;25:729-37.

[169] Ortiz M. A constitutive theory for the inelastic behavior of concrete. Mechanics of materials. 1985;4:67-93.

[170] Krajcinovic D. Constitutive equations for damaging materials. Journal of applied Mechanics. 1983;50:355-60.

[171] Lu D, Du X, Wang G, Zhou A, Li A. A three-dimensional elastoplastic constitutive model for concrete. Computers & Structures. 2016;163:41-55.

[172] Parisio F, Samat S, Laloui L. Constitutive analysis of shale: a coupled damage plasticity approach. International Journal of Solids and Structures. 2015;75:88-98.

[173] Grassl P, Xenos D, Nyström U, Rempling R, Gylltoft K. CDPM2: A damage-plasticity approach to modelling the failure of concrete. International Journal of Solids and Structures. 2013;50:3805-16.

[174] Voyiadjis GZ, Taqieddin ZN, Kattan PI. Anisotropic damage–plasticity model for concrete. International Journal of Plasticity. 2008;24:1946-65.

[175] Cicekli U, Voyiadjis GZ, Al-Rub RKA. A plasticity and anisotropic damage model for plain concrete. International Journal of plasticity. 2007;23:1874-900.

[176] Shao J-F, Jia Y, Kondo D, Chiarelli A-S. A coupled elastoplastic damage model for semi-brittle materials and extension to unsaturated conditions. Mechanics of materials. 2006;38:218-32.

[177] Jason L, Huerta A, Pijaudier-Cabot G, Ghavamian S. An elastic plastic damage formulation for concrete: Application to elementary tests and comparison with an isotropic damage model. Computer methods in applied mechanics and engineering. 2006;195:7077-92.

[178] Contrafatto L, Cuomo M. A framework of elastic–plastic damaging model for concrete under multiaxial stress states. International Journal of Plasticity. 2006;22:2272-300.

[179] Salari M, Saeb S, Willam K, Patchet S, Carrasco R. A coupled elastoplastic damage model for geomaterials. Computer methods in applied mechanics and engineering. 2004;193:2625-43.

[180] Nguyen G, Houlsby G. A thermodynamic approach to constitutive modelling of concrete. Proc 12th Conf, Association for Computational Mechanics in Engineering (ACME-UK), Cardiff, UK2004.

[181] Jefferson A. Craft—a plastic-damage-contact model for concrete. I. Model theory and thermodynamic considerations. International journal of solids and structures. 2003;40:5973-99.

[182] Hansen N, Schreyer H. Thermodynamically consistent theories for elastoplasticity coupled with damage. Sandia National Labs., Albuquerque, NM (United States); 1992.

[183] Yazdani S, Schreyer H. Combined plasticity and damage mechanics model for plain concrete. Journal of engineering mechanics. 1990.

[184] Pouya A, Yazdi PB. A damage-plasticity model for cohesive fractures. International Journal of Rock Mechanics and Mining Sciences. 2015;73:194-202.

[185] Krätzig WB, Pölling R. An elasto-plastic damage model for reinforced concrete with minimum number of material parameters. Computers & Structures. 2004;82:1201-15.

[186] Issen K, Rudnicki J. Theory of compaction bands in porous rock. Physics and Chemistry of the Earth, Part A: Solid Earth and Geodesy. 2001;26:95-100.

[187] Voyiadjis GZ, Abu-Lebdeh TM. Damage model for concrete using bounding surface concept. Journal of engineering mechanics. 1993;119:1865-85.

[188] Lubliner J, Oliver J, Oller S, Onate E. A plastic-damage model for concrete. International Journal of solids and structures. 1989;25:299-326.

[189] Nguyen G, Einav I, Guiamatsia I, Korsunsky AM. From Diffuse to Localised Damage: the Role of Friction. The International Conference on Advances in Computational Mechanics. Ho Chi Minh City, Vietnam2012.

[190] Grassl P, Jirásek M. Damage-plastic model for concrete failure. International journal of solids and structures. 2006;43:7166-96.

[191] Collins I, Houlsby G. Application of thermomechanical principles to the modelling of geotechnical materials. Proceedings of the Royal Society of London A: Mathematical, Physical and Engineering Sciences: The Royal Society; 1997. p. 1975-2001.

[192] !!! INVALID CITATION !!! [95, 135, 136].

[193] Nguyen GD, Einav I. Nonlocal regularisation of a model based on breakage mechanics for granular materials. International Journal of Solids and Structures. 2010;47:1350-60.

[194] Sulem J, Vardoulakis I. Bifurcation analysis in geomechanics: CRC Press; 2004.

[195] Rice JR. The localization of plastic deformation. 1976.

[196] Hill R. Elastic properties of reinforced solids: some theoretical principles. Journal of the Mechanics and Physics of Solids. 1963;11:357-72.

[197] Hill R. A general theory of uniqueness and stability in elastic-plastic solids. Journal of the Mechanics and Physics of Solids. 1958;6:236-49.

[198] Bigoni D, Hueckel T. Uniqueness and localization—I. Associative and non-associative elastoplasticity. International Journal of Solids and Structures. 1991;28:197-213.

[199] Valanis K. Banding and stability in plastic materials. Acta Mechanica. 1989;79:113-41.

[200] Runesson K, Ottosen NS, Dunja P. Discontinuous bifurcations of elastic-plastic solutions at plane stress and plane strain. International Journal of Plasticity. 1991;7:99-121.

[201] Rice J, Rudnicki J. A note on some features of the theory of localization of deformation. International Journal of solids and structures. 1980;16:597-605.

[202] Rudnicki JW, Rice J. Conditions for the localization of deformation in pressure-sensitive dilatant materials. Journal of the Mechanics and Physics of Solids. 1975;23:371-94.

[203] Schreyer H. Analytical solutions for nonlinear strain-gradient softening and localization. ASME J Appl Mech. 1990;57:522-8.

[204] Das A, Tengattini A, Nguyen GD, Viggiani G, Hall SA, Einav I. A thermomechanical constitutive model for cemented granular materials with quantifiable internal variables. Part II–validation and localization analysis. Journal of the Mechanics and Physics of Solids. 2014;70:382-405.

[205] Bésuelle P, Desrues J, Raynaud S. Experimental characterisation of the localisation phenomenon inside a Vosges sandstone in a triaxial cell. International Journal of Rock Mechanics and Mining Sciences. 2000;37:1223-37.

[206] Hall S, Bornert M, Desrues J, Pannier Y, Lenoir N, Viggiani G et al. Discrete and continuum analysis of localised deformation in sand using X-ray μCT and volumetric digital image correlation. Géotechnique. 2010;60:315-22.

[207] Maugin GA. The thermomechanics of nonlinear irreversible behaviors: an introduction: World Scientific; 1999.

[208] Maugin G. The Thermodynamics of Plasticity and Fracture, Cambridge Texts in Applied Mathematics. Cambridge University Press, Cambridge; 1992.

[209] Houlsby GT. Derivation of incremental stress-strain response for plasticity models based on thermodynamic functions. IUTAM Symposium on Mechanics of Granular and Porous Materials: Springer; 1997. p. 161-72.

[210] Houlsby GT. Study of plasticity theories and their applicability to soils: University of Cambridge; 1981.

[211] Houlsby G. A derivation of the small-strain incremental theory of plasticity from thermodynamics. Soil. Mech. Rep. SM020//GTH/81, OUEL Rep. 1371/81, University of Oxford; 1981.

[212] Collins IF, Hilder T. A theoretical framework for constructing elastic/plastic constitutive models of triaxial tests. International Journal for Numerical and Analytical Methods in Geomechanics. 2002;26:1313-47.

[213] Collins I, Kelly P. A thermomechanical analysis of a family of soil models. Geotechnique. 2002;52:507-18.

[214] Houlsby G, Kolymbas D. Interpretation of dilation as a kinematic constraint. Modern approaches to plasticity. 1993:119-38.

[215] Haimson B. Micromechanisms of borehole instability leading to breakouts in rocks. International Journal of Rock Mechanics and Mining Sciences. 2007;44:157-73.

[216] Holcomb D, Olsson W. Compaction localization and fluid flow. Journal of Geophysical Research: Solid Earth. 2003;108.

[217] Einav I. Breakage mechanics—Part II: Modelling granular materials. Journal of the Mechanics and Physics of Solids. 2007;55:1298-320.

[218] Einav I. Breakage mechanics—part I: theory. Journal of the Mechanics and Physics of Solids. 2007;55:1274-97.

[219] Perzyna P. Fundamental problems in viscoplasticity. Advances in applied mechanics. 1966;9:243-377.

[220] Coussy O. Poromechanics: John Wiley & Sons; 2004.

[221] Lubliner J. Plasticity theory: Courier Corporation; 2008.

[222] Reddy B, Martin J. Internal variable formulations of problems in elastoplasticity: constitutive and algorithmic aspects. Appl Mech Rev. 1994;47:429-56.

[223] Lubliner J. On the thermodynamic foundations of non-linear solid mechanics. International Journal of Non-Linear Mechanics. 1972;7:237-54.

[224] Collins IF. Elastic/plastic models for soils and sands. International Journal of Mechanical Sciences. 2005;47:493-508.

[225] Collins IF. The concept of stored plastic work or frozen elastic energy in soil mechanics. Geotechnique. 2005;55:373-82.

[226] Tengattini A, Das A, Einav I. A constitutive modelling framework predicting critical state in sand undergoing crushing and dilation. Géotechnique. 2016;66:695-710.

[227] Tembe S, Baud P, Wong Tf. Stress conditions for the propagation of discrete compaction bands in porous sandstone. Journal of Geophysical Research: Solid Earth. 2008;113.

[228] Rudnicki JW. Shear and compaction band formation on an elliptic yield cap. Journal of Geophysical Research: Solid Earth. 2004;109.

[229] De Borst R, Crisfield MA, Remmers JJ, Verhoosel CV. Nonlinear finite element analysis of solids and structures: John Wiley & Sons; 2012.

[230] de Souza Neto EA, Peric D, Owen DRJ. Computational methods for plasticity: theory and applications: John Wiley & Sons; 2011.

[231] Criesfield M. Non linear finite element analysis of solids and structures, vol. 1. Wiley, New York; 1991.

[232] Marinelli F, Buscarnera G. Parameter calibration for high-porosity sandstones deformed in the compaction banding regime. International Journal of Rock Mechanics and Mining Sciences. 2015;78:240-52.

[233] Borja RI, Aydin A. Computational modeling of deformation bands in granular media. I. Geological and mathematical framework. Computer Methods in Applied Mechanics and Engineering. 2004;193:2667-98.

[234] Chemenda AI. Origin of compaction bands: Anti-cracking or constitutive instability? Tectonophysics. 2011;499:156-64.

[235] Chemenda A. The formation of tabular compaction-band arrays: theoretical and numerical analysis. Journal of the Mechanics and Physics of Solids. 2009;57:851-68.

[236] Qi C, Wang M, Qian Q. Strain-rate effects on the strength and fragmentation size of rocks. International journal of impact engineering. 2009;36:1355-64.

[237] Cho SH, Ogata Y, Kaneko K. Strain-rate dependency of the dynamic tensile strength of rock. International Journal of Rock Mechanics and Mining Sciences. 2003;40:763-77.

[238] Li Y, Xia C. Time-dependent tests on intact rocks in uniaxial compression. International Journal of Rock Mechanics and Mining Sciences. 2000;37:467-75.

[239] Lajtai E, Duncan ES, Carter B. The effect of strain rate on rock strength. Rock Mechanics and Rock Engineering. 1991;24:99-109.

[240] Sano O, Terada M, Ehara S. A study on the time-dependent microfracturing and strength of Oshima granite. Tectonophysics. 1982;84:343-62.

[241] Brantut N, Heap M, Baud P, Meredith P. Rate-and strain-dependent brittle deformation of rocks. Journal of Geophysical Research: Solid Earth. 2014;119:1818-36.

[242] Gary G, Bailly P. Behaviour of quasi-brittle material at high strain rate. Experiment and modelling. European Journal of Mechanics-A/Solids. 1998;17:403-20.

[243] Mitra G. Brittle to ductile transition due to large strains along the White Rock thrust, Wind River Mountains, Wyoming. Journal of Structural Geology. 1984;6:51-61.

[244] Ben-David O, Cohen G, Fineberg J. Short-time dynamics of frictional strength in dry friction. Tribology letters. 2010;39:235-45.

[245] Di Toro G, Goldsby DL, Tullis TE. Friction falls towards zero in quartz rock as slip velocity approaches seismic rates. Nature. 2004;427:436-9.

[246] Dieterich JH. Time-dependent friction and the mechanics of stick-slip. pure and applied geophysics. 1978;116:790-806.

[247] Dieterich JH. Time-dependent friction in rocks. Journal of Geophysical Research. 1972;77:3690-7.

[248] Li Q, Meng H. About the dynamic strength enhancement of concrete-like materials in a split Hopkinson pressure bar test. International Journal of solids and structures. 2003;40:343-60.

[249] Etse G, Willam K. Failure analysis of elastoviscoplastic material models. Journal of engineering mechanics. 1999;125:60-9.

[250] Hickman RJ, Gutierrez M. Influence of implicit integration scheme on prediction of shear band formation. Journal of engineering mechanics. 2005;131:791-800.

[251] Carosio A, Willam K, Etse G. On the consistency of viscoplastic formulations. International Journal of Solids and Structures. 2000;37:7349-69.

[252] Stanchits S, Fortin J, Gueguen Y, Dresen G. Initiation and propagation of compaction bands in dry and wet Bentheim Sandstone. Rock Physics and Natural Hazards: Springer; 2009. p. 846-68.

[253] Thill RE. Acoustic methods for monitoring failure in rock. The 14th US Symposium on Rock Mechanics (USRMS): American Rock Mechanics Association; 1973.

[254] Crouch S. The post-failure behavior of norite in triaxial compression. Engineering Geology. 1972;6:19-30.

[255] Crouch S. Experimental determination of volumetric strains in failed rock. International Journal of Rock Mechanics and Mining Sciences & Geomechanics Abstracts: Elsevier; 1970. p. 589-603.

[256] Handin J, Hager Jr RV, Friedman M, Feather JN. Experimental deformation of sedimentary rocks under confining pressure: pore pressure tests. Aapg Bulletin. 1963;47:717-55.

[257] Matsushima S. On the deformation and fracture of granite under high confining pressure. 1960.

[258] Brace W, Paulding B, Scholz C. Dilatancy in the fracture of crystalline rocks. Journal of Geophysical Research. 1966;71:3939-53.

[259] Rawling GC, Baud P, Wong Tf. Dilatancy, brittle strength, and anisotropy of foliated rocks: Experimental deformation and micromechanical modeling. Journal of Geophysical Research: Solid Earth. 2002;107.

[260] Chang C, Haimson B. True triaxial strength and deformability of the German Continental Deep Drilling Program (KTB) deep hole amphibolite. Journal of Geophysical Research: Solid Earth. 2000;105:18999-9013.

[261] Gottschalk RR, Kronenberg AK, Russell JE, Handin J. Mechanical anisotropy of gneiss: failure criterion and textural sources of directional behavior. Journal of Geophysical Research: Solid Earth. 1990;95:21613-34.

[262] Kranz RL. Crack growth and development during creep of Barre granite. International Journal of Rock Mechanics and Mining Sciences & Geomechanics Abstracts: Elsevier; 1979. p. 23-35.

[263] Kiyoo M. Dilatancy of rocks under general triaxial stress states with special reference to earthquake precursors. Journal of Physics of the Earth. 1977;25:S203-S17.

[264] Tapponnier P, Brace W. Development of stress-induced microcracks in Westerly granite. International Journal of Rock Mechanics and Mining Sciences & Geomechanics Abstracts: Elsevier; 1976. p. 103-12.

[265] Wimmer SA, Karr DG. Compressive failure of microcracked porous brittle solids. Mechanics of materials. 1996;22:265-77.

[266] Isida M, Nemat-Nasser S. On mechanics of crack growth and its effects on the overall response of brittle porous solids. Acta metallurgica. 1987;35:2887-98.

[267] Isida M, Nemat-Nasser S. A unified analysis of various problems relating to circular holes with edge cracks. Engineering fracture mechanics. 1987;27:571-91.

[268] Sammis C, Ashby M. The failure of brittle porous solids under compressive stress states. Acta Metallurgica. 1986;34:511-26.

[269] Gupta V, Bergström JS. Compressive failure of rocks. International Journal of Rock Mechanics and Mining Sciences. 1997;34:112. e1-. e23.

[270] Pestman B, Van Munster J. An acoustic emission study of damage development and stress-memory effects in sandstone. International journal of rock mechanics and mining sciences & geomechanics abstracts: Elsevier; 1996. p. 585-93.

[271] Atkinson C, Cook J. Effect of loading rate on crack propagation under compressive stress in a saturated porous material. Journal of Geophysical Research: Solid Earth. 1993;98:6383-95.

[272] Ashby M, Sammis C. The damage mechanics of brittle solids in compression. Pure and Applied Geophysics. 1990;133:489-521.

[273] Costin L. Damage mechanics in the post-failure regime. Mechanics of Materials. 1985;4:149-60.

[274] Yazdani S, Schreyer H. An anisotropic damage model with dilatation for concrete. Mechanics of Materials. 1988;7:231-44.

[275] Krajcinovic D. Continuum damage mechanics. 1984.

[276] Wong TF. A note on the propagation behavior of a crack nucleated by a dislocation pileup. Journal of Geophysical Research: Solid Earth. 1990;95:8639-46.

[277] Zhang S, Paterson MS, Cox SF. Porosity and permeability evolution during hot isostatic pressing of calcite aggregates. Journal of Geophysical Research: Solid Earth. 1994;99:15741-60.

[278] Fredrich JT, Evans B, Wong TF. Micromechanics of the brittle to plastic transition in Carrara marble. Journal of Geophysical Research: Solid Earth. 1989;94:4129-45.

[279] Schrodt JK, Holder JT. Temperature and strain rate effects on micromechanical behavior in triaxially compressed marbles. The 24th US Symposium on Rock Mechanics (USRMS): American Rock Mechanics Association; 1983.

[280] Edmond J, Paterson M. Volume changes during the deformation of rocks at high pressures. International Journal of Rock Mechanics and Mining Sciences & Geomechanics Abstracts: Elsevier; 1972. p. 161-82.

[281] Popp T, Kern H, Schulze O. Evolution of dilatancy and permeability in rock salt during hydrostatic compaction and triaxial deformation. Journal of Geophysical Research: Solid Earth. 2001;106:4061-78.

[282] Peach CJ, Spiers CJ. Influence of crystal plastic deformation on dilatancy and permeability development in synthetic salt rock. Tectonophysics. 1996;256:101-28.

[283] Lajtai E, Schmidtke R, Bielus L. The effect of water on the time-dependent deformation and fracture of a granite. International Journal of Rock Mechanics and Mining Sciences & Geomechanics Abstracts: Elsevier; 1987. p. 247-55.

[284] Kranz RL. The effects of confining pressure and stress difference on static fatigue of granite. Journal of Geophysical Research: Solid Earth. 1980;85:1854-66.

[285] Kranz R, Scholz C. Critical dilatant volume of rocks at the onset of tertiary creep. Journal of Geophysical Research. 1977;82:4893-8.

[286] Cogan J. Triaxial creep tests of Opohonga limestone and Ophir shale. International Journal of Rock Mechanics and Mining Sciences & Geomechanics Abstracts: Elsevier; 1976. p. 1-10.

[287] Wu FT, Thomsen L. Microfracturing and deformation of Westerly granite under creep condition. International Journal of Rock Mechanics and Mining Sciences & Geomechanics Abstracts: Elsevier; 1975. p. 167-73.

[288] Wawersik W. Time-dependent behaviour of rock in compression. Advances in rock mechanics: proceedings of the third Congress of the International society for rock mechanics, Denver, Colorado1974. p. 1-7.

[289] Scholz C, Kranz R. Notes on dilatancy recovery. Journal of Geophysical Research. 1974;79:2132-5.

[290] Scholz C. Mechanism of creep in brittle rock. Journal of Geophysical Research. 1968;73:3295-302.

[291] Masuda K, Mizutani H, Yamada I. Experimental study of strain-rate dependence and pressure dependence of failure properties of granite. Journal of Physics of the Earth. 1987;35:37-66.

[292] Sano O, Ito I, Terada M. Influence of strain rate on dilatancy and strength of Oshima granite under uniaxial compression. Journal of Geophysical Research: Solid Earth. 1981;86:9299-311.

[293] Jirásek M. Mathematical analysis of strain localization. Revue européenne de génie civil. 2007;11:977-91.

[294] Cedolin L, Bažant ZP. Effect of finite element choice in blunt crack band analysis. Computer Methods in Applied Mechanics and Engineering. 1980;24:305-16.

[295] Vardoulakis I. Shear-banding and liquefaction in granular materials on the basis of a Cosserat continuum theory. Ing arch. 1989;59:106-13.

[296] Bažant ZP. Why continuum damage is nonlocal: Micromechanics arguments. Journal of Engineering Mechanics. 1991;117:1070-87.

[297] Chen Z, Schreyer H. Simulation of soil-concrete interfaces with nonlocal constitutive models. Journal of engineering mechanics. 1987;113:1665-77.

[298] Pijaudier-Cabot G, Bažant ZP. Nonlocal damage theory. Journal of engineering mechanics. 1987;113:1512-33.

[299] De Borst R, Mühlhaus HB. Gradient-dependent plasticity: Formulation and algorithmic aspects. International Journal for Numerical Methods in Engineering. 1992;35:521-39.

[300] DE RPR, De Vree J. Gradient enhanced damage for quasi-brittle materials. International Journal for numerical methods in engineering. 1996;39:3391-403.

[301] Jirasek M. Nonlocal models for damage and fracture: comparison of approaches. International Journal of Solids and Structures. 1998;35:4133-45.

[302] Poh LH, Swaddiwudhipong S. Over-nonlocal gradient enhanced plastic-damage model for concrete. International Journal of Solids and Structures. 2009;46:4369-78.

[303] Borja RI. A finite element model for strain localization analysis of strongly discontinuous fields based on standard galerkin approximation. Computer Methods in Applied Mechanics and Engineering. 2000;190:1529-49.

[304] Foster C, Borja R, Regueiro R. Embedded strong discontinuity finite elements for fractured geomaterials with variable friction. International Journal for Numerical Methods in Engineering. 2007;72:549-81.

[305] Larsson R, Runesson K, Sture S. Embedded localization band in undrained soil based on regularized strong discontinuity—theory and FE-analysis. International Journal of Solids and Structures. 1996;33:3081-101.

[306] Oliver J. Modelling strong discontinuities in solid mechanics via strain softening constitutive equations. Part 1: Fundamentals. International journal for numerical methods in engineering. 1996;39:3575-600.

[307] Borja RI. Assumed enhanced strain and the extended finite element methods: A unification of concepts. Computer Methods in Applied Mechanics and Engineering. 2008;197:2789-803.

[308] Samaniego E, Belytschko T. Continuum–discontinuum modelling of shear bands. International Journal for Numerical Methods in Engineering. 2005;62:1857-72.

[309] Wells G, Sluys L. A new method for modelling cohesive cracks using finite elements. International Journal for Numerical Methods in Engineering. 2001;50:2667-82.

[310] Sanborn SE, Prévost JH. Frictional slip plane growth by localization detection and the extended finite element method (XFEM). International Journal for Numerical and Analytical Methods in Geomechanics. 2011;35:1278-98.

[311] Belytschko T, Fish J, Engelmann BE. A finite element with embedded localization zones. Computer methods in applied mechanics and engineering. 1988;70:59-89.

[312] Sluys L, Berends A. Discontinuous failure analysis for mode-I and mode-II localization problems. International Journal of Solids and Structures. 1998;35:4257-74.

[313] Garikipati K, Hughes TJ. A study of strain localization in a multiple scale framework—the one-dimensional problem. Computer Methods in Applied Mechanics and Engineering. 1998;159:193-222.

[314] Garikipati K, Hughes T. A variational multiscale approach to strain localization–formulation for multidimensional problems. Computer Methods in Applied Mechanics and Engineering. 2000;188:39-60.

[315] Huespe AE, Needleman A, Oliver J, Sánchez PJ. A finite thickness band method for ductile fracture analysis. International Journal of Plasticity. 2009;25:2349-65.

[316] Nguyen CT, Nguyen GD, Das A, Bui HH. Constitutive modelling of progressive localised failure in porous sandstones under shearing at high confining pressures. International Journal of Rock Mechanics and Mining Sciences. 2017;93:179-95.

[317] Vardoulakis I, Goldscheider M, Gudehus G. Formation of shear bands in sand bodies as a bifurcation problem. International Journal for numerical and analytical methods in Geomechanics. 1978;2:99-128.

[318] Kolymbas D. Kinematics of shear bands. Acta Geotechnica. 2009;4:315.

[319] Borja RI. Cam-Clay plasticity, Part II: Implicit integration of constitutive equation based on a nonlinear elastic stress predictor. Computer Methods in Applied Mechanics and Engineering. 1991;88:225-40.

[320] Simo JC, Hughes TJ. Computational inelasticity: Springer Science & Business Media; 2006.

[321] Finno R, Harris W, Mooney MA, Viggiani G. Shear bands in plane strain compression of loose sand. Geotechnique. 1997;47:149-65.

[322] Alshibli KA, Sture S. Sand shear band thickness measurements by digital imaging techniques. Journal of computing in civil engineering. 1999;13:103-9.

[323] Bažant ZP, Pijaudier-Cabot G. Measurement of characteristic length of nonlocal continuum. Journal of Engineering Mechanics. 1989;115:755-67.

[324] Mukherjee M, Nguyen GD, Mir A, Bui HH, Shen L, El-Zein A et al. Capturing pressure-and rate-dependent behaviour of rocks using a new damage-plasticity model. International Journal of Impact Engineering. 2017.

[325] Frew DJ, Parker QA. Planetary Nebulae: Observational Properties, Mimics and Diagnostics. Publications of the Astronomical Society of Australia. 2010;27:129-48.

Appendix A

A Thermodynamics-based formulation for constitutive modelling using damage mechanics and plasticity theory

Vu, V.D., Mir, A., Nguyen, G.D. and Sheikh, A.H., 2017. A thermodynamics-based formulation for constitutive modelling using damage mechanics and plasticity theory. *Engineering Structures*, *143*, pp.22-39.

Statement of Authorship

Title of Paper	A Thermodynamics-based formulation for constitutive modelling using damage mechanics and plasticity theory
Publication Status	☑ Published ☐ Accepted for Publication ☐ Submitted for Publication ☐ Unpublished and Unsubmitted w ork w ritten in manuscript style
Publication Details	Vu, V.D., Mir, A., Nguyen, G.D. and Sheikh, A.H., 2017. A thermodynamics-based formulation for constitutive modelling using damage mechanics and plasticity theory. *Engineering Structures*, *143*, pp.22-39.

Principal Author

Name of Principal Author (Candidate)	Van Duc Vu		
Contribution to the Paper	Developed and wrote the generic formulation and its application and numerical examples for concrete and metal.		
Overall percentage (%)	60 %		
Signature		Date	25/05/2017

Co-Author Contributions

By signing the Statement of Authorship, each author certifies that:

i. the candidate's stated contribution to the publication is accurate (as detailed above);
ii. permission is granted for the candidate in include the publication in the thesis; and
iii. the sum of all co-author contributions is equal to 100% less the candidate's stated contribution.

Name of Co-Author	Arash Mir		
Contribution to the Paper	Developed and wrote the section on the behaviour of geomaterials. Wrote the introduction and actively participated in writing the manuscript		
Certification:	This paper reports on original research I conducted during the period of my Higher Degree by Research candidature and is not subject to any obligations or contractual agreements with a third party that would constrain its inclusion in this thesis. I am the primary author of this paper.		
Signature		Date	25/05/2017

Name of Co-Author	Giang D. Nguyen		
Contribution to the Paper	Supervision of the technical work, write-up and revision of the manuscript		
Signature		Date	25/05/2017

Name of Co-Author	Abdul Hamid Sheikh		
Contribution to the Paper	Supervision of the technical work, write-up and revision of the manuscript		
Signature		Date	25/05/2017

End of document

Engineering Structures 143 (2017) 22–39

Contents lists available at ScienceDirect

Engineering Structures

journal homepage: www.elsevier.com/locate/engstruct

A thermodynamics-based formulation for constitutive modelling using damage mechanics and plasticity theory

Van D. Vu, Arash Mir, Giang D. Nguyen *, Abdul Hamid Sheikh

School of Civil, Environmental and Mining Engineering, The University of Adelaide, Australia

ARTICLE INFO

Article history:
Received 24 November 2016
Revised 2 April 2017
Accepted 6 April 2017
Available online 12 April 2017

Keywords:
Constitutive modelling
Thermodynamics
Damage mechanics
Plasticity theory
Coupled damage-plasticity
Concrete
Rocks
Ductile
Brittle

ABSTRACT

In this study, a generic formulation for constitutive modelling of engineering materials is developed, employing theories of plasticity and continuum damage mechanics. The development of the proposed formulation is carried out within the framework of thermodynamics with internal variables. In this regard, the complete constitutive relations are determined by explicitly defining a free energy potential and a dissipation potential. The focus is put on the rigour and consistency of the proposed formulation in accommodating the coupling between damage and plasticity, while keeping its structure sufficiently generic to be applicable to a wide range of engineering materials. In particular, by specifying the coupling between damage and plasticity in the dissipation function, a single generalised loading function that controls the simultaneous evolution of these dissipative mechanisms is obtained. The proposed formulation can be readily used for either enriching existing plasticity models with damage, or for the developments of new coupled damage-plasticity models. The promising features and the applications of the proposed formulation for describing the behaviour of different engineering materials are discussed in details.

1. Introduction

Computer simulations of the mechanical response of structures, by means of a numerical technique, such as finite element method (FEM), play a key role in many modern civil and mechanical engineering applications. The accuracy of analysis of any numerical simulation, however, depends on a constitutive model, capable of adequately capturing the material behaviour under complex loading scenarios. Theories of plasticity and continuum damage mechanics (CDM) have been widely used for the development of constitutive models in order to describe the inelastic behaviour of materials. At the macroscopic scale, inelastic behaviour can be observed as the reduction in strength and stiffness as well as the occurrence of residual strains. The observable macroscopic behaviour of materials is mainly governed by several underlying microscopic dissipative mechanisms. These dissipative mechanisms are the direct result of progressive, irreversible changes in the material microstructure. Examples of such changes are closure or expansion of micro-voids, micro-crack initiation and coalescence, frictional sliding between the two surfaces of microcracks, dislocation of defects in the crystal structure of metals and so forth. From a phenomenological perspective, the effects of all underlying mechanisms which cause the occurrence of residual deformations (e.g. frictional sliding, dislocation of defects, etc.) can be represented by a plastic strain tensor as a macroscopic variable. Similarly, the effects of all mechanisms giving rise to strength and stiffness degradation may be accounted for by a damage variable, which can be a scalar or a tensor of higher orders. In general, for any constitutive model, a set of internal variables is required for a complete description of inelastic behaviours of not only the current state but also the previous history of deformations [1–10].

During the course of inelastic deformation of engineering materials, plasticity and damage processes normally occur together and one influences the evolution of the other. Hence, constitutive models which take only one of these two mechanisms into account may not adequately represent the observed behaviour of materials. Formulations based merely on plasticity theory [11–19], for instance, generally suffer from limitations in capturing the stiffness reduction due to damage growth [11], although they may be successful in modelling the overall stress-strain response, by explicitly defining some kind of hardening/softening rules for the yield function. Elastic-damage models [20–27], on the other hand, can successfully capture the material stiffness reduction due to damage processes, yet they may be criticised for their inadequacy in properly modelling the residual strains due to plastic deforma-

* Corresponding author at: School of Civil, Environmental and Mining Engineering, The University of Adelaide, Adelaide, SA 5005, Australia.
E-mail addresses: giang.nguyen@trinity.oxon.org, g.nguyen@adelaide.edu.au (G.D. Nguyen).

http://dx.doi.org/10.1016/j.engstruct.2017.04.018
0141-0296/

Nomenclature

Ψ	Helmholtz free energy potential
Φ	total dissipation rate function
Φ_v	dissipation rate function corresponding to volumetric plastic deformation
Φ_s	dissipation rate function corresponding to shear plastic deformation
Φ_D	dissipation rate function corresponding to damage
D	scalar damage variable
K	bulk modulus
G	shear modulus
ε_V	total volumetric strain
ε_S	total effective shear strain
α_V	volumetric plastic strain
α_S	effective shear plastic strain
ε_p	accumulative plastic strain
ε_{pc}	critical value of the accumulative plastic strain
σ_{ij}	stress tensor
S_{ij}	deviatoric stress tensor
J_2	second invariant of the deviatoric stress tensor
I_1	first invariant of the stress tensor
ε_{ij}	strain tensor
e_{ij}	deviatoric strain tensor
α_{ij}	plastic strain tensor
λ	non-negative multiplier
δ_{ij}	Kronecker delta
C_{ijkl}	elastic stiffness tensor
C^t_{ijkl}	tangent stiffness tensor
p	mean pressure
q	deviatoric stress
$\bar{\chi}_{ij}$	generalised stress tensor
$\bar{\chi}_V$	generalised mean pressure
$\bar{\chi}_s$	generalised shear stress
$\bar{\chi}_D$	conjugate damage energy
χ_{ij}	generalised dissipative stress tensor
χ_V	generalised dissipative mean pressure
χ_s	generalised dissipative shear stress
χ_D	conjugate dissipative damage energy
y	yield function in true stress space
y^*	yield function in generalised dissipative stress space
ϕ_v	function representing the effect of α_V in total dissipation
ϕ_v	function representing the effect of α_s in total dissipation
ϕ_D	function representing the effect of D in total dissipation
E	function of stresses and internal variables
F	function of stresses and internal variables
f_v	dimensionless function of stresses and internal variables
f_s	dimensionless function of stresses and internal variables
a	dimensionless function of stresses and internal variables
b	dimensionless function of stresses and internal variables
c	dimensionless function of stresses and internal variables
r_d	dimensionless function of stresses and internal variables
r_p	dimensionless function of stresses and internal variables
f_y	dimensionless function of stresses and internal variables
f_{cy}	dimensionless function of stresses and internal variables
f_{ty}	dimensionless function of stresses and internal variables
Q	ultimate stress (Von Mises model)
Q_t	ultimate stress in tension (parabolic Drucker-Prager model)
Q_c	ultimate stress in compression (parabolic Drucker-Prager model)
H	material parameter determining the rate of expansion of the yield surface
H_t	the value of parameter H in tension
H_c	the value of parameter H in compression
k	material shear strength (Von Mises model)
α	parabolic Drucker-Prager material parameter
β	parabolic Drucker-Prager material parameter
p_c	initial yield pressure under isotropic compression
p_t	initial yield under isotropic decompression (expansion)
ω	material parameter controlling the shape of the yield surface (geomaterials model)
γ	material parameter controlling the shape of the yield surface (geomaterials model)
ρ	back stress (geomaterials model)
M	slope of the final failure envelope (geomaterials model)

tions, which may only be included into these models by means of some empirical definitions [20]. Hence, a combination of both plasticity theory and CDM is necessary for the development of a realistic and rigorous constitutive model.

Significant efforts have been made during the past few decades to construct coupled damage-plasticity models by specifying the interaction between the two dissipative mechanisms. One of the existing approaches for coupling damage and plasticity is to employ two separate loading functions pertaining to damage and plasticity. In this approach, the two inelastic mechanisms are linked through the constitutive relations and the plastic yield function is expressed in the effective stress space, associated with the undamaged state of the material [8,28–51]. In these models, hardening rules are usually introduced to control the evolution of the yield function, while a softening rule controls the evolution of the damage function, and their coupling results in an overall hardening or softening behaviour, owing to the combined effects of both damage and plasticity. Nevertheless, due to the use of two separate loading functions, it is usually difficult to correlate these two surfaces with the experimentally obtained yield envelope and its evolution to failure, especially in multiaxial loading scenarios. In particular, the coupling between damage and plasticity can only take place if the inner loading surface (usually the plastic yield surface) evolves and hits the outer one, after which the two surfaces evolve together.

In another class of coupled damage-plasticity models [9,52–59], the above-mentioned issues associated with employing two loading surfaces are alleviated by explicitly defining the damage growth as a function of plastic strain. In these models, the only role of the damage function is to determine the onset of damage-induced softening, while the overall inelastic behaviour relies on the yield function and its flow rules. A physical interpretation of these models is that plasticity can be considered as an active mechanism of deformation and energy dissipation followed by damage as a passive mechanism, that is, damage can occur only after some plastic deformation has already taken place. Such

models have shown great success in modelling the deformation and failure of a wide range of materials. Nevertheless, the concept of active and passive mechanisms can be used to assess the characteristics of such models for further improvements. For instance, in quasi-brittle materials, such as rocks and concrete under tension, energy dissipation processes usually begin with the development of micro-cracking as an active mechanism, followed by frictional sliding between the newly created crack surfaces (passive mechanism). In compression, on the other hand, experimental observations from geological materials [60–67] suggest that plastic dissipation due to micro-crack closure and the subsequent frictional sliding takes place together with the initiation of new micro-cracks, where the stress condition is favourable. Another example is grain boundary sliding in metallic materials which can be inferred as an active plasticity mechanism, followed by the stiffness degradation due to debonding process (damage) as a passive mechanism [68]. In our opinion, it is always better to have these features reflected in the constitutive model, in addition to the requirements on its ease of implementation and adequate predictive capability.

Furthermore, it is essential for any constitutive model to conform to the principles of thermodynamics. Although the requirements for the thermodynamic admissibility of a constitutive model can be applied upon completion of its development, a more rigorous and consistent approach is to build a constitutive model within a well-established thermodynamic framework. Keeping all these aspects in view, the development of a generic thermodynamic approach for coupling damage and plasticity by addressing the interaction between these two dissipative mechanisms, as well as controlling the contribution of each of these mechanisms in the total dissipation, is desired. This study is an attempt towards this goal by further developing the results of our previous works [68–70] that are based on a thermodynamic framework proposed earlier by Houlsby and Puzrin [71]. Emphasis is put on the coupling scheme of the proposed formulation so that a single plastic-damage loading function can be obtained to describe both yielding and the ultimate failure of a material. The evolution rules for both damage and plastic strains appear naturally during the derivation of the model from only two scalar thermodynamic functions (i.e. the free energy potential and the dissipation potential). In addition, the degree of contribution of each of these dissipative processes can be controlled on the basis of the observed behaviour of materials. This will allow for a more convenient and easier implementation and calibration of models, particularly, under multi-axial loading. In addition, dilative and/or contractive behaviour of engineering materials can be conveniently specified in cases of either enhancing an existing material model or developing new material models.

The outline of this paper is as follows; in Section 2, a complete presentation of the proposed formulation for coupling damage and plasticity along with a detailed discussion on some of its promising features, are provided. In Section 3, the applications of the proposed formulation for enhancing the currently existing material models as well as constructing a new material model are demonstrated through a number of numerical examples.

2. A new formulation for coupling damage and plasticity

The framework of generalised thermodynamics by Houlsby and Puzrin [71,72] is adopted in this study to ensure the thermodynamic consistency of the model. A detailed discussion on the development and different features of the proposed formulation is provided in this section. The generic formulation provides a consistent and robust scheme for coupling damage and plasticity and allows for adequately simulating various aspects of material behaviour including dilation, compaction and non-associated flow.

2.1. Thermodynamic-based formulation

In the formulation presented in this section the notation appropriate for triaxial tests is used, with the total volumetric strain being defined as $\varepsilon_V = -\varepsilon_{ii}$ and the total equivalent shear strain as $\varepsilon_S = \sqrt{2/3 e_{ij} e_{ij}}$, where $e_{ij} = \varepsilon_{ij} + \delta_{ij}\varepsilon_V/3$ and δ_{ij} is the Kronecker delta. Similarly, the plastic volumetric strain is denoted as $\alpha_V = -\alpha_{ii}$ and the equivalent plastic shear strain is represented by $\alpha_S = \sqrt{2/3 e^p_{ij} e^p_{ij}}$, where $e^p_{ij} = \alpha_{ij} + \delta_{ij}\alpha_V/3$. In addition, the hydrostatic pressure and the deviatoric stress are defined as $p = -I_1/3 = -\sigma_{ii}/3$ and $q = \sqrt{3J_2} = \sqrt{3/2 s_{ij} s_{ij}}$, respectively, where $s_{ij} = \sigma_{ij} + \delta_{ij} p$.For isothermal processes, the Helmholtz free energy potential is the same as the elastic strain energy and may be written as:

$$\Psi = (1-D)\left[\frac{1}{2}K(\varepsilon_V - \alpha_V)^2 + \frac{3}{2}G(\varepsilon_S - \alpha_S)^2\right] \tag{1}$$

where K is the bulk modulus and G is the shear modulus, and D is a scalar damage variable controlling the strength and stiffness degradation of the material [23,24]. Despite the popularity of this type of isotropic damage formulation used in several well regarded models e.g. [8,26,46,47,57,58], it has been pointed out [29,73,74] that this formulation cannot capture well the change in the Poisson's ratio due to material deterioration. This is acknowledged as a shortcoming of the proposed approach, and this isotropic damage formulation is adopted here due to the simplicity in both the formulation and the physical interpretation of damage. The resolution of this problem may be the use of tensorial damage [29], or non-linear elasticity coupled with scalar damage [73,74].

The stresses, p and q can be obtained from the Helmholtz free energy as follows:

$$p = \frac{\partial \Psi}{\partial \varepsilon_V} = (1-D)K(\varepsilon_V - \alpha_V) \tag{2}$$

$$q = \frac{\partial \Psi}{\partial \varepsilon_S} = (1-D)3G(\varepsilon_S - \alpha_S) \tag{3}$$

The generalised stresses $\bar{\chi}_V$, $\bar{\chi}_S$ and $\bar{\chi}_D$, associated with internal variables α_V, α_S and D, can also be obtained as:

$$\bar{\chi}_V = -\frac{\partial \Psi}{\partial \alpha_V} = (1-D)K(\varepsilon_V - \alpha_V) = p \tag{4}$$

$$\bar{\chi}_S = -\frac{\partial \Psi}{\partial \alpha_S} = (1-D)3G(\varepsilon_S - \alpha_S) = q \tag{5}$$

$$\begin{aligned}\bar{\chi}_D &= -\frac{\partial \Psi}{\partial D} = \frac{1}{2}K(\varepsilon_V - \alpha_V)^2 + \frac{3}{2}G(\varepsilon_S - \alpha_S)^2 \\ &= \frac{p^2}{2K(1-D)^2} + \frac{q^2}{6G(1-D)^2}\end{aligned} \tag{6}$$

In order to specify the coupling between damage and plasticity the following form of the dissipation rate function is proposed:

$$\Phi = \sqrt{\varphi_V^2 + \varphi_S^2 + \varphi_D^2} + f_V\varphi_V + f_S\varphi_S \geqslant 0 \tag{7}$$

where ϕ_v, ϕ_s and ϕ_D are homogeneous first order functions in the rates of the internal variables ($\dot{\alpha}_V$, $\dot{\alpha}_S$ and $\dot{D}$), representing the effect of each dissipative mechanism on the total dissipation rate function, Φ. The dimensionless quantities f_v and f_s are functions of stresses and internal variables, which are responsible for controlling the direction of plastic flow vectors in the true stress space by moving

the centre of yield surface in the dissipative stress space (Fig. 1). The physical meaning of these functions will be clearer when the formulation of yield surface will be considered in the dissipative stress space (Eq. (17)). The generic forms of these functions along with the dissipation components (ϕ_v, ϕ_s and ϕ_D) used in the above equation are expressed as follows:

$$f_V = \frac{p - a\sqrt{E(p,q,D,\varepsilon_p)}}{F(p,q,D,\varepsilon_p)} \tag{8}$$

$$f_S = \frac{q - b\sqrt{E(p,q,D,\varepsilon_p)}}{F(p,q,D,\varepsilon_p)} \tag{9}$$

$$\varphi_V = F(p,q,D,\varepsilon_p)\dot{\alpha}_V \tag{10}$$

$$\varphi_S = F(p,q,D,\varepsilon_p)\dot{\alpha}_S \tag{11}$$

$$\varphi_D = \frac{F(p,q,D,\varepsilon_p)\bar{\chi}_D}{\sqrt{r_d E(p,q,D,\varepsilon_p)}}\dot{D} \tag{12}$$

where ε_p is the accumulative effective plastic strain the rate of which is given as $\dot{\varepsilon}_p = \sqrt{2\dot{\alpha}_{ij}\dot{\alpha}_{ij}/3}$. In addition, $E(p,q,D,\varepsilon_p)$ and $F(p,q,D,\varepsilon_p)$ are functions of stresses and internal variables and define the form of the yield function in true stress space. Throughout the remainder of this paper, these functions are simply referred to as E and F for notational convenience. Functions a and b are used to control the energy dissipation due to plastic volumetric strain and equivalent shear plastic strain and also to control the direction of the plastic flow vector in the stress space (see Section 2.2 for more details). In addition, the function r_d, in Eq. (12), controls the activation and evolution of damage processes. Further discussions on the role of the functions a, b and r_d and their relationship will be provided later when deriving the evolution rules for the internal variables. Considering the definitions given in Eqs. (8)–(12), the general condition required for thermodynamic admissibility ($\Phi \geq 0$) can be given as (see Appendix A):

$$|pa| \leqslant qb + r_d F \tag{13}$$

The above condition imposes some restrictions on the selection of model parameters and on the definition of generic functions when their explicit definitions are to be specified for constructing a material model. The further details illustrating the proof of thermodynamic admissibility of the constitutive models used in this study are provided in Appendix A.

The expression of the dissipation rate function as provided in Eq. (7) offers some advantages over the existing models which employ similar expressions for the dissipation potential [68–70]. It facilitates to control the direction of plastic flow vector in the stress space for better simulations of dilative and contractive behaviour. Furthermore, the existence of a single generalised yield function which controls the simultaneous evolution of damage and plastic deformations arises as a consequence of expressing the dissipation rate function in the form of Eq. (7). Within the framework of generalised thermodynamics, the yield function in generalised dissipative stress space (not true stress space) can be derived by performing a Legendre transformation on the dissipation rate function. Since the dissipation rate function is a homogeneous first order function in rates, this transformation is a degenerate special case of Legendre transformation [71,72]. Using Eq. (7), the generalised dissipative stresses [71] are defined as follows:

$$\chi_V = \frac{\partial\Phi}{\partial\dot{\alpha}_V} = \frac{\partial\Phi}{\partial\varphi_V}\frac{\partial\varphi_V}{\partial\dot{\alpha}_V} = \left(\frac{\varphi_V}{\sqrt{\varphi_V^2+\varphi_S^2+\varphi_D^2}} + f_V\right)\frac{\partial\varphi_V}{\partial\dot{\alpha}_V} \tag{14}$$

$$\chi_S = \frac{\partial\Phi}{\partial\dot{\alpha}_S} = \frac{\partial\Phi}{\partial\varphi_S}\frac{\partial\varphi_S}{\partial\dot{\alpha}_S} = \left(\frac{\varphi_S}{\sqrt{\varphi_V^2+\varphi_S^2+\varphi_D^2}} + f_S\right)\frac{\partial\varphi_S}{\partial\dot{\alpha}_S} \tag{15}$$

$$\chi_D = \frac{\partial\Phi}{\partial\dot{D}} = \frac{\partial\Phi}{\partial\varphi_D}\frac{\partial\varphi_D}{\partial\dot{D}} = \left(\frac{\varphi_D}{\sqrt{\varphi_V^2+\varphi_S^2+\varphi_D^2}}\right)\frac{\partial\varphi_D}{\partial\dot{D}} \tag{16}$$

It is inferred from the above equations and Eqs. (10)–(12) that the generalised dissipative stresses are functions of the rates of all the internal variables. This is a consequence of expressing the dissipation function in the form of Eq. (7), instead of using the usual additive form in earlier studies [8,9,46], in which dissipative stresses are dependent on the rate of their associated internal variable only. Material models constructed based on the proposed formulation will benefit from possessing a single loading function, which is obtained from the Legendre transformation of the dissipation function, instead of two separate loading functions corresponding to damage and plasticity, had the additive form of the dissipation potential been used. Eqs. (14)–(16) can be used to obtain a single generalised loading function as:

$$y^* = \left(\frac{\chi_V}{\partial\varphi_V/\partial\dot{\alpha}_V} - f_V\right)^2 + \left(\frac{\chi_S}{\partial\varphi_S/\partial\dot{\alpha}_S} - f_S\right)^2 + \left(\frac{\chi_D}{\partial\varphi_D/\partial\dot{D}}\right)^2 - 1 \leqslant 0 \tag{17}$$

As illustrated in Fig. 1, the above loading function represents an ellipsoid with its centre at the point $(f_V\frac{\partial\varphi_V}{\partial\dot{\alpha}_V}, f_S\frac{\partial\varphi_S}{\partial\dot{\alpha}_S}, 0)$ in the generalised dissipative stress space (χ_V, χ_S, χ_D). The radii of this ellipsoid are also denoted by $l = \partial\varphi_V/\partial\dot{\alpha}_V$, $m = \partial\varphi_S/\partial\dot{\alpha}_S$ and $n = \partial\varphi_D/\partial\dot{D}$ (Fig. 1).

With the evolution of internal variables upon yielding, the size of the loading surface and its position in generalised dissipative stress space will vary, however, its centre will always remain in the (χ_V, χ_S) plane (Eq. (17)). The evolution of plastic strains and the scalar damage variable can be determined using this loading function and by taking its derivatives with respect to the corresponding generalised dissipative stresses. Therefore, by making use of Eqs. (4), (5), (8)–(12) and (17), the evolution rules are derived as:

$$\dot{\alpha}_V = \dot{\lambda}\frac{\partial y^*}{\partial\chi_V} = 2\dot{\lambda}\left(\frac{a\sqrt{E}}{F^2}\right) \tag{18}$$

$$\dot{\alpha}_S = \dot{\lambda}\frac{\partial y^*}{\partial\chi_S} = 2\dot{\lambda}\left(\frac{b\sqrt{E}}{F^2}\right) \tag{19}$$

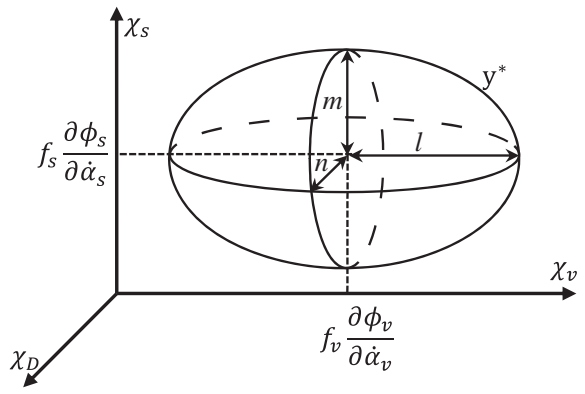

Fig. 1. Geometric interpretation of the yield potential in generalised dissipative stress space.

$$\dot{D} = \dot{\lambda}\frac{\partial y^*}{\partial \chi_D} = 2\dot{\lambda}\frac{r_d E}{F^2 \chi_D} \tag{20}$$

where $\dot{\lambda}$ is a non-negative multiplier. In deriving the above equations, a constitutive postulate (i.e. $\chi_V = \bar{\chi}_V$ and $\chi_S = \bar{\chi}_S$) equivalent to Ziegler's orthogonality condition [71] is invoked. It is deduced, from Eqs. (18)–(20), that the plastic flow vector is always normal to the loading surface in the generalised dissipative stress space, regardless of the plastic flow being associated or non-associated in true stress space. Furthermore, by making use of Eqs. (4)–(6) and substitution of Eqs. (8)–(12) into Eq. (17), the general form of the yield function in true stress space can be given as:

$$y = (a^2 + b^2 + r_d)E - F^2 = 0 \tag{21}$$

As can be seen in Eq. (21) for the yield function, a, b and r_d will affect the initial shape and size of the yield surface. As these functions a, b and r_d are also involved in the evolution rules for plastic strains and the scalar damage variable (Eqs. (18)–(20)), they will have effects on the evolution of the yield surface. It should be noted that the evolution of the yield surface in a damage-plasticity model is governed by both damage and plastic strains. In this sense, the functions a, b and r_d will have both direct (Eq. (21)) and indirect (Eqs. (18)–(20)) influence on the evolution of the yield surface. In order to simplify the calibration procedure of the initial yield surface against experimental data, the effects of model parameters on the initial the yield surface, and its evolution need to be separated. In other words, the calibration of the initial yield can be independent from its evolution. For this purpose, the following conditions are imposed to eliminate the direct effects of a, b and r_d on the initial size and shape of the yield function in true stress space:

$$a^2 + b^2 = r_p \text{ and } r_d + r_p = 1 \tag{22}$$

By imposing the above conditions, the functions a, b and r_d will only control the evolution of the yield surface and not its initial size and shape in true stress space. Accordingly, a user input with $r_d = 1$ implies that damage is the only active dissipative mechanism and no plastic deformation will take place, whereas the reverse is true when $r_p = 1$. For all other cases ($0 < r_d < 1$ and $0 < r_p < 1$), damage and plasticity occur together, while $r_d > r_p$ (or $r_p > r_d$) indicates that damage (or plasticity) is the dominant mechanism. Therefore, in order to control the coupling between damage and plasticity, the model requires only one input parameter r_d (or r_p). Similarly, for controlling the direction of plastic flow vector in stress space, only one parameter a (or b) is needed. Finally, by imposing the condition of Eq. (22) on Eq. (21), the general form of the yield in true stress space is expressed as:

$$y = E - F^2 = 0 \tag{23}$$

The explicit form of the yield function can be determined by specifying the functions E and F which in turn are defined on the basis of the specific application and the problem to be solved. Further discussion on the various forms of these functions E and F is provided in Section 3. In addition, it is important to examine the proportion of energy dissipation due to damage and plasticity relative to the total dissipation rate (defined as R_D and R_P, respectively). Since for rate independent material behaviour, the dissipation potential is a homogeneous first-order function in terms of the rates of internal variables [71], by making use of Euler's theorem for homogeneous functions, the dissipation function can be written as:

$$\begin{aligned}\Phi &= \frac{\partial \Phi}{\partial \dot{\alpha}_V}\dot{\alpha}_V + \frac{\partial \Phi}{\partial \dot{\alpha}_S}\dot{\alpha}_S + \frac{\partial \Phi}{\partial \dot{D}}\dot{D} = \chi_V \dot{\alpha}_V + \chi_S \dot{\alpha}_S + \chi_D \dot{\alpha}_D \\ &= \Phi_V + \Phi_S + \Phi_D \geqslant 0\end{aligned} \tag{24}$$

where Φ_V, Φ_S and Φ_D are the dissipation rate functions corresponding to plastic volumetric deformation, plastic shear deformation and damage, respectively (note that they are different form functions φ_V, φ_S and φ_D in Eq. (7)). As the functions Φ_V, Φ_S and Φ_D can be written explicitly in term of stresses (see Appendix B), the ratios between the dissipation rate due to plasticity or damage and the total dissipation rate can be obtained as follows:

$$\frac{\Phi_D}{\Phi} = \frac{r_d\sqrt{E}}{r_d\sqrt{E} + pa + qb} \tag{25}$$

$$\frac{\Phi_V + \Phi_S}{\Phi} = \frac{pa + qb}{r_d\sqrt{E} + pa + qb} \tag{26}$$

Also, the expressions of Φ_V and Φ_S (Appendix B) can be used to obtain the ratio between the dissipation rates associated with volumetric and shear components of the plastic deformations ($\bar{R}_P$) as:

$$\frac{\Phi_V}{\Phi_S} = \frac{pa}{qb} \tag{27}$$

In order to facilitate the calibration of model parameters, the total dissipated energy during the entire course of deformation are calculated and compared with the experimentally measured total dissipation. This can be achieved if the total dissipation rate function can be expressed as an integrable function in terms of the rate of one internal variable. For instance, the total dissipation rate function can be expressed as a homogeneous first order function in term of $\dot{\alpha}_s$ as (see Appendix B):

$$\Phi = \left(\frac{r_d\sqrt{E}}{b} + \frac{pa}{b} + q\right)\dot{\alpha}_S = \Gamma(\alpha_S)\dot{\alpha}_S \tag{28}$$

The final form of $\Gamma(\alpha_S)$ is determined by specifying the function E. The above discussion is further clarified through an example, given in Section 3.1, for a one-dimensional Von Mises model, where an explicit form of the total energy dissipation (fracture energy) is obtained by integrating the dissipation rate function.

2.2. Controlling the direction of plastic flow vector

As discussed previously, the evolutions of plastic strains (Eqs. (18), (19)) can be controlled by functions a (or b) and r_d (or r_p), where the relationship between these functions is given through the conditions of Eq. (22). In this regard, Eqs. (18) and (19) can be used to give the ratio between the rates of plastic volumetric strain and equivalent shear plastic strain as:

$$\frac{\dot{\alpha}_V}{\dot{\alpha}_S} = \frac{a}{b} \tag{29}$$

As mentioned earlier, the plastic flow vector is always normal to the loading surface y^* in the generalised dissipative stress space. However, it is normal to the yield surface y in $p - q$ stress space only if the flow rule is associated, where it will satisfy the following condition:

$$\frac{a}{b} = \frac{\partial y/\partial p}{\partial y/\partial q} \tag{30}$$

In order to control the ratio between the plastic volumetric strain and the equivalent shear plastic strain rates for simulating non-associated flow, a dimensionless function c can be introduced as:

$$\frac{a}{b} = c\frac{\partial y/\partial p}{\partial y/\partial q} \tag{31}$$

where the flow rule is associated if $c = 1$, and it is non-associated if $c \neq 1$. By making use of the conditions of Eq. (22) functions, a and b can be expressed in term of c as follows:

$$a = \pm\sqrt{\frac{c^2 r_p}{c^2 + \left(\frac{\partial y/\partial q}{\partial y/\partial p}\right)^2}} \tag{32}$$

$$b = \sqrt{\frac{r_p}{1 + c^2\left(\frac{\partial y/\partial p}{\partial y/\partial q}\right)^2}} \tag{33}$$

Thus, a and b can, in general, be determined indirectly by defining the function c. Following the sign convention adopted in this study (compression is positive), positive values of a ($a > 0$) correspond to plastic compaction, whereas negative values of a ($a < 0$) indicate plastic dilation (see Eqs. (18) and (19)). Furthermore, $a = 0$ implies pure plastic shear deformations (no plastic volumetric deformation), which is commonly observed in metals. The role of the function c in modelling the material behaviour and its influences on the plastic flow direction is illustrated by providing an example in Section 3.

2.3. Tangent stiffness tensor

In this section, the formulation of the tangent stiffness tensor C^t_{ijkl} is presented as it may be necessary for integration of the rate equations if an explicit integration scheme is used. The stress tensor can be given, by making use of Eq. (1) as:

$$\begin{aligned}\sigma_{ij} &= \frac{\partial \Psi}{\partial \varepsilon_{ij}} = \frac{\partial \Psi}{\partial \varepsilon_V}\frac{\partial \varepsilon_V}{\partial \varepsilon_{ij}} + \frac{\partial \Psi}{\partial \varepsilon_S}\frac{\partial \varepsilon_S}{\partial \varepsilon_{ij}} = (1-D)(K\varepsilon^e_V \delta_{ij} + 2Ge^e_{ij}) \\ &= (1-D)C_{ijkl}(\varepsilon_{kl} - \alpha_{kl})\end{aligned} \tag{34}$$

From the above equation, the incremental stress tensor can be determined as:

$$\dot{\sigma}_{ij} = (1-D)C_{ijkl}(\dot{\varepsilon}_{kl} - \dot{\alpha}_{kl}) - \frac{\sigma_{ij}}{(1-D)}\dot{D} \tag{35}$$

Furthermore, Eqs. (18) and (19) can be used to obtain the incremental plastic strain tensor $\dot{\alpha}_{ij}$, which can be written as:

$$\dot{\alpha}_{ij} = \dot{\lambda}\frac{\partial y^*}{\partial \chi_{ij}} = \dot{\lambda}\left(\frac{\partial y^*}{\partial \chi_V}\frac{\partial \chi_V}{\partial \sigma_{ij}} + \frac{\partial y^*}{\partial \chi_S}\frac{\partial \chi_S}{\partial \sigma_{ij}}\right) \tag{36}$$

The consistency condition can now be written by utilising the yield function of Eq. (23) as:

$$\dot{y} = \frac{\partial y}{\partial \sigma_{ij}}\dot{\sigma}_{ij} + \frac{\partial y}{\partial \varepsilon_p}\dot{\varepsilon}_p + \frac{\partial y}{\partial D}\dot{D} = 0 \tag{37}$$

where the rate of effective plastic strain $\dot{\varepsilon}_p$ can be obtained using Eq. (36) as:

$$\dot{\varepsilon}_p = \sqrt{\frac{2}{3}\dot{\alpha}_{ij}\dot{\alpha}_{ij}} = \dot{\lambda}\sqrt{\frac{2}{3}\frac{\partial y^*}{\partial \chi_{ij}}\frac{\partial y^*}{\partial \chi_{ij}}} \tag{38}$$

Therefore, the non-negative multiplier $\dot{\lambda}$ is obtained, by making use of Eqs. (20) and (35)–(38), as:

$$\dot{\lambda} = M_{kl}\dot{\varepsilon}_{kl} \tag{39}$$

where

$$M_{kl} = \frac{(1-D)\frac{\partial y}{\partial \sigma_{ij}}C_{ijkl}}{(1-D)\frac{\partial y}{\partial \sigma_{ij}}C_{ijkl}\frac{\partial y^*}{\partial \chi_{kl}} + \frac{\partial y}{\partial \sigma_{ij}}\frac{\sigma_{ij}}{1-D}\frac{\partial y^*}{\partial \chi_D} - \frac{\partial y}{\partial \varepsilon_p}\sqrt{\frac{2}{3}\frac{\partial y^*}{\partial \chi_{ij}}\frac{\partial y^*}{\partial \chi_{ij}}} - \frac{\partial y}{\partial D}\frac{\partial y^*}{\partial \chi_D}} \tag{40}$$

Finally, the incremental stress-strain relationship is expressed as:

$$\begin{aligned}\dot{\sigma}_{ij} &= \left[(1-D)C_{ijkl} - (1-D)C_{ijst}\frac{\partial y^*}{\partial \chi_{st}}M_{kl} - \frac{\sigma_{ij}}{1-D}M_{kl}\frac{\partial y^*}{\partial \chi_D}\right]\dot{\varepsilon}_{kl} \\ &= C^t_{ijkl}\dot{\varepsilon}_{kl}\end{aligned} \tag{41}$$

where C^t_{ijkl} represents the tangent stiffness tensor.

2.4. Stress return algorithm

Numerical implementations require the stress state be updated for a given strain increment. For infinitesimal increments in strains, stresses can be updated explicitly using the tangent stiffness or a forward-Euler scheme. However, in practical applications, the strain field within a structure is not uniform and hence, strain increments at material points (e.g. Gauss points in FEM) may not be infinitesimal throughout the body and consequently, the updated stresses may lie outside the yield surface. Unless the stresses are corrected and returned onto the yield surface, the forward-Euler scheme may give rise to erroneous values for stresses at the material point which in turn may result in a divergence in numerical scheme applied for satisfying equilibrium equations at the structural level. Hence, a form of backward-Euler scheme is adopted here to return the stresses to the yield surface following an elastic trial predictor. Returning procedures, which involve returning the trial stresses onto a new yield surface (in cases of hardening or softening), are activated only if the trial stresses lie outside the yield surface. To this end, the new yield surface is approximated at the trial stress values using a first order Taylor expansion as follows:

$$y^{n+1} = y^{trial} + \frac{\partial y}{\partial \sigma_{ij}}\Delta\sigma^{re}_{ij}\Big|^{trial} + \frac{\partial y}{\partial \varepsilon_p}\Delta\varepsilon_p\Big|^{trial} + \frac{\partial y}{\partial D}\Delta D\Big|^{trial} = 0 \tag{42}$$

As the strain increment has been utilised to move to trial stress values, the return stress increments, $\Delta\sigma^{re}_{ij}$, in the above equation can be obtained as:

$$\Delta\sigma^{re}_{ij} = \sigma^{n+1}_{ij} - \sigma^{trial} = \left[-(1-D)C_{ijkl}\Delta\alpha_{kl} - \frac{\sigma_{ij}}{(1-D)}\Delta D\right]\Big|^{trial} \tag{43}$$

This stress return algorithm is slightly different from a full backward-Euler scheme in which $\Delta\sigma^{re}_{ij}$ are calculated as normal to the new yield surface (y^{n+1}) by applying an iterative scheme. By substituting Eqs. (20), (36), (38) and (43) into Eq. (42), the non-negative multiplayer $\Delta\lambda$ can be obtained as follows:

$$\Delta\lambda = \frac{y^{trial}}{\frac{\partial y}{\partial \sigma_{ij}}\left[(1-D)C_{ijkl}\frac{\partial y^*}{\partial \sigma_{kl}} + \frac{\sigma_{ij}}{(1-D)}\frac{\partial y^*}{\partial \chi_D}\right]\Big|^{trial} - \frac{\partial y}{\partial \varepsilon_p}\dot{\lambda}\sqrt{\frac{2}{3}\frac{\partial y^*}{\partial \chi_{ij}}\frac{\partial y^*}{\partial \chi_{ij}}}\Big|^{trial} - \frac{\partial y}{\partial D}\dot{\lambda}\frac{\partial y^*}{\partial \chi_D}\Big|^{trial}} \tag{44}$$

Therefore, the final updated stresses can be obtained as:

$$\begin{aligned}\sigma^{n+1}_{ij} &= \sigma^{trial}_{ij} + \Delta\sigma^{re}_{ij} \\ &= \sigma^{trial}_{ij} - (1-D)C_{ijkl}\Delta\lambda\frac{\partial y^*}{\partial \sigma_{kl}} - \frac{\sigma_{ij}}{(1-D)}\Delta\lambda\frac{\partial y^*}{\partial \chi_D}\end{aligned} \tag{45}$$

3. Applications

In this section, the applicability of the proposed formulation for modelling the inelastic behaviour of a wide range of materials is discussed and its promising features are demonstrated through some numerical examples. In each case, the model predictions are validated against experimental data available in the literature. In what follows, firstly, the features of the proposed formulation are illustrated through coupling damage with the Von Mises plasticity model, which is widely utilised for modelling the behaviour

of pressure independent materials. Secondly, the influence of the plastic flow direction on the material response is investigated through the development of a coupled damage plasticity model for pressure dependent materials based on the parabolic Drucker-Prager yield function. Finally, through constructing a new model for cohesive frictional geomaterials, it is demonstrated that the proposed formulation can also facilitate the development of new elastoplastic damage models.

On the other hand, it should be noted that the focus of this paper is on the development of a thermodynamic-based formulation at the constitutive level and the issues related to material stability of the model in solving Boundary Value Problems are not considered in this study. The enhancements of the proposed models using nonlocal theory or viscous regularisation to effectively deal with the issues related to solution of boundary value problems will be the next step of developments. Our experience with these kinds of regularisation [8,9,32,70,81,82] showed that these techniques can be readily added to an existing constitutive model obtain discretisation-independent numerical solutions.

3.1. Coupling damage with the Von Mises plasticity model

The yield function of the classical Von Mises model in the $(p-q)$ stress space can be written in the following form:

$$y = \sqrt{3J_2} - k(D,\varepsilon_p) = q - k(D,\varepsilon_p) = 0 \tag{46}$$

The exclusion of pressure (or the first invariant of stresses I_1) in the above expression indicates its pressure independency. In order to incorporate the effects of plastic deformations and damage in the model the shear strength, k is defined as a function of two internal variables, namely, the scalar damage variable, D and accumulated plastic strain, ε_p as:

$$k = (1-D)(f_y + Q(1-e^{-H\varepsilon_p})) \tag{47}$$

where f_y and Q are the initial yield and the ultimate stresses, respectively, and H is a material parameter which determines the rate of expansion/contraction of the yield surface. It can be seen from Eqs. (46) and (47) that the evolution of the yield surface is governed by evolutions of damage D and equivalent plastic strain ε_p, where the evolution of ε_p is defined by Eq. (38). Comparing Eq. (46) with the generic form of yield function as stated by Eq. (23), it can be inferred that $E = q$ and $F^2 = k$ for von Mises yield function. Therefore, the flow rules can be obtained by making use of Eqs. (18)–(20) as follows:

$$\dot{\alpha}_V = 2\dot{\lambda}\frac{a\sqrt{q}}{k} \tag{48}$$

$$\dot{\alpha}_S = 2\dot{\lambda}\frac{b\sqrt{q}}{k} \tag{49}$$

$$\dot{D} = 2\dot{\lambda}\frac{r_d q}{k\bar{\chi}_D} \tag{50}$$

In addition, the plastic flow rule in the tensorial form can be derived using Eq. (36) as:

$$\dot{\alpha}_{ij} = \dot{\lambda}\frac{\partial y^*}{\partial \chi_{ij}} = \dot{\lambda}\left(2\frac{a\sqrt{q}}{k}\frac{\delta_{ij}}{3} + 2\frac{b\sqrt{q}}{k}\frac{3}{2\sqrt{3J_2}}\frac{\partial J_2}{\partial \sigma_{ij}}\right) \tag{51}$$

The stress-strain response produced by the above model definitions is illustrated in Fig. 2. The effect of different levels of damage activity, for different values of r_d, can also be observed in Fig. 2. Also, the model parameters used are: Young's modulus = 200,000 MPa, Poisson's ratio $(\nu) = 0.3$, $f_y = 250$ MPa, $Q = 50$ MPa and $H = 1000$. It should be noted that the incompressibility condition $(\dot{\alpha}_v = 0)$ of the Von Mises model can be accounted for by setting $a = 0$. In Fig. 2, the curve associated with $r_d = 0$ indicates a pure plastic deformation of the material without having any damage, while for other cases, where the damage and plastic deformations evolve together $(0 < r_d < 1)$, the effect of damage is observed as reduction in the ultimate stress and the softening behaviour (Fig. 2).

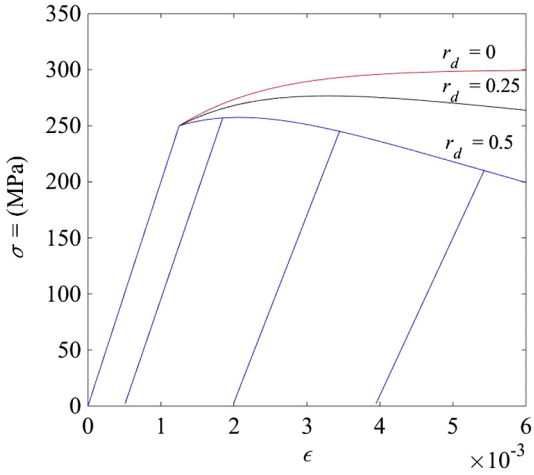

Fig. 2. Stress-strain response of a coupled damage-plasticity model based on Von Mises model under uniaxial stress condition for various values of r_d.

In general, the strain hardening behaviour of ductile metals (e.g. steel) under uniaxial tensile loading is accompanied by an insignificant reduction in stiffness immediately after the initial yielding. For these materials, softening behaviour is observed after the ultimate stress is reached followed by complete failure of the material. This behaviour can be replicated by making use of the enhanced Von Mises model, introduced here, by controlling the degree of activation of damage and plasticity. For instance, damage can be switched off during the strain hardening process, where no considerable stiffness reduction is observed (Fig. 3(a)), by setting $r_d = 0$ (see Eqs. (48)–(50)).

The softening behaviour, however, can be modelled through activation of damage by using a value of r_d greater than 0, once the accumulated plastic strain reaches a critical value ε_{pc} (Fig. 3 (b)). As illustrated in Fig. 3 (a), higher values of r_d correspond to more brittle behaviour with steeper slopes in the post-peak response. Furthermore, the stress-strain response of Aluminium Alloy 6082 under uniaxial tension [75] can be adequately captured by the proposed model as illustrated in Fig. 4. The model parameters used for this analysis are: Young's modulus = 30,000 MPa, Poisson's ratio $(\nu) = 0.3$, $f_y = 40$ MPa, $Q = 85$ MPa, $H = 50$, and $\varepsilon_{pc} = 0.48$ and $r_d = 0.97$.

As discussed earlier in Section 2, the calibration of model parameters can be facilitated by calculating the total energy dissipation during the course of inelastic deformation and also by comparing the calculated and experimentally measured total dissipated energy. The explicit analytical expression of the total dissipation for the enhanced Von Mises model under uniaxial stress condition is provided in Appendix C.

3.2. Coupling damage with the parabolic Drucker-Prager plasticity model

Fig. 5 illustrates a typical yield surface of plain epoxy resin which has a parabolic shape in its initial and final yielding states [76]. In this section, based on the coupling scheme of the generic formulation, the parabolic Drucker-Prager model is enhanced by coupling this pressure-dependent plasticity model with damage.

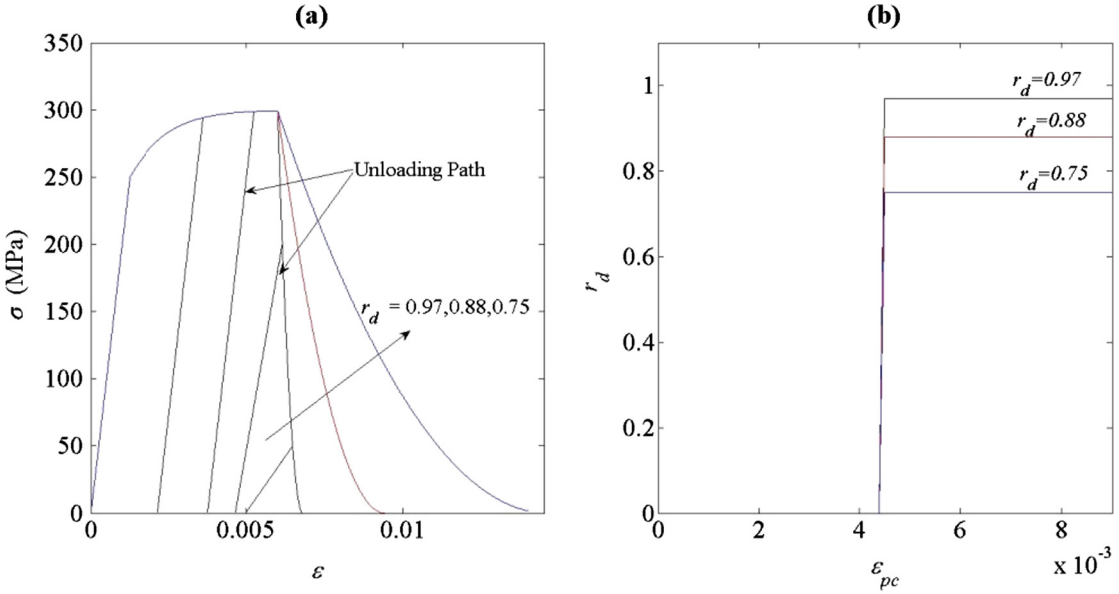

Fig. 3. (a) Effects of different values of r_d on the stress-strain response of steel under uniaxial tension (b) Corresponding values of r_d for activation of damage mechanism at a critical value of plastic strain $\varepsilon_{pc} = 4.5 \times 10^{-3}$.

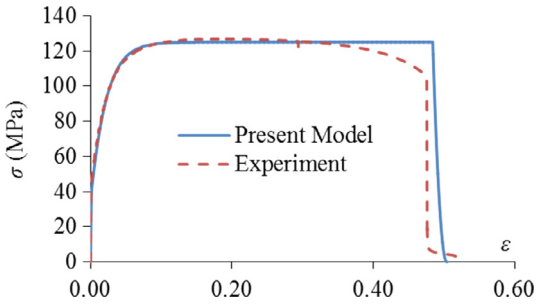

Fig. 4. Stress-strain response of Aluminium Alloy 6082 under uniaxial tension. Damage is activated at a critical value of the plastic strain $\varepsilon_{pc} = 0.48$ and $r_d = 0.97$.

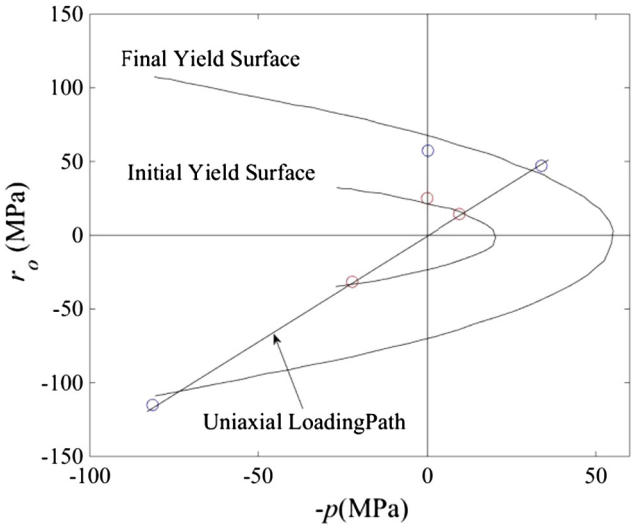

Fig. 5. Parabolic Drucker-Prager yield function applied to plain epoxy resin [76] where $\tau_o = \pm\sqrt{\frac{9}{2}}q$ is the octahedral shear stress (Circles indicate experimental data points).

In addition, the non-associated flow and inelastic volumetric deformations (dilation and compaction) are successfully modelled thanks to the coupling scheme of the proposed generic formulation.

The parabolic Drucker-Prager yield function can be expressed in terms of pressure p and deviatoric stress q as:

$$y = 3J_2 + \frac{\alpha}{3}I_1 - \beta(D, \varepsilon_p) = q^2 - \alpha p - \beta(D, \varepsilon_p) = 0 \tag{52}$$

The parameters α and β in the above expression are given as:

$$\beta = f_{cy}f_{ty} \text{ and } \alpha = 3(f_{cy} - f_{ty}) \tag{53}$$

where f_{cy} and f_{ty} are the uniaxial yield stress in compression and tension, respectively. It is assumed that, f_{cy} and f_{ty} will vary progressively with the evolution of plastic deformation and therefore their dependency on the damage variable and accumulated plastic strain can be defined as:

$$\begin{aligned} f_{cy} &= (1-D)(f_{c0} + Q_c(1 - e^{-H_c\varepsilon_p})); \text{ and } f_{ty} \\ &= (1-D)(f_{t0} + Q_t(1 - e^{-H_t\varepsilon_p})) \end{aligned} \tag{54}$$

where f_{t0} and f_{c0} are initial yield stresses, and Q_t, Q_c, H_t, H_c are material constants with subscript t and c corresponding to tension and compression, respectively. The growth of damage will progressively reduce the values of α and β leading to the contraction of the yield surface (Eq. (54)). On the other hand, the growth the effective plastic strain ε_p will give rise to the expansion of the yield surface. By comparing Eq. (52) with Eq. (23), it is deduced that E and F can be defined as: $E = q^2 - \alpha p$ and $F^2 = \beta$. With these expressions of E and F, the flow rules can be obtained using Eqs. (18)–(20) as follows:

$$\dot{\alpha}_V = 2\dot{\lambda}\frac{a\sqrt{q^2 - \alpha p}}{k} \tag{55}$$

$$\dot{\alpha}_S = 2\dot{\lambda}\frac{b\sqrt{q^2 - \alpha p}}{k} \tag{56}$$

$$\dot{D} = 2\dot{\lambda}\frac{r_d(q^2 - \alpha p)}{\beta\chi_D} \tag{57}$$

Furthermore, by making use of Eq. (34), the plastic flow rule is obtained in its tensorial form as:

$$\dot{\alpha}_{ij} = \dot{\lambda}\frac{\partial y^*}{\partial \sigma_{ij}} = \dot{\lambda}\left(2\frac{a\sqrt{q^2-\alpha p}}{\beta}\frac{(-\delta_{ij})}{3} + 2\frac{b\sqrt{q^2-\alpha p}}{\beta}\frac{3}{2\sqrt{3J_2}}\frac{\partial J_2}{\partial \sigma_{ij}}\right) \quad (58)$$

3.2.1. The effect of r_d and c on the model response

The stress-strain response of the coupled damage-plasticity model based on the parabolic Drucker-Prager yield function, for uniaxial loading, is illustrated in Fig. 6. The parameters used for this analysis are: young's modulus = 35,000 MPa, Poisson's ratio (ν) = 0.18, f_{t0} = 5 MPa, f_{c0} = 10 MPa, Q_t = 15 MPa, Q_c = 30 MPa, H_t = 2000, H_c = 2000. The effect of r_d on the material behaviour is also shown in Fig. 6, where r_d varies from 0 (no damage activation) to 0.18. As can be observed in Fig. 6 a higher value of r_d leads to a higher level of damage activity gives rise to a lower ultimate stress with a more significant softening behaviour.

The direction of the plastic flow vector in stress space is indicative of the level of contribution of the volumetric and the shear plastic strains to the total plastic dissipation. In addition, dilational and/or contractive modes of deformation give rise to different directions of the plastic flow vector in stress space. The reverse scenario is, however, pursuit here as the model response is controlled by the direction of the plastic flow vector in stress space. The variation in the model behaviour due to changes in the direction of plastic flow vector (different values of the parameter c) is illustrated in Fig. 7. Cases with $c > 1$ correspond to larger plastic volumetric strain rates, with the plastic flow vector being more inclined towards the p axis in the $(p-q)$ stress space, compared to that in the case of associated flow ($c = 1$), and the reverse is true for cases with $c < 1$. In addition, a higher value of c gives rise to more dilational behaviour, as illustrated in Fig. 7 (b).

3.2.2. Behaviour of concrete under uniaxial cyclic loading

The nonlinear responses of concrete materials under cyclic tensile and compressive loading [77] are predicted by the proposed model and the results obtained are presented in Fig. 8. The model parameters used for the tensile loading are: young's modulus = 31,700 MPa, Poisson's ratio (ν) = 0.18, f_t' = 3.48 MPa, f_{t0} = 3.48 MPa, f_{c0} = 10 MPa Q_t = 0 MPa, Q_c = 15 MPa, H_t = 0, H_c = 1000 and r_d = 0.14. Fig. 8(a) shows a reasonable agreement between the model prediction and the experimental data.

In addition, Fig. 8(b) compares the model prediction with the experimental data from cyclic compressive loading on concrete [78]. In this case, the model parameters used are: young's modulus = 31,000 MPa, Poisson's ratio (ν) = 0.18, f_c' = 27.6 MPa, f_{t0} = 3.48 MPa, f_{c0} = 12 MPa, Q_t = 0 MPa, Q_c = 38 MPa, H_t = 0, H_c = 1600 and r_d = 0.28. Fig. 8(b) also shows a very good agreement between the model predictions and the experimental data which indicates a successful performance of the proposed model.

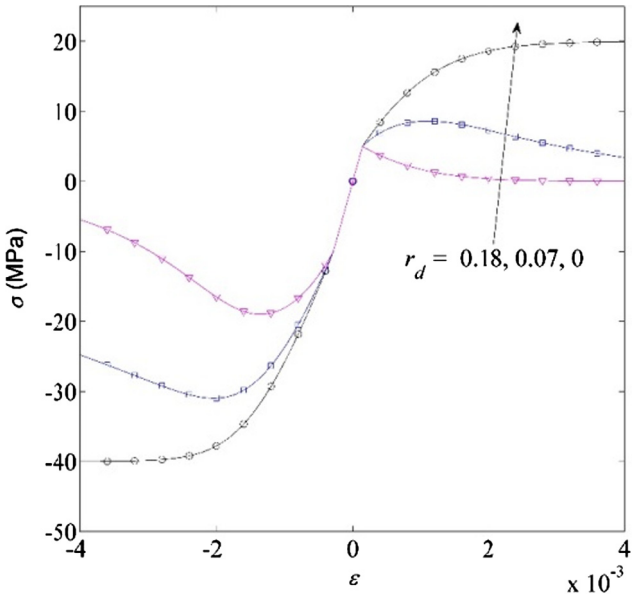

Fig. 6. Effect of r_d on the stress-strain response of a material under uniaxial loading based on the associated flow rule.

3.2.3. Dilation of unconfined concrete under uniaxial compression

The dilative or contractive behaviour of material models constructed following the proposed generic formulation can be controlled by appropriately defining the parameter c (or functions a and b (see Section 3.3)). The experimental results of an unconfined concrete specimen under uniaxial compression [79] is used to determine the variation of parameter c with respect to the equivalent shear strain ε_s, as illustrated in Fig. 9.

The nonlinear response of the concrete specimen is predicted by the proposed model using material properties as; young's modulus = 35,000 MPa, Poisson's ratio (ν) = 0.18, f_t' = 2.4 MPa, and f_c' = 32 MPa [79]. The model parameters used are: f_{t0} = 2.4 MPa, f_{c0} = 10 MPa, Q_t = 0 MPa, Q_c = 29 MPa, H_t = 0, H_c = 2600 and r_d = 0.17 along with the values of c as indicated in Fig. 9. The comparison between the model prediction and experimental data, as illustrated in Fig. 10, highlights the capability of the proposed model.

3.3. Development of an elastoplastic damage model for cohesive-frictional geomaterials

In laboratory experiments, inelastic deformation of cohesive-frictional geomaterials such as rocks, hard clays, etc., is observed as a reduction in stiffness and strength as well as the occurrence of residual strains. The failure process begins with a relatively uniform distribution of micro-cracks throughout the material followed by localisation of microcracks within a band which finally leads to the formation of a macro-crack and then shear sliding of the two faces of the macroscopic fracture. A common strategy for modelling such failure process is to employ a yield function or a plastic potential, which controls the evolution of dissipative processes (damage and plasticity), for the states before the formation of the final macro-fracture, and a separate failure function to describe the shear sliding between the two faces of the macro-fracture [36]. In this section, specific definitions of the functions E and F, in the generic formulation, are given so that a single-surface yield function in true stress space is obtained. This yield surface is then transformed to a final failure function as the scalar damage variable grows from zero to one. This is a promising feature of this model which facilitates capturing the brittle and ductile responses as well as the brittle-ductile transition, without any need for separately introducing hardening/softening rules. It is also demonstrated briefly that the features of proposed generic formulation facilitate the modelling of dilative and contractive responses of cohesive geomaterials.

3.3.1. The yield function

In order for the model to be capable of capturing the inelastic volumetric deformation of the material under isotropic compression (or expansion), it is required that the yield function have a closed envelope in the principal stress space. Hence, a single-surface yield function with a tear-drop shape in true stress space

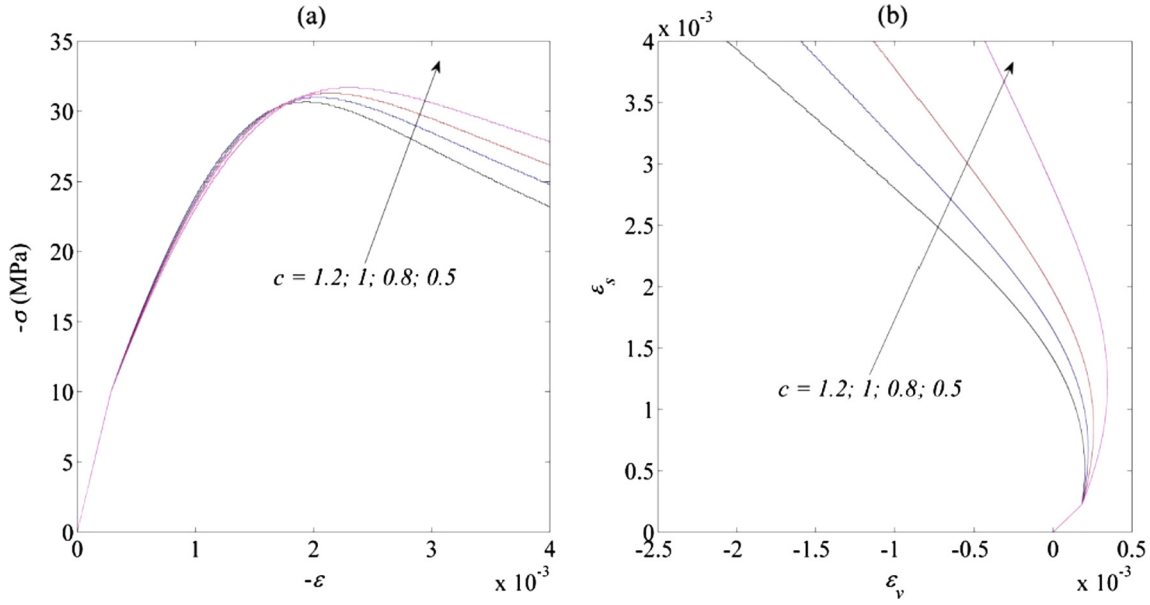

Fig. 7. (a) Effect of c on the stress-strain response of a material under uniaxial compression (r_d = 0.07), (b) Effect of c on the total volumetric strain and equivalent shear strain under uniaxial compression (r_d = 0.07).

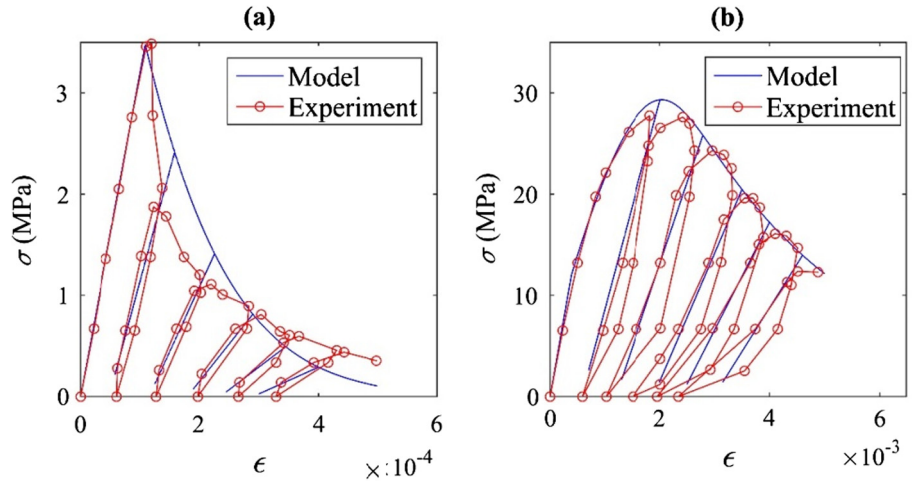

Fig. 8. Behaviour of concrete under cyclic loading: (a) uniaxial tension (experimental data obtained from [77]); (b) uniaxial compression (experimental data obtained from [78]).

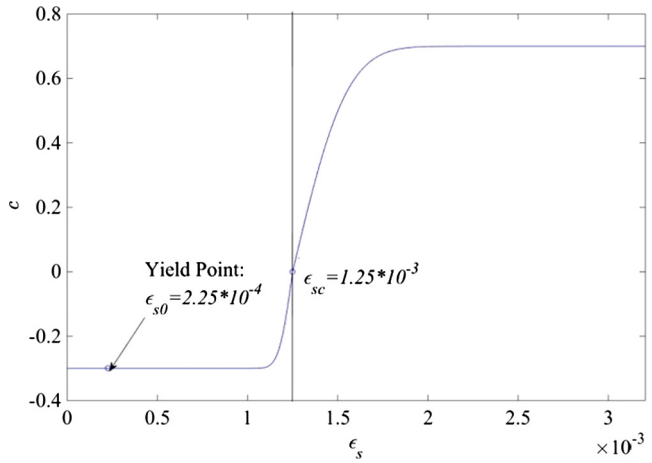

Fig. 9. Evolution of c for unconfined concrete under uniaxial compression.

[4] is derived following the structure of the proposed generic formulation. In this regard, the damage is incorporated in the model formulation in such a way that the initial yield function is transformed gradually into a linear frictional failure function as the damage variable grows from zero to unity. To this end, the functions E and F in Eqs. (8)–(12) are defined as follows:

$$E = \left[\frac{(1-D)(p-\rho)(p-\sqrt{(1-D)}\omega(p-\rho))}{(\frac{(1-\gamma)p_c-p_t}{p_c+p_t})p+\frac{1}{2}(1-D)\gamma p_c}\right]^2 + \left[\frac{q}{M}\right]^2 \tag{59}$$

$$F = p - \sqrt{(1-D)}\,\omega\,(p-\rho) \tag{60}$$

In the above expressions, $0 \leqslant \omega \leqslant 1$ and $0 \leqslant \gamma \leqslant 1$ are materials parameters while p_c and p_t represent pressures at initial yield under isotropic compression and expansion, respectively. The parameter M represents the slope of the final failure envelope in

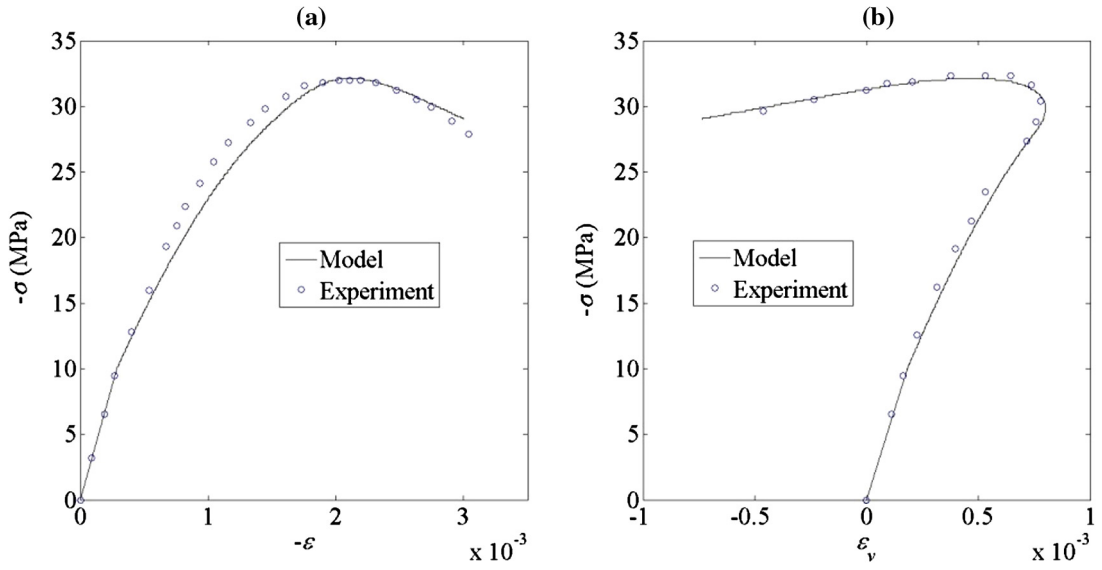

Fig. 10. (a) Stress-strain response of concrete under uniaxial compressive loading; (b) Variation of volumetric strain (experimental validation).

true stress space. By making use of the above definitions and the general form of the yield function, given by Eq. (23), the yield function in true stress space isobtained as:

$$y = \left(\frac{(1-D)(p-\rho)}{(\frac{(1-\gamma)p_c-p_t}{p_c+p_t})p + \frac{1}{2}(1-D)\gamma p_c}\right)^2 + \left(\frac{q}{M(p - \sqrt{(1-D)}\,\omega\,(p-\rho))}\right)^2 - 1 = 0 \quad (61)$$

In the above expressions, parameter ρ represents the pressure at the intersection of the final failure envelope and the initial yield surface and it can be calculated by considering the yield condition under isotropic compression as:

$$\rho = \frac{(4-\gamma)p_c p_t + \gamma p_c^2}{2(p_c + p_t)} \quad (62)$$

In addition, for $\gamma = \omega = 1$ and $p_t = 0$ the yield function of Eq. (61) is the same as the modified Cam-Clay. Fig. 11 illustrates the evolution of the yield surface with damage growth and the transformation of the initial yield surface to the final failure surface when the damage variable is one.

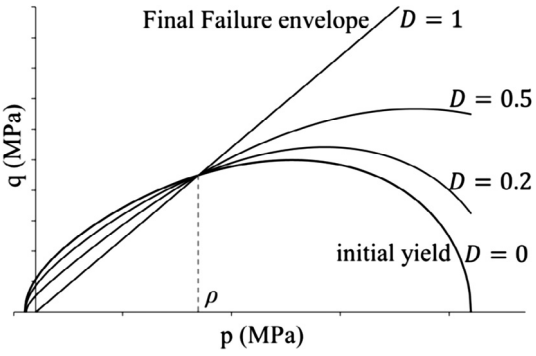

Fig. 11. Evolution of the yield surface with damage growth.

3.3.2. Dilative and contractive responses with non-associated flow rules

For any point (stress state) on the initial yield surface y in true stress space $(p-q)$, there exists an elliptical loading surface y^* in generalised dissipative stress space $(\chi_V - \chi_S)$ which can be expressed by making use of Eq. (17) as:

$$y^* = [\chi_V - (p - a\sqrt{\bar{E}})]^2 + [\chi_S - (q - b\sqrt{\bar{E}})]^2 - F^2 - r_d E = 0 \quad (63)$$

These loading functions in dissipative stress space are analogous to the concept of plastic potential in conventional plasticity. As illustrated in Fig. 12, the flow vectors in true stress space are defined as normal to the corresponding elliptical loading function in dissipative stress space. Furthermore, functions a and b, appeared in Eq. (63), can be defined in terms of true stresses which helps to predict the directions of flow vectors in true stress space. Possible definitions of these functions are proposed as follows:

$$a = \pm\sqrt{r_p\left[1 - \frac{q^2}{M^2F^2}\right]} \quad (64)$$

$$b = \sqrt{r_p\frac{q^2}{M^2F^2}} \quad (65)$$

Following the sign convention of compression positive, the plus and minus signs used in Eq. (64) correspond to plastic volumetric contraction and dilation, respectively. Hence, a dilative or contractive response at any point on the yield surface can be simulated by choosing the appropriate sign of parameter a. For instance, Fig. 12 (a)–(c) illustrates the directions of flow vectors on the initial yield surface of Bentheim sandstone corresponding to confining pressures (σ_r) of 30 MPa, 120 MPa and 300 MPa. For any positive value of parameter a, the model behaviour is contractive, whereas the model exhibits dilational behaviour if a negative value of a is chosen (Fig. 12).

In order to set a criterion for appropriately choosing the sign of parameter a, the pressure at the intersection of the final failure line and the initial yield locus, i.e. ρ (Eq. (62)), is defined as the critical pressure. Any point on the yield surface with a pressure below the critical pressure ($p < \rho$) corresponds to dilative response and softening behaviour, where the parameter a is negative. If, on the other

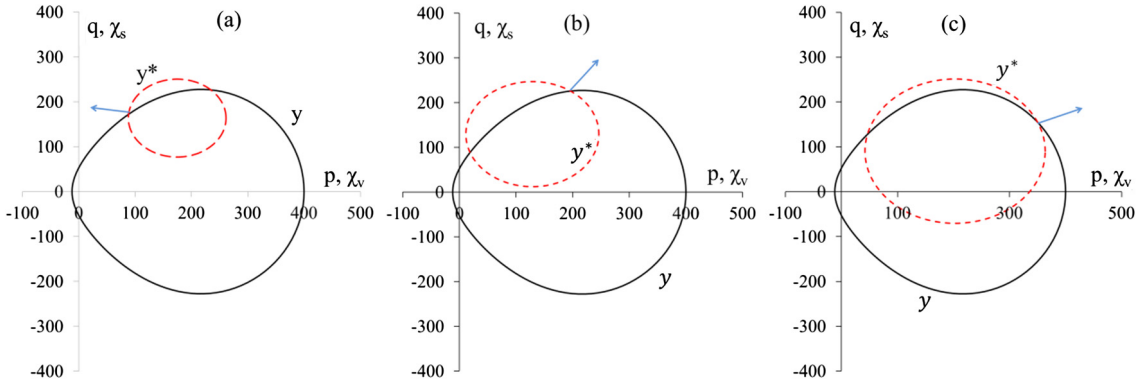

Fig. 12. Initial yield loci in dissipative stress space (y^*) and in true stress space(y), with directions of flow vectors for Bentheim sandstone at the onset of yielding under triaxial loading at (a) 30 MPa, (b) 120 MPa and (c) 300 MPa confinement.

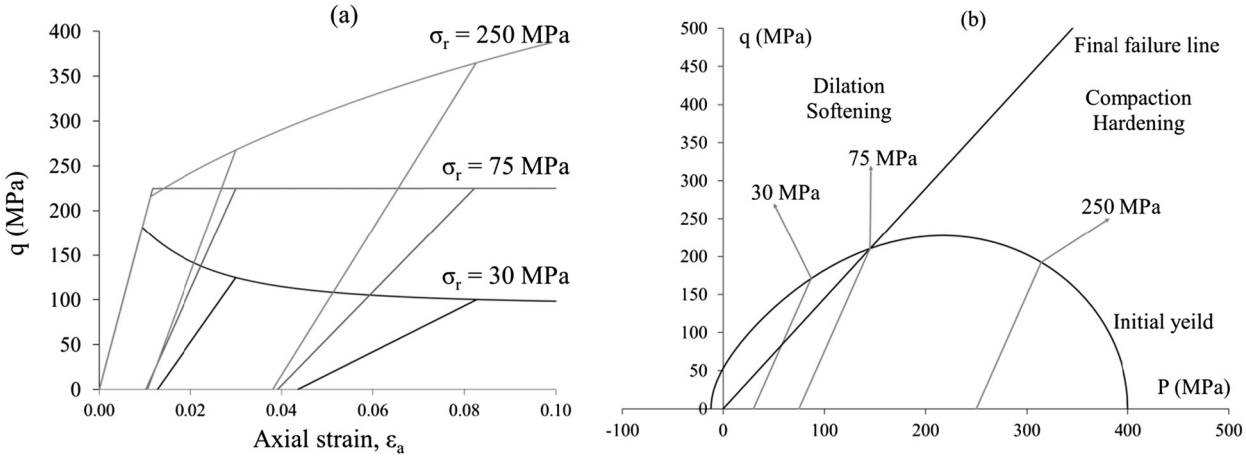

Fig. 13. (a) Brittle, brittle-ductile transition and ductile responses and (b) Dilation/softening and compaction/hardening regions with their transition for Bentheim sandstone ($p_c = 400$ MPa, $p_t = 10$ MPa, $M = 1.45$, $\omega = 0.6$ and $\lambda = 0.8$).

hand, this pressure exceeds the critical pressure ($p > \rho$), the model exhibits compaction and hardening or ductile behaviour where parameter a will be positive. The model behaviour at the intersection of the initial yield surface and the final failure line ($p = \rho$) is perfectly plastic (brittle-ductile transition), as shown in Fig. 13. It is also important to note that regardless of the sign of a, the dissipation rate function, as given in Eq. (7), is always positive (see Appendix C).

3.3.3. Behaviour and validation of the proposed model

A series of experimental data of Bentheim sandstone [80] is used to assess the performance of the model. A number of yield points (Fig. 14) corresponding to different confining pressures are used for the calibration of initial yield parameters, i.e. p_c, p_t, M, ω and γ .

Fig. 15 illustrates the performance of the model with the same level of activity for damage and plasticity processes, i.e. $r_d = r_p = 0.5$. It is expected, however, that the contributions of damage and plasticity in energy dissipation vary for different levels of confining pressure. In the dilation/softening region (see Fig. 13(b)), under low confining pressures, damage is the dominant mechanism of the inelastic deformation, while at medium to relatively high confining pressure, the dominant mechanism of deformation and energy dissipation is plasticity. At significantly high confining pressures, however, damage is envisaged to be the dominant mechanism again. The dominance of the damage dissipation at significantly high pressures in granular materials can be attributed to phenomena like grain crushing [5,6,81,82]. Model predictions, in general, show a reasonable agreement with the experimental data (Fig. 15). However, as can be seen in Fig. 15(b), the model prediction does not closely follow the experimental data in the brittle/-softening region. The main reason for this deviation is that the material behaviour, produced by the model, is compared with that of the specimen without considering the size effect of the specimen used for recording the experimental data. The size effect of a structure (or a specimen) on the nominal strength and post-peak beha-

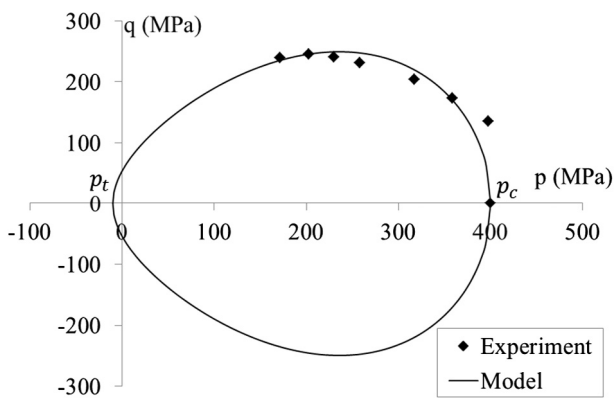

Fig. 14. Calibration of the model parameters ($p_c = 400$ MPa,$p_t = 10$MPa, $M = 1.45, \omega = 0.6$ and $\gamma = 0.8$).

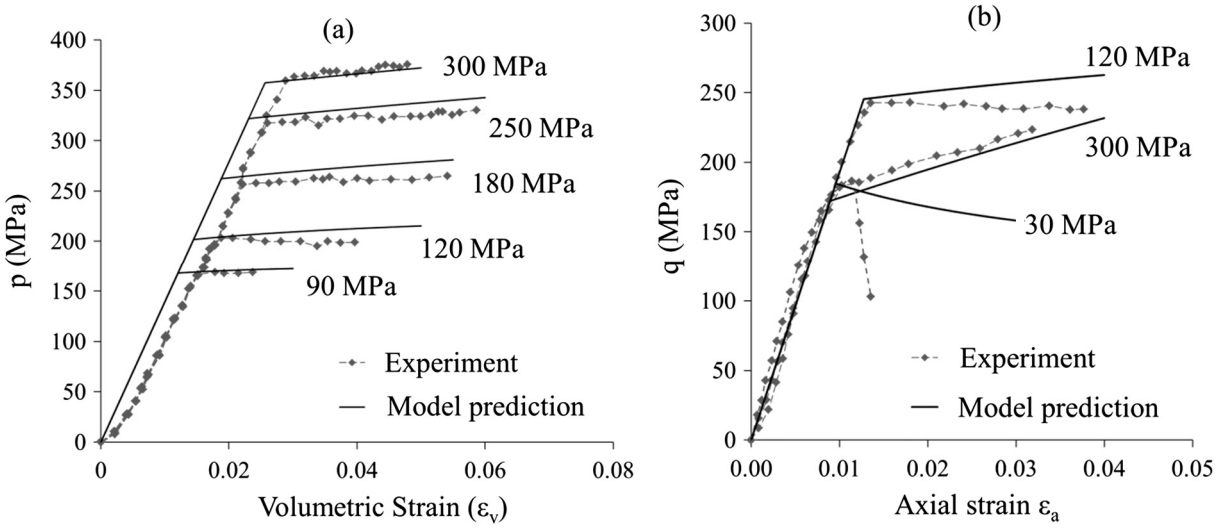

Fig. 15. Model validation against experimental data of Bentheim sandstone [79], (a) pressure-volumetric strain (b) differential stress-axial strain with $r_d = r_p = 0.5$.

viour is a well-known issue and it is more profound when the material undergoes softening [see e.g. [83]]. The issues of localised failure and size effects can be resolved by using a regularisation technique which is not considered in this study as this is not the primary focus of this investigation.

4. Discussions and conclusions

A thermodynamically consistent generic formulation for constructing constitutive models for engineering materials is proposed in this study. The focus of the study is to obtain a rigorous and consistent method for coupling damage and plasticity for a range of engineering materials. As a result, a general form of the total dissipation rate function is developed which can be conveniently transformed to get a single generalised loading surface for both yield and failure states. This single loading surface governs the simultaneous evolutions of both damage and plasticity where the coupling between these two mechanisms is effectively specified through a model parameter without imposing any restrictions to the model. In addition, the inherent features of the generic formulation also facilitate the modelling of the inelastic dilative and contractive behaviour of materials.

It is shows that the proposed generic formulation possess good potentials for enhancing existing as well as developing new constitutive models. Despite the impression that a large number of parameters is needed for the model, it should be noted that the majority of these parameters are in fact used for defining the yielding behaviour of three different types of materials in a generic form utilising functions E and F. Since the yield points in stress space are usually obtained from experiments (see the example of porous rocks in Section 3.3), these parameters can be readily calibrated. It is to be noted that these parameters are independent from the remaining small number of parameters used for defining the failure evolutions, and this feature facilitates the calibration of the remaining parameters for the inelastic behaviour. For defining the inelastic response, besides the elastic modulus and the Poisson's ratio, the proposed formulation requires two mandatory parameters which are r_d (or r_p) to specify the proportion of energy dissipation due to damage (or plasticity), and a (or b) to control the direction of the plastic flow vector. Besides these mandatory parameters, an additional set of 3 to 4 parameters are needed to control the hardening and softening processes of metal (Fig. 4) and concrete (Fig. 8) while the model for porous rocks (Fig. 13) does not need any additional parameters. We also acknowledge that all models used in this work are relatively simple, as they are just used for the purpose of illustrating the applicability of the proposed generic approach. In this sense, future focus on a particular material and/or behaviour may help to identify shortcoming of the approach for further developments and improvements.

Acknowledgements

This research was supported by the Australian Government through Australian Government Research Training Program Scholarship (Van D. Vu). Funding support from the Australian Research Council via projects DP110102645 and FT140100408 (Giang D. Nguyen) is also gratefully acknowledged.

Appendix A: The general condition for thermodynamic admissibility

The general condition for thermodynamic admissibility is derived from the premise of strictly non-negativeness of the dissipation rate function, given by Eq. (7). This condition can be derived by making use of the general definition of functions and parameters appearing in Eq. (7), and defined through Eqs. (8)–(12) as well as the flow rules of Eqs. (18)–(20) and the yield condition, as given by Eq. (23). For convenience these Eqs. and definitions are also repeated here:

The dissipation potential

$$\Phi = \sqrt{\varphi_V^2 + \varphi_S^2 + \varphi_D^2} + f_V\varphi_V + f_S\varphi_S \geqslant 0 \tag{A-1}$$

Definition of functions

$$f_V = \frac{p - a\sqrt{E(p,q,D,\varepsilon_p)}}{F(p,q,D,\varepsilon_p)} \tag{A-2}$$

$$f_S = \frac{q - b\sqrt{E(p,q,D,\varepsilon_p)}}{F(p,q,D,\varepsilon_p)} \tag{A-3}$$

$$\varphi_V = F(p,q,D,\varepsilon_p)\dot{\alpha}_V \tag{A-4}$$

$$\varphi_S = F(p,q,D,\varepsilon_p)\dot{\alpha}_S \tag{A-5}$$

$$\varphi_D = \frac{F(p,q,D,\varepsilon_p)\bar{\chi}_D}{\sqrt{r_d E(p,q,D,\varepsilon_p)}}\dot{D} \tag{A-6}$$

Flow rules

$$\dot{\alpha}_V = \dot{\lambda}\frac{\partial y^*}{\partial \chi_V} = 2\dot{\lambda}\left(\frac{a\sqrt{E}}{F^2}\right) \tag{A-7}$$

$$\dot{\alpha}_S = \dot{\lambda}\frac{\partial y^*}{\partial \chi_S} = 2\dot{\lambda}\left(\frac{b\sqrt{E}}{F^2}\right) \tag{A-8}$$

$$\dot{D} = \dot{\lambda}\frac{\partial y^*}{\partial \chi_D} = 2\dot{\lambda}\frac{r_d E}{F^2 \chi_D} \tag{A-9}$$

The yield function in true stress space

$$y = E - F^2 = 0 \tag{A-10}$$

Substitution of Eqs. (A-2)–(A-9) into Eq. (A-1) and making use of Eq. (A-10), results in:

$$\Phi = 2\dot{\lambda}\left(\sqrt{a^2+b^2+r_d} + \left(\frac{pa}{F}+\frac{qb}{F}\right) - (a^2+b^2)\right) \geqslant 0 \tag{A-11}$$

Since $\dot{\lambda} \geqslant 0$ the non-negativeness of the term in the parentheses is required, i.e.

$$\sqrt{a^2+b^2+r_d} + \left(\frac{pa}{F}+\frac{qb}{F}\right) - (a^2+b^2) \geqslant 0 \tag{A-12}$$

Since $F \geqslant 0$, recalling the condition of Eq. (22) ($a^2 + b^2 = r_p$ and $r_p + r_d = 1$) and, the above expression is reduced to:

$$pa + qb + r_d F \geqslant 0 \tag{A-13}$$

In the above expression, the second and the third terms are always non-negative. The first term, however, can be negative when the model behaviour is dilative ($a < 0$) under compression ($p > 0$). The following general condition is therefore required to be satisfied for thermodynamic admissibility:

$$|pa| \leqslant qb + r_d F \tag{A-14}$$

It should be noted that the expression at the right-hand side of the inequality in the above condition is always non-negative.

In the case of the Von Mises model, due to incompressibility constraint, i.e. $\alpha_v = a = 0$, the condition of Eq. (A-14) is always satisfied. For the case of the enhanced Drucker-Prager model, in which an additional parameter c is used to control the direction of the plastic flow vector in stress space, no general proof can be given for thermodynamic admissibility. However, by making use of the general condition of Eq. (A-14), some restriction is put on selecting the parameter c for modelling the dilational behaviour under compression. In this regards, parameter a in (A-14) can be substituted for form Eq. (31) to give the following restrictive condition on c:

$$c \leqslant \frac{qb + r_d F}{|pb\frac{\partial y/\partial p}{\partial y/\partial q}|} \tag{A-15}$$

Considering the Drucker-Prager yield function, as stated by Eq. (52) the above condition can be rewritten as:

$$-\frac{2q(qb + r_d\sqrt{\beta})}{pb\alpha} \leqslant c \leqslant \frac{2q(qb + r_d\sqrt{\beta})}{pb\alpha} \tag{A-16}$$

This condition imposes a restriction on the direction of the flow vector and is met for the example presented in the manuscript.

In the case of the new geomaterial model it is required to demonstrate that the model conforms to the condition of Eq. (A-14) for modelling the dilative behaviour under compression. To this end, parameters a and b in (A-14) are substituted for from Eqs. (64) and (65) to give:

$$\left|p\sqrt{r_p\left(1-\frac{q^2}{M^2F^2}\right)}\right| \leqslant q\sqrt{r_p\frac{q^2}{M^2F^2}} + r_d F \tag{A-17}$$

Comparing the above expression with the yield function of Eq. (61), the above expression can be rewritten as:

$$\left|p\sqrt{r_p\left(\frac{(1-D)(p-\rho)}{A}\right)^2}\right| \leqslant q\sqrt{r_p\left(1-\left(\frac{(1-D)(p-\rho)}{A}\right)^2\right)} + r_d F \tag{A-18}$$

where

$$A = \frac{(1-\gamma)p_c - p_t}{p_c + p_t}p + \frac{1}{2}(1-D)\gamma p_c \tag{A-19}$$

Functions F and A are always positive or non-negative, therefore, (A-18) can be rearranged to give:

$$p - \rho \leqslant \frac{A\left(q\sqrt{r_p\left(1-\left(\frac{(1-D)(p-\rho)}{A}\right)^2\right)} + Fr_d\right)}{(1-D)p\sqrt{r_p}} \tag{A-20}$$

In the dilation regime the term $(p - \rho)$ is always negative See Fig. A1, while the right-hand side of the above expression is always positive. Therefore, it is deduced that the model follows the general condition for thermodynamic admissibility as stated by Eq. (A-14).

Appendix B: Energy dissipation potential as a function of stresses and $\dot{\alpha}_s$

Using the definition of χ_V, χ_S and χ_D, Eq. (24) can be rewritten as:

$$\Phi = \chi_V\dot{\alpha}_V + \chi_S\dot{\alpha}_S + \chi_D\dot{D} \geqslant 0 \tag{B-1}$$

Substitutions of Eqs. (18)–(20) into Eq. (B-1), gives:

$$\Phi = \chi_V 2\dot{\lambda}\frac{a\sqrt{E}}{F^2} + \chi_S 2\dot{\lambda}\frac{b\sqrt{E}}{F^2} + 2\dot{\lambda}\frac{r_d E}{F^2} \tag{B-2}$$

Recalling the constitutive postulate of $\bar{\chi}_v = \phi\chi_v$ and $\bar{\chi}_s = \chi_s$ and using Eqs. (4) and (5), the above expression can be rewritten as:

$$\Phi = p2\dot{\lambda}\frac{a\sqrt{E}}{F^2} + q2\dot{\lambda}\frac{b\sqrt{E}}{F^2} + 2\dot{\lambda}\frac{r_d E}{F^2} \tag{B-3}$$

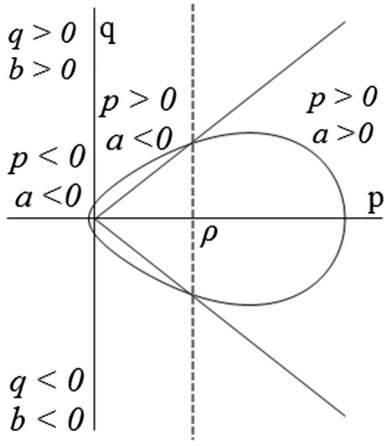

Fig. A1. Sign determination diagram for volumetric and shear dissipation rate functions.

Therefore, the following expressions for the dissipation rate functions corresponding to each internal variable can be obtained, using Eq. (B-3), as:

$$\Phi_V = p2\dot{\lambda}\frac{a\sqrt{E}}{F^2} \tag{B-4}$$

$$\Phi_S = q2\dot{\lambda}\frac{b\sqrt{E}}{F^2} \tag{B-5}$$

$$\Phi_D = 2\dot{\lambda}\frac{r_d E}{F^2} \tag{B-6}$$

From the above equations, the following ratios are defined:

$$\frac{\Phi_S}{\Phi_D} = \frac{qb}{r_d\sqrt{E}} \tag{B-7}$$

$$\frac{\Phi_V}{\Phi_S} = \frac{pa}{qb} \tag{B-8}$$

Substituting the above ratios into Eq. (24), the total dissipation rate function Φ can be expressed in terms of Φ_S and stresses as:

$$\Phi = \frac{pa}{qb}\Phi_S + \Phi_S + \frac{r_d\sqrt{E}}{qb}\Phi_S = \left(\frac{pa}{qb} + 1 + \frac{r_d\sqrt{E}}{qb}\right)\Phi_S \tag{B-9}$$

Since $\Phi_S = \chi_S\dot{\alpha}_S$ and $\chi_s = \bar{\chi}_s = q$, it follows that:

$$\Phi_S = q\dot{\alpha}_S \tag{B-10}$$

Thus, substitution of Eq. (B-10) into Eq. (B-9), the expression of the total dissipation rate function, Φ, in terms of $\dot{\alpha}_S$ and stresses is obtained as:

$$\Phi = \left(\frac{pa}{b} + q + \frac{r_d\sqrt{E}}{b}\right)\dot{\alpha}_S \tag{B-11}$$

Appendix C: Energy dissipation aspects of Von-Mises materials under uniaxial loading

As $\alpha_V = 0$ in the Von-Mises material model, $e^p_{ij} = \alpha_{ij} - \frac{\alpha_V}{3} = \alpha_{ij}$ and thus $\dot{\alpha}_S$ can be written as:

$$\dot{\alpha}_S = \sqrt{\frac{2}{3}\dot{e}^p_{ij}\dot{e}^p_{ij}} = \sqrt{\frac{2}{3}\dot{\alpha}_{ij}\dot{\alpha}_{ij}} = \dot{\varepsilon}_p \tag{C-1}$$

Furthermore, using Eqs. (47) and (48), the relationship between $\dot{D}$ and $\dot{\varepsilon}_p$ is expressed as:

$$\frac{\dot{D}}{\dot{\varepsilon}_p} = \frac{\dot{D}}{\dot{\alpha}_S} = \frac{r_d\sqrt{q}}{b\bar{\chi}_D} \tag{C-2}$$

For the case of uniaxial stress, the pressure p and the deviatoric stress q are given as follows:

$$p = -\frac{\sigma}{3}, \{s\} = \{2/3\sigma \quad -1/3\sigma \quad -1/3\sigma \quad 0 \quad 0 \quad 0\} \tag{C-3}$$

$$q = \sqrt{\frac{3}{2}\{s\}^T[T]\{s\}} = \sqrt{\frac{3}{2}\left(\frac{4}{9}+\frac{1}{9}+\frac{1}{9}\right)\sigma^2} = \sigma \tag{C-4}$$

Using Eq. (7) and Eqs. (C-3) and (C-4), χ_D can be expressed as:

$$\chi_D = T\frac{q^2}{(1-D)^2} \tag{C-5}$$

where $T = \frac{G+3K}{18KG}$

Substitution of Eq. (C-5) into Eq. (C-2) gives the following relationship:

$$\frac{\dot{D}}{\dot{\varepsilon}_p} = \frac{r_d\sqrt{q}}{bT\frac{q^2}{(1-D)^2}} \tag{C-6}$$

From the yield function, given by Eq. (46), q can be obtained as:

$$q = k = (1-D)(f_y + Q(1-e^{-H\varepsilon_p})) \tag{C-7}$$

Thus, the following expression can be derived by making use of Eqs. (C-6) and (C-7):

$$\frac{1}{\sqrt{(1-D)}}\dot{D} = \frac{r_d}{bT}\frac{1}{(f_y + Q(1-e^{-H\varepsilon_p}))^{3/2}}\dot{\varepsilon}_p \tag{C-8}$$

Integrating both sides of Eq. (C-8) with results in the following expression:

$$2\sqrt{(1-D)} = \frac{r_d}{bT}(f_y + Q(1-e^{-H\varepsilon_p}))^{-1/2}\frac{1}{-0.5QHe^{-H\varepsilon_p}} + C \tag{C-9}$$

The integration constant C is calculated for the following cases:

Case 1: Evolution of damage and plasticity together at yielding (see Fig. 1 for $r_d = 0.5$ and 0.25)

For the case of damage being initiated at the onset of yielding together with plastic strains, the expression of C can be obtained by using $\varepsilon_p = 0, D = 0$ as the initial conditions which are substituted into Eq. (C-9) to give the following expression for the constant C:

$$C = 2 - \frac{r_d}{bT}(f_y)^{-1/2}\frac{1}{-0.5QH} \tag{C-10}$$

Case 2: Only plasticity occurs at yielding and damage initiates when $\varepsilon_p > \varepsilon_{pc}$ (see Fig. 2(a))

In the example provided in Section 3.1, damage is not initiated ($r_d = 0$) until $\varepsilon_p > \varepsilon_{pc}(= 4.5\times10^{-3})$. Hence, the initial conditions are: $D = 0, \varepsilon_p = 4.5\times10^{-3}$ which are substituted into Eq. (C-9) to obtain the integration constant C as follows:

$$C = 2 - \frac{r_d}{bT}(f_y + Q(1-e^{-H\varepsilon_{pc}}))^{-1/2}\frac{1}{-0.5QHe^{-H\varepsilon_{pc}}} \tag{C-11}$$

In order to obtain the explicit expression of D in term of the accumulated plastic strain, ε_p, Eq. (C-9) is rearranged to give:

$$D = 1 - 0.25\left[\frac{r_d}{bT}(f_y + Q(1-e^{-H\varepsilon_p}))^{-1/2}\frac{1}{-0.5QHe^{-H\varepsilon_p}} + C\right]^2 = 1 - M \tag{C-12}$$

where: $M = 0.25\left[\frac{r_d}{bT}(f_y + Q(1-e^{-H\varepsilon_p}))^{-1/2}\frac{1}{-0.5QHe^{-H\varepsilon_p}} + C\right]^2$

It is critical to note that the expression of D in Eq. (C-12) is defined only for $\varepsilon_p \in (\varepsilon_{pc}, \varepsilon_{pf})$ where ε_{pc} is the effective plastic strain at the onset of damage initiation, and ε_{pf} is the effective plastic strain at failure. By substituting Eq. (C-12) into Eq. (C-8), $\dot{D}$ can be expressed explicitly in term of $\dot{\varepsilon}_p$ as:

$$\dot{D} = \frac{r_d}{bT}\frac{\sqrt{(1-D)}}{(f_y + Q(1-e^{-H\varepsilon_p}))^{3/2}}\dot{\varepsilon}_p = \frac{r_d}{bT}\frac{\sqrt{M}}{(f_y + Q(1-e^{-H\varepsilon_p}))^{3/2}}\dot{\varepsilon}_p = N\dot{\varepsilon}_p \tag{C-13}$$

where: $N = \frac{r_d}{bT}\frac{\sqrt{M}}{(f_y+Q(1-e^{-H\varepsilon_p}))^{3/2}}$

Now the total dissipation rate function can be expressed as:

$$\dot{\Phi} = \chi_D\dot{D} + \chi_S\dot{\alpha}_S \quad \text{(no volumetric plastic strain)} \tag{C-14}$$

Substituting (C-5), (C-7), (C-12) and (C-13) into the above equation, gives:

$$\dot{\Phi} = \chi_D \dot{D} + q\dot{\varepsilon}_p = [\chi_D N + q]\dot{\varepsilon}_p = \left[T\frac{q^2}{M^2}N + q\right]\dot{\varepsilon}_p$$
$$= \left[T\frac{\left(M\left(f_y + Q\left(1-e^{-H\varepsilon_p}\right)\right)\right)^2}{M^2}N + M\left(f_y + Q\left(1-e^{-H\varepsilon_p}\right)\right)\right]\dot{\varepsilon}_p \quad \text{(C-15)}$$
$$= \left[T\left(f_y + Q\left(1-e^{-H\varepsilon_p}\right)\right)^2 N + M\left(f_y + Q\left(1-e^{-H\varepsilon_p}\right)\right)\right]\dot{\varepsilon}_p$$

Thus, the total energy dissipated during the entire deformation process (or the total fracture energy) can be calculated by integrating both sides of Eq. (C-15) with respect to ε_p. In addition, the damage dissipation rate ratio R_D, given in Eq. (25), can also be defined as a function of ε_p by making use of Eq. (C-7) as:

$$R_D = \frac{r_d}{\sqrt{r_p M\left(f_y + Q\left(1-e^{-H\varepsilon_p}\right)\right)}} \quad \text{(C-16)}$$

The above equation provides the explicit link between the proportion of energy dissipation due to damage and plasticity. With the expressions given in Eqs. (C-12) and (C-16), the variation of R_D and D with respect to ε_p is plotted for different values of r_d in Fig. B1 (Case 1) and Fig. B2 (Case 2).

As illustrated in Figs. B1 and B2, a higher level of damage activation (by assigning a larger r_d) associates with a higher proportion of damage dissipation rate R_D and a faster damage growth compared to a lower level of damage activity (lower r_d). Furthermore, Figs. B1(a) and B2(a) show a sharp increase in damage dissipation rate at sufficiently high plastic strain which indicates a complete disintegration of material towards the end of loading procedure where damage is the dominant mechanism of energy dissipation.

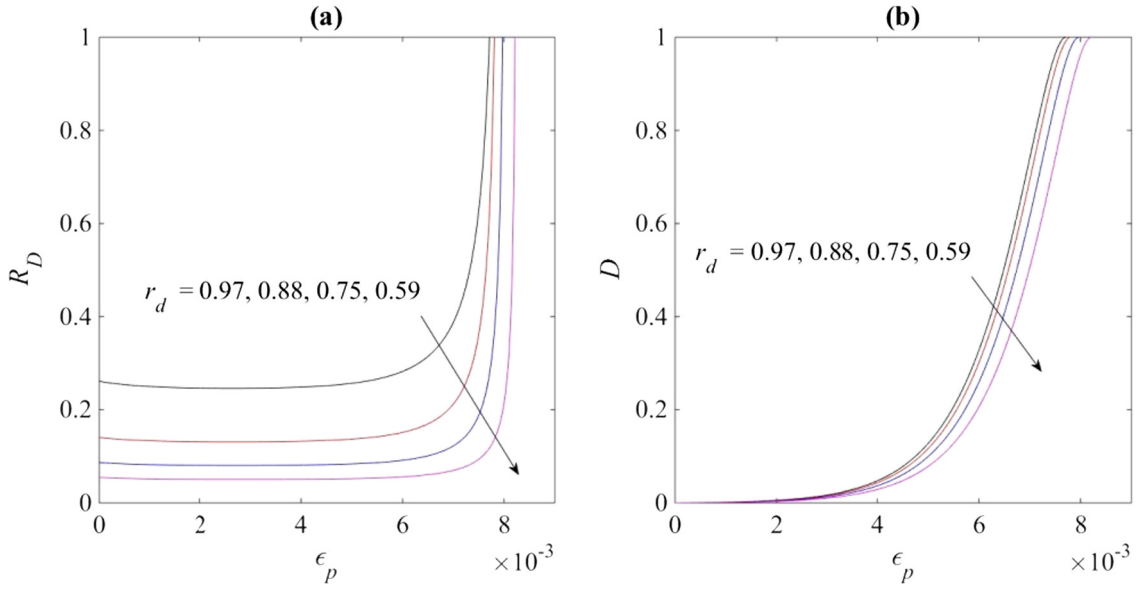

Fig. B1. Von Mises material model under uniaxial tension (Case 1: damage is activated simultaneously with plasticity).

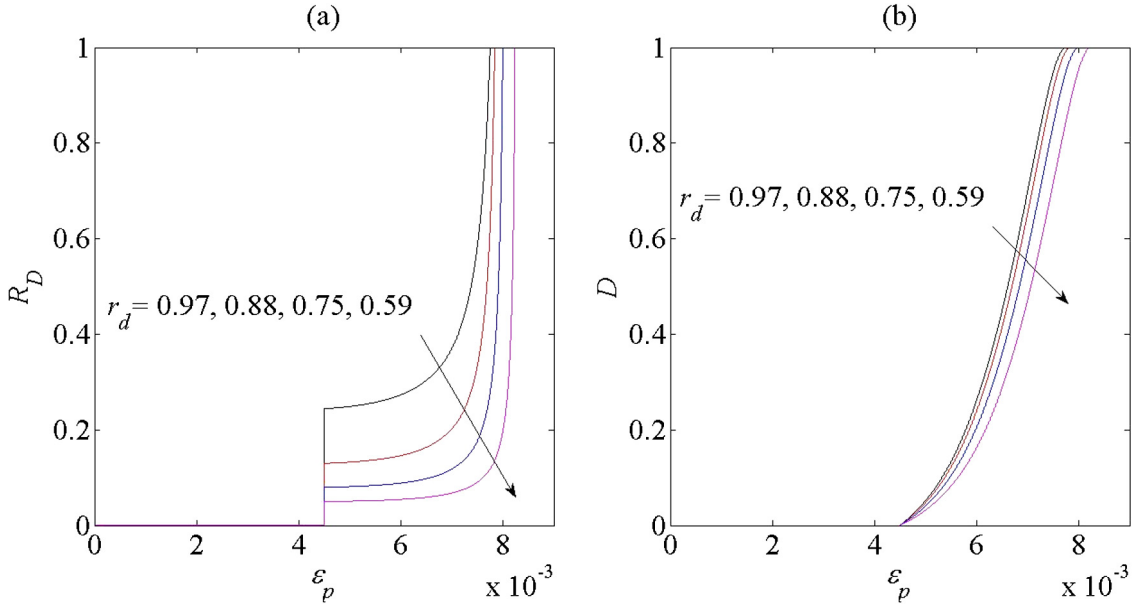

Fig. B2. Von Mises material model under uniaxial tension (Case 2: damage is activated at ($\varepsilon_p = 4.5 \times 10^{-3}$).

References

[1] Alessi R, Marigo J-J, Vidoli S. Gradient damage models coupled with plasticity: variational formulation and main properties. Mech Mater 2015;80:351–67.
[2] Bourdin B, Marigo J-J, Maurini C, Sicsic P. Morphogenesis and propagation of complex cracks induced by thermal shocks. Phys Rev Lett 2014;112:014301.
[3] Collins I, Kelly P. A thermomechanical analysis of a family of soil models. Geotechnique 2002;52:507–18.
[4] Collins IF, Hilder T. A theoretical framework for constructing elastic/plastic constitutive models of triaxial tests. Int J Numer Anal Meth Geomech 2002;26:1313–47.
[5] Einav I. Breakage mechanics—part I: theory. J Mech Phys Solids 2007;55:1274–97.
[6] Einav I. Breakage mechanics—Part II: Modelling granular materials. J Mech Phys Solids 2007;55:1298–320.
[7] Mozaffari N, Voyiadjis GZ. Phase field based nonlocal anisotropic damage mechanics model. Physica D 2015;308:11–25.
[8] Nguyen GD, Korsunsky AM. Development of an approach to constitutive modelling of concrete: isotropic damage coupled with plasticity. Int J Solids Struct 2008;45:5483–501.
[9] Nguyen GD, Korsunsky AM, Belnoue JP-H. A nonlocal coupled damage-plasticity model for the analysis of ductile failure. Int J Plast 2015;64:56–75.
[10] Voyiadjis GZ, Mozaffari N. Nonlocal damage model using the phase field method: theory and applications. Int J Solids Struct 2013;50:3136–51.
[11] Feenstra PH, De Borst R. A composite plasticity model for concrete. Int J Solids Struct 1996;33:707–30.
[12] Grassl P, Lundgren K, Gylltoft K. Concrete in compression: a plasticity theory with a novel hardening law. Int J Solids Struct 2002;39:5205–23.
[13] Park H, Kim J-Y. Plasticity model using multiple failure criteria for concrete in compression. Int J Solids Struct 2005;42:2303–22.
[14] Folino P, Etse G. Performance dependent model for normal and high strength concretes. Int J Solids Struct 2012;49:701–19.
[15] Chi Y, Xu L, Yu H-S. Constitutive modeling of steel-polypropylene hybrid fiber reinforced concrete using a non-associated plasticity and its numerical implementation. Compos Struct 2014;111:497–509.
[16] Lu D, Du X, Wang G, Zhou A, Li A. A three-dimensional elastoplastic constitutive model for concrete. Comput Struct 2016;163:41–55.
[17] Dinh TD, Rezaei A, De Laet L, Mollaert M, Van Hemelrijck D, Van Paepegem W. A new elasto-plastic material model for coated fabric. Eng Struct 2014;71:12.
[18] Kumar N, Rajagopal A, Pandey M. Plasticity based approach for failure modelling of unreinforced masonry. Eng Struct 2014;80:13.
[19] Carrazedo R, Mirmiran A, Hanai JBD. Plasticity based stress–strain model for concrete confinement. Eng Struct 2013;48:13.
[20] Comi C, Perego U. Fracture energy based bi-dissipative damage model for concrete. Int J Solids Struct 2001;38:6427–54.
[21] Guangming Z, Lixiang X, Xiangrui M. A damage-based constitutive model for rock under impacting load. Int J Mining Sci Technol 2014;24:7.
[22] Khan A, Al-Gadhib A, Baluch M. Elasto-damage model for high strength concrete subjected to multiaxial loading. Int J Damage Mech 2007.
[23] Lemaitre J. A course on damage mechanics. Springer Verlag; 1992.
[24] Lemaitre J, Chaboche JL. Mechanics of solid materials. Cambridge: Cambridge University Press; 1990.
[25] Mazars J. A description of micro- and macroscale damage of concrete structures. Eng Fract Mech 1986;25:729–37.
[26] Mazars J, Pijaudier-Cabot G. Continuum damage theory-application to concrete. J. Eng. Mech. 1989;115:345–65.
[27] Pituba J, Fernandes G. Anisotropic damage model for concrete. J. Eng. Mech. 2011;137:610–24.
[28] Yazdani S, Schreyer H. Combined plasticity and damage mechanics model for plain concrete. J Eng Mech 1990.
[29] Hansen N, Schreyer H. A thermodynamically consistent framework for theories of elasticity coupled with damage. Int J Solids Struct 1994;31:359–89.
[30] Lee J, Fenves GL. Plastic-damage model for cyclic loading of concrete structures. J Eng Mech 1998;124:892–900.
[31] Jefferson A. Craft––a plastic-damage-contact model for concrete. I. Model theory and thermodynamic considerations. Int J Solids Struct 2003;40:5973–99.
[32] Nguyen G, Houlsby G. A coupled damage–plasticity model for concrete based on thermodynamic principles: Part II: nonlocal regularization and numerical implementation. Int J Numer Anal Meth Geomech 2008;32(4):353–89.
[33] Salari M, Saeb S, Willam K, Patchet S, Carrasco R. A coupled elastoplastic damage model for geomaterials. Comput Methods Appl Mech Eng 2004;193:2625–43.
[34] Contrafatto L, Cuomo M. A framework of elastic–plastic damaging model for concrete under multiaxial stress states. Int J Plast 2006;22:2272–300.
[35] Jason L, Huerta A, Pijaudier-Cabot G, Ghavamian S. An elastic plastic damage formulation for concrete: application to elementary tests and comparison with an isotropic damage model. Comput Methods Appl Mech Eng 2006;195:7077–92.
[36] Shao J-F, Jia Y, Kondo D, Chiarelli A-S. A coupled elastoplastic damage model for semi-brittle materials and extension to unsaturated conditions. Mech Mater 2006;38:218–32.
[37] Cicekli U, Voyiadjis GZ, Al-Rub RKA. A plasticity and anisotropic damage model for plain concrete. Int J Plast 2007;23:1874–900.
[38] Voyiadjis GZ, Taqieddin ZN, Kattan PI. Anisotropic damage–plasticity model for concrete. Int J Plast 2008;24:1946–65.
[39] Parisio F, Samat S, Laloui L. Constitutive analysis of shale: a coupled damage plasticity approach. Int J Solids Struct 2015;75:88–98.
[40] Pouya A, Yazdi PB. A damage-plasticity model for cohesive fractures. Int J Rock Mech Min Sci 2015;73:194–202.
[41] Kim D, Dargush GF, Basaran C. A cyclic two-surface thermoplastic damage model with application to metallic plate dampers. Eng Struct 2013;53:608–20.
[42] Valentini B, Theiner Y, Aschaber M, Lehar H, Hofstetter G. Single-phase and multi-phase modeling of concrete structures. Eng Struct 2013;47:10.
[43] Ayhan B, Jehel P, Brancherie D, Ibrahimbegovic A. Coupled damage–plasticity model for cyclic loading: theoretical formulation and numerical implementation. Eng Struct 2013;50:13.
[44] Chen L, Shao J, Huang H. Coupled elastoplastic damage modeling of anisotropic rocks. Comput Geotech 2010:8.
[45] Chiarelli A, Shao J, Hoteit N. Modeling of elastoplastic damage behavior of a claystone. Int J Plast 2003:23.
[46] Nguyen G, Houlsby G. A coupled damage–plasticity model for concrete based on thermodynamic principles: Part I: model formulation and parameter identification. Int J Numer Anal Meth Geomech 2008;32:37.
[47] Luccioni B, Rougier V. A plastic damage approach for confined concrete. Comput Struct 2005:19.
[48] Zhang J, Xu W, Wang H, Wang R, Meng Q, Du S. A coupled elastoplastic damage model for brittle rocks and its application in modelling underground excavation. Int J Rock Mech Mining Sci Geomech Abstr 2016:12.
[49] Zhou C, Zhu F. An elasto-plastic damage constitutive model with double yield surfaces for saturated soft rock. Int J Rock Mech Mining Sci 2010:11.
[50] Karrech A, Regenauer-Lieb K, Poulet T. A damaged visco-plasticity model for pressure and temperature sensitive geomaterials. Int J Eng Sci 2011;49:10.
[51] Karrech A, Regenauer-Lieb K, Poulet T. Continuum damage mechanics for the lithosphere. J Geophys Res 2011;116:14.
[52] Krätzig WB, Pölling R. An elasto-plastic damage model for reinforced concrete with minimum number of material parameters. Comput Struct 2004;82:1201–15.
[53] Liu S, Ning JG, Tan YL, Gu QH. Damage constitutive model based on energy dissipation for intact rock subjected to cyclic loading. Int J Rock Mech Min Sci 2016;85:6.
[54] Lubliner J, Oliver J, Oller S, Onate E. A plastic-damage model for concrete. Int J Solids Struct 1989;25:299–326.
[55] Mozaffari N, George ZV. Coupled gradient damage–Viscoplasticty model for ductile materials: phase field approach. Int J Plast 2016;83:19.
[56] Voyiadjis GZ, Abu-Lebdeh TM. Damage model for concrete using bounding surface concept. J Eng Mech 1993;119:1865–85.
[57] Xenos D, Grassl P. Modelling the failure of reinforced concrete with nonlocal and crack band approaches using the damage-plasticity model CDPM2. Finite Elem Anal Des 2016;117–118:10.
[58] Grassl P, Xenos D, Nyström U, Rempling R, Gylltoft K. CDPM2: a damage-plasticity approach to modelling the failure of concrete. Int J Solids Struct 2013;50:3805–16.
[59] Unteregger D, Fuchs B, Hofstetter G. A damage plasticity model for different types of intact rock. Int J Rock Mech Min Sci 2015;80:12.
[60] Tapponnier P, Brace W. Development of stress-induced microcracks in Westerly granite. Int J Rock Mech Mining Sci Geomech Abstr 1976:103–12.
[61] Batzle ML, Simmons G, Siegfried RW. Microcrack closure in rocks under stress: direct observation. J Geophys Res: Solid Earth 1980;85:7072–90.
[62] Kranz RL. Microcracks in rocks: a review. Tectonophysics 1983;100:449–80.
[63] Eberhardt E, Stead D, Stimpson B, Read R. Identifying crack initiation and propagation thresholds in brittle rock. Can Geotech J 1998;35:222–33.
[64] Xie H, Gao F. The mechanics of cracks and a statistical strength theory for rocks. Int J Rock Mech Min Sci 2000;37:477–88.
[65] Seo Y, Jeong G, Kim J, Ichikawa Y. Microscopic observation and contact stress analysis of granite under compression. Eng Geol 2002;63:259–75.
[66] Vajdova V, Zhu W, Chen T-MN, Wong T-F. Micromechanics of brittle faulting and cataclastic flow in Tavel limestone. J Struct Geol 2010;32:1158–69.
[67] Hoek E, Martin C. Fracture initiation and propagation in intact rock–a review. J Rock Mech Geotech Eng 2014;6:287–300.
[68] Nguyen G, Einav I, Guiamatsia I, Korsunsky AM. From Diffuse to Localised Damage: the Role of Friction. Presented at The International Conference on Advances in Computational Mechanics, Ho Chi Minh City, Vietnam; 2012.
[69] Einav I, Houlsby G, Nguyen G. Coupled damage and plasticity models derived from energy and dissipation potentials. Int J Solids Struct 2007;44:2487–508.
[70] Nguyen GD, Einav I. Nonlocal regularisation of a model based on breakage mechanics for granular materials. Int J Solids Struct 2010;47:1350–60.
[71] Houlsby G, Puzrin A. A thermomechanical framework for constitutive models for rate-independent dissipative materials. Int J Plast 2000;16:1017–47.
[72] Houlsby GT, Puzrin AM. Principles of hyperplasticity: an approach to plasticity theory based on thermodynamic principles. Springer Science & Business Media; 2007.
[73] Lyakhovsky V, Ben-Zion Y, Agnon A. Distributed damage, faulting, and friction. J Geophys Res 1997;102:27635–49.
[74] Lyakhovsky V, Reches Z, Weinberger R, Scott TE. Nonlinear elastic behavior of damaged rocks. Geophys J Int 1997;130:157–66.
[75] Korsunsky AM, Nguyen GD, Kim K. The analysis of deformation size effects using multiple gauge length extensometry and the essential work of rupture concept. Mater Sci Eng, A 2006;423:7.

[76] Fiedler B, Hojo M, Ochiai S, Schulte K, Ando M. Failure behavior of an epoxy matrix under different kinds of static loading. Compos Sci Technol 2001;61:10.
[77] Gopalaratnam VS, Shah SP. Sofnening response of plain concrete in direct tension. ACI Mater J 1985;82:14.
[78] Karsan ID, Jirsa JO. Behavior of concrete under compressive loadings. ASCE J Struct Eng 1969;95.
[79] Kupfer H, Hilsdorf K, Rusch H. Behavior of concrete under biaxial stresses. J Am Concr Inst 1969;66:11.
[80] Wong TF, Baud P, Klein E. Localized failure modes in a compactant porous rock. Geophys Res Lett 2001;28:2521–4.
[81] Das A, Nguyen GD, Einav I. The propagation of compaction bands in porous rocks based on breakage mechanics. J Geophys Res: Solid Earth 2013;118:2049–66.
[82] Das A, Tengattini A, Nguyen GD, Viggiani G, Hall SA, Einav I. A thermomechanical constitutive model for cemented granular materials with quantifiable internal variables. Part II–validation and localization analysis. J Mech Phys Solids 2014;70:382–405.
[83] Bažant ZP, Cedolin L. Stability of structures: elastic, inelastic, fracture and damage theories. World Sci 2010.

Appendix B

A Continuum Model with an Embedded Fracture Process Zone Modelled as a Cohesive Frictional Interface

Mir, A., Nguyen, G.D. and Sheikh, A.H., 2016. A CONTINUUM MODEL WITH AN EMBEDDED FRACTURE PROCESS ZONE MODELLED AS A COHESIVE FRICTIONAL INTERFACE. *Applied Mechanics & Materials, 846*.

The formulation presented in this appendix is slightly different from that originally presented in the paper.

Statement of Authorship

Title of Paper	A Continuum Model with an Embedded Fracture Process Zone Modelled as a Cohesive Frictional Interface
Publication Status	Published
Publication Details	Mir, A., Nguyen, G.D. and Sheikh, A.H., 2016. A CONTINUUM MODEL WITH AN EMBEDDED FRACTURE PROCESS ZONE MODELLED AS A COHESIVE FRICTIONAL INTERFACE. *Applied Mechanics & Materials*, *846*. (doi:10.4028/www.scientific.net/AMM.846.360)

Principal Author

Name of Principal Author (Candidate)	Arash Mir		
Contribution to the Paper	Developed the technical approach including the framework and the cohesive model. Performed analysis & wrote the manuscript.		
Overall percentage (%)	70%		
Certification:	This paper reports on original research I conducted during the period of my Higher Degree by Research candidature and is not subject to any obligations or contractual agreements with a third party that would constrain its inclusion in this thesis. I am the primary author of this paper.		
Signature		Date	25 / 05 / 2017

Co-Author Contributions

By signing the Statement of Authorship, each author certifies that:

i. the candidate's stated contribution to the publication is accurate (as detailed above);
ii. permission is granted for the candidate in include the publication in the thesis; and
iii. the sum of all co-author contributions is equal to 100% less the candidate's stated contribution.

Name of Co-Author	Giang D. Nguyen		
Contribution to the Paper	Supervised the technical developments. Revised the manuscript.		
Signature		Date	25 / 05 / 2017

Name of Co-Author	Abdul Hamid Sheikh		
Contribution to the Paper	Supervised the technical developments. Revised the manuscript.		
Signature		Date	

End of document

A Continuum Model with an Embedded Fracture Process Zone Modelled as a Cohesive Frictional Interface

B.1. Introduction

Strain localisation and stress redistribution due to propagation of fracture or damage and the inherent energy release cause a size effect in quasi-brittle structure. This means the nominal strength and the post-peak behaviour of quasi-brittle structures vary with the size of the structure. The dependence of the structural behaviour on the size (or the characteristic dimension) due to the existence of a localised damage or fracture process zone is known as the deterministic size effect in solid mechanics [1]. The size effect is the most important practical consequence of fracturing phenomena as it is observed in reinforced concrete structures [2, 3] and even more significantly in the explosive breakout of boreholes and/or mining stopes [4-6]. Upon the onset of localisation in quasi-brittle structures a small part of the solid/structure (the FPZ) undergoes further damage and softening while the remaining part (surrounding bulk) unloads. When the thickness of the FPZ is negligible ($h \to 0$), a cohesive frictional interface can, in general, be used to model the dissipative behaviour of material inside FPZ. In this study, the fundamental mechanisms responsible for energy dissipation are assumed to be micro-crack opening in mode I and frictional sliding. One important advantage of the current model is that it takes the frictional dissipation into account and further it produces the nonlinear softening behaviour by only controlling the amount of energy being dissipated due to damage and frictional mechanisms. It is essential for a cohesive model to take the frictional dissipation into account as about 50% -75% of the total energy budget in failure process of quasi-brittle materials is dissipated due to friction [7]. The total amount of dissipated energy in the failure process of quasi-brittle structures is controlled by the width of FPZ which depends on the material microstructure and it is characteristic of the material [8]. The performance of the model is demonstrated through investigating the size effect on structural behaviour and more specifically on the post-peak softening curve for specimens of different slenderness. In the following Sections the essential features of the cohesive frictional interface model is presented and then the model performance in describing size effect is presented.

B.2. A Cohesive Frictional Interface

A unit volume/length of the fracture process zone can be represented as a cohesive frictional interface, as illustrated in Fig. 2.

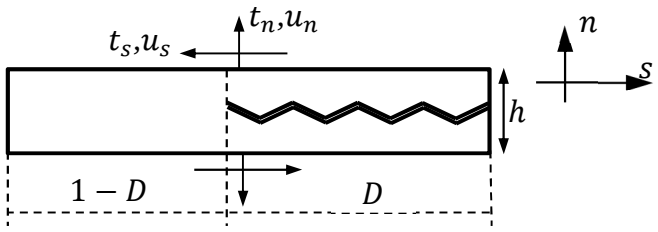

Figure B-1: A unit volume of the FPZ represented as a cohesive frictional inter face

Following the framework of Thermodynamic with internal variables, the complete constitutive relation between the tractions and corresponding displacements is given by only determining two scalar potentials, namely, an energy potential and a dissipation potential. The Helmholtz free energy potential for a unit volume/length of the fracture process zone can be given as:

$$\Psi = \frac{1}{2}(1-D)K_n {u_n^e}^2 + \frac{1}{2}(1-D)K_s {u_s^e}^2 + \frac{1}{2}DK_n\langle -u_n^e\rangle^2 \tag{B-1}$$

In the above expression K_n and K_s are the stiffness of the FPZ and u_n^e and u_s^e are reversible displacements in normal and shear directions, respectively. Also, $\langle . \rangle$ is the Macaulay bracket and D is the scalar damage variable which also represents the volume fraction of the damaged part of the unit length of the FPZ (Figure B-1). The relation between the elastic or reversible displacements (u_n^e and u_s^e) and the irreversible displacements (u_n^p and u_s^p) are given through the following constraint equations:

$$\mathrm{C}_1 = \dot{u}_n - \dot{u}_n^e - \dot{u}_n^p = 0 \tag{B-2}$$

$$\mathrm{C}_2 = \dot{u}_s - \dot{u}_s^e - \dot{u}_s^p = 0 \tag{B-3}$$

Furthermore, for a coupled model the dissipation potential can be defined as follows:

$$\delta\Phi = \sqrt{{\varphi_D}^2 + {\varphi_n}^2 + {\varphi_s}^2} \tag{B-4}$$

In the above expression, φ_D, φ_n and φ_s are homogeneous first order functions in terms of the rates of internal variables ($\dot{D}$, $\dot{u}_n^p$ and $\dot{u}_s^p$), representing the effect of the individual mechanisms on the total dissipation rate $\delta\Phi$, and they can be defined as:

$$\varphi_D = \frac{\chi_D}{\sqrt{\frac{R_n^D \chi_{Dn}}{F_n(D)} + \frac{2R_s^D \chi_{Ds}(1-D)^2 K_s}{\left[(1-D)\sqrt{2F_s(D)K_s} + \mu\langle -t_n\rangle\right]^2}}}\dot{D} \tag{B-5}$$

$$\varphi_n = \frac{\sqrt{F_n(D)}t_n}{\sqrt{R_n^p \chi_{Dn}}}\dot{u}_n^p \tag{B-6}$$

$$\varphi_s = \frac{t_s\left[(1-D)\sqrt{2F_s(D)K_s} + \mu\langle -t_n\rangle\right]}{(1-D)\sqrt{2R_s^p \chi_{Ds} K_s}}\dot{u}_s^p \tag{B-7}$$

In the above expression, χ_D is the total conjugate damage energy and χ_{Dn} and χ_{Ds} represent conjugate damage energy corresponding to mode I and II of fracturing, respectively. The definition of these damage energies are given subsequently. R_i^D and R_i^p $(i = n, s)$ are ratios controlling the damage and frictional dissipation, respectively and $R_i^D + R_i^p = 1$. In addition, $F_n(D)$ and $F_s(D)$ are functions controlling the damage process in the n- and s-directions, respectively, and for the sake of simplicity they are defined to have the same form in the current model as:

$$F_i(D) = \frac{{f_i}^2}{2K_i}\frac{\left(1 + {f_i}^2/(2K_i G_f - {f_i}^2)\right)^2}{\left((1-D) + {f_i}^2/(2K_i G_f - {f_i}^2)\right)^2} \tag{B-8}$$

In the above expression, G_f is the fracture energy, and i stands for either n or s, and f_i and K_i are the strength and stiffness. Furthermore, the constraint equations (B-2) and (B-3) can be used to supplement the dissipation function of equation (B-4) to give:

$$\delta\Phi' = \sqrt{{\varphi_D}^2 + {\varphi_n}^2 + {\varphi_s}^2} + \Lambda_1 C_1 + \Lambda_2 C_2 \tag{B-9}$$

Following the standard procedures of the generalised thermodynamics framework, as outlined in Chapter 3, the following set of equations is obtained:

$$t_n = \frac{\partial\Psi}{\partial u_n} + \frac{\partial\delta\Phi'}{\partial\dot{u}_n} = \frac{\partial\Psi}{\partial u_n} + \frac{\partial\Phi}{\partial\dot{u}_n} + \Lambda_1\frac{\partial C_1}{\partial\dot{u}_n} + \Lambda_2\frac{\partial C_2}{\partial\dot{u}_n} = \Lambda_1 \tag{B-10}$$

$$t_s = \frac{\partial\Psi}{\partial u_s} + \frac{\partial\delta\Phi'}{\partial\dot{u}_s} = \frac{\partial\Psi}{\partial u_s} + \frac{\partial\Phi}{\partial\dot{u}_s} + \Lambda_1\frac{\partial C_1}{\partial\dot{u}_s} + \Lambda_2\frac{\partial C_2}{\partial\dot{u}_s} = \Lambda_2 \tag{B-11}$$

$$0 = \frac{\partial\Psi}{\partial u_n^e} + \frac{\partial\Phi}{\partial\dot{u}_n^e} + \Lambda_1\frac{\partial C_1}{\partial\dot{u}_n^e} + \Lambda_2\frac{\partial C_2}{\partial\dot{u}_n^e} = (1-D)K_n u_n^e + DK_n\langle -u_n^e\rangle \tag{B-12}$$

$$0 = \frac{\partial\Psi}{\partial u_s^e} + \frac{\partial\Phi}{\partial\dot{u}_s^e} + \Lambda_1\frac{\partial C_1}{\partial\dot{u}_s^e} + \Lambda_2\frac{\partial C_2}{\partial\dot{u}_s^e} = (1-D)K_s u_s^e \tag{B-13}$$

$$0 = \frac{\partial \Psi}{\partial u_n^p} + \frac{\partial \Phi}{\partial \dot{u}_n^p} + \Lambda_1 \frac{\partial C_1}{\partial \dot{u}_n^p} + \Lambda_2 \frac{\partial C_2}{\partial \dot{u}_n^p} = \chi_n - \Lambda_1 \tag{B-14}$$

$$0 = \frac{\partial \Psi}{\partial u_s^p} + \frac{\partial \Phi}{\partial \dot{u}_s^p} + \Lambda_1 \frac{\partial C_1}{\partial \dot{u}_s^p} + \Lambda_2 \frac{\partial C_2}{\partial \dot{u}_s^p} = \chi_s - \Lambda_2 \tag{B-15}$$

$$0 = \frac{\partial \Psi}{\partial D} + \frac{\partial \Phi}{\partial \dot{D}} + \Lambda_1 \frac{\partial C_1}{\partial \dot{D}} + \Lambda_2 \frac{\partial C_2}{\partial \dot{D}} = \chi_D - \frac{1}{2} K_n \left({u_n^e}^2 - \langle -u_n^e \rangle^2 \right) - \frac{1}{2} K_s {u_s^e}^2 \tag{B-16}$$

By eliminating the Lagrangian multipliers between the above set of equations the normal and shear tractions are given as:

$$t_n = (1 - D) K_n u_n^e + D K_n \langle -u_n^e \rangle \tag{B-17}$$

$$t_s = (1 - D) K_s u_s^e \tag{B-18}$$

In addition, the dissipative part of the internal forces and the conjugate damage energy are given as follows:

$$\chi_n = t_n \tag{B-19}$$

$$\chi_s = t_s \tag{B-20}$$

$$\chi_D = \frac{1}{2} K_n \left({u_n^e}^2 - \langle -u_n^e \rangle^2 \right) + \frac{1}{2} K_s {u_s^e}^2 = \chi_{Dn} + \chi_{Ds} \tag{B-21}$$

Following the principles of generalised thermodynamics (see Chapter 3), by performing a degenerate Legendre transformation on the dissipation rate function the yield function in the generalised dissipative stress space can be given as a function of the dissipative stresses and the conjugate damage energy. By making use of Ziegler's orthogonality principle for rate-independent behaviour the following relations ensues (see Sections 3.2.2 and 3.2.3):

$$\chi_n = \frac{\partial \delta\Phi}{\partial \dot{u}_n^p} = \frac{\partial \delta\Phi}{\partial \varphi_n} \frac{\partial \varphi_n}{\partial \dot{u}_n^p} = \frac{\varphi_n}{\sqrt{{\varphi_D}^2 + {\varphi_n}^2 + {\varphi_s}^2}} \frac{\partial \varphi_n}{\partial \dot{u}_n^p} \tag{B-22}$$

$$\chi_s = \frac{\partial \delta\Phi}{\partial \dot{u}_s^p} = \frac{\partial \delta\Phi}{\partial \varphi_s} \frac{\partial \varphi_s}{\partial \dot{u}_s^p} = \frac{\varphi_s}{\sqrt{{\varphi_D}^2 + {\varphi_n}^2 + {\varphi_s}^2}} \frac{\partial \varphi_s}{\partial \dot{u}_s^p} \tag{B-23}$$

$$\chi_D = \frac{\partial \delta\Phi}{\partial \dot{D}} = \frac{\partial \delta\Phi}{\partial \varphi_D} \frac{\partial \varphi_D}{\partial \dot{D}} = \frac{\varphi_D}{\sqrt{{\varphi_D}^2 + {\varphi_n}^2 + {\varphi_s}^2}} \frac{\partial \varphi_D}{\partial \dot{D}} \tag{B-24}$$

Therefore, the yield function in the dissipative stress space is obtained as:

$$y^* = \left(\frac{\chi_n}{\partial \varphi_n / \partial \dot{u}_n^p} \right)^2 + \left(\frac{\chi_s}{\partial \varphi_s / \partial \dot{u}_s^p} \right)^2 + \left(\frac{\chi_D}{\partial \varphi_D / \partial \dot{D}} \right)^2 - 1 \leq 0 \tag{B-25}$$

By virtue of the above expression of the yield in the dissipative stress space, the evolution rules for internal variables are given as follows:

$$\dot{D} = \dot{\lambda}\frac{\partial y^*}{\partial \chi_D} = 2\dot{\lambda}\frac{\chi_D}{\left(\partial \varphi_D/\partial \dot{D}\right)^2}$$
$$= 2\dot{\lambda}\left(\frac{R_n^D \chi_{Dn}}{F_n(D)\chi_D} + \frac{2R_s^D \chi_{Dn}(1-D)^2 K_s}{\left[(1-D)\sqrt{2F_s(D)K_s} + \mu\langle -t_n\rangle\right]^2 \chi_D}\right) \quad \text{(B-26)}$$

$$\dot{u}_n^p = \dot{\lambda}\frac{\partial y^*}{\partial \chi_n} = 2\dot{\lambda}\frac{\chi_n}{\left(\partial \varphi_n/\partial \dot{u}_n^p\right)^2} = 2\dot{\lambda}\left(\frac{R_n^p \chi_{Dn}}{F_n(D)t_n}\right) \quad \text{(B-27)}$$

$$\dot{u}_s^p = \dot{\lambda}\frac{\partial y^*}{\partial \chi_s} = 2\dot{\lambda}\frac{\chi_s}{\left(\partial \varphi_s/\partial \dot{u}_s^p\right)^2} = 2\dot{\lambda}\left(\frac{2(1-D)^2 R_s^p \chi_{Ds} K_s}{t_s\left[(1-D)\sqrt{2F_s(D)K_s} + \mu\langle -t_n\rangle\right]^2}\right) \quad \text{(B-28)}$$

Furthermore, by substituting equations (B-5) – (B-7) into equation (B-25) and making use of equations (B-17) and (B-18) the expression of the yield function in the true stress space is given as:

$$y = \frac{x_{Dn}}{F_n(D)} + \frac{2\chi_{Ds}(1-D)^2 K_s}{\left[(1-D)\sqrt{2F_s(D)K_s} + \mu\langle -t_n\rangle\right]^2} - 1 \leq 0 \quad \text{(B-29)}$$

Figure B-2 shows the loading function (or initial yield surface) in the $t_n - t_s$ space. Also the loading function evolves to the failure surface of Coulomb criterion when damage variable grows from 0 to 1.

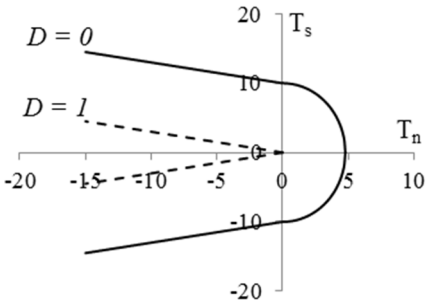

Figure B-2: The initial yield surface ($D = 0$) and the final failure surface ($D = 1$)

For a coupled model the function $F_n(D)$ is calibrated to control energy dissipation only due to damaging processes while the rest of the total energy budget is dissipated due to frictional sliding. Figure B-3(a) shows the linear softening behaviour for a material with Young's modulus of $E = 43600N/mm^2$, uniaxial tensile strength of $f_t = 4.77N/mm^2$ and fracture energy of $G_f^I = 0.08917N/mm$. The thickness of the FPZ is assumed to be $0.1mm$.

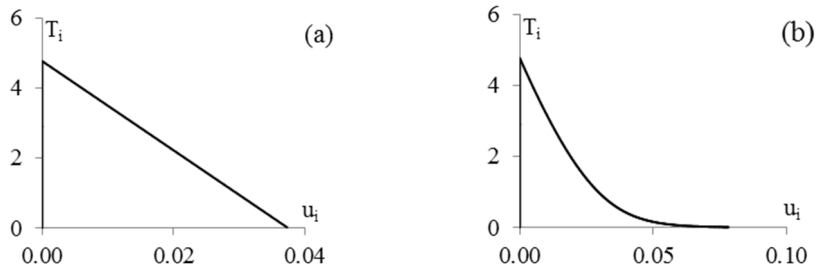

Figure B-3: (a) Linear softening model for pure damage in mode I. (b) Nonlinear softening model for the case when 50% of energy dissipation is due to frictional loss ($R_n^p = 0.5$)

The nonlinear behaviour (Figure B-3(b)) is produced due to dissipation properties of the model. A physical explanation is that when damaging processes take place, some of the total energy budget for fracturing the material is spent on frictional sliding which in effect will delay the damaging process.

B.3. Size Effect

Specimens with different slenderness were considered to be axially loaded in tension and compression. As illustrated in Figure B-4 (a) and (b), the model predicts a steeper post-peak softening curve for more slender specimen and a sharp snapback for a significantly more slender specimen.

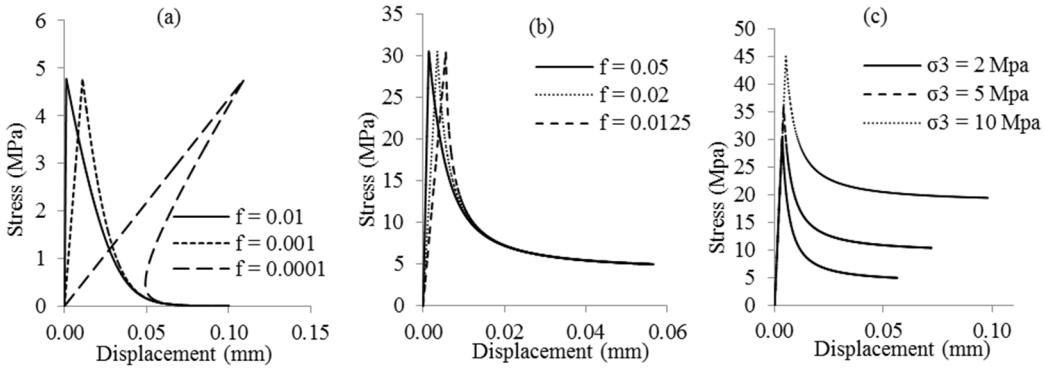

Figure B-4: (a) Stress-displacement curves for uniaxial tensile loading, (b) stress-displacement curves for triaxial compression, (c) triaxial compression with different confining pressures

It should be noted that in all cases the same amount of energy is dissipated as the width of the FPZ is kept constant. The model also predicts higher failure stress at higher confining pressures in compression (Figure B-4 (c)). The current model is not yet capable of capturing snapback in compression. However, as shown in Figure B-4 (b), the model

produces a progressively more brittle behaviour as the slenderness of specimens is increased, in agreement with experimental observations.

B.4. Summary and Conclusion

Size effects due to localised failure are encapsulated in a new continuum model in this study. The key point is to note that beyond the onset of localisation the strain field is no longer uniform. Upon localisation one part of the structure (the FPZ) undergoes inelastic loading and exhibits softening behaviour while the remaining part (elastic bulk) undergoes elastic unloading. A modelling framework such as the one used in this study can be applied to establish links between the FPZ and the surrounding elastic bulk. The fundamental mechanisms of material degradation and energy dissipation can be formulated within a thermodynamically consistent framework to address the inelastic softening behaviour of the material inside FPZ. The promising features of the model are demonstrated and validation will come in our future work.

References

[1] Bažant ZP. Size effect on structural strength: a review. Archive of applied Mechanics. 1999;69:703-25.

[2] Bažant ZP, Xiang Y. Size effect in compression fracture: splitting crack band propagation. Journal of engineering mechanics. 1997;123:162-72.

[3] Bažant ZP. Fracturing truss model: Size effect in shear failure of reinforced concrete. Journal of engineering mechanics. 1997;123:1276-88.

[4] Carter B. Size and stress gradient effects on fracture around cavities. Rock Mechanics and Rock Engineering. 1992;25:167-86.

[5] Carter BJ, Lajtai EZ, Yuan Y. Tensile fracture from circular cavities loaded in compression. International journal of fracture. 1992;57:221-36.

[6] Haimson B, Herrick C. In-situ stress calculation from borehole breakout experimental studies. Proc, 26th US Symp Rock Mech1989. p. 1207-18.

[7] Bažant ZP. Analysis of work-of-fracture method for measuring fracture energy of concrete. Journal of Engineering Mechanics. 1996;122:138-44.

[8] Jirásek M. Objective modeling of strain localization. Revue française de génie civil. 2002;6:1119-32.

Appendix C

Capturing pressure- and rate-dependent behaviour of rocks using a new damage-plasticity model

Mukherjee, M., Nguyen, G.D., Mir, A., Bui, H.H., Shen, L., El-Zein, A. and Maggi, F., 2017. Capturing pressure-and rate-dependent behaviour of rocks using a new damage-plasticity model. *International Journal of Impact Engineering*.

Statement of Authorship

Title of Paper	Capturing pressure- and rate-dependent behaviour of rocks using a new damage-plasticity model
Publication Status	Published
Publication Details	Mukherjee, M., Nguyen, G.D., Mir, A., Bui, H.H., Shen, L., El-Zein, A. and Maggi, F., 2017. Capturing pressure-and rate-dependent behaviour of rocks using a new damage-plasticity model. *International Journal of Impact Engineering*. (https://doi.org/10.1016/j.ijimpeng.2017.01.006).

Principal Author

Name of Principal Author	Mousumi Mukherjee		
Contribution to the Paper	Developed the complete model based on a generic approach, using results on the shape of the yield-failure function in Arash Mir's PhD work. Performed the analysis & wrote major part of the manuscript.		
Overall percentage (%)	40%		
Signature		Date	25 / 05 / 2017

Co-Author Contributions

By signing the Statement of Authorship, each author certifies that:

i. the candidate's stated contribution to the publication is accurate (as detailed above);
ii. permission is granted for the candidate in include the publication in the thesis; and
iii. the sum of all co-author contributions is equal to 100% less the candidate's stated contribution.

Name of Co-Author	Giang D. Nguyen		
Contribution to the Paper	Developed the generic framework on damage-plasticity modelling. Supervised the technical developments and contributed to the write-up and revision.		
Signature		Date	25 / 05 / 2017

Name of Co-Author	Arash Mir		
Contribution to the Paper	Developed the yield-failure function and its evolution. Plotted results on the evolution of the yield function. Wrote part of the Introduction.		
Certification:	This paper reports on original research I conducted during the period of my Higher Degree by Research candidature and is not subject to any obligations or contractual agreements with a third party that would constrain its inclusion in this thesis.		
Signature		Date	25 / 05 / 2017

Name of Co-Author	Ha H. Bui		
Contribution to the Paper	Contributed to the development of the generic framework on damage-plasticity modelling, discussion, write-up and revision.		
Signature		Date	25/05/2017

Name of Co-Author	Luming Shen		
Contribution to the Paper	Contributed to the discussion, write-up and revision.		
Signature		Date	25/05/2017

Name of Co-Author	Abbas El-Zein		
Contribution to the Paper	Contributed to the discussion, write-up and revision.		
Signature		Date	25/05/2017

Name of Co-Author	Federico Maggi		
Contribution to the Paper	Contributed to the discussion, write-up and revision.		
Signature		Date	25/05/2017

End of document

International Journal of Impact Engineering 000 (2017) 1–11

Contents lists available at ScienceDirect

International Journal of Impact Engineering

journal homepage: www.elsevier.com/locate/ijimpeng

Capturing pressure- and rate-dependent behaviour of rocks using a new damage-plasticity model

Mousumi Mukherjee[a], Giang D. Nguyen[a,*], Arash Mir[a], Ha H. Bui[b], Luming Shen[c], Abbas El-Zein[c], Federico Maggi[c]

[a] School of Civil, Environmental and Mining Engineering, The University of Adelaide, Australia
[b] Department of Civil Engineering, Monash University, Australia
[c] School of Civil Engineering, The University of Sydney, Australia

ARTICLE INFO

Article History:

Keywords:
Constitutive models
Rocks
Geomaterials
Pressure-dependent
Rate-dependent
Strain rate
Damage
Plasticity
Brittle
Ductile

ABSTRACT

Rock response to confining pressure and strain rate can change dramatically from very brittle to ductile. Capturing this transition is crucial for a correct prediction of rock mass failure due to blasting, explosion or drilling in mining. In this work, a new constitutive model that accounts for the effects of both confining pressure and strain rate on the nominal strength and post peak behaviour is proposed for dry intact rocks and other similar geological materials. The key features of the proposed constitutive model are the employment of a single loading function that evolves from initial yielding to ultimate failure during damaging and the rate-dependent enhancement so that the strain rate effects can be faithfully described at different confining pressures. The model can adequately capture both the brittle and ductile responses as well as the brittle-ductile transition as a result of both strain rate and confining pressure.

1. Introduction

Understanding and modelling the behaviour of rocks would pave the way towards a safe and economical design in geotechnical and mining engineering. Like any other geological material, rock behaviour depends on both strain rate and pressure, that is, its response can change from very brittle to ductile under significantly high confining pressure [1–10] or high strain rate [11–19]. In mining and geotechnical operations in crustal rock formations the effects of blasting, drilling or tunnelling and/or tectonic and earthquake forces can dramatically change the stress state. Therefore, the prediction of failure would require a model that can capture, as accurately as possible, the macroscopic response of rocks under rather complex stress states and different loading rates.

Inelastic rock deformation at microscopic scale involves a series of micro-mechanical processes leading to degradation of the material micro-structure. These processes usually begin with initiation of micro-cracks within the material matrix (at low pressures) and/or grains (at high pressures), followed by localization of micro-cracks with a band of certain thickness where micro-cracks finally coalesce to form the macroscopic fracture. Throughout the entire course of inelastic deformation, frictional sliding between the two faces of micro-cracks, asperity interlocking, granular and/or diffusional flow, crystal plasticity, and other processes may accompany micro-cracking and fracturing [20–24]. These micro-mechanisms of deformation are observed at macro-scale as stiffness and strength reduction, inelastic dilation/compaction and residual strains. From a phenomenological perspective, all the mechanisms that cause stiffness and strength reduction may be described as damage and all those phenomena that lead to the occurrence of the residual strains can be interpreted as plastic deformations. Furthermore, the micro-mechanical processes of deformation in rocks are mostly time/rate-dependent, which consequently give rise to the macroscopically observed rate dependent behaviour of rocks. Examples of such time/rate dependent micro-mechanisms may be given as time dependency of static friction and the evolution of frictional strength with the loading rate [25–29] and/or time dependent micro-crack growth [19,30]. Rate dependent macroscopic rock behaviour may be characterized by the increase in the rock strength under tension and compression at high strain rates [31–36]. In addition, at higher strain rates rocks show a tendency towards more ductile behaviour, while in quasi-static loading, under the same confining pressure, the behaviour can be completely brittle [13,14,19,37].

Phenomenological coupled damage-plasticity models with different levels of complexity and applicability have been proposed for

* Corresponding author.
E-mail addresses: g.nguyen@adelaide.edu.au, giang.nguyen@trinity.oxon.org (G.D. Nguyen).

http://dx.doi.org/10.1016/j.ijimpeng.2017.01.006
0734-743X/

List of symbols

dt	Time increment
g	Plastic-damage potential
g_f	Local or specific fracture energy
m	Strain rate parameter
p	Hydrostatic stress
p_{c0}, p_{t0}	Pressures at initial yield under isotropic compression and tension, respectively
q	Shear stress
y	Yield function
A, B	Material parameters controlling damage evolution
C_{ijkl}	Secant elastic stiffness tensor
C^{epd}_{ijkl}	Elasto-plastic-damage tangent stiffness tensor
D_{mnkl}	Secant compliance tensor
D	Damage parameter
G	Shear modulus
G_f	Fracture energy
H	Heaviside function of hydrostatic pressure
I_1	First invariant of the stress tensor
J_2	Second invariant of the deviatoric stress tensor
K	Bulk modulus
M_0	Material constant controlling the shape of the yield surface
M_u	Stress ratio at failure
S_{ij}	Deviatoric stress
α_0	Material constant controlling the shape of the yield surface
β	Parameter controlling the dilational response
γ	Material constant controlling the shape of the yield surface
ε_{ij}	Total strain tensor
ε^p_{ij}	Plastic strain tensor
ε_s, ε_v	Total shear and volumetric strains, respectively
ε^p_s, ε^p_v	Plastic shear and volumetric strains, respectively
ϵ_p	Accumulated plastic strain
η	Viscosity parameter
λ	Damage-plastic multiplier
σ_{ij}	Stress tensor
$\sigma_1, \sigma_2, \sigma_3$	Major, intermediate and minor principal stresses, respectively
σ_t	Tensile strength
ψ	Elastic energy potential

modelling the mechanical behaviour of rocks [10,38–44]. These models, in general, specify the interaction between damage and plasticity processes in the model formulation in order to account for both stiffness and strength reduction and residual strains, observed during the course of inelastic deformation. Various approaches may be taken for constructing coupled damage-plasticity models for rocks which can reflect the effect of confining pressure on the mechanical behaviour of rock. Examples of such approaches can be given as models with two loading surfaces [39,45–48] or models in which damage evolution is defined as a function of volumetric plastic strain rate [41,49–52]. Although many coupled damage-plasticity models can be found in the literature, which are capable of describing the mechanical behaviour of rocks under different confining pressures, not much attention has been given to constructing models which take into account the combined effects of both confining pressure and loading rate, particularly, on the brittle-to-ductile transition in rocks.

A new formulation is developed in this study by employing a combined yield-failure function, which eliminates the need for multiple loading surfaces, while facilitating both the implementation and applications of the model to cover a wide range of responses under different pressures and strain rates. In this formulation, an initial yield surface evolves, with the evolution of the damage variable, defined as a function of the rate of accumulated plastic strain, into a linear frictional failure envelope [53]. This is an important feature of the proposed model as the brittle/softening and ductile/hardening responses together with the transition between the two states of behaviour, with increasing confining pressure, can be automatically captured by the model without any need for separately defining hardening or softening laws. The fundamental mechanisms which determine the rock behaviour when switching from tensile to compressive loading is also accounted for, through mimicking the influence of micro-crack closure on the rock mechanical response. Furthermore, strain rate dependency of the behaviour, which has been experimentally observed in rocks and other similar geological materials, is incorporated in the model through the Perzyna type viscosity. It should be noted that rate dependency in the proposed model is viewed as an intrinsic feature of the model rather than a regularization technique in numerical implementation. In addition, rate dependent response induced by pore pressures in moist rocks is not taken into account yet in this study, and this is acknowledged as an issue to be addressed in our future work. The separation of pressure and rate dependence in the proposed model formulation allows for independent calibration of the model in quasi-static and dynamic loading conditions. In our opinion, this facilitates both the development and calibration of the model.

The paper is organised as follows; at first the model formulation is described, while providing links between the model formulation and the rock behaviour under different confining pressures and strain rates. Numerical implementation algorithms are then described and numerical examples of rock behaviour under different confining pressures and strain rates are given to demonstrate promising features of the new model.

2. Model formulation

2.1. Convention and definition

In the present study, the tensile stresses are assumed to be positive and the compressive stresses are considered as negative. However, in order to be consistent with the rock mechanics convention, the stress-strain signs will be switched when presenting the model predictions at the material level. The principal stresses are assumed to satisfy the condition $\sigma_1 \geq \sigma_2 \geq \sigma_3$. The first invariant of the stress tensor, σ_{ij}, is denoted as $I_1 = \sigma_{kk}$ and the second invariant of the deviatoric stress tensor, S_{ij}, is $J_2 = \frac{S_{ij}S_{ij}}{2}$, where $s_{ij} = \sigma_{ij} - \sigma_{kk}\delta_{ij}/3$. In addition, two stress invariants, the hydrostatic stress $p = -\sigma_{kk}/3$ and the shear stress $q = \sqrt{3J_2}$ are used in the model formulation.

2.2. Stress-strain relationship

The proposed constitutive model for intact rock has been formulated within the framework of continuum damage mechanics and plasticity theory. In addition to the compressive response, the model accounts for the tensile regime and includes micro-crack closure effects when switching from tension to compression modes. Such effects are indirectly modelled by considering an enhanced elastic stiffness under compressive loading. Instead of introducing an isotropic damage parameter, the unilateral behaviour of rock due to crack closure has been described by coupling the damage parameter D with the elastic stiffness tensor. The following form of the elastic energy potential has been assumed for this purpose:

$$\psi = \frac{1}{2}[(1-D) + DH(-\sigma_{kk})]K\left(\varepsilon_v - \varepsilon^p_v\right)^2 + \frac{3}{2}(1-D)G\left(\varepsilon_s - \varepsilon^p_s\right)^2 \quad (1)$$

Please cite this article as: M. Mukherjee et al., Capturing pressure- and rate-dependent behaviour of rocks using a new damage-plasticity model, International Journal of Impact Engineering (2017), http://dx.doi.org/10.1016/j.ijimpeng.2017.01.006

In the above expression, K, G, ε_v and ε_s are bulk modulus, shear modulus and volumetric and shear strains, respectively, D is the scalar damage variable, H denotes the Heaviside function of hydrostatic pressure, with $H=1$ under compressive loading ($\sigma_{kk}<0$). The damage parameter has a bound, $0 \le D \le 1$, where 0 and 1 represent an undamaged and fully damaged material state, respectively. The elastic constitutive law can be written as follows:

$$p = \frac{\partial \psi}{\partial \varepsilon_v} = [(1-D) + DH(-\sigma_{kk})]K\left(\varepsilon_v - \varepsilon_v^p\right) \tag{2}$$

$$q = \frac{\partial \psi}{\partial \varepsilon_s} = 3(1-D)G\left(\varepsilon_s - \varepsilon_s^p\right) \tag{3}$$

The generalised stress-strain relation and secant elastic stiffness C_{ijkl} is given by:

$$\sigma_{ij} = \frac{\partial \psi}{\partial \varepsilon_{ij}} = \frac{\partial \psi}{\partial \varepsilon_v}\frac{\partial \varepsilon_v}{\partial \varepsilon_{ij}} + \frac{\partial \psi}{\partial \varepsilon_s}\frac{\partial \varepsilon_s}{\partial \varepsilon_{ij}} = p\frac{\partial \varepsilon_v}{\partial \varepsilon_{ij}} + q\frac{\partial \varepsilon_s}{\partial \varepsilon_{ij}} = C_{ijkl}\left(\varepsilon_{kl} - \varepsilon_{kl}^p\right) \tag{4}$$

where

$$C_{ijkl} = \left[\{(1-D) + DH(-\sigma_{kk})\}K - \frac{2}{3}(1-D)G\right]\delta_{ij}\delta_{kl} + (1-D)G\left[\delta_{ik}\delta_{jl} + \delta_{il}\delta_{jk}\right] \tag{5}$$

The damage-plasticity model assumes an evolving yield-failure function which is a function of stresses and the scalar damage variable D. This function evolves from an initial yield surface to a final linear frictional failure surface as the damage variable grows from zero to unity (Fig. 1). The initial yield surface marks the onset of inelastic behaviour; whereas, the final failure surface corresponds to a state where material loses all its cohesion and its residual frictional shear strength is fully mobilised. The damage evolution is coupled with plastic strain which is further governed by a non-associative flow rule.

Following Mir et al. [53], a tear drop-shaped yield function y has been assumed as:

$$y(p,\ q, D) = \left[\frac{(1-D)(p-\rho)}{\frac{(1-\gamma)p_c - p_t}{p_c + p_t}p + \frac{1}{2}(1-D)\gamma p_c}\right]^2 + \left[\frac{q}{M[p-\alpha(p-\rho)]}\right]^2 - 1 \le 0 \tag{6}$$

In the above expression, p_c, p_t, α, ρ, and M are defined as functions of D as follows:

$$p_c = \left(1 + \frac{D}{2}\right)p_{c0} \tag{7}$$

$$p_t = (1-D)p_{t0} \tag{8}$$

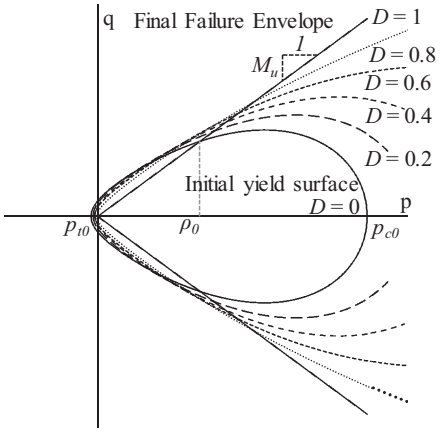

Fig. 1. Evolution of yield surface with damage in the stress space.

$$\alpha = \sqrt{1-D}\alpha_0 \tag{9}$$

$$M = DM_u + (1-D)M_0 \tag{10}$$

$$\rho = \frac{(4-\gamma)p_c p_t + \gamma {p_c}^2}{2(p_c + p_t)} \tag{11}$$

where p_{c0} and p_{t0} are the pressures at initial yield under isotropic compression and tension, respectively; γ, α_0 and M_0 are the material constants which control the shape of the yield surface; and M_u is the slope of the failure surface in triaxial stress space. The parameter M_u represents the stress ratio (q/p) at failure ($D=1$); whereas, M_0 is a fitting parameter which controls the shape of the initial yield surface. The variation of M in Eq. (10) can allow for some minor hardening prior to peak stress under shearing at low confining pressure. This feature is however not explored in this work. It should be noted that both hardening and softening responses of the model are encapsulated in the evolution of the initial yield function to a final failure envelope, governed by the damage variable (Fig. 1). This evolution takes into account the effects of confining pressure to give the model appropriate behaviour in both tension and compression.

2.3. Plastic damage potential

In order to describe the dilation behaviour with the proposed constitutive model, a non-associative flow rule has been adopted. A plastic-damage potential has been introduced which allows us to calibrate the dilational behaviour against experimental data. The plastic-damage potential takes the following form:

$$g(p,\ q, D) = \left[\frac{(1-D)(p-\rho)}{\frac{(1-\gamma)p_c - p_t}{p_c + p_t}p + \frac{1}{2}(1-D)\gamma p_c}\right]^2 + \left[\frac{\beta q}{M\{p-\alpha(p-\rho)\}}\right]^2 - 1 \tag{12}$$

The non-dimensional parameter β controls the dilational response of the model. It is assumed that the material reaches a critical state with zero volumetric strain when the material becomes fully damaged, $D=1$. The flow rule is governed by the proposed damage potential

$$\dot{\varepsilon}_{kl}^p = \dot{\lambda}\frac{\partial g}{\partial \sigma_{kl}} \tag{13}$$

where $\dot{\lambda}$ is the rate of damage-plastic multiplier.

2.4. Damage evolution law

Since even intact rocks contain microscopic flaws (micro-cracks and micro voids), frictional sliding between the two faces of pre-existing micro-cracks as well as initiation of new micro-cracks can take place at microscopic scale during the inelastic loading of rocks. At the macroscopic level these mechanisms are described as softening/hardening phenomena in terms of strength and stiffness reduction/enhancement. In regard to a damage plasticity model, such macroscopic behaviour can be modelled through a plastic strain tensor and a damage variable. For a coupled approach, further characterisation is required to identify the inter-dependence of these two internal variables. An exponential relationship between damage (ΔD) and increasing accumulated plastic strain ($\Delta\epsilon_p = \sqrt{\frac{2}{3}\Delta\varepsilon_{ij}^p \Delta\varepsilon_{ij}^p}$) is generally adopted to effectively represent the coupling effect [54]. To better describe rock behaviour under both tensile and compressive regimes, a new damage evolution law is proposed here taking into account different contributions between plastic shear and volumetric responses:

$$D = 1 - e^{-\epsilon_p}, \tag{14}$$

Please cite this article as: M. Mukherjee et al., Capturing pressure- and rate-dependent behaviour of rocks using a new damage-plasticity model, International Journal of Impact Engineering (2017), http://dx.doi.org/10.1016/j.ijimpeng.2017.01.006

where

$$\Delta\epsilon_p = \sqrt{\frac{2}{9}\left(A\Delta\varepsilon_v^p\right)^2 + \left(B\Delta\varepsilon_s^p\right)^2} \tag{15}$$

where, A and B are model parameters. After calibrating the parameters related to the initial yield surface, the parameters β, A and B are calibrated iteratively by considering stress-strain-volumetric response from both compressive and tensile experimental data.

3. Numerical implementation

A brief summary of the model is provided here before the formulation of the tangent stiffness and stress update algorithms. The constitutive equations governing the behaviour of the model include the stress-strain-damage relationship (Eqs. (4) and (5)), yield surface (Eq. (6)) with non-associated flow rules governed by the plastic potential (Eq. (12)), and the damage evolution (Eqs. (14) and (15)). As can be seen, both hardening and softening responses of the model are encapsulated in the evolution of the initial yield function to a final failure envelope, governed by the damage variable (Fig. 1). This evolution takes into account the effects of confining pressure to give the model appropriate behaviour in both tension and compression.

3.1. Tangent stiffness formulation

The formulation of the tangent stiffness tensor for the proposed damage-plasticity model is presented in this section. The tangent stiffness tensor is necessary for localisation analysis and for solving boundary value problems (BVP) where the constitutive models are implemented within a numerical framework. The following form of the stress rate tensor can be derived from Eq. (4):

$$\dot{\sigma}_{ij} = C_{ijkl}\dot{\varepsilon}_{kl} - C_{ijkl}\dot{\varepsilon}_{kl}^p + \frac{\partial C_{ijkl}}{\partial D} D_{klmn}\sigma_{mn}\dot{D} \tag{16}$$

where D_{mnkl} is the secant compliance tensor. The plastic flow rule leads to the following expression for plastic volumetric and shear strain rate:

$$\dot{\varepsilon}_v^p = \dot{\lambda}\frac{\partial g}{\partial p} \text{ and } \dot{\varepsilon}_s^p = \dot{\lambda}\frac{\partial g}{\partial q} \tag{17}$$

The rate of damage variable can be calculated from Eqs. (15) and (17):

$$\dot{D} = (e^{-\epsilon_p})\dot{\epsilon_p} = \dot{\lambda}(e^{-\epsilon_p})\sqrt{\frac{2}{9}\left(A\frac{\partial g}{\partial p}\right)^2 + \left(B\frac{\partial g}{\partial q}\right)^2} \tag{18}$$

The consistency condition for the yield function results in:

$$\dot{y} = \frac{\partial y}{\partial \sigma_{ij}}\dot{\sigma}_{ij} + \frac{\partial y}{\partial D}\dot{D} = 0 \tag{19}$$

Furthermore, substitution of Eqs. (16)–(19) into the consistency condition leads to the following expression for $\dot{\lambda}$:

$$\dot{\lambda} = M_{kl}\dot{\varepsilon}_{kl} \tag{20}$$

where

$$M_{kl} = \frac{\frac{\partial y}{\partial \sigma_{ij}} C_{ijkl}}{\left(\frac{\partial y}{\partial \sigma_{ab}} C_{abmn}\frac{\partial g}{\partial \sigma_{mn}}\right) - \left\{\left(\frac{\partial y}{\partial \sigma_{ab}}\frac{\partial C_{abrs}}{\partial D} D_{mnrs}\sigma_{mn}\right) + \frac{\partial y}{\partial D}\right\}\left((e^{-\epsilon_p})\sqrt{\frac{2}{9}\left(A\frac{\partial g}{\partial p}\right)^2 + \left(B\frac{\partial g}{\partial q}\right)^2}\right)} \tag{21}$$

The incremental stress-strain relation can now be reduced to:

$$\dot{\sigma}_{ij} = C_{ijkl}^{epd}\dot{\varepsilon}_{kl} \tag{22}$$

where C_{ijkl}^{epd} is the elasto-plastic-damage tangent stiffness tensor:

$$C_{ijkl}^{epd} = C_{ijkl} - C_{ijrs}\frac{\partial g}{\partial \sigma_{rs}} M_{kl} + \frac{\partial C_{ijab}}{\partial D} D_{mnab}\sigma_{mn} M_{kl}(e^{-\epsilon_p})\sqrt{\frac{2}{9}\left(A\frac{\partial g}{\partial p}\right)^2 + \left(B\frac{\partial g}{\partial q}\right)^2} \tag{23}$$

3.2. Semi-implicit stress return algorithm

The rate constitutive equations presented in the previous section are numerically integrated in order to give the stress update for a given strain increment. At any time step, the stress tensor can be represented in the following incremental form:

$$\sigma_{ij}^{k+1} = \sigma_{ij}^k + \Delta\sigma_{ij} \tag{24}$$

where σ_{ij}^{k+1} is the stress state in the current time step, σ_{ij}^k is the previous stress state and $\Delta\sigma_{ij}$ is the increment of stress from the previous step to the current one. First a trial stress increment is evaluated elastically using the following relation:

$$\sigma_{ij}^{trial} = \sigma_{ij}^k + \Delta\sigma_{ij}^{trial} \tag{25}$$

In the above expression, $\Delta\sigma_{ij}^{trial}$ is given as:

$$\Delta\sigma_{ij}^{trial} = C_{ijkl}^k \Delta\varepsilon_{kl} \tag{26}$$

where $\Delta\sigma_{ij}^{trial}$ is the trial stress increment, σ_{ij}^{trial} is the elastically evaluated trial stress, C_{ijkl}^k is the secant elastic stiffness evaluated at state k, and $\Delta\varepsilon_{kl}$ is the total strain increment from step k to $k+1$. The yield function $y(p, q, D)$ is next evaluated based on this trial stress to determine whether the material is elastic or has already yielded. Hence, if $y(p, q, D) < 0$ the elastic solution is accepted; however, if $y(p, q, D) \geq 0$, a stress return algorithm must be employed to correct the stress increment based on damage and plasticity evolutions in the previous step (Fig. 2).

The semi-implicit stress return algorithm is a simplified form of the fully implicit backward Euler [55]. The yield function at the trial point can be approximated by a first-order Taylor expansion as:

$$y^{k+1} = y^{trial} + \Delta\sigma_{ij}^{corrector}\frac{\partial y}{\partial \sigma_{ij}}\bigg|^{trial} + \Delta D\frac{\partial y}{\partial D}\bigg|^{trial} = 0 \tag{27}$$

where y^{k+1} is the updated yield surface, and $\frac{\partial y}{\partial \sigma_{ij}}|^{trial}$ and $\frac{\partial y}{\partial D}|^{trial}$ are the derivatives of the yield function at the trial stress state with respect to stress and the scalar damage variable, respectively. The explicit form of $\partial y/\partial\sigma_{ij}$ and $\partial y/\partial D$ are given in Appendix A.

In addition, by virtue of Eq. (16) the corrector stress can be given as:

$$\Delta\sigma_{ij}^{\text{corrector}} = -C_{ijkl}^k\Delta\varepsilon_{kl}^p + \frac{\partial C_{ijkl}}{\partial D} D_{klmn}^k \sigma_{mn}^{\text{trial}}\Delta D \tag{28}$$

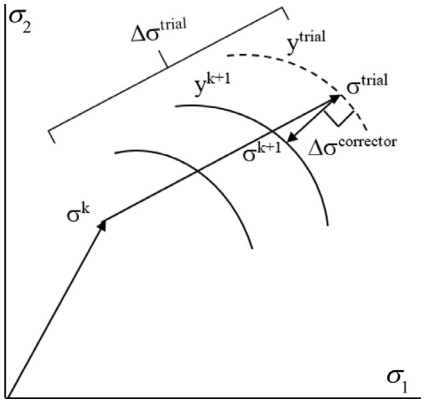

Fig. 2. An illustration of the stress return algorithm in two dimensions.

Please cite this article as: M. Mukherjee et al., Capturing pressure- and rate-dependent behaviour of rocks using a new damage-plasticity model, International Journal of Impact Engineering (2017), http://dx.doi.org/10.1016/j.ijimpeng.2017.01.006

Substitution of the flow rule and incremental damage variable into Eq. (27) and setting $y^{k+1} = 0$ results in:

$$\Delta\lambda = \frac{y^{trial}}{\left(\frac{\partial y}{\partial \sigma_{ij}} C^k_{ijkl} \frac{\partial g}{\partial \sigma_{kl}}\right) - \left\{\left(\frac{\partial y}{\partial \sigma_{ij}} \frac{\partial C_{ijkl}}{\partial D} D^k_{mnkl} \sigma^{trial}_{mn}\right) + \frac{\partial y}{\partial D}\right\}\left(\left(e^{-\epsilon^k_p}\right)\sqrt{\frac{2}{9}\left(A\frac{\partial g}{\partial p}\right)^2 + \left(B\frac{\partial g}{\partial q}\right)^2}\right)} \tag{29}$$

At each time step, $\Delta\lambda$ can be evaluated from the above expression, which can be further used to calculate $\Delta\varepsilon^p_{kl}$, ΔD, and $\Delta\sigma^{corrector}_{ij}$. The new stress increment and the updated stress state are given by the following relationships.

$$\Delta\sigma^{new}_{ij} = \Delta\sigma^{trial}_{ij} + \Delta\sigma^{corrector}_{ij} \tag{30}$$

$$\sigma^{k+1}_{ij} = \sigma^k_{ij} + \Delta\sigma^{new}_{ij} \tag{31}$$

4. Model responses: calibration and validation

In this section, the proposed material model is calibrated and validated against experimental data from triaxial tests on Augig Granite [56] and Gosford Sandstone [57]. This process is carried out by considering the mechanical behaviour of rock under both compressive and tensile loading conditions. In the case of tensile tests, the fracture energy (G_f) and tensile strength (σ_t) of rock are two key parameters considered during calibration. A local or specific fracture energy ($g_f = G_f/h$), which can be given as the area under the stress-strain curve in uniaxial tensile loading, is calculated and compared against the experimental data [58]. It should be noted that inclusion of the sample height (h) induces a length scale dependency into the characterisation of constitutive properties.

Model parameters associated with initial yield surface, p_{c0}, p_{t0}, α_0, γ, M_0 are calibrated using the data set showing softening response, specifically experiments with lower confinement. These parameter values are obtained iteratively by carrying out a best fit for the equation of yield surface (Eq. (6)) against the initial yield points for each data set (Fig. 3). The slope of the yield surface at failure, M_u, is identified by plotting the residual stress data in the p–q space and minimizing the error associated with the curve fitting, while for simplicity we take $M_0 = M_u$, ignoring the minor pre-peak hardening under shearing at low confining pressure. The calibration of initial yield and failure surfaces for the two rock types have been presented in Figs. 3 and 4, respectively. The elastic parameters, Young's modulus E and Poisson's ratio ν are calibrated using the initial stress-strain response of such data set.

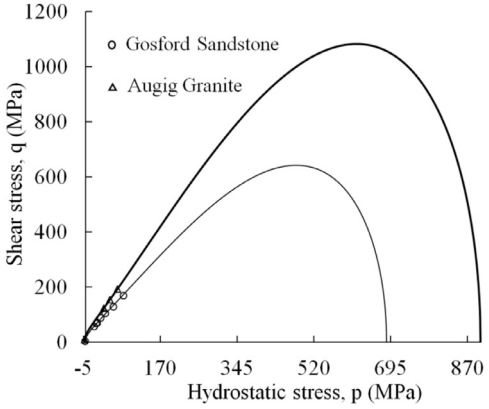

Fig. 3. Initial yield surface for Augig Granite and Gosford Sandstone.

The dilation (β) and damage evolution parameters, A and B, are calibrated for each rock type by comparing against their corresponding stress-strain and volumetric data from compressive and tensile tests. In order to perform the calibration in tensile regime, the magnitude of G_f and σ_t for these two rock specimens have been adopted from the literature. A value has been assumed for the specimen length (h) due to the lack of information regarding the specimen dimension in these uniaxial tension tests. Fig. 5 presents the model predictions for triaxial compression test of Gosford Sandstone over a range of confining pressures varying from 0 to 30 MPa. The stress-strain and volumetric behaviour have been compared against experimental data available for two different specimen diameters, i.e., 50 mm and 96 mm, respectively. A single set of material parameter has been calibrated for these two specimens and further employed for rock behaviour prediction. It can be observed from the figure that the model can adequately capture the brittle behaviour of rock at lower confinement and also predicts the gradual change in such responses due to increase in the confining pressure.

Fig. 6 illustrates the constitutive response of Augig Granite under triaxial compression. The material parameters for this case have been calibrated mainly by focusing on the stress-strain response, as limited data was available for the volumetric characterization. Similar to the previous case, the influence of confining stress has been well accounted for by the proposed model. At higher confining pressure, the model is also capable of predicting the ductile response along with the brittle-ductile transition for hard rocks like granite. The evolution of the initial yield surface with damage endows the

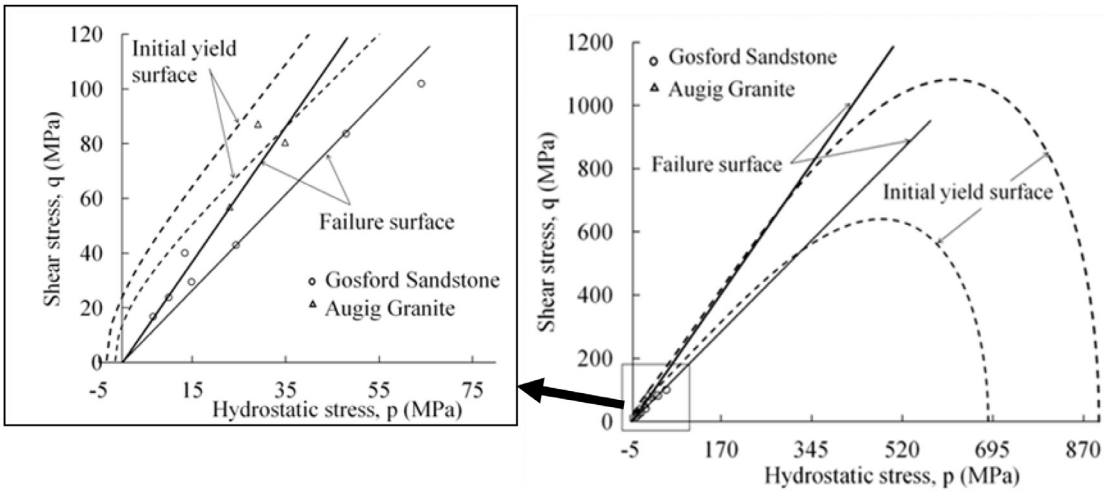

Fig. 4. Calibration of failure surface for Augig Granite and Gosford Sandstone.

Please cite this article as: M. Mukherjee et al., Capturing pressure- and rate-dependent behaviour of rocks using a new damage-plasticity model, International Journal of Impact Engineering (2017), http://dx.doi.org/10.1016/j.ijimpeng.2017.01.006

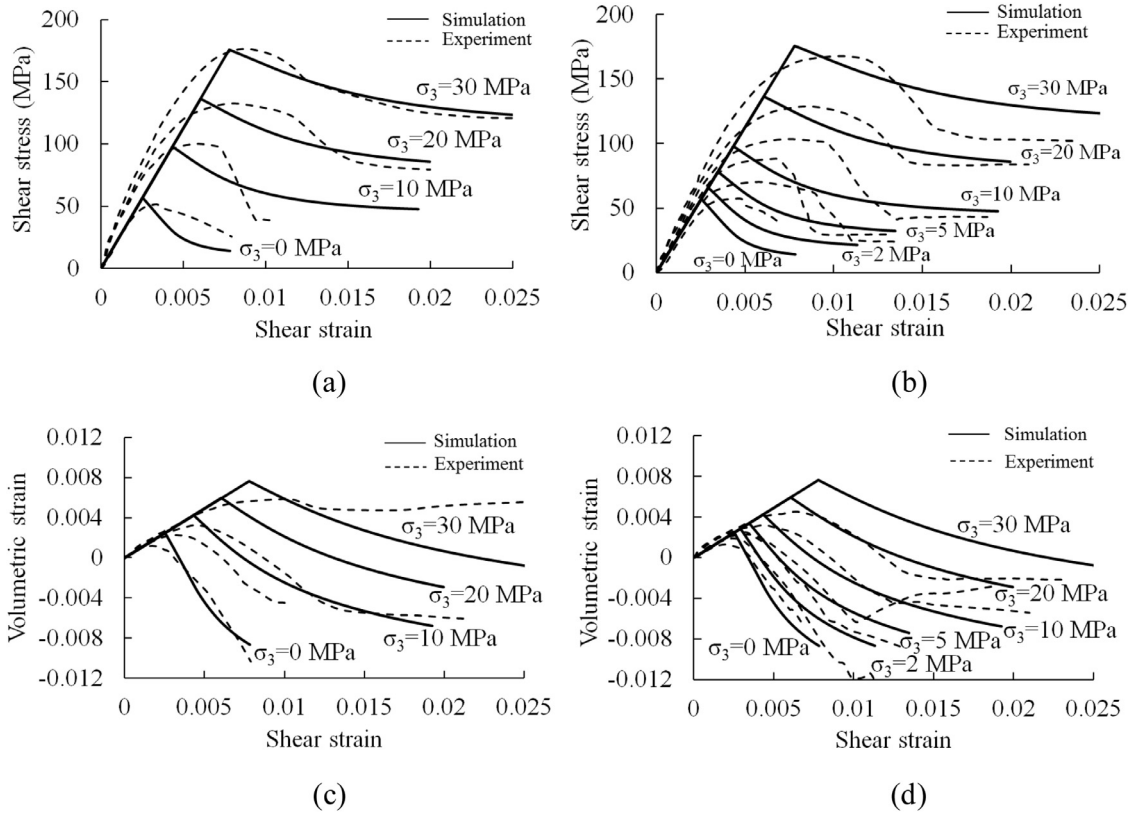

Fig. 5. (a, b) Stress-strain and (c, d) volumetric response for Gosford Sandstone under triaxial compression test; $E=17$ GPa, $\nu=0.13$, $p_{c0}=686$ MPa, $p_{t0}=-1.48$ MPa, $\alpha_0=0.245$, $\gamma=0.88$, $M_0=M_u=1.7$, $\beta=0.5$, $A=500$ and $B=100$ (experimental data for specimen with 50 mm (a, c) and 96 mm diameter (b, d)).

model with the ability of capturing such gradual transition from brittle to ductile behaviour with increasing confining stress. The details of the parameter sets used for the prediction of two rock types are mentioned in the relevant figures.

The behaviour in uniaxial tension predicted for Gosford Sandstone and Augig Granite is illustrated in Fig. 7. Due to the limited availability of experimental data related to the uniaxial test, the simulated tensile response for these two rocks could not be compared with the experiments. However, the obtained magnitudes of peak stresses comply well with their respective tensile strengths. As mentioned earlier, the post peak responses for such cases are primarily determined based on the material fracture energy and depend on the assumed sample size. The parameters used for tensile characterization are listed in the figure.

5. Rate-dependent enhancement

Strain rate is another important aspect that can significantly influence the rock behaviour. Such rate-dependent response of rock is of utmost importance for designing against dynamic loading, such as rock blast. Existing literature suggests that both compressive and tensile strength of dry intact rock increase significantly with increase in the strain rate [34,59–65]. In the quasi-static regime, i.e., 10^{-7}–10^{-2}/sec, the compressive strength was noticed to increase by 30–40% when the strain rate is increased by five orders of magnitude [59]. However, the rate induced strength increase becomes more prominent at higher confining pressure [66]. Furthermore, a marked increase in the dynamic compressive strength has been reported for an applied strain rate beyond 10/sec [64,67]. Apart from

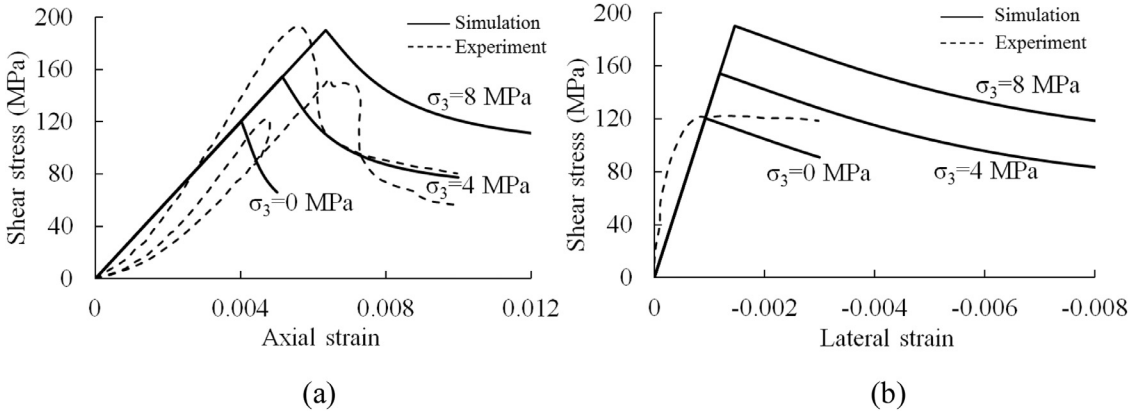

Fig. 6. Shear stress response of Augig Granite with (a) axial and (b) lateral strain under triaxial compression test; $E=30$ GPa, $\nu=0.23$, $p_{c0}=900$ MPa, $p_{t0}=-3.4$ MPa, $\alpha_0=0.195$, $\gamma=0.78$, $M_0=M_u=2.3$, $\beta=0.75$, $A=300$ and $B=30$.

Please cite this article as: M. Mukherjee et al., Capturing pressure- and rate-dependent behaviour of rocks using a new damage-plasticity model, International Journal of Impact Engineering (2017), http://dx.doi.org/10.1016/j.ijimpeng.2017.01.006

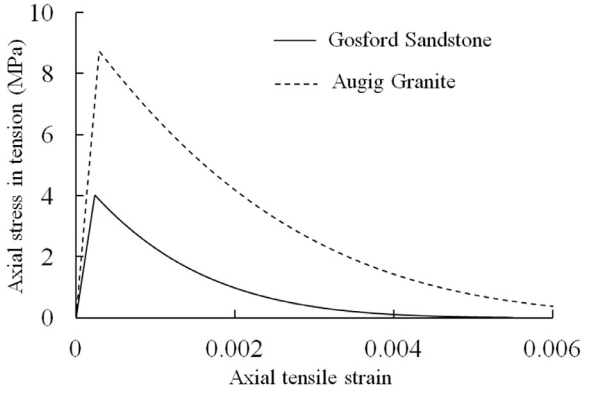

Fig. 7. Axial stress-strain response of Augig Granite ($G_f = 0.0872$ MPa mm, $\sigma_t = 8.8$ MPa, $h = 4.5$ mm) and Gosford Sandstone ($G_f = 0.02$ MPa mm, $\sigma_t = 4$ MPa, $h = 3.77$ mm) under uniaxial tension test.

strength increase, higher strain rates also result in a more ductile response of rocks even at low confining pressures [68].

A viscoplastic framework is often employed in order to model the behaviour of rate sensitive materials [69,70]. The rate-dependent extension of the proposed damage model has been implemented within the general framework of visco-plasticity following the overstress concept proposed by Perzyna [71]. The evolution of plastic strain is therefore given by the following modified flow rule:

$$\dot{\varepsilon}^p_{kl} = \frac{\langle y \rangle^m}{\eta} \frac{\partial g}{\partial \sigma_{kl}} \tag{32}$$

where η is the viscosity parameter, having the dimension $M^{-1}LT^3$; the power-law exponent m is a dimensionless coefficient, and $\langle y \rangle$ is the dimensionless overstress function derived from the rate-independent damage yield-function y. The McCauley bracket implies that:

$$\langle y \rangle = \begin{cases} y, & \text{when } y \geq 0, \text{ i.e. at inelastic state} \\ 0, & \text{when } y < 0, \text{ i.e. at elastic state} \end{cases} \tag{33}$$

It is important to note that, unlike conventional viscosity parameter, the parameter η has a inversed stress dimension due to dimensionless representation of the damaged yield function in the present model [72]. The viscosity parameter is calibrated in such a way that the material behaviour at quasi-static range predicted from the rate-dependent model becomes identical to the rate-independent response. The parameter m in Eq. (32) controls the rate-induced strength increase of the material over a strain rate range of concern. The proposed model attempts to address the rate-dependent response of dry intact rock and it does not consider the rate effects that are usually observed in moist rocks due to the development of pore pressure.

Unlike the consistency condition in rate-independent formulations, the Perzyna type framework provides an explicit form of the non-negative plastic multiplier which for the present model can be expressed as follows:

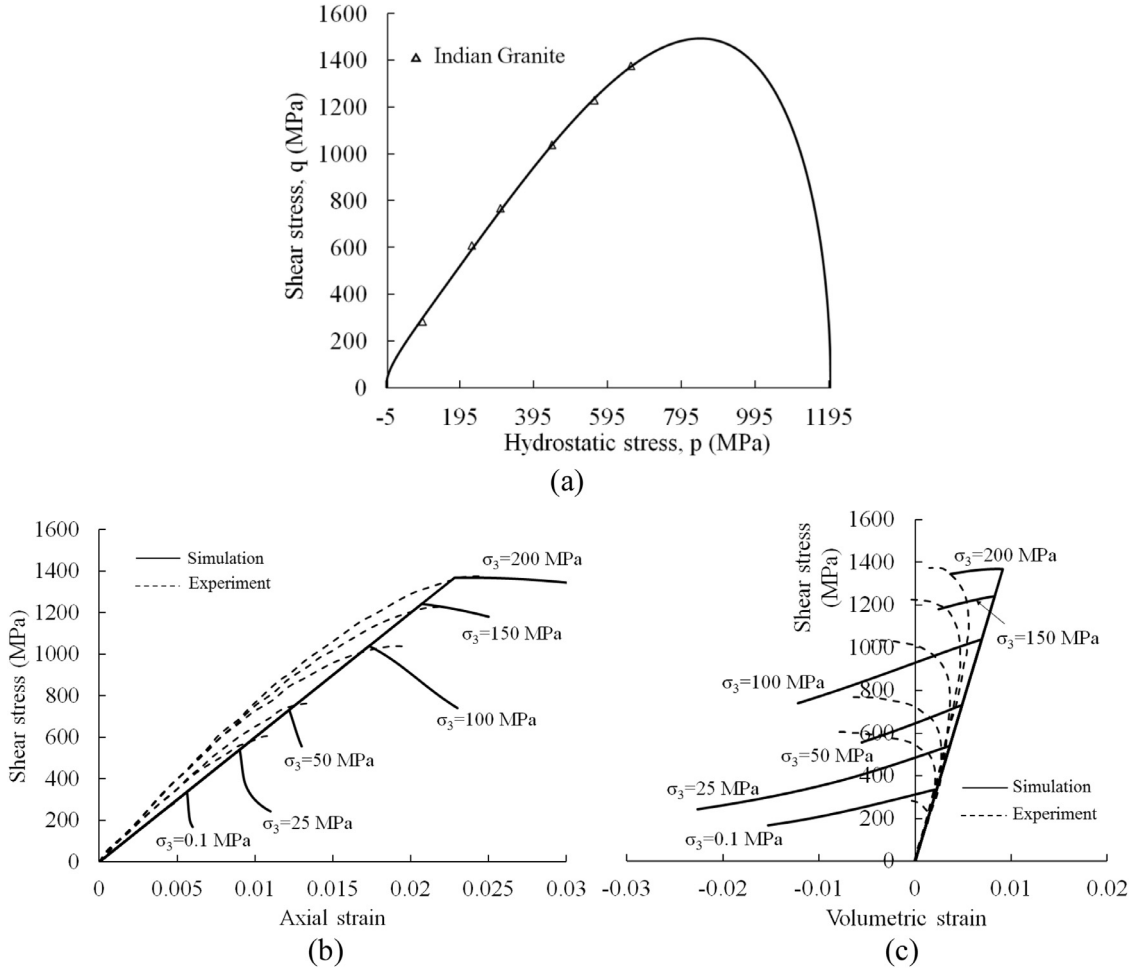

Fig. 8. Calibration and predictions of rate-independent behaviour of Indian granite (a) initial yield surface, (b) axial strain-shear stress and (c) volumetric strain-shear stress response.

Please cite this article as: M. Mukherjee et al., Capturing pressure- and rate-dependent behaviour of rocks using a new damage-plasticity model, International Journal of Impact Engineering (2017), http://dx.doi.org/10.1016/j.ijimpeng.2017.01.006

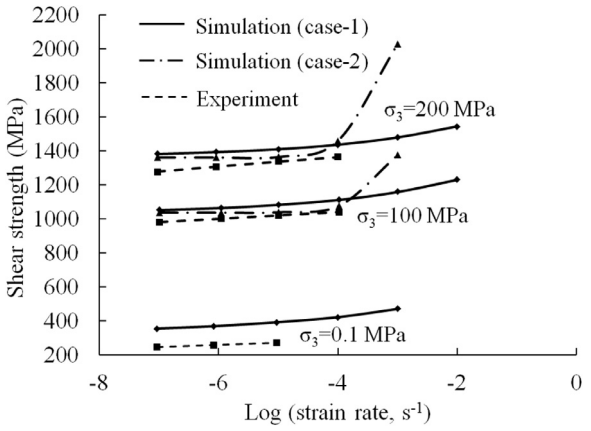

Fig. 9. Variation in shear strength of Indian Granite with strain rate at different confining pressure under triaxial compression.

$$d\lambda = \frac{\langle y \rangle^m}{\eta} dt \tag{34}$$

Eq. (32) along with Eq. (16) can be employed to obtain the stress update directly for a given strain increment.

The rate-dependent enhancement of the proposed damage model has been calibrated against the triaxial compression data available for Indian Granite at varying strain rates [66]. First, the rate-independent parameters are calibrated against the complete stress-strain-volumetric data at 10^{-5}/sec ($E = 60$ GPa, $\nu = 0.3$, $p_{c0} = 1200$ MPa, $p_{t0} = -4$ MPa, $\alpha_0 = 0.3$, $\gamma = 0.95$, $M_u = 2.2$, $M_0 = 1.7$, $\beta = 0.9$, $A = 50$ and $B = 50$). The detail calibration and rate-independent predictions are presented in Fig. 8. The available experimental results were restricted to the pre-peak regime and hence, necessary assumptions are made to capture the residual response. As expected at lower confinement (0–50 MPa), the rock exhibits strong brittle response with significant softening. However, a gradual change can be noticed in the post-peak softening response as the rock becomes more ductile with increasing the confinement.

The rate parameters are calibrated against the same data set (10^{-5}/sec strain rate) and the peak strengths are predicted for Indian Granite at different confining pressure and over a range of strain rate varying from 10^{-7}–10^{-2}/sec. The experimental observation along with the simulation predictions for two sets of rate-dependent parameter have been presented in Fig. 9 (case-1 with $\eta = 2 \times 10^{-11}$ s/Pa and $m = 5$, case-2 with $\eta = 1 \times 10^{-6}$ s/Pa and $m = 1$). The rate-dependent response of Indian Granite could be captured well at different confinement for the parameter set given by case-1. A strength increase of 15–20% has been noticed for this case as the strain rate increased from 10^{-7} to 10^{-2}/sec. A lower magnitude of parameter m results in much higher rate sensitivity which can be easily inferred from the predictions of two cases as presented in Fig. 9.

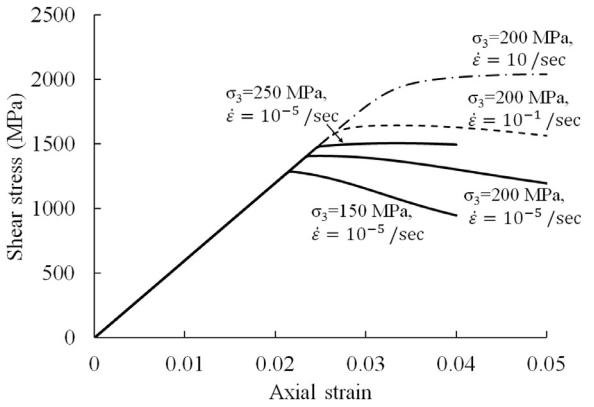

Fig. 11. Influence of strain rate on brittle-ductile transition for Indian Granite.

The mechanical response of rock can change significantly when the applied strain rate goes beyond 10/sec. [64]. The proposed model has been employed to further explore its applicability in predicting the rock behaviour at such high strain rates. The unconfined compressive strength (UCS) of Granite has been predicted over a strain rate range 26–88/sec ($\eta = 5 \times 10^{-12}$ s/Pa and $m = 1$) and compared against the experimental data of Zhang [64] in Fig. 10(a). The rate induced strength increase noted for this case is around 30–40%, which is captured by assigning a lower value of parameter m. Attempt has also been made to compare the shear strength predictions for other confining pressures at such higher rates. The same rate parameters are used to predict the compressive strength of Granite at three confining pressures with average strain rate of 75–82/sec and presented in Fig. 10(b). As can be seen, the numerical predictions compare fairly well with experimental observations at lower confinement. Such predictions can also be improved by a robust calibration which cannot be carried out here due to the lack of experimental data.

The influence of strain rate on brittle-ductile transition of rock has been further explored numerically using the parameter set calibrated for Indian Granite and the simulation results are presented in Fig. 11 in the form of stress-strain response. In case of 10^{-5}/sec strain

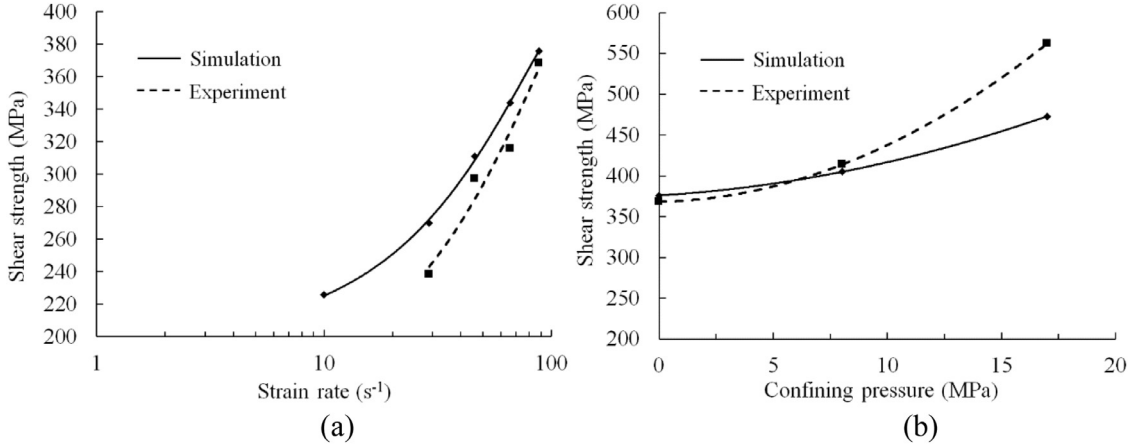

Fig. 10. Variation in shear strength of Granite - (a) UCS predictions over varying strain rate and (b) shear strength at different confining pressures for strain rate 75–82/sec.

Please cite this article as: M. Mukherjee et al., Capturing pressure- and rate-dependent behaviour of rocks using a new damage-plasticity model, International Journal of Impact Engineering (2017), http://dx.doi.org/10.1016/j.ijimpeng.2017.01.006

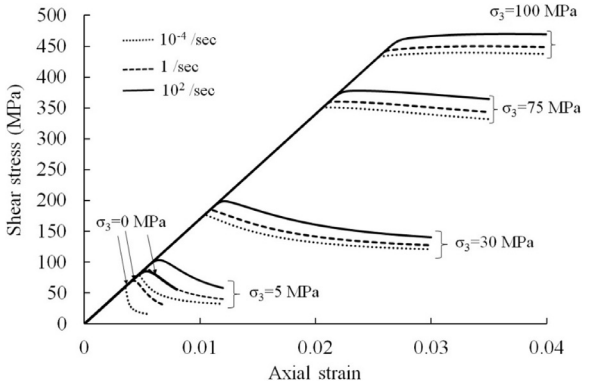

Fig. 12. Combined influence of confinement and strain rate on the stress-strain behaviour of Gosford Sandstone under triaxial compression ($\eta = 2.15 \times 10^{-16}$ s/Pa and $m = 5$).

rate, the brittle-ductile transition occurs around 250 MPa confining pressure. However, with increasing strain rate such transition can be achieved even at a lower confinement, e.g., at 200 MPa confining pressure with an axial strain rate 10/sec. Hence, the model can effectively capture the combined influence of pressure and strain rate on the brittle-ductile transition of hard rock. It is important to mention here that such rate-dependent modelling requires good quality experimental data representing compressive and tensile behaviour of rock at both quasistatic and high strain rate range; however, only few such experimental data are available in the literature and further work is required in this regard.

A parametric study has been carried out employing the proposed constitutive model to further explore the combined influence of confinement and strain rate on the rock behaviour qualitatively. The stress-strain data of Gosford Sandstone (from Section 4) has been considered to represent the rate-independent response and the rate parameter η is calibrated against an assumed rate-independent threshold strain rate of 10^{-4}/sec, using $m = 5$. The predicted stress-strain behaviour under triaxial compression has been shown in Fig. 12 at different confining pressure and strain rate. At lower confinement (0–5 MPa), significant amount of post peak softening has been noticed which gradually diminishes with increase in the confining pressure and finally a brittle-ductile transition occurs around 100 MPa. However, increase in the strain rate affects such post peak softening and results into a more ductile response. A general trend of increasing peak compressive strength has been noted with increasing strain rate over the whole confining regime. A similar trend has also been observed in the uniaxial tensile simulations which are presented in Fig. 13(a). However, the nature of post-peak softening response in this case nearly remains independent of the strain rate. The evolution of damage parameter under uniaxial tension has been shown in Fig. 13(b) for different strain rates. The rate of damage evolution decreases with increase in the strain rate which further causes an enhanced stress response for a given strain level.

6. Conclusions

We have proposed a new model taking into account the effects of both confining pressure and strain rate on the behaviour of rock. The proposed model is simple while versatile enough to capture a wide range of behaviour under the combined effects of confining pressure and strain rate. Its evolving yield function allows the description of both brittle and ductile responses, together with their transition, without requiring explicit softening/hardening law, while the rate-dependent enhancement relies on a single viscosity parameter and is effective for a wide range of confining pressures. Tests against experiments show promising features of the model in predicting complex behaviour of rocks under different loading conditions. This is essential for the analysis of large scale failure in mining and resource engineering. On the other hand, the present model still needs improvements to take into account the rate dependency induced by pore pressures in moist rocks.

Acknowledgements

This work was supported by the Australian Research Council through Discovery Projects DP140100945 (Shen, Nguyen, El-Zein, Maggi), FT140100408 (Nguyen), and DP160100775 (Bui).

Appendix A

The explicit form of the stress and damage derivatives of the yield surface and plastic potential have been discussed here. The stress derivatives are as follows:

$$\frac{\partial y}{\partial \sigma_{ij}} = \frac{\partial y}{\partial p}\frac{\partial p}{\partial \sigma_{ij}} + \frac{\partial y}{\partial q}\frac{\partial q}{\partial J_2}\frac{\partial J_2}{\partial \sigma_{ij}}$$

$$\frac{\partial g}{\partial \sigma_{ij}} = \frac{\partial g}{\partial p}\frac{\partial p}{\partial \sigma_{ij}} + \frac{\partial g}{\partial q}\frac{\partial q}{\partial J_2}\frac{\partial J_2}{\partial \sigma_{ij}}$$

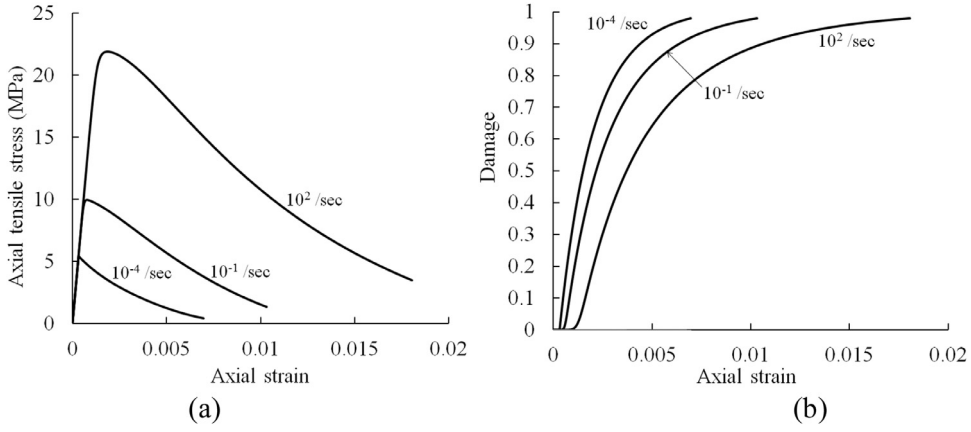

Fig. 13. Influence of strain rate on the (a) stress-strain response of Gosford Sandstone under uniaxial tension and (b) subsequent damage evolution ($\eta = 2.15 \times 10^{-16}$ s/Pa and $m = 5$).

$$\frac{\partial y}{\partial p}=2\left[\frac{(1-D)^2(p-\rho)}{\left\{\frac{(1-\gamma)p_c-p_t}{p_c+p_t}p+\frac{1}{2}(1-D)\gamma p_c\right\}^2}-\frac{(1-D)^2(p-\rho)^2}{\left\{\frac{(1-\gamma)p_c-p_t}{p_c+p_t}p+\frac{1}{2}(1-D)\gamma p_c\right\}^3}\times\left\{\frac{(1-\gamma)p_c-p_t}{p_c+p_t}\right\}-\frac{q^2}{M^2}\frac{(1-\alpha)}{\{p-\alpha(p-\rho)\}^3}\right]$$

$$\frac{\partial y}{\partial q}=2\frac{q}{M^2\{p-\alpha(p-\rho)\}^2}$$

$$\frac{\partial g}{\partial p}=2\left[\frac{(1-D)^2(p-\rho)}{\left\{\frac{(1-\gamma)p_c-p_t}{p_c+p_t}p+\frac{1}{2}(1-D)\gamma p_c\right\}^2}-\frac{(1-D)^2(p-\rho)^2}{\left\{\frac{(1-\gamma)p_c-p_t}{p_c+p_t}p+\frac{1}{2}(1-D)\gamma p_c\right\}^3}\times\left\{\frac{(1-\gamma)p_c-p_t}{p_c+p_t}\right\}-\frac{\beta^2q^2}{M^2}\frac{(1-\alpha)}{\{p-\alpha(p-\rho)\}^3}\right]$$

$$\frac{\partial g}{\partial q}=\beta^2\frac{\partial y}{\partial q}$$

The derivative of yield surface with respect to damage variable is given below:

$$\frac{\partial y}{\partial D}=2\left[\frac{I_1}{I_2^3}\left\{\frac{\partial I_1}{\partial D}I_2-I_1\frac{\partial I_2}{\partial D}\right\}-\frac{q^2}{I_3^3}\frac{\partial I_3}{\partial D}\right]$$

where,

$$I_1=(1-D)(p-\rho)$$

$$I_2=\frac{(1-\gamma)p_c-p_t}{p_c+p_t}p+\frac{1}{2}(1-D)\gamma p_c$$

$$I_3=M\{p-\alpha(p-\rho)\}$$

$$\frac{\partial I_1}{\partial D}=(1-D)\left[-\frac{(4-\gamma)p_{c0}p_t-2(4-\gamma)p_cp_{t0}+2\gamma p_cp_{c0}}{4(p_c+p_t)}+\frac{\{(4-\gamma)p_cp_{t+}\gamma p_c{}^2\}(p_{c0}-2p_{t0})}{4(p_c+p_t)^2}\right]-(p-\rho)$$

$$\frac{\partial I_2}{\partial D}=p\left[\frac{(1-\gamma)p_{c0}+2p_{t0}}{2(p_c+p_t)}-\frac{\{(1-\gamma)p_c-p_t\}\{p_{c0}-2p_{t0}\}}{2(p_c+p_t)^2}\right]+\frac{1}{4}(1-D)\gamma p_{c0}-\frac{1}{2}\gamma p_c$$

$$\frac{\partial I_3}{\partial D}=(-M_0+M_u)\{p-\alpha(p-\rho)\}+M\left[\frac{\alpha_0}{2\sqrt{1-D}}(p-\rho)+\alpha\frac{(4-\gamma)p_{c0}p_t-2(4-\gamma)p_cp_{t0}+2\gamma p_cp_{c0}}{4(p_c+p_t)}-\frac{\{(4-\gamma)p_cp_{t+}\gamma p_c{}^2\}(p_{c0}-2p_{t0})}{4(p_c+p_t)^2}\right]$$

References

[1] Gowd TN, Rummel F. Effect of confining pressure on the fracture behaviour of a porous rock. Int J Rock Mech Min Sci Geomech Abstr 1980;17(4).
[2] Wong T. Effects of temperature and pressure on failure and post-failure behavior of Westerly granite. Mech Mater 1982;1(1):3–17.
[3] Evans B, Fredrich JT, Wong TF. The brittle–ductile transition in rocks: recent experimental and theoretical progress. The brittle-ductile transition in rocks; 19901–20.
[4] Paterson MS. Rock deformation experimentation. The brittle-ductile transition in rocks; 1990187–94.
[5] Menéndez B, Zhu W, Wong TF. Micromechanics of brittle faulting and cataclastic flow in Berea sandstone. J Struct Geol 1996;18(1):1–16.
[6] Amitrano D. Brittle–ductile transition and associated seismicity: Experimental and numerical studies and relationship with the b value. J Geophys Res: Solid Earth 2003;108(B1).
[7] Nygard R, Gutierrez M, Bratli RK, Høeg K. Brittle–ductile transition, shear failure and leakage in shales and mudrocks. Mar Pet Geol 2006;23(2):201–12.
[8] Arzúa J, Alejano L. Dilation in granite during servo-controlled triaxial strength tests. Int J Rock Mech Min Sci 2013;61:43–56.
[9] Zhao X, Cai M, Wang J, Ma L. Damage and acoustic emission characteristics of the Beishan granite. Int J Rock Mech Min Sci 2013;64:258–69.
[10] Chen L, Wang C, Liu J, Liu J, Wang J, Jia Y, et al. Damage and plastic deformation modelling of Beishan granite under compressive stress conditions. Rock Mech Rock Eng 2015;48:1623–33.
[11] Rummel F, Fairhurst C. Determination of the post-failure behavior of brittle rock using a servo-controlled testing machine. Rock Mech 1970;2(4):189–204.
[12] Peng SS. A note on the fracture propagation and time-dependent behavior of rocks in uniaxial tension. Int J Rock Mech Min Sci Geomech Abstr 1975;12 (4):125–7.
[13] Mitra G. Brittle to ductile transition due to large strains along the White Rock thrust, Wind River Mountains, Wyoming. J Struct Geol 1984;6(1-2):51–61.
[14] Gary G, Bailly P. Behaviour of quasi-brittle material at high strain rate. Experiment and modelling. Eur J Mech-A/Solids 1998;17(3):403–20.
[15] Shan R, Jiang Y, Li B. Obtaining dynamic complete stress–strain curves for rock using the split Hopkinson pressure bar technique. Int J Rock Mech Min Sci 2000;37(6):983–92.
[16] Frew DJ, Akers SA, Chen W, Green ML. Development of a dynamic triaxial Kolsky bar. Meas Sci Tech 2010;21(10):105704.
[17] Cadoni E. Dynamic characterization of orthogneiss rock subjected to intermediate and high strain rates in tension. Rock Mech Rock Eng 2010;43(6):667–76.
[18] Huang B, Liu J. The effect of loading rate on the behavior of samples composed of coal and rock. Int J Rock Mech Min Sci 2013;61:23–30.
[19] Brantut N, Heap MJ, Baud P, Meredith PG. Rate–and strain–dependent brittle deformation of rocks. J Geophys Res: Solid Earth 2014;119(3):1818–36.
[20] Wong T. Micromechanics of faulting in Westerly granite. Int J Rock Mech Min Sci Geomech Abstr 1982;19:19–49.
[21] Fredrich J, Wong T. Micromechanics of thermally induced cracking in three crustal rocks. J Geophys Res 1986;91(B12):12743–64.
[22] Martin C, Chandler N. The progressive fracture of Lac du Bonnet granite. Int J Rock Mech Min Sci Geomech Abstr 1994;31(6):643–59.
[23] Oda M, Takemura T, Aoki T. Damage growth and permeability change in triaxial compression tests of Inada granite. Mech Mater 2002;34:313–31.
[24] Paterson MS, Wong TF. Experimental rock deformation-the brittle field. Springer Science & Business Media; 2005.
[25] Dieterich JH. Time–dependent friction in rocks. J Geophys Res 1972;77 (20):3690–7.
[26] Dieterich JH. Time-dependent friction and the mechanics of stick-slip. Pure Appl Geophys 1978;116(4-5):790–806.
[27] Johnson T. Time–dependent friction of granite: Implications for precursory slip on faults. J Geophys Res: Solid Earth 1981;86(B7):6017–28.
[28] Di Toro G, Goldsby DL, Tullis TE. Friction falls towards zero in quartz rock as slip velocity approaches seismic rates. Nature 2004;427(6973):436–9.
[29] Ben-David O, Cohen G, Fineberg J. Short-time dynamics of frictional strength in dry friction. Tribol Lett 2010;39(3):235–45.
[30] Li QM, Meng H. About the dynamic strength enhancement of concrete-like materials in a split Hopkinson pressure bar test. Int J Solids Struct 2003;40(2):343–60.
[31] Sano O, Ito I, Terada M. Influence of strain rate on dilatancy and strength of Oshima granite under uniaxial compression. J Geophys Res: Solid Earth 1981;86 (B10):9299–311.
[32] Lajtai EZ, Duncan ES, Carter BJ. The effect of strain rate on rock strength. Rock Mech and Rock Eng 1991;24(2):99–109.
[33] Li Y, Xia C. Time-dependent tests on intact rocks in uniaxial compression. Int J Rock Mech Min Sci 2000;37(3):467–75.
[34] Cho SH, Ogata Y, Kaneko K. Strain-rate dependency of the dynamic tensile strength of rock. Int J Rock Mech Min Sci 2003;40(5):763–77.
[35] Qi C, Wang M, Qian Q. Strain-rate effects on the strength and fragmentation size of rocks. Int J Impact Eng 2009;36(12):1355–64.
[36] Okubo S, Hashiba K, Fukui K. Loading rate dependency of the strengths of some Japanese rocks. Int J Rock Mech Min Sci 2013;58:180–5.
[37] Wong TF, Baud P. The brittle-ductile transition in porous rock: a review. J Struct Geol 2012;44:25–53.
[38] Chiarelli A, Shao J, Hoteit N. Modelling of elastoplastic damage behaviour of a claystone. Int J Plast 2003;19:23–45.
[39] Salari M, Saeb S, William K, Pachet S, Carrasco R. A coupled elastoplastic damage model for geomaterials. Comp Methods Appl Mech Eng 2004;193:2625–43.
[40] Zhou C, Zhu F. An elasto-plastic damage constitutive model with double yield surfaces for saturated soft rock. Int J Rock Mech Min Sci 2010;47:385–95.
[41] Unteregger D, Fuchs B, Hofstetter G. A damage plasticity model for different types of intact rock. Int J Rock Mech Min Sci 2015;80:402–11.
[42] Lyakhovsky V, Zhu W, Shalev E. Visco-poroelastic damage model for brittle-ductile failure of porous rocks. J Geophys Res: Solid Earth 2015;120:2179–99.
[43] Chen L, Shao J, Huang H. Coupled elastoplastic damage modelling of anisotropic rocks. Comput Geotech 2010;37:187–94.
[44] Zhang J, Xu W, Wang H, Wang R, Meng Q, Du S. A coupled elastoplastic damage model for brittle rocks and its application in modelling underground excavation. Int J Rock Mech Min Sci Geomech Abstr 2016;84:130–41.
[45] Hansen N, Schreyer H. Thermodynamically consistent theories for elastoplasticity coupled with damage. Albuquerque, NM (United States): Sandia National Labs.; 1992.
[46] Shao JF, Jia Y, Kondo D, Chiarelli AS. A coupled elastoplastic damage model for semi-brittle materials and extension to unsaturated conditions. Mech Mater 2006;38:218–32.
[47] Parisio F, Samat S, Laloui L. Constitutive analysis of shale: a coupled damage plasticity approach. Int J Solids Struct 2015;75:88–98.

Please cite this article as: M. Mukherjee et al., Capturing pressure- and rate-dependent behaviour of rocks using a new damage-plasticity model, International Journal of Impact Engineering (2017), http://dx.doi.org/10.1016/j.ijimpeng.2017.01.006

[48] Pouya A, Yazdi PB. A damage-plasticity model for cohesive fractures. Int J Rock Mech Min Sci 2015;73:194–202.
[49] Issen K, Rudnicki J. Theory of compaction bands in porous rock. Phys Chem Earth, Part A 2001;26:95–100.
[50] Krätzig WB, Pölling R. An elasto-plastic damage model for reinforced concrete with minimum number of material parameters. Comput Geotech 2004;82 (15):1201–15.
[51] Lubliner J, Oliver J, Oller S, Onate E. A plastic-damage model for concrete. Int J Solids Struct 1989;25(3):299–326.
[52] Abu-Lebdeh TM, Voyiadjis GZ. Plasticity-damage model for concrete under cyclic multiaxial loading. J Eng Mech 1993;119(7):1465–84.
[53] Mir A, Nguyen GD, Sheikh AH, Vu VD. Modelling dilatant and contractive behaviour in soft rocks. In: International conference on geomechanics, geo-energy and geo-resources IC3G; 2016.
[54] Nguyen GD, Korsunsky AM, Belnoue JP. A nonlocal coupled damage-plasticity model for the analysis of ductile failure. Int J Plast 2015;64:56–75.
[55] Crisfield M. Non-linear finite element analysis of solids and structures. West Sussex, England: John Wiley & Sons; 2000.
[56] Kazerani T. Effect of micromechanical parameters of microstructure on compressive and tensile failure process of rock. Int J Rock Mech Min Sci 2013;64:44–55.
[57] Masoumi H, Douglas KJ, Russell AR. A bounding surface plasticity model for intact rock exhibiting size-dependent behaviour. Rock Mech Rock Eng 2016;49:47–62.
[58] Nguyen GD. A thermodynamic approach to constitutive modelling of concrete using damage mechanics and plasticity theory. Trinity College, University of Oxford; 2005.
[59] Donath FA, Fruth LS. Dependence of strain-rate effects on deformation mechanism and rock type. J Geol Soc 1971;79:343–71.
[60] Blanton TL. Effect of strain rate from 10^{-2} to 10 sec^{-1} in triaxial compression tests on three rocks. Int J Rock Mech Min Sci Geomech Abstr 1981;18(1):47–62.
[61] Olsson WA. The compressive strength of tuff as a function of strain rate from 10^{-6} to 10^{3}/sec. Int J Rock Mech Min Sci Geomech Abstr 1991;28(1):115–8.
[62] Li HB, Zhao J, Li TJ. Triaxial compression tests on a granite at different strain rates and confining pressures. Int J Rock Mech Min Sci 1999;36:1057–63.
[63] Zhao J, Li HB, Wu MB, Li TJ. Dynamic uniaxial compression tests on a granite. Int J Rock Mech Min Sci 1999;36(2):273–7.
[64] Zhang Q. Mechanical behaviour of rock materials under dynamic loading. Rock Mechanics Laboratory, Swiss Federal Institute of Technology in Lausanne; 2014.
[65] Wasantha PLP, Ranjith PG, Zhao J, Shao SS, Permata G. Strain rate effect on the mechanical behaviour of sandstones with different grain sizes. Rock Mech Rock Eng 2015;48:1883–95.
[66] Masuda K, Mizutani H, Yamada I. Experimental study of strain-rate dependence and pressure dependence of failure properties of granite. J Phys Earth 1987;35:37–66.
[67] Qian Q, Qi C, Wang M. Dynamic strength of rocks and physical nature of rock strength. J Rock Mech Geotech Eng 2009;26(1):1–10.
[68] Sato K, Kawakita M, Kinoshita S. The dynamic fracture properties of rocks under confining pressure, 15. Japan: Hokkaido University; 1981. p. 467–78.
[69] Wang WM, Sluys LJ, De Borst R. Viscoplasticity for instabilities due to strain softening and strain-rate softening. Int J Numer Methods Eng 1997;40(20):3839–64.
[70] Etse G, William K. Failure analysis of elastoviscoplastic material models. J Eng Mech 1999;125(1):60–9.
[71] Perzyna P. Fundamental problems in viscoplasticity. Adv Appl Mech 1966;9:243–377.
[72] Das A. A theoretical study of grain crushing induced compaction localisation in porous sandstone. School of Civil Engineering, The University of Sydney; 2013.

Please cite this article as: M. Mukherjee et al., Capturing pressure- and rate-dependent behaviour of rocks using a new damage-plasticity model, International Journal of Impact Engineering (2017), http://dx.doi.org/10.1016/j.ijimpeng.2017.01.006